Analysis Of The Isotropy Of The Cosmic Microwave Background Temperature Anisotropies

A thesis submitted in partial fulfilment of the requirements
for the award of the degree of

DOCTOR OF PHILOSOPHY

by

MD ISHAQUE KHAN

160509

to the

DEPARTMENT OF PHYSICS

INDIAN INSTITUTE OF SCIENCE EDUCATION AND RESEARCH BHOPAL

Bhopal – 462 066

June, 2023

Analysis Of The Isotropy Of The Cosmic Microwave Background Temperature Anisotropies

A thesis submitted in partial fulfilment of the requirements
for the award of the degree of

DOCTOR OF PHILOSOPHY

by

MD ISHAQUE KHAN

160509

to the

DEPARTMENT OF PHYSICS

INDIAN INSTITUTE OF SCIENCE EDUCATION AND RESEARCH BHOPAL

Bhopal – 462 066

June, 2023

CERTIFICATE

The undersigned have examined the Ph.D. thesis entitled:

Analysis Of The Isotropy Of The Cosmic Microwave Background Temperature Anisotropies

presented by Md Ishaque Khan, a candidate for the degree of Doctor of Philosophy in Physics, and hereby certify that it is worthy of acceptance.

[Date]

[Signature]
[Name of the oral board examiner]
External Examiner

[Signature]
[Name of the oral board examiner]
Supervisor

[Signature]
[Name of the oral board examiner]
Member

[Signature]
[Name of the oral board examiner]
Member

[Signature]
[Name of the oral board examiner]
Member

ACADEMIC INTEGRITY AND COPYRIGHT DISCLAIMER

I hereby declare that this thesis is my own work and, to the best of my knowledge, it contains no materials previously published or written by any other person, or substantial proportions of material which have been accepted for the award of any other degree or diploma at IISER Bhopal or any other educational institution, except where due acknowledgement is made in the thesis.

I certify that all copyrighted material incorporated into this thesis is in compliance with the Indian Copyright (Amendment) Act, 2012 and that I have received written permission from the copyright owners for my use of their work, which is beyond the scope of the law. I agree to indemnify and save harmless IISER Bhopal from any and all claims that may be asserted or that may arise from any copyright violation.

Md. Ishaque Khan

June 2023
IISER Bhopal

Md Ishaque Khan

ACKNOWLEDGEMENTS

About seven years ago, in 2016, I along with several other fresh graduates with Bachelor's degrees plunged headlong into a programme which was envisaged to provide us both Masters and Ph.D. degrees in Physics, at IISER Bhopal. Since then, I have met and interacted with some absolutely amazing and intuitive individuals, both students and teachers, who have benefited me immensely with respect to academics or by keeping my morale high in times of distress. Many individuals I have known left, many fresh entrants arrived in campus, and while I have waited for my caravan to reach its destination, it all feels worthwhile.

I wish to convey my sincerest gratitude to my supervisor, Dr. Rajib Saha for constant encouragement, support and guidance with regard to novel and interesting approaches of inspecting cosmological anomalies, (as we apprehensively eschew calling them). My teachers, Dr. Subhash Chaturvedi, Dr. Sukanta Panda, Dr. Snigdha Thakur, Dr. Ambar Jain, Dr. Suvankar Dutta, Dr. Nabamita Banerjee, Dr. Ritam Mallick, Dr. Nirmal Ganguli, Dr. Sebastian Wuester, Dr. Sunil Pratap Singh, Dr. Suhas Gangadharaiah and Dr. Auditya Sharma for grooming us into curious, incisive young physicists (I hope we can call ourselves that now!). I was privileged to meet Dr. Daniel J. Chung of the University of Wisconsin, Madison through the S.N. Bose Scholars Program, and to learn so much from him about theoretical cosmology and the fact that being rigorously industrious in academia is the only way to thrive in it. I am especially grateful to my Integrated Ph.D. batchmates Riyanka, Kaustav, Vinod, Kushal, Santu, and Chandan, for staying aboard this ship with me, and also to other batchmates who left at different junctures: Harshit, Sachin, Vivek, and Dipankar, for starting out this rewarding odyssey together. I further thank my seniors and group members, Ujjal, and Vipin for being simply a text message away whenever I have needed help related to research, in addition to Albin, Sarvesh and Srikanta for making my academic life wholesome.

As my life in IISERB unfolded, I met several people in diverse areas of perfoming arts and creative writing. My stints with Hoonkaar, the street play group of IISERB, Uday, the Institute Magazine, and Uttarang, the Music Club of IISERB nurtured and nourished my soul as I befriended some amazing individuals like Akanksha, Rahul, Faizan, Yagna, Yudhajit, Viplav, Radhika, Anand, Vibhuti, Aayushi, Antara, Hitaishi, Aditya, Gourilekshmi, Arjav, Jatin, Alankrit, Sonal, Nikhila, Shamim, Arghya, Sourayan, Subhadip, Shreeja, Muktajyoti, Amey, Revati, Saurav, and Chinmayi, with whom I have had some very interesting discussions, and learnt and questioned various ideologies and themes relating to the arts in particular, and their juxtaposition with the elistism of Science. Further, I wish to extend my sincere gratitude and affection to Shreeja, Shamim, and Muktajyoti for being my chosen subfamily within the Music Club.

Many of such IISERB fellows have become friends for life, and I am highly indebted to them for being part and parcel of many circumstances where I have had to endure life and they've been there to support me. My special thanks goes out to Shreeja, Tanishka, Avni, Upasana, Rahul, Akanksha, Viplav and Aamna, for being there, and for holding views similar to my own while most of the world around us runs differently. You all have fortified my resolve at times which Rudyard Kipling describes in his didactic poem 'If': "If you can keep your head when all about you / Are losing theirs and blaming it on you,...". Further, I am thankful for many recently strengthened friendships with Misha, Sai, Nitu, Amey and Rohit, who have augmented my life at IISERB with their charming presence.

I feel blessed to have grown under the tutelage of my teachers from Scottish Church College, where I completed my undergraduate studies: Dr. Jayeeta Chowdhury, Dr. Upendranath Nandi, Dr. Arup Roychoudhury, Dr. Joydip Mitra, Dr. Pradipta Kumar Mandal, Dr. Satadal Bhattacharyya, and Dr. Rabindranath Sasmal, for their relentless endorsement of understanding the minutest details in Physics which has inspired me to delve deeper in my courses, and also in research, instead of limiting myself to scraping the surface. Further, I thank my batchmates there, Soumalya, Barun, Aditya, Asif, Amitrajit, Baibhab, Ayantika, Bahnishikha, Anirban, Saunav, Nirnoy, Jibak, and Amit, for making my college days filled with fun and the zing of a competitive fervour. I also thank my private tuition teacher, Sanju Da whose lectures after college added to my learning by providing novel perspectives, especially when my family was undergoing a difficult time at home.

I am indebted to my sister for giving me the necessary impetus to take up Physics as my

Honours subject as a Bachelor's student, and for always being there during my formative years in school, by help me undergo those twelve hour crash courses before exams, especially when Mummy had become very busy with work. There is absolutely no volume of writing that can do justice to an acknowledgement of the efforts my father and mother have undertaken painstakingly to raise my sister and myself. They have taught me lessons before my school would, inspired me to stay curious and to study hard; they have cared for me and protected me in every walk of my life, and quite surprisingly, despite all odds they have never let me feel that we are deprived in any way: in fact, I have always felt the exact opposite! Their constant presence in my life is a surreal blessing. Even to this day, I keep them apprised of my academic pursuits, and they help me through thick and thin. They are paragons of unconditional love and empathy. Also, Khalammi for being such an invaluably nurturing presence in my life. I have imbibed those virtuous gems of endurance and kindness from you. I wish you had lived longer to see my progress today. I wish to convey my heartfelt thanks to Uncle Abbu for nurturing my initial love for Chemistry by purchasing chemicals and lab equipment when I was still a child, Chhote Abbu for inspiring art and craft and gardening, and for recreational lessons in Maths, and Anita Aunty, and Atique Bhaijan for support, love and prayers.

As I write this piece, I am sitting in the library, watching the rains pour incessantly, as they have been over the past few days. IISER Bhopal has an aesthetic charm and wonder, in terms of its infrastructure and natural ambience, which have been absolutely indispensable to my growth as a researcher. I wish to therefore also thank the Institute for its opulent resources, including the library, which has been my haunt for most years of my Ph.D. life, so much so that people have spoken in jest, "The Library is Ishaque's office". Suddenly there is a clap of thunder and my eyes swiftly look out of the window to my left, while the trees sway in a lovely breeze, and the moist and wet surroundings beckon the chirpings of birds anew, as our campus prepares for a new semester. It was probably around this time that we had arrived at IISERB, and the time has possibly come to say farewell.

DEDICATION

To Mummy who taught me the charms of good diction,

To Abba who groomed me to question and strategise;

For Ma’s journey of constant toil serving inspiration,

And Abba’s advice on how diligence is sans condition,

Have built up the edifice that my labours characterise.

ABSTRACT

One of the foundational assumptions of the Standard Model of Cosmology is that of isotropy of the universe on its largest scales. The Cosmic Microwave Background (CMB) temperature anisotropy field has been mapped over the full sky with good precision, and reasonably high signal-to-noise ratio, making it one of the most suitable probes of the early universe. Cosmic inflation is hypothesised to have facilitated the large scale homogeneity and isotropy of the universe, while also contributing to the growth of small fluctuations that resulted in large scale structures today. The primordial power spectrum of these perturbations is thus expected to be rotationally invariant due to the absence of any preferred direction. This leads to the rotational invariance of the two-point angular correlation of temperature anisotropies of the CMB, known as Statistical Isotropy (SI).

Under the assumption of SI, we expect (a) the spherical harmonic coefficients and hence the estimator for the angular power spectrum of the CMB temperature anisotropies to be uncorrelated, (b) the local extrema or hot and cold spots of the CMB to be distributed uniformly on the 2-sphere of observation, and (c) that one must not be able to find a preferred direction which violates SI. With this three-fold motivation, we subject the CMB temperature anisotropies to three novel investigations: (a) in the harmonic space, we analyse the spacings of the CMB temperature angular power spectrum (APS) to understand the nature of correlations in the APS, (b) in pixel or real space, we study the overall distribution of the local extrema of the CMB temperature anisotropies to measure their strength of isotropy, and (c) we employ Machine Learning for detecting the preferred direction which modulates the CMB temperature fluctuations.

In our first work, we present a novel technique to understand any possible correlations of the APS measures (C_ℓ and $\mathcal{D}_\ell = \frac{\ell(\ell+1)}{2\pi} C_\ell$) of the foreground-cleaned CMB temperature anisotropy maps. We derive our motivation from the concepts of level clustering and repulsion for uncorrelated and correlated eigenvalues of random matrix eigenvalues, by analysing their level spacings. In case of statistically isotropic CMB, the spacings of C_ℓ's

and $\mathcal{D}_\ell$'s closely obey Poisson statistics whereas on introducing correlations, the distribution changes appropriately to a form of Wigner-Dyson statistics. We devise an average spacing estimator that helps discern departures from the null hypothesis of statistically isotropic and uncorrelated APS measures of the CMB. With full sky coverage, we analyse WMAP 9 year ILC and 2018 Planck foreground-cleaned maps of Commander, NILC and SMICA. When no distinctions of the multipoles based on parity are considered, we see that the average spacings agree with theoretical expectations. When distinctions based on parity are considered, the average spacings between even multipoles are found to be unusually small for C_ℓ's at $\geq 98.86\%$ C.L., and for $\mathcal{D}_\ell$'s at $\geq 95.07\%$ C.L. We repeat our analysis on 10^3 inpainted (constrained Gaussian) realisations of the masked foreground-cleaned maps. We show using the Planck $U73$ and WMAP $KQ75$ masks with and without a mask for the non-Gaussian cold spot (NGCS), that all the foreground cleaned inpainted CMB realisations exhibit unusually low mean spacings between even multipoles. This establishes the robustness of our finding.

In our second work, we explore the orientation matrix to study the isotropy of local temperature extrema of the CMB. This matrix formed from position vectors of unit-mass points on the surface of a 2-sphere, was first given by Watson (1965) and Scheidegger (1965). We modify this matrix, by introducing non-unit mass weights i.e., magnitudes of the local extrema of the CMB, to characterise their distribution. The shape and strength parameters formed from eigenvalues of the orientation matrix were given by Woodcock (1977) to discern if the points are grouped in clumps or rings, and what the intensity of their non-uniformity is. We simulate toy maps containing clustered and girdled spots and demonstrate that the shape and strength estimators from our mass weighted orientation matrix adequately quantify the non-uniformity in the CMB spots. On actual foreground-minimized full sky CMB maps from WMAP and Planck satellites we find a conspicuously weak non-uniformity in the distribution of hot spots which is robust against the cleaning methods of WMAP-ILC, Commander, NILC and SMICA, and is independent of the NGCS. Partial sky analysis reveals an anomalously weak non-uniformity for cold spots which is robust against several foreground-cleaning methods, masks, observational instruments and frequencies, and the presence of the NGCS. Intriguingly we find that this signal of unusually weak non-uniformity of spots in either full or partial sky coverage is possibly due to the quadrupole and octupole and hence shares a common origin with the anomalously low CMB temperature variance.

In our third work, we explore Machine learning for the first time, to detect a signal of statistical anisotropy known as dipolar modulation. The hemispherical power asymmetry in the CMB is attributed to a preferred direction which modulates the temperature fluctuations. From maps of the foreground-minimised CMB, local variances in several small regions on the spherical surface can be appropriately bias subtracted and normalised to reveal the underlying dipolar pattern. As an unprecedented technique, we present Artificial Neural Networks (ANNs) with such re-scaled local variance maps as input features to train them to distinguish SI obeying CMB maps from the dipole-modulated ones. The ANNs once trained, are capable of predicting components of the amplitude times the unit vector of the dipole direction for sets containing a mixture of modulated and unmodulated maps. The goodness-of-fit (R^2) scores for these predictions are > 0.97 for full sky maps and > 0.96 for partial sky maps. Further, the predicted amplitudes and directions for all the observed foreground-cleaned CMB maps have reasonably consistent values. Additionally, the detection of the dipolar modulation signal is significant at $97.21\% - 99.38\%$ C.L. for full sky coverage, and at $98.34\% - 100\%$ C.L. for partial sky coverage. Moreover, the signal is robust against sky coverages, several foreground cleaning methods, inpainting algorithms, instruments, and all the various periods of observation for Planck and WMAP satellites. Thus the statistical significance and robustness of the detection of this signal, in addition to the consistency in the values of amplitude and directions, found using an independent technique, further weakens the criticisms attributed to look-elsewhere effects and a posteriori inferences for the dipole modulation of the CMB.

Thus, if these three findings are not attributable to any unknown or unaccounted residual systematics, then such violations of SI in addition to the considerable volume of work in existing literature lend us an impetus to study exotic physics to explain our unlikely existence as a viable extension of the standard model of cosmology.

TABLE OF CONTENTS

List of Symbols and Abbreviations

CMB	Cosmic Microwave Background
a	Scale factor
H	Hubble parameter
r_H	Comoving Hubble radius
h	Planck constant
$\hbar$	Reduced Planck constant
m_{Pl}	Reduced Planck mass
G	Gravitational constant
FLRW	Friedmann-Lemaitre-Robertson-Walker
$g_{\alpha\beta}$	Metric of spacetime
Φ	Inflaton field
$R_{\alpha\beta}$	Ricci curvature tensor
R	Ricci scalar
$G_{\mu\nu}$	Einstein tensor
$T_{\mu\nu}$	Stress-energy tensor
ε	First slow-roll parameter
ρ	Energy density
P	Pressure
τ	Conformal time

ζ	Comoving curvature perturbation
z	Cosmological redshift
n_s	Scalar spectral index
n_t	Tensor spectral index
C_ℓ or C_ℓ^{th}	Theoretical angular power spectrum
$\hat{C}_\ell$	Estimator of the angular power spectrum
$\langle\rangle$	Ensemble average, unless specified otherwise
ΛCDM	Lambda Cold Dark Matter model
SI	Statistical Isotropy
$\Delta_{X\ell}$	Transfer function for temperature fluctuations ($X = T$) or polarisation ($X = E$ and $X = B$ modes)
(r,θ,ϕ)	Spherical polar coordinates
$\hat{n}$	A direction on the 2-sphere corresponding to θ, ϕ
$\Delta T(\hat{n})$	Temperature anisotropy at $\hat{n}$
$Y_{\ell m}(\hat{n})$	Spherical harmonic function
$a_{\ell m}$	Spherical harmonic coefficients
$D(\chi,\xi,\psi)$	Wigner-D matrix
$D^{(\ell)}_{m'm}(\chi,\xi,\psi)$	Wigner-D matrix in harmonic space
$\delta_{\ell\ell'}$	Kronecker delta
MC	Monte Carlo
MCMC	Markov Chain Monte Carlo

C.L.	Confidence Level
WMAP	Wilkinson Microwave Anisotropy Probe
WMAP-ILC	Wilkinson Microwave Anisotropy Probe - Internal Linear Combination
TOH	Tegmark, de Oliveira-Costa, & Hamilton
NILC	Needlet Inter Linear Combination
SMICA	Spectral Matching Independent Component Analysis
Commander	Optimal Monte-Carlo Markov Chain Driven Estimator
C-R	Commander-Ruler (resulting low-resolution spectral parameter samples to solve for the component amplitudes)
SEVEM	Spectral estimation via expectation maximisation
HEALPix	Hierarchical Equal Area isoLatitude Pixelation of a sphere
$C(\theta)$	Two-point angular correlation function of temperature anisotropies
$\begin{pmatrix} \ell_1 & \ell_2 & \ell_3 \\ m_1 & m_2 & m_3 \end{pmatrix}$	Wigner-$3j$ symbol
$A_{ij}(\ell)$	Power tensor
$\mathcal{L}$	Likelihood
Ω	Solid angle
$\eth$	Spin raising operator
$\eth^*$	Spin lowering operator
$P_\ell(\cos\theta)$	Legendre polynomial function

$\vec{A} \otimes \vec{B}$	Tensor product of $\vec{A}$ and $\vec{B}$, i.e, $\frac{(A_iB_j+A_jB_i)}{2}$
$\mathcal{D}_\ell$	$\frac{\ell(\ell+1)}{2\pi}\hat{C}_\ell$
ΔC_ℓ	Spacing between consecutive $\hat{C}_\ell$'s
$\Delta\mathcal{D}_\ell$	Spacing between consecutive $\mathcal{D}_\ell$'s
r_ℓ	Gap ratio
avg_i	Average spacing estimator, where i stands for either all, even or odd multipole spacings
n_{side}	HEALPix Resolution parameter
n_{pix} or N_{pix}	Number of pixels in a CMB map, $n_{pix} = 12 \times n_{side}^2$ for full sky maps
FWHM	Full-width-at-half-maximum
NGCS	Non-Gaussian cold spot
$^{(s)}$	Superscript $s = h, c$, i.e, hot and cold spots
$\mathcal{T}^{(s)}$	Orientation matrix weighted by the magnitudes of the respective local extrema
$(x_i^{(s)}, y_i^{(s)}, z_i^{(s)})$	Direction cosines of the i^{th} local extremum
$\lambda_j^{(s)}$	Eigenvalues of $\mathcal{T}^{(s)}$, where $j = 1, 2, 3$
$\gamma^{(s)}$	Shape parameter
$\zeta^{(s)}$	Strength parameter
A	Amplitude of dipolar modulation
$\hat{\lambda}$	Preferred direction causing dipolar modulation
$\langle\rangle_d$	Average over a disc on a 2-sphere

AI	Artificial Intelligence
ANN	Artificial Neural Network
CNN	Convolutional Neural Network
$ReLU$	Rectified Linear Unit activation function
$LeakyReLU$	Leaky Rectified Linear Unit activation function
mse	Mean squared error
n_l	Lower n_{side} resolution
n_h	Higher n_{side} resolution
r_h	Radius of disc on map at resolution n_h
R^2	R-2 score or coefficient of determination
(l, b)	Direction in galactic coordinates of longitude and latitude

List of Figures

List of Tables

CHAPTER 1

STANDARD COSMOLOGY AND ISOTROPY OF THE UNIVERSE

1.1 Introduction

As macroscopic beings, it is a intriguing proposition that our existence, and that of all sorts of structures, that is, planets, stars, galaxies, and so on, began at the smallest of scales [303], which cannot be explained by Newtonian mechanics. Instead we resort to quantum mechanics which entails the notion of random fluctuations [238] in the vacuum of the densely packed space allocated to the universe as it was being cradled into existence. Alan Guth [121], Andrei Linde [180], Alexei Starobinsky [263] and Paul Steinhardt [16, 17, 25] are known as the principal architects of the theory of cosmic inflation, which associates the initial energy density of the universe to be dominated by the potential energy density of an inflaton field with quantum fluctuations [168]. Vacuum fluctuations can be thought of as spontaneous production and annihilation of pairs of particles and antiparticles that essentially appear out of and disappear into the quantum vacuum. Inflation is hypothesised to homogeneously and isotropically stretch out the space fabric by a factor a. This means that such virtual particle pairs separated initially by an uncertainty of distance Δx, happen to lie at $a\Delta x$ approximately. As and when this approximate distance between the pair crosses the causal horizon, they manifest as real particles. We illustrate the expansion as modelled with the notion of a scale factor in Figure 1.1.

Moreover, quantum fluctuations were pulled apart or inflated to macroscopic scales and frozen out of the existing causal horizon at the time, making them classical fluctuation modes [155] such that they could thereafter aid in varying degrees of gravitational accretion

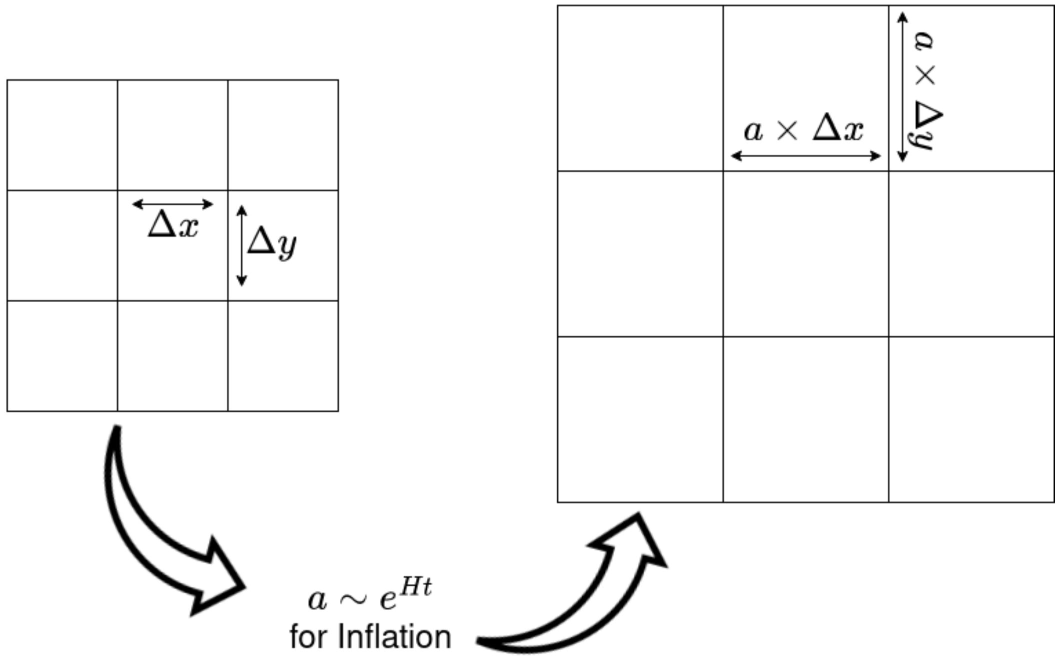

Figure 1.1: A schematic diagram to show inflationary expansion as modelled with a scale factor a. The z-axis is pointing outside the plane of the paper. Here, $\Delta x, \Delta y$, and Δz (not shown) are called "comoving" distances.

of matter depending on strengths of the matter density fluctuations [224]. This eventually leads to formation of structure, as and when these fluctuations reenter the causal horizon in radiation or matter dominated eras.

Inflation is purported to be an exponential accelerated expansion of space in a fraction of a second, hence $a \sim e^{Ht}$, where, $H = \frac{\dot{a}}{a}$, is the Hubble rate of expansion and t is the proper time. Further, a condition on the scale factor is $\ddot{a} > 0$ for the accelerated expansion, which can be shown to be equivalent to $\frac{d}{dt}\left(\frac{1}{aH}\right) < 0$. This gives us $r_H = 1/(aH)$ as the radius of the comoving Hubble sphere which delineates our causal horizon at any given time, and it shrinks as inflation occurs [114]. It can be understood as follows. For two points on the space mesh which are receding from each other with a relative velocity of light, and using Hubble's law, $v = H \times r$ where, $v =$ recession speed and r is the proper radius. Hence when the speed of recession is $v = c = 1$ (in natural units), $r = 1/H$. Further as $r = a \times r_H$, therefore the comoving Hubble radius is $r_H = \frac{1}{aH}$.

Once inflation decays, it degenerates into standard model particles [3, 86], and ushers in the later eras of radiation domination, followed by matter domination, leading up to the current state of the universe which predominantly contains dark energy. In the radiation and matter dominated eras, the scale factor has a power law dependence on physical time, thus the comoving Hubble sphere in these eras enlarges such that the smallest scale modes which left the horizon later reenter first followed by larger scale modes which reenter at latest times.

Currently, the standard model of cosmology enshrines the notions of space having a flat curvature, and comprising a strikingly low percentage of about 5% in the form of ordinary matter, 27% dark matter, and 68% dark energy. Here, dark matter refers to usually undiscovered particles which have been theorised to be massive, but weakly interacting, and which do not fall in the Standard model of Particle physics [110]. Additionally the mysterious component called dark energy which pervades all of space predominantly, is responsible for the current accelerated expansion of the universe [69].

This chapter is organised as follows. In Section 1.2, we enlist a chronologically arranged set of epochs that are widely believed to have led to the present universe. In Section 1.3, we describe specifically the hypotheses governing the inflationary epoch and how those could translate into the observable universe today. In Section 1.4, we discuss some of the observational probes in Cosmology which help us investigate the various periods of evolution of the universe. In Section 1.5, we discuss the basic observables which characterise the CMB. In Section 1.6, we elucidate our principal motivation towards studying the isotropy of the CMB. In Section 1.7, we discuss the challenges that come one's way in observing and extracting a clean signal of the CMB. In Section 1.8, we discuss some state-of-the-art methods of probing the isotropy of the CMB, present in existing literature. In Section 1.9, we imbibe motivation from existing works in probing isotropy of the CMB, to explore the novel techniques that we have developed in this thesis, and which are presented in the subsequent chapters.

1.2 Epochs of the universe

The actual conversion of quantum fluctuations of the inflaton field which transfers as classical perturbations in the metric, is an area of active research, due to the lack of correspondence between the general theory of relativity and quantum mechanics [187]. Thus it becomes fairly non-trivial to assign an energy scale to the beginning and end of inflation. It is known from various models of inflation [193] that the energy scale would primarily lie in the order of 10^{16} GeV [178], which is approximately 10^{-3} GeV lower than the Planck scale.

Initially the Big Bang was the standard picture of how the universe and all the large scale structure (LSS), in terms of networks of galaxies arranged in filaments and clusters interspersed with voids, came into being. It was first hypothesised by Lemaitre [175, 174] as being a singularity which grew out into the universe today, as space stretched out homogeneously and isotropically. However there were problems with the approach, such as that of the "horizon problem" which states that today at the largest scales, there exist two observable regions which are not in causal connection with each other and yet look very similar. Then the theory of cosmic inflation was invoked to solve such problems [121]. Thus, with our current understanding of Particle Physics and Cosmology, the chronology of the universe can be outlined in the following manner, considering time to start from the "Big Bang" at 0 seconds:

1. *Planck Epoch:* In this epoch, the universe is envisaged as being compact and occupying space at the scale of Planck length. It is achieved after 10^{-43} seconds of elapse after the Big Bang, and the temperature of the universe is approximately 10^{32}K. It is presumed that all the four fundamental forces (electromagnetic force, weak nuclear force, strong nuclear force and gravitational force) have the same strength, and could be unified into a single force [257]. Before the Planck era, we do not have any theory in physics to account for the state of the universe.

2. *Grand unification theory (GUT) era:* Due to the expansion of the universe that began at the Big Bang, the universe is expected to cool down, and when it reaches a temperature of about 10^{16} GeV, the GUT era begins. This happens in the period between 10^{-43} seconds to 10^{-36} seconds, such that the gravitational force dissociates from the other three fundamental forces which are still unified [75]. This is when the first elementary particles and their antiparticles would have been created.

3. *Inflationary epoch:* As the universe cools, the strong nuclear force is gradually beginning to decouple from the electroweak force. Hypothesised to have lasted from 10^{-36} seconds to 10^{-32} seconds, the epoch of inflation is one of an exponential expansion of space. Thus the elementary particles in the form of the hot and dense quark-gluon plasma [231] which were left over from the GUT epoch are spread out across the universe, leading to a reduced density of these particles.

4. *Electroweak epoch:* It occurs at temperatures of about $10^{15} - 10^{9}$ GeV, when the time is nearly $< 10^{-32}$ seconds, and lasts until about 10^{-12} seconds. In this epoch, the strong nuclear force completely decouples from the electroweak force, and particle interactions produce many exotic particles. Since the Higgs boson has been discovered [2], our assumption of the electroweak era following the GUT era is reasonable. The Higgs boson would be the only particle present during the GUT era, and in the Electroweak era, simultaneous collisions of Higgs bosons would lead to the production of W and Z bosons [18]. The Higgs field itself slows particles down, and bestows mass on them.

5. *Quark Epoch:* Towards the end of the electroweak era, there are no new W and Z bosons being produced, and existing ones would decay away, such that in their absence, the short-range weak nuclear force separates from the electromagnetic component. The quark epoch lasts from 10^{-12} seconds to 10^{-6} seconds in which large numbers of quarks, electrons and neutrinos are generated [250]. Randomly quarks and anti-quarks are expected to keep annihilating each other. However an overabundance of quarks relative to anti-quarks exists such that later on they can coalesce into matter. This happens due to a process known as baryogenesis [108] which by definition creates an excess of baryons over anti-baryons starting from equal amounts of both in the early universe.

6. *Hadron Epoch:* This lasts from 10^{-6} seconds to 1 second when the temperature of the universe has fallen to about 10^{12} K. At this temperature, the quarks can combine to form hadrons (e.g., protons and neutrons) [44]. An interesting phenomenon of production

of neutrinos occurs, as and when electrons and protons collide at this epoch to form neutrons and massless neutrinos, that can free-stream throughout space even till today, at relativistic velocities. Since the reaction is reversible, some neutron-neutrino pairs could also recombine into electron-proton pairs [182].

7. *Lepton Epoch:* From a second to about three minutes, after a majority of hadrons have annihilated with anti-hadrons, the universe predominantly contains leptons and anti-leptons such as electrons and positrons, respectively [146]. Electron-positron pairs collide and annihilate each other producing energy in the form of photons, which in turn collide and generate more electron-positron pairs.

8. *Phase of Nucleosynthesis:* This takes place between 3 minutes to 20 minutes, when the temperature of the universe has fallen to about 10^9 K. Thus, with nuclear fusion, protons and neutrons coalesce to form nuclei of various atoms, starting with the lightest ones such as hydrogen, helium and lithium [105]. Towards the end of this epoch however, nuclear fusion cannot continue further and heavier elements have to be produced in the cores of stars later on [225].

9. *Radiation dominated Epoch:* A rather prolonged epoch which occurs between 3 minutes to $240,000$ years, called the radiation dominated epoch entails that the universe is filled with a photon-baryon fluid or plasma, which is very hot and opaque, as the photons are tightly coupled to the atomic nuclei, protons and electrons [222]. The photons here are the major constituents which arose out of the annihilations of leptons and anti-leptons towards the end of the lepton era.

10. *Recombination era:* It is a very important period in the history of the universe, when the photons decoupled from the plasma, from about $240,000$ to $300,000$ years. Above temperatures of 3000 K, hydrogen, the simplest atom, is ionised, and hence the heavier atomic nuclei like helium and the like are obviously ionised. Below this temperature, as the density of these particles also depreciates, the ionised hydrogen and helium atoms reunite with electrons in this period of recombination and become neutral atoms [254]. Thus the photons essentially decouple from the baryon-photon plasma and the

universe becomes transparent as the first light in the universe is released and can travel freely. These photons are observable even today, albeit at the very low energy scale of microwaves, thus forming the Cosmic Microwave Background (CMB). At the end of the recombination era, the universe predominantly comprises hydrogen atoms (75%), followed by helium (25%), and trace quantities of lithium [266].

11. *The Dark Ages and the Matter dominated era:* This era of darkness which began from $300,000$ and continued to about 150 million years is preceded by the recombination era when the first atoms formed and is followed by the appearance of the first stars [201]. Ironically, despite the presence of a large number of photons, this period is called the Dark Ages since, we do not have any luminescent sources like stars as yet. Since matter is primarily left out and predominantly dark matter causes gravitational accretion acting as centres for growth of structure [41], the overall energy levels of the universe are low, such that the temperature is $\simeq 1$ eV. Thus the first clusters of stars and galaxies begin to form gradually as gravitational force competes with and tries to overcomes radiation pressure, nearing the end of the dark ages.

12. *Structure formation and the Epoch of Reionization (EoR):* The initial generation of stars comprises "Population III" stars [109] which are essentially supermassive, metal free and formed as a result of the gravitational collapse of matter in its gaseous state, leading to production of heat and occurrence of nuclear fusion of hydrogen atoms. Formation of "Population II & I" stars consequently occurs with the material left over from previous stars [130]. For e.g., as more gigantic stars combust rapidly and explode in massive supernova events, their remnant matter is spewed out in space and goes on to form subsequent generations of stars. Thereafter, structure in the universe forms hierarchically [228], such that massive volumes of matter coalesce under gravity to form galaxies, and further gravitational attraction leads to the arrangement of several galaxies into groups, then clusters, and super-clusters.

    The EoR [300] is an important period, lasting between 150 million to 1 billion years, since it is associated with the production of ultraviolet radiation from the first generation of galaxies, stars and supermassive black holes [46], which ionises the regions around them. With increasing number of ionising sources, the amount of ionised gas also increases leading to a complete ionisation of all the hydrogen, hence the name “reionization”. It can be understood by a scrutiny of electromagnetic radiation from this era [198], in the form of quasar absorption spectra, Lyman-α emission from high redshift quasi-stellar-objects, 21cm emission line from hyperfine transition in hydrogen, intensity mapping of carbon monoxide emission lines, and so on.

13. *Continual Star and Galaxy Formation and the present Dark energy era:* A transition from a decelerating universe to an accelerating one gradually occurs around 6 billion years after the Big Bang. However, the formation of late generation stars and galaxies continues, and our own sun and the solar system come into existence at roughly $8.5-9$ billion years after the Big Bang [221]. The advent of dark energy domination in the universe begins when the temperature of the universe has fallen to about 10^{-3} eV or ~ 11K. Dark energy is a mysterious entity that causes late time acceleration of the universe. This era began approximately 3 billion years ago and has continued till the present day [74], which is ~ 13.8 billion years after the Big Bang. Thus expansion of the universe continues and simultaneously remnants of old stars upon their death get utilised in the formation of newer stars.

In the next Section 1.3, we focus on the inflationary epoch of the universe, and the theoretical framework underlying the same that aids in understanding the development and evolution of the universe we see today.

1.3 Inflationary origins of the universe

Essentially there are four aspects which frame our understanding of modern cosmology [85, 206] and hence our own origins from cosmic inflation:

1. *The Cosmological Principle (CP):* This states that on the largest cosmological scales, the universe is (a) homogeneous, meaning to say that along a given direction there is no preferred position to observe the universe and (b) it is isotropic, meaning that the

universe appears the same from all directions, or when viewed from different angles. However, the edifice of these concepts is the assumption of their validity when averaged over largest of cosmic scales ($\gtrsim 100$ Mpc). The CP is encapsulated in the background metric of spacetime called the FLRW (Friedmann-Lemaitre-Robertson-Walker) metric, which is maximally symmetric and describes a completely homogeneous and isotropic expansion of the universe. The metric is of the form

$$ds^2 = -dt^2 + a(t)^2 \left(\frac{dr^2}{1-\mathcal{K}r^2} + r^2(d\theta^2 + \sin\theta^2 d\phi^2) \right) = g_{\alpha\beta}^{(FLRW)}(t) du^\alpha du^\beta. \quad (1.1)$$

Here, r, θ, ϕ are the usual spherical polar comoving coordinates, $\mathcal{K}$ is the curvature parameter, and equals $\pm 1, 0$ for spherical, hyperbolic and Euclidean geometry of comoving spacelike hypersurfaces. The scale factor $a(t)$ is a function of time and defines the size of the actual spacelike hypersurfaces. The variable $u = (t, r\sin\theta\cos\phi, r\sin\theta\sin\phi, r\cos\theta)$ denotes the time coordinate and the other comoving space coordinates.

2. *The inflationary field (inflaton)* which causes an exponential expansion of space in a fraction of a second. In simplest models of inflation, this is usually a single, self-interacting scalar field Φ. It ensures the conditions for cosmic inflation, such as those of providing a negative pressure, and constant energy density which fills the primordial universe. The action for such a field can be defined as

$$S_\Phi = \int d^4x \sqrt{-g} \left(\frac{1}{2} g_{\alpha\beta} \partial^\alpha \Phi \partial^\beta \Phi - V(\Phi) \right). \quad (1.2)$$

Here, we have set $m_{pl} = 1$. Further, g is the determinant of the metric $g_{\alpha\beta}$ and $V(\Phi)$ is the potential for the scalar field which is generally considered to be almost flat until inflation occurs, and then has power law behaviour in Φ such as a simple harmonic quadratic term in Φ as Φ nears a global minimum in $V(\Phi)$ towards the end of inflation. The action for Φ is added to the standard Einstein-Hilbert action $S_R = \int d^4x \sqrt{-g} \frac{R}{2}$, where R is the Ricci scalar. Thus the summed action with both Einstein-Hilbert and inflationary terms contains the complete information of our inflationary universe.

3. *Quantum fluctuations in inflaton and the metric:* As we have mentioned in the In-

troduction 1.1 of this chapter, the quantum fluctuations in both the metric and the inflationary field act as seeds for the small local irregularities in our universe, which have led to the plethora of distinct structures on scales (1 kpc to 1 Mpc) smaller than large cosmological scales. These quantum fluctuations were stretched out into classical perturbations during cosmic inflation. Hence the inflaton has two components, one which is time dependent $\Phi(t)$ and the other which is the small contribution depending on both space and time ($\delta\Phi(\vec{x}, t)$). Similarly the generic form of the metric $g_{\alpha\beta}$ contains the background FLRW metric ($g_{\alpha\beta}^{(FLRW)}(t)$), on which are added some small perturbations, which introduce inhomogeneities in the form of a perturbation metric, say $\delta g_{\alpha\beta}$. The fluctuations or perturbations to the background inflaton or the background (FLRW) metric are considered to be negligible at the second order in linear perturbation theory, which is the standard paradigm of cosmology.

4. *Connecting the end of inflation and our current state:* We require a set of transfer functions which provide us a mathematical machinery to connect primordial perturbations with inhomogeneities in our universe today. These are provided primarily for photons or radiation and the LSS. The radiation transfer function helps us link the primordial power spectrum of perturbations with the temperature and polarisation anisotropies in the CMB. The matter transfer function provides a connection between the primordial power spectrum and the current matter power spectrum observed for the LSS.

In the next four subsections, we discuss firstly about the cosmological principle and what the conditions for inflation are, secondly we elucidate the notion of the inflationary field further to assess its characteristics, and thirdly how metric fluctuations translate into actual inhomogeneities alongside the fluctuations in the inflaton, and fourthly how these perturbations manifest into the current state of the observable universe.

1.3.1 Cosmological principle and the unperturbed Friedmann's equations

The Friedmann's equations for the background FLRW metric can be obtained directly from the Einstein's field equations, since it is widely accepted that the General Theory of Relativity describes gravity. The Einstein's field equations connect the curvature of spacetime with the energy density and pressure of the fluid filling that spacetime. The field equations are

$$G_{\alpha\beta} = R_{\alpha\beta} - \frac{1}{2}\bar{g}_{\alpha\beta}R = \kappa T_{\alpha\beta}. \tag{1.3}$$

Here, $\kappa = \frac{8\pi G}{c^4} = \frac{8\pi}{m_{pl}^2}$. When considering $\bar{g}_{\alpha\beta} = g_{\alpha\beta}^{(FLRW)}$ which is the background (unperturbed) metric, some significant mathematical rigour leads us to the following equations for understanding how the scale factor $a(t)$ evolves with time:

1. First Friedmann equation,

$$\left(\frac{\dot{a}}{a}\right)^2 = \frac{8\pi G}{3}\rho - \frac{k}{a^2}. \tag{1.4}$$

2. Second Friedmann equation,

$$\frac{\ddot{a}}{a} = -\frac{4\pi G}{3}(\rho + 3P). \tag{1.5}$$

These equations are written in natural units, setting $c = 1$. Here, $\rho = \sum_{i=1}^{N} \rho_i$, and $P = \sum_{i=1}^{N} p_i$, such that they are the total energy density and pressure of all the components which fill the universe at time t. Since inflation is a phase of an accelerated expansion, this means that the mathematical condition is $\frac{d^2a}{dt^2} > 0$. And from equation (1.5), we have $(\rho + 3P) < 0$ or that $P < -\frac{\rho}{3}$. It is interesting to see how the inflaton as the dominant component in the primordial universe satisfies this property, as discussed in the next subsection.

1.3.2 The background inflaton

Since cosmic inflation can take place when we have a dominant component in the universe which has a negative pressure and constant energy density, these conditions can be fulfilled by a scalar field called the inflaton Φ. For convenience, we will firstly refer to the background $\Phi = \Phi(t)$. Following equation (1.2), we can write the energy-momentum tensor as

$$T_{\alpha\beta} = -\frac{2}{\sqrt{-g}}\frac{\delta S}{\delta g^{\alpha\beta}} = \partial_\alpha \Phi \partial_\beta \Phi - g_{\alpha\beta}\mathcal{L}, \tag{1.6}$$

which resembles the energy momentum tensor of a perfect isotropic fluid $T = \text{diag}(-\rho, P, P, P)$. We deduce the expressions for energy density and pressure from $T_{\alpha\beta}$ of this perfect fluid corresponding to the background metric $g_{\alpha\beta}^{(FLRW)}$ and the background inflaton ($\Phi(t)$) as

$$\rho = \frac{1}{2}\dot{\Phi}^2 + V(\Phi), \quad P = \frac{1}{2}\dot{\Phi}^2 - V(\Phi). \tag{1.7}$$

Thus $(\rho + 3P) < 0$ implies that $\dot{\Phi}^2 < V(\Phi)$. Hence the condition of an accelerated expansion is that the dominant component of the perfect fluid exerts negative pressure, and rolls very slowly along the potential gradient due to a very small kinetic energy.

In order to infer how inflation obeys conservation equations of a perfect fluid of its kind, we state the composite energy-momentum tensor of a set of N perfect fluids:

$$T_{\alpha\beta} = \sum_{i=1}^{N} T_{\alpha\beta}^{(i)} = (\rho + P)v_\alpha v_\beta + P g_{\alpha\beta}, \tag{1.8}$$

where ρ, P contain contributions from all the N perfect fluids. These can be considered to be equal to the energy density and pressure of the inflaton when the universe is dominated by such a single scalar field. Generally, the pressure and energy density are related by the equation of state $P = w\rho$, where w is the equation of state parameter. In addition, the v_α vector is the velocity four vector, and obeys the relation $v_\alpha v^\alpha = -1$. The conservation of the stress-energy tensor ($\nabla^\alpha T_{\alpha\beta} = 0$, ∇ denotes a covariant derivative) ascertains that

$$\dot{\rho} = -3(\rho + P)\frac{\dot{a}}{a}, \tag{1.9}$$

and for $\rho = \frac{1}{2}\dot{\Phi}^2 + V(\Phi)$, $P = \frac{1}{2}\dot{\Phi}^2 - V(\Phi)$ of the background unperturbed inflaton, we get,

$$\ddot{\Phi} + 3\frac{\dot{a}}{a}\dot{\Phi} + \frac{dV(\Phi)}{d\Phi} = 0. \tag{1.10}$$

This equation encapsulates the overall evolution of the unperturbed inflaton field, such that the first derivative of the potential provides a restoring force like term, whereas the $\frac{\dot{a}}{a}\dot{\Phi}$ provides frictional damping effect on Φ due to the expansion of the universe. It is convenient to define a slow roll parameter of the first kind called $\varepsilon = \frac{\dot{H}}{H^2}$. We know that for inflation to occur, the Hubble radius must shrink, hence $\frac{d}{dt}\left(aH^{-1}\right) < 0$ which gives, $-\frac{\dot{H}}{H^2} < 1$ or $\varepsilon < 1$. Additionally, using the first Friedmann equation, and assuming flatness of space due to inflation, we have $H^2 \sim \rho/3$ in natural units of $m_{pl} = 1$. For $\rho = \frac{1}{2}\dot{\Phi}^2 + V(\Phi)$ and using evolution equation (1.10), we obtain $\dot{H} = -\frac{1}{2}\dot{\Phi}^2$. Thus, saying that

$$\varepsilon = \frac{\dot{\Phi}^2}{2H^2} < 1, \tag{1.11}$$

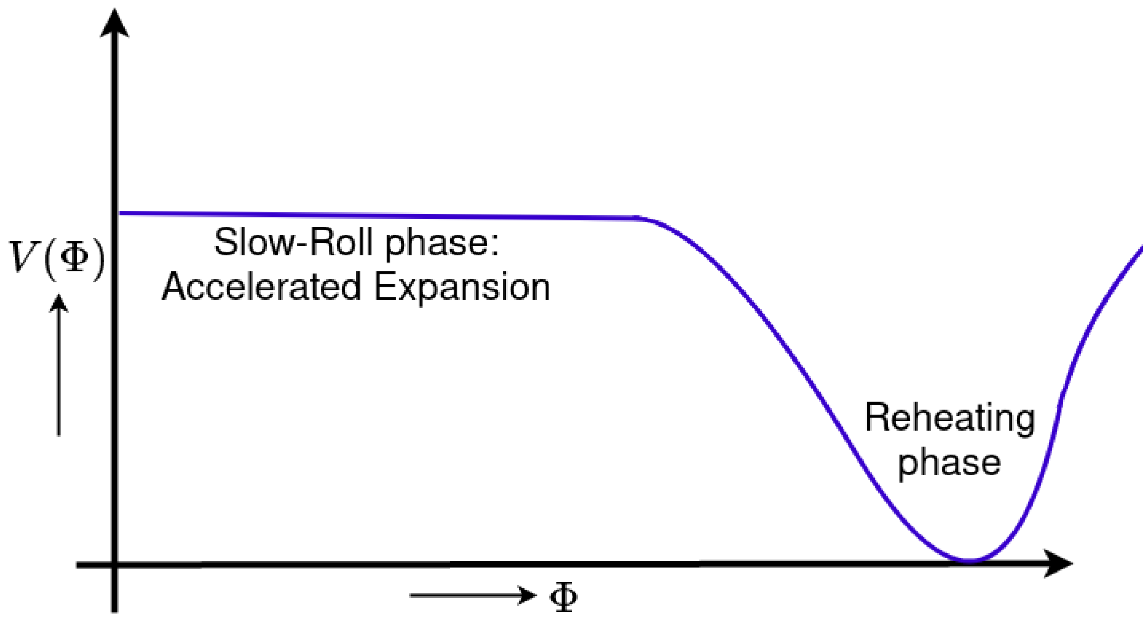

Figure 1.2: A probable form of the inflationary potential, which illustrates the two phases of the inflaton. The slow roll phase corresponds to the exponential expansion of the universe, and the reheating phase corresponds to an oscillatory phase of the inflaton as it decays into Standard Model particles.

is another way of imposing the condition for an accelerated expansion of the universe.

Since inflation must end for small fluctuations in the inflaton and the metric to seed density perturbations to grow into structure as time progresses, chaotic inflationary potentials were suggested by [181]. Such potentials are of a polynomial form: $V(\Phi) \sim \Phi^n$, where n is an integer. Once slow roll is over, the accelerated expansion reaches an end, the inflaton then starts to oscillate about the minimum of the potential. The inflaton interacts with other subdominant particle species, leading to its decay into Standard Model particles including radiation, in a process called reheating. Thus, to summarise, the first phase of the evolution of the inflaton is a slow roll phase which causes the exponential expansion of the universe and the second phase involves a decay of the inflaton into Standard Model particles. This is illustrated with a sketch (Figure 1.2) of a probable inflationary potential.

1.3.3 Fluctuations of the inflaton and the metric

Despite the largely smooth, homogeneous and isotropic expansion of the universe created by inflation, we must account for the generation of the local irregularities in our universe today. Thus, in addition to $\Phi(t)$, and $g_{\alpha\beta}^{(FLRW)}$, there must be some very small perturbations in the metric or fluctuations in the inflaton field.

Since the potential energy ($V(\Phi)$) dominates the energy density (ρ) of the inflating universe, the fluctuations in the inflaton field ($\delta\Phi(\vec{x},t)$) manifest as fluctuations in the energy density of the universe: $\delta\rho \propto \delta V[\Phi(t)+\delta\Phi(\vec{x},t))]$. These perturbations enter into $T_{\alpha\beta}$, which is the source for the metric, hence leading to metric perturbations $\delta g_{\alpha\beta}$ as well.

Using the concept of conformal time (τ), which is given as $d\tau = \frac{dt}{a(t)}$, we have the unperturbed metric $ds^2 = a(\tau)^2\left[-d\tau^2 + d\vec{x}^2\right]$, the perturbed form of which is [165],

$$ds^2 = a^2(\tau)[-(1+2A)d\tau^2 - 2B_i d\tau dx^i + \{(1-2D)\delta_{ij} + 2E_{ij}\}dx^i dx^j]. \tag{1.12}$$

In a scalar-vector-tensor (SVT) decomposition [165] with respect to $SO(3)$ rotations, the A and D are scalars, B_i can be broken up into a scalar and a divergence-less vector, and the traceless tensor E_{ij} into a scalar, divergence-less vector and traceless transverse tensor,

$$B_i = -B_{,i} + B_i^{(v)}, \quad \text{such that} \quad \vec{\nabla}\cdot\vec{B}^{(v)} = 0, \tag{1.13}$$

$$\text{and} \quad E_{ij} = (\partial_i\partial_j - \frac{1}{3}\delta_{ij}\vec{\nabla}^2)E - \frac{1}{2}(E_{i,j} + E_{j,i}) + E^t_{ij}, \tag{1.14}$$

$$\text{where,} \quad \delta^{ij}E_{i,j} = \vec{\nabla}\cdot\vec{E} = 0; \quad \delta^{ik}E^t_{ij,k} = 0; \quad \delta^{ij}E_{ij} = 0. \tag{1.15}$$

Here, $\vec{\nabla}$ denotes the 3D differential operator. We note that the divergence-less vector $\vec{B}^{(v)}$ reduces the degrees of freedom by one and hence 2 degrees of vector freedom and one scalar B give the required total of 3 degrees of freedom for B_i. In a similar fashion, $(\partial_i\partial_j - \frac{1}{3}\delta_{ij}\vec{\nabla}^2)E$ is symmetric and traceless given its structure, and $-\frac{1}{2}(E_{i,j}+E_{j,i})$ is symmetric, and the condition of zero divergence makes that part traceless as well. We assume the tensor E^t_{ij} to be symmetric and the two conditions on it make it traceless and 'transverse'.

The manner in which the decomposition is carried out constitutes a specific choice of time slicing and choice of spatial coordinates on these time slices, which constitutes a gauge choice. In linear perturbation theory these perturbations are considered to be negligible at second order. Thus on writing the Einstein's equations for this metric and separating out the perturbations of the $\delta G_{\alpha\beta}$ and $\delta T_{\alpha\beta}$ we find that the scalar, vector, and tensor perturbations can be treated independently because they decouple.

The scalar fluctuations in the metric are known to couple to matter and radiation density, giving rise to the small scale inhomogeneities and anisotropies in the universe. As discussed in [85] in the conformal Newtonian gauge, the tensor perturbations produce gravity waves and not being coupled with the density, they play no role in LSS formation in the universe. Vector perturbations couple to rotational velocity perturbations in the 'fluid' of the cosmos which tend to decay in our expanding universe, hence they are neglected in further analysis.

For simplicity we discuss how the scalar perturbations evolve, and similar mathematics can be used for the other perturbations. If we define a curvature perturbation $\psi = D + \frac{1}{3}\vec{\nabla}^2 E$, this gives us the form of the metric with only scalar parts of perturbations,

$$ds^2 = a(\tau)^2[-(1+2A)d\tau^2 + 2B_{,i}d\tau dx^i + \{(1-2\psi)\delta_{ij} + 2E_{,ij}\}dx^i dx^j]. \tag{1.16}$$

Further, the action for the inflaton-dominated universe non-minimally coupled to gravity is,

$$S = \int d^4x\sqrt{-g}[\frac{1}{2}R - \frac{1}{2}g_{\alpha\beta}\partial^\alpha\Phi\partial^\beta\Phi - V(\Phi)]. \tag{1.17}$$

In this expression, we note that both the metric and the inflaton are now perturbed. In the inflaton, we have one scalar degree of freedom ($\delta\Phi$), and in the metric, we have four: A, B, D, E. Thus, from among these five degrees of freedom, we can eliminate two, since the equations of motion must be gauge invariant with respect to translations in time and space, i.e., $t \to t + \xi_0$, and $x_i \to x_i + \partial_i\xi$. Further, the Einstein constraint equations (Hamiltonian and momentum constraint equations) [30] reduce two more degrees of freedom. Hence it suffices to consider a gauge in which we have one scalar perturbation.

In the comoving gauge, the slow roll inflaton has no fluctuation ($\delta\Phi = 0$). The perturbed metric confined to the spacelike hypersurfaces can be written as

$$g_{ij} = a^2[(1-2\zeta)\delta_{ij} + h_{ij}], \quad \partial_i h_{ij} = h^i_i = 0. \tag{1.18}$$

The conditions on h_{ij} make it transverse and traceless and ζ carries the single scalar degree of freedom. Using g_{ij}, one can show ${}^{(3)}R = \frac{4}{a^2}\vec{\nabla}^2\zeta$, and the ${}^{(3)}R$ denotes the intrinsic curvature of the spatial hypersurfaces. Hence, ζ is called the comoving curvature perturbation.

Applying the Arnowitt-Deser-Misner formalism [30] to expand the action for a quadratic in derivatives of ζ, one gets the following after significant mathematical rigour,

$$S = \frac{1}{2}\int \mathrm{d}^4x\, a^3\frac{\dot{\Phi}^2}{H^2}\left[\dot{\zeta}^2 - a^{-2}(\partial_i\zeta)^2\right]. \tag{1.19}$$

We consider the Mukhanov variable $v = \bar{z}\zeta$, where, $\bar{z}^2 \equiv a^2 \frac{\dot{\Phi}^2}{H^2} = 2a^2\varepsilon$ and ε is the first slow roll parameter (Equation (1.11)). For derivatives with respect to τ, ($\frac{d}{d\tau} \equiv'$),

$$S = \frac{1}{2}\int d\tau d^3x \left[(v')^2 + (\partial_i v)^2 + \frac{\bar{z}''}{\bar{z}}v^2\right]. \tag{1.20}$$

Transforming the Mukhanov variable to Fourier space, $v(\tau,\vec{x}) = \int \frac{d^3k}{(2\pi)^3} v_{\vec{k}}(\tau)e^{i\vec{k}\cdot\vec{x}}$ where $v_{\vec{k}}(\tau)$ are the mode functions, we arrive at the Mukhanov-Sasaki equation,

$$v''_{\vec{k}} + \left(k^2 - \frac{\bar{z}''}{\bar{z}}\right)v_{\vec{k}} = 0, \tag{1.21}$$

resembling a simple harmonic oscillator with a time dependent frequency $\left(k^2 - \frac{\bar{z}''}{\bar{z}}\right)$.

Further, as these perturbations originate from quantum fluctuations, we must promote the mode function and its conjugate to quantum operators, $v_{\vec{k}} \;\rightarrow\; \hat{v}_{\vec{k}} = v_{\vec{k}}(\tau)\hat{a}_{\vec{k}} + v^*_{-\vec{k}}(\tau)\hat{a}^\dagger_{-\vec{k}}$. Here the creation and annihilation operators $\hat{a}^\dagger_{-\vec{k}}$ and $\hat{a}_{\vec{k}}$ respectively satisfy the canonical commutation relations $[\hat{a}_{\vec{k}}, \hat{a}^\dagger_{\vec{k}'}] = \delta(\vec{k} - \vec{k}')$, and the commutation bracket of the mode function and its momentum conjugate gives us the normalization condition (with $\hbar = 1$),

$$\langle v_{\vec{k}}, v_{\vec{k}}\rangle \equiv i(v^*_{\vec{k}}v'_{\vec{k}} - v^{*\prime}_{\vec{k}}v_{\vec{k}}) = 1. \tag{1.22}$$

It is known that the vacuum state of a time dependent harmonic oscillator cannot be uniquely defined [164]. Therefore we consider the Bunch-Davies vacuum state which is the Minkowski ground state for all comoving observers. It is defined by taking the deep sub horizon limit when all mode functions were inside the horizon, and hence $\tau = -\infty$ or $(|k\tau| > 1)$, using which limit the Equation 1.21 reduces to

$$v''_{\vec{k}} + k^2 v_{\vec{k}} = 0. \tag{1.23}$$

The Bunch Davies vacuum state $(v_{\vec{k}}(\tau)|_{BD})$ is a solution to this equation obtained when the energy associated with the general solution to the equation is minimised.

$$v_{\vec{k}}(\tau)|_{BD} = \lim_{\tau\rightarrow-\infty} v_{\vec{k}}(\tau) = \frac{e^{-ik\tau}}{\sqrt{2k}}. \tag{1.24}$$

Further, to understand how the zero point fluctuations are auto-correlated, we may evaluate the power spectrum of the scalar perturbation using

$$\langle \hat{v}_{\vec{k}}\hat{v}_{\vec{k}'}\rangle = \langle 0|\hat{v}_{\vec{k}}\hat{v}_{\vec{k}'}|0\rangle = \langle 0|(v_{\vec{k}}(\tau)\hat{a}_{\vec{k}} + v^*_{-\vec{k}}(\tau)\hat{a}^\dagger_{-\vec{k}})(v_{\vec{k}'}(\tau)\hat{a}_{\vec{k}'} + v^*_{-\vec{k}'}(\tau)\hat{a}^\dagger_{-\vec{k}'})|0\rangle \tag{1.25}$$

$$\implies \langle \hat{v}_{\vec{k}}\hat{v}_{\vec{k}'}\rangle = v_{\vec{k}}(\tau)v^*_{-\vec{k}'}(\tau)\langle 0|\hat{a}_{\vec{k}}\hat{a}^\dagger_{-\vec{k}'}|0\rangle = v_{\vec{k}}(\tau)v^*_{-\vec{k}'}(\tau)\langle 0|[\hat{a}_{\vec{k}},\hat{a}^\dagger_{-\vec{k}'}]|0\rangle$$

$$= (2\pi)^3|v_{\vec{k}}(\tau)|^2\delta(\vec{k}+\vec{k}') = (2\pi)^3 P_v(k)\delta(\vec{k}+\vec{k}').$$

Hence, $P_v(k) = |v_{\vec{k}}|^2$ is known as the Power spectrum for $v_{\vec{k}}$. Since $v = \bar{z}\zeta$, thus, $P_\zeta = \frac{1}{\bar{z}^2}P_v$. Once a solution for $v_{\vec{k}}$ has been found from the Mukhanov-Sasaki equation, the $|v_{\vec{k}}|^2$ can be computed to get the Power spectrum P_v and subsequently P_ζ. So the power spectrum for the curvature perturbation (ζ) reads

$$P_\zeta = \frac{1}{\bar{z}^2}P_v = \frac{1}{2a^2\varepsilon}P_v. \tag{1.26}$$

This can be rewritten in a dimensionless form of the power spectrum (Δ_s^2), where

$$\Delta_s^2 = \frac{k^3}{2\pi^2}P_\zeta = A_s k^{n_s-1}. \tag{1.27}$$

Here, n_s is called the scalar spectral index and A_s is an associated constant. If $n_s = 1$, the power spectrum is scale-invariant or that the scalar spectrum does not depend on the scale measured with k.

Employing a similar approach for tensor perturbations, one may compute the corresponding action up to second order in the derivatives of h_{ij}. For appropriate dimensionality of the fields, we associate the Planck mass as a proportionality constant again, and rewrite the expression for the action of the tensor perturbations,

$$S = \frac{M_{pl}}{8}\int d\tau d^3x a^2\left[(h'_{ij})^2 - (\vec{\nabla}h_{ij})^2\right]. \tag{1.28}$$

In Fourier space, the mode functions for the transverse and traceless tensor h_{ij} are

$$h_{ij}(\tau,\vec{x}) = \int \frac{d^3k}{(2\pi)^{3/2}}\sum_s \epsilon^s_{ij}(k)h_{\vec{k},s}(\tau)e^{i\vec{k}.\vec{x}}, \tag{1.29}$$

where, $\epsilon_{ii} = k^i\epsilon_{ij} = 0$, and $\epsilon^s_{ij}(k)\epsilon^{s'}_{ij}(k) = 2\delta_{ss'}$. The two states of polarization of the tensor perturbation are denoted by s. Thus the quadratic action is

$$S = \sum_s\int d\tau d^3k\frac{a^2}{4}M_{pl}^2\left[(h'_{\vec{k},s})^2 + k^2(h_{\vec{k},s})\right]. \tag{1.30}$$

Canonically normalising the mode function as, $v_{\vec{k},s} = \frac{a}{2}M_{pl}h_{\vec{k},s}$, we obtain,

$$S = \sum_s\frac{1}{2}\int d\tau d^3k\left[(v'_{\vec{k},s})^2 + \left(k^2 - \frac{a''}{a}\right)(v_{\vec{k},s})^2\right]. \tag{1.31}$$

Upon variation of this action with respect to $v_{\vec{k},s}$, we will again arrive at an equation like,

$$v''_{\vec{k},s} + \left(k^2 - \frac{a''}{a}\right) v_{\vec{k},s} = 0, \tag{1.32}$$

which is very similar to the Mukhanov-Sasaki equation (1.21). Hence, applying a similar approach as before to determine the power spectrum of the tensor perturbations, the power spectrum in dimensionless form for the tensor part can be written as

$$\Delta_t^2 = 2 \times \frac{k^3}{2\pi^2} P_h = 2 \times \left(\frac{2}{aM_{pl}}\right)^2 |v_{\vec{k},s}|^2. \tag{1.33}$$

The factor of 2 in this equation accounts for the contribution from both states of polarisation as denoted by s. Finally we can define the tensor to scalar ratio,

$$r = \frac{\Delta_t^2}{\Delta_s^2}, \tag{1.34}$$

which measures the strength of the tensor power spectrum relative to that of the scalar power spectrum. Moreover, there are spectral indices associated with these power spectra, as

$$\Delta_s^2 \propto k^{n_s - 1}, \quad \Delta_t^2 \propto k^{n_t - 1}, \tag{1.35}$$

such that n_s is the scalar spectral index and n_t is the tensor spectral index.

1.3.4 Connecting the primordial power spectrum with current observations

Transfer functions are mathematical devices to explain one or a set of physical phenomena in the period between inflation and observations of the CMB or the LSS that are made today, and can be obtained using numerical solutions [255, 176] to two sets of equations, namely,

(a) *Einstein field equations:* The choice of a gauge introduces some potentials which are perturbations to the background metric. Additionally, we define other perturbed quantities such as those of the density and the temperature,

$$\delta = \frac{\delta\rho}{\rho}, \quad \Theta = \frac{\delta T}{T}. \tag{1.36}$$

An evolution equation for photons can be found in Θ, and that of matter can be found in the perturbation of density of the predominant matter component which is cold dark matter, δ_{CDM}, and its velocity v_{CDM}. Thus, the Einstein field equations can be solved to obtain relations between the metric perturbations of a specific gauge choice, and the density and temperature perturbations.

(b) *Boltzmann equation:* This equation relates the matter density and photon temperature perturbations, and the peculiar velocity of matter with the metric perturbations, starting from,

$$\frac{df}{dt} = C[f], \tag{1.37}$$

where, f denotes the distribution function for the species, and $C[f]$ known as the collision term, represents the complex interactions among different components with the species under consideration.

We can evaluate transfer functions to connect the initial perturbations (of curvature $\zeta_{\vec{k}}$ or the tensor modes $h_{\vec{k},s}$) after inflation with the observable fluctuations in matter density or CMB temperature or polarisation, or neutrino number density, or the radio fluctuations in the redshifted background of the 21 cm Hydrogen line, and so on. For example, if we currently measure an entity $\mathcal{E}_{\vec{k}}(\tau)$, in Fourier ($\vec{k}$) space, and at the time τ today, the the transfer function $\mathcal{T}(k,\tau,\tau_*)$ will connect $Q_{\vec{k}}$ with a primordial perturbation at a pivot scale $k_* = a(\tau_*)H(\tau_*)$ corresponding to a time τ_* when the mode exits the horizon. Thus,

$$\begin{aligned} \mathcal{E}_{\vec{k}}(\tau) &= \mathcal{T}(k,\tau,\tau_*)\zeta_{\vec{k}}(\tau_*), \text{ or,} \\ \mathcal{E}_{\vec{k}}(\tau) &= \mathcal{T}(k,\tau,\tau_*)h_{\vec{k},s}(\tau_*). \end{aligned} \tag{1.38}$$

In the following we discuss mainly about the radiation and matter transfer functions [278], which are useful for understanding the CMB and the LSS, respectively.

1. *The radiation transfer function* is obtained by solving the equations for Θ. It contains contributions primarily from (a) the Sachs-Wolfe effect which describes the evolution of Θ as it interacts with the gravitational potential, (b) the Doppler effect which explains the impact of the peculiar velocity of the baryons on the distribution of the photons, (c) the Integrated Sachs-Wolfe effect, which describes how the gravitational potentials evolve over the course of time from photon decoupling until today. The radiation transfer function shows constant behaviour for super-horizon scales as the

photons are not expected to interact causally with the other particles. On the other hand for sub-horizon scales, the radiation transfer function is oscillatory due to the baryon acoustic oscillations caused by photon-baryon interactions.

2. *The matter transfer function* is a solution to a complete equation in δ_{CDM} obtained from the evolution equations of δ_{CDM} and v_{CDM}. Similar to the case of the radiation transfer function, the matter transfer function is also constant for super-horizon scales. However, on sub-horizon scales, one sees a growth in the matter perturbations which exists in the radiation dominated era but becomes significant only in the matter dominated era of the universe. It is in the matter dominated era that LSS begins to form. Although currently we live in a Dark energy dominated universe which is causing the present expansion of the universe, the behaviour of the matter transfer function indicates that the perturbations will keep growing and LSS will continue to form.

Using transfer functions, we can connect primordial perturbations with those that exist in the several probes of Cosmology today. Such probes attest to the existence of different eras in the formation of the universe, as we trace the chronology of its evolution. We briefly discuss some observational probes and their importance in the next Section 1.4.

1.4 Observational probes in cosmology

Several interesting probes in Cosmology exist, which help us frame our understanding and theories about the various stages of evolution of the universe [204]. In the following, we describe a few probes among the many that exist in cosmology.

1. *The Cosmic Microwave Background (CMB)* is the first light from the earliest stages of the universe. It was very hot, and formed approximately $380,000$ years after the Big Bang. The CMB is the most accessible probe [51] for studying the earliest state of the universe when it became transparent, since this microwave radiation surrounds us with a strikingly uniform temperature of about 2.7K [103]. The directionally dependent fluctuations (called anisotropies [27]) from this temperature $\sim \mathcal{O}(10^{-5}\text{K})$ are primarily the imprints of gravitational perturbations at the era of recombination.

2. *The Cosmic Neutrino Background (CνB)* if detected successfully, will provide information of a period of time (about a second after Big Bang [295]) earlier than that carried by the CMB photons. This is because the neutrinos decoupled from other particles like electrons, positrons and photons at temperatures $\sim$ MeV , whereas recombination happened at ~ 0.3 eV . There are both direct and indirect methods of detecting the CνB [29]. The direct ones pertain to effects of CνB neutrinos on some targets [239]. The indirect probes include analysis of cosmic rays for any interactions with neutrinos [302].

3. *Cosmic Infrared Background (CIB):* This is a background radiation which helps probe the evolution of the universe after the CMB photons decouple and structure begins to form [131]. It is a cumulative radiation from various sources such as the first generation (Population-III or Pop-III) of stars [151], which cannot be accessed by present day telescopes. The CIB upon careful separation from radiation of known stars, diffuse emission, and galaxies, is seen to contain fluctuations which are imprints of large structural features attributable to the first generation of stars about 12 billion years ago.

4. *Active Galactic Nuclei (AGNs), Blazars and Quasars:* Active galaxies are those for which the luminosities are $\sim 10^{11} - 10^{15}$ times that of the sun. They are sources of Hydrogen emission lines, radio synchrotron emission [230] and X-rays. When such AGNs have their jet directions along our line of sight, then they are called blazars, with relativistic jets of radio to very high energy gamma-rays [143]. For intermediate angular alignments, such AGNs are called quasars [152]. AGNs primarily comprise supermassive black holes, which pull in gas and dust to emit radiation across the electromagnetic spectrum [97]. Quasars are distinguishable from other AGNs due to their characteristically intense luminosity [245], such that the ones we see today could be from the first galaxies. Due to the finite speed of light, the light from the nearest quasars observable from earth at a hundred million light years away from us were likely produced in quasars 600 million years ago [213].

5. *Lyman-α forest:* Some quasars emit radiation of shorter wavelength than the Lyman-α line, but enroute to us, due to the expansion of the universe, they get redshifted into a strong Lyman-α emission line [275], in addition to subsidiary peaks. In the intervening medium of neutral hydrogen (H-I) several absorption lines arise. This set of a strong Lyman-α peak and other absorption lines forms a dense structure called the Lyman-α forest [287]. A study of this "forest" provides information of the content and distribution of neutral hydrogen between us and the quasars, rate of expansion of the universe and so on [214]. Further, we can trace dark matter [219] since Lyman α lines may be formed due to gravitational effects of non-luminous matter as well.

6. *The 21 cm hydrogen line* arises due to the hyperfine splitting of the $1s$ ground state of the hydrogen atom due to the interactions of the magnetic moments of the electron and proton [119] into the singlet state (antisymmetric state) and the triplet state (symmetric state). These states have an energy difference which corresponds to approximately 21 cm wavelength of electromagnetic radiation [273]. The 21 cm light is produced as a radio signal by hydrogen atoms in the primordial universe, as the radiation pervades the dust clouds, providing us a map of hydrogen and hence that of the first structures in the universe [226].

7. *Carbon monoxide (CO) emission lines:* CO has a set of rotation spectra produced due to rotational energy transitions that forms a ladder for use in mapping structures at different redshifts [203]. Various CO lines are useful for determining different redshifts and structures: $CO(1-0)$ line is useful for determining redshifts, $CO(6-5)$ is used for probing protoplanetary disks [171] and molecular clouds at large distances $(z > 6)$. Assuming virial stability of the cloud, one can calculate the mass of the cloud; and assuming a specific CO to H_2 factor, the mass of a possibly distant molecular cloud can be calculated [220]. Given different isotopic presences of carbon and oxygen, the wavelengths of the CO lines are affected and that helps us to investigate the kinds of isotopes present [291]. The extraction of such information can be undertaken with the help of line intensity mapping of the CO lines [179]. Intensity mapping of lines captures the spatial variations in the integrated or combined emission from spectral

lines emanating from several individually unresolved galaxies. Line fluctuations help survey the underlying the LSS of the Universe and the frequency dependencies can be used to estimate the distribution of the lines of emission with redshift [288] aligning with our line of sight.

In this thesis, we shall focus on the Cosmic Microwave Background and its small anisotropies. We discuss at length about the CMB in the subsequent sections.

1.5 The CMB and its observables

The CMB was discovered in a serendipitous effort by Robert Wilson and Arno Penzias in 1964, while they were looking for radio emissions from the Milky Way galaxy, confirming the existence of this primordial radiation. In the early universe, electrons and baryons were tightly coupled to photons in a hot plasma due to continual Thomson (elastic) scattering,

$$\gamma + e^- \rightleftharpoons \gamma + e^-, \tag{1.39}$$

occurring at a rate, say, Γ_e. These collisions ensured the opacity of the cosmos, since photons could not travel very far sans interactions with matter. The temperature at which recombination into stable atoms or decoupling of photons occurs is dependent on the baryon-photon ratio (η), and the ionisation potential (Q) of the atomic species. Considering only stable atom formation for hydrogen, the process

$$p + e^- \rightarrow H + \gamma, \tag{1.40}$$

can be explained using the Saha equation [243],

$$\frac{1 - X_e}{X_e^2} = \frac{\pm\sqrt{2}\zeta(3)}{\sqrt{\pi}} \eta \left(\frac{T}{m_e}\right)^{3/2} \left(\frac{Q}{T}\right), \tag{1.41}$$

where the equilibrium ionization fraction of Hydrogen is given by X_e, m_e is the mass of the electron, $Q = 13.6$eV is the ionisation energy of hydrogen, T is the temperature, and ratio of baryons to photons is

$$\eta = \frac{n_b - n_{\bar{b}}}{n_\gamma} = 2.68 \times 10^{-8} \left(\Omega_b h_0^2\right). \tag{1.42}$$

Here, $n_b, n_{\bar{b}}, n_\gamma$ represent the number densities of baryons, anti-baryons and photons, respectively, and Ω_b is the baryon mass density, and h_0 is the Hubble constant in units of 100km/s/Mpc, i.e, $h_0 = H_0/(100 \text{ km/s/Mpc})$. The process of recombination takes place over a range of redshifts $\Delta z \sim 200$. Given an ionisation fraction say, $X_e = 0.1$, the recombination temperature is $T_R \sim 0.3$ eV. Once recombination has occurred, there is an increase of the photon mean free path beyond the Hubble radius. These photons propagate freely throughout the universe and match an almost perfect blackbody distribution of frequencies, since they decoupled from a state of nearly ideal thermal equilibrium.

Those photons at recombination were at an approximate temperature of $T_R \sim 3000$K and have redshifted towards the microwave region of the spectrum, due to the expansion of the universe, as $T \propto \frac{1}{a(t)}$. If on the contrary, we had a contracting universe, the photons would have blueshifted. The photons of the CMB today constitute a nearly uniform background with temperature of $T_0 \sim 2.726$ K, corresponding to the background metric dictating a homogeneous and isotropic expansion of the universe. The photons travel towards us from a spherical shell where they scattered for the last time, and were released thereafter. Using T_0, we can estimate the redshift of the last scattering surface as:

$$1 + z_R = \frac{a(t_0)}{a(t_R)} = \frac{T_R}{T_0} \simeq 1100. \tag{1.43}$$

1.5.1 Gleaning information from the CMB

Principally, three aspects of the CMB are studied separately for their auto-correlations, and also in combination with each other in terms of cross-correlations. Namely, these are (a) its temperature (T) fluctuations or anisotropies, (b) the curl-free component (E) of the polarisation anisotropies, and (c) the curl-containing component (B) of the polarisation anisotropies. Temperature anisotropies are primarily due to those very small inhomogeneities in the distribution of matter which led to variations in the gravitational potential wells curving space, from which photons had to crawl out. Before decoupling, there could be relativistic effects and hence, considering Compton scattering between photons and electrons is important. Such scattering leads to polarisation in the CMB photons in the following manner.

1. If the incoming radiation is isotropic in the rest frame of the electron, then the outgoing radiation emerges unpolarised.

2. If the incoming radiation is anisotropic in a dipolar pattern, such that from say, the $\hat{x}$ direction, there is a ray going towards the origin from a hot spot and that from the $-\hat{x}$ direction comes from a cold spot, then the outgoing radiation remains unpolarised, assuming that the radiation from other directions comes in isotropically.

3. If there is a quadrupolar anisotropy in the incoming radiation, i.e, if there is a ray coming from a hot spot from the $\hat{x}$ direction and another coming from a cold spot from the $\hat{y}$ direction, then the resulting radiation propagating in the $\hat{z}$ direction is linearly polarised.

We note however, that a quadrupolar anisotropy in the incoming radiation can be generated only when the photons decouple shortly before the electrons and protons recombine to form hydrogen atoms. This being a rare condition, means that the expected amplitude of the polarisation anisotropies is lower than that of the temperature fluctuations.

For extracting information from the CMB, the angular power spectrum (C_ℓ^{XY}) of CMB temperature and polarisation anisotropies (here, X,Y can take T,E,B as labels) can be connected with the power spectrum of the primordial perturbations $P_\zeta(k)$ and $P_h(k)$,

$$C_\ell^{XY} = \frac{2}{\pi}\int k^2 dk P_\psi(k)\Delta_{X\ell}(k)\Delta_{Yl}(k), \tag{1.44}$$

where, $\psi \equiv \zeta, h$, and $\Delta_{X\ell}, \Delta_{Y\ell}$ are the transfer functions in the multipole ℓ and the Fourier mode k,

$$\Delta_{X\ell} = \int_0^{\tau_0} d\tau S_X(k,\tau) P_{X\ell}\left[k(\tau_0 - \tau)\right]. \tag{1.45}$$

These line-of-sight integrals factorize into two terms: a physical source term $S_X(k,\tau)$ and a geometric projection factor $P_{X\ell}\left[k(\tau_0-\tau)\right]$ which are combinations of Bessel's functions.

1.5.2 Temperature anisotropies

The CMB temperature fluctuations relative to the background can be decomposed in spherical harmonics as,

$$\frac{\Delta T(\hat{n})}{T_0} = \sum_{\ell,m} a_{\ell m} Y_{\ell m}(\hat{n}), \quad \text{where,} \quad a_{\ell m} = \int d\Omega Y^*_{\ell m}(\hat{n}) \frac{\Delta T(\hat{n})}{T_0}. \tag{1.46}$$

The spherical harmonics ($Y_{\ell m}(\hat{n})$) on a 2-sphere correspond to the projection of the spherical sky of observation for photons coming from the last scattering surface. Thus, the multipoles ℓ's give the monopole, dipole and so on for $\ell = 0, 1, ...$, and m's take the values $[-\ell, \ell]$. When the temperature itself is decomposed in spherical harmonics, a measurement of the monopole corresponds to the uniform temperature of the CMB. However, since we have decomposed $\Delta T/T_0$'s, we must obtain a value of zero for the monopole. Further the dipole is non-cosmological, since it is dominated by the dipole corresponding to our peculiar motion in the rest frame of the CMB.

In order to elucidate the relation between these temperature fluctuations and primordial perturbations, we note that while reentering the horizon at any time, the curvature perturbation (ζ) induces density fluctuations $\delta\rho$ in the primordial plasma, from which photons decouple and free-stream while getting redshifted into the CMB. Thus,

$$a_{\ell m} = 4\pi(-1)^\ell \int \frac{d^3k}{(2\pi)^3} \Delta_{T\ell}(k) \zeta_{\vec{k}} Y_{\ell m}(\hat{k}), \tag{1.47}$$

since scalar perturbations contribute most significantly to the temperature fluctuations in the CMB as the tensor-to-scalar ratio $r < 0.3$ with current bounds.

As we will be discussing in Section 1.6, for rotationally invariant two-point angular correlation of $\Delta T/T_0$, the angular power spectrum estimator is

$$\hat{C}_\ell^{TT} = \frac{1}{2\ell+1} \sum_m a^*_{\ell m} a_{\ell m}, \text{ and,} \quad \langle \hat{C}_\ell^{TT} \rangle = C_\ell^{TT}, \text{ for } \langle a^*_{\ell m} a_{\ell' m'} \rangle = C_\ell^{TT} \delta_{\ell\ell'} \delta_{mm'}. \tag{1.48}$$

Here, $\langle ... \rangle$ denotes an average over an ensemble of various similar universes.

A noteworthy behaviour of the CMB fluctuations is at large angular scales or low ℓ's. Since the largest scale modes left the horizon earliest and reenter at the latest times, they are mostly unaffected by sub-horizon evolution. This is the Sachs-Wolfe regime for which the transfer functions are geometric projections from recombination until today: $\Delta_{T\ell}(k) =$

$\frac{1}{2}j_\ell\left[k(\tau_0-\tau_{rec})\right]$, and

$$C_\ell^{TT}=\frac{2}{9\pi}\int k^2dkP_\zeta(k)j_\ell^2\left[k(\tau_0-\tau_{rec})\right],\quad \text{or,}\quad C_\ell^{TT}\propto\frac{2\pi}{\ell(\ell+1)}\ell^{n_s-1}, \tag{1.49}$$

for a power spectrum of the form, $\Delta_s^2(k)\propto k^{n_s-1}$. Thus for a scale invariant spectrum, $n_s=1$, the quantity $\mathcal{D}_\ell=\frac{\ell(\ell+1)}{2\pi}C_\ell^{TT}$ is independent of ℓ. This ensures that for the largest of scales, assuming an approximately scale-invariant spectrum, the curve of $\mathcal{D}_\ell$ is nearly a straight line.

1.5.3 Polarisation anisotropies

Polarisation of the CMB photons primarily occurs due to a quadrupolar anisotropy just before recombination as discussed in Section 1.5.1. Such polarised light can be represented using the Stokes parameters I,Q,U,V. If we suppose that the light is traveling in the $\hat{z}$ direction, then the electric fields in $\hat{x},\hat{y}$ directions can be written as follows:

$$E_x=a_x(t)\cos\left[\omega_0t-\theta_x(t)\right],\quad E_y=a_y(t)\cos\left[\omega_0t-\theta_y(t)\right]. \tag{1.50}$$

Since the CMB photons are nearly monochromatic with principal frequency ω_0, this necessitates that the amplitudes a_x and a_y and the phase angles θ_x and θ_y will be very slowly varying functions of time as compared to the time scale $\sim\omega_0^{-1}$. Additionally, correlations between E_x and E_y mean that the wave is polarised, and can be understood with the help of the Stokes parameters ($\langle\rangle_t$ is average over time):

$$\begin{aligned} I&=\langle a_x^2\rangle_t+\langle a_y^2\rangle_t, & Q&=\langle a_x^2\rangle_t-\langle a_y^2\rangle_t, \\ U&=\langle 2a_xa_y\cos(\theta_x-\theta_y)\rangle_t, & V&=\langle 2a_xa_y\sin(\theta_x-\theta_y)\rangle_t. \end{aligned} \tag{1.51}$$

The quantity I is always positive, whereas Q,U,V denote the state of polarisation and can be both positive or negative. Unpolarised light entails $Q=U=V=0$. Linear polarisation is measured using I,Q,U, whereas V measures circular polarisation, and hence we expect $V=0$ due to lack of conditions for circular polarisation in the early universe.

Considering the intensity of light tensor $I_{ij}(\hat{n})$ in the $2D$ plane of the oscillating electric field, normal to the direction of propagation ($-\hat{n}$) of the light ray, for two orthogonal basis vectors $\hat{e_1}$ and $\hat{e_2}$ perpendicular to $\hat{n}$, we quantify linear polarisation using the components:

$$Q = \frac{1}{4}(I_{11} - I_{22}), \quad U = \frac{1}{2}I_{12}. \tag{1.52}$$

The temperature anisotropy can be measured as $\frac{1}{4}(I_{11}+I_{22})$. The polarisation is represented as a headless vector having a magnitude, and phase angle given by

$$P = \sqrt{Q^2+U^2}, \quad \alpha = \frac{1}{2}\tan^{-1}\frac{U}{Q}. \tag{1.53}$$

Unlike the temperature fluctuations, the fields Q and U transform under a rotation by γ in the plane of $\hat{e_1} \times \hat{e_2}$, as $(Q \pm iU)(\hat{n}) \to e^{\mp 2i\gamma}(Q \pm iU)(\hat{n})$ like a spin-2 field, requiring an expansion of the same in terms of the spin-2 or tensor spherical harmonics, as

$$(Q \pm iU)(\hat{n}) = \sum_{\ell,m} a_{\pm 2\ell m \pm 2}Y_{\ell m}(\hat{n}). \tag{1.54}$$

For convenience we form linear combinations of the spherical harmonic coefficients,

$$a_{E,\ell m} = -\frac{1}{2}\left(a_{2,\ell m} + a_{-2,\ell m}\right), \quad a_{B,\ell m} = -\frac{1}{2i}\left(a_{2,\ell m} - a_{-2,\ell m}\right), \tag{1.55}$$

to obtain spin-0 or scalar fields E and B,

$$E(\hat{n}) = \sum_{\ell,m} a_{E,\ell m}Y_{\ell m}(\hat{n}), \quad B(\hat{n}) = \sum_{\ell,m} a_{B,\ell m}Y_{\ell m}(\hat{n}). \tag{1.56}$$

The E modes are curl free, and shown as radial lines around a cold spot, or tangential lines around a hot spot. The B mode is not curl free, but has null divergence, and is represented as lines of vorticity around hot or cold spot centres with different handedness. Both modes are rotationally invariant, but only E modes are invariant under a parity transformation.

In existing literature [299, 150], there are interpretations of the origin of E and B modes. Scalar (density) perturbations generate only E modes. Vector (vorticity) perturbations generate only B modes, but as vector perturbations decay in an expanding universe, they are ignored for practical purposes. Tensor (gravitational wave) perturbations generate both E and B modes. Hence, if primordial gravitational waves can be detected through the imprint of B modes in the CMB polarisation data, then inflation can be well corroborated. Among angular power spectra, while C_ℓ^{TB}, C_ℓ^{EB} vanish for symmetry reasons, these exist:

$$C_\ell^{EE} \approx (4\pi)^2 \int k^2 dk P_\zeta(k) \Delta_{E\ell}^2(k), \qquad C_\ell^{TE} \approx (4\pi^2) \int k^2 dk P_\zeta(k) \Delta_{T\ell}(k) \Delta_{E\ell}(k),$$
$$C_\ell^{BB} \approx (4\pi^2) \int k^2 dk P_h(k) \Delta_{B\ell}^2(k). \tag{1.57}$$

These equations clearly indicate the correspondence between the angular power and their primordial power spectrum counterparts, $P_\zeta(k)$ in the case of E modes, and $P_h(k)$ in the case of B modes. The $C_\ell^{TT}, C_\ell^{TE}, C_\ell^{EE}$ provide us complementary information about $P_\zeta(k)$. On the other hand, the measurement of C_ℓ^{BB} is very useful for understanding the possibility of primordial gravitational waves arising from primordial tensor perturbations.

1.6 Why should we study the isotropy of the CMB?

Our principal aim in this thesis is to study the isotropy of the CMB temperature anisotropy field in the context of an inflationary origin of these temperature anisotropies. This is because such a study helps us investigate (a) the assumptions of large scale homogeneity and isotropy which dictate the current paradigm of cosmic inflation, and (b) the earliest epochs of the evolution of our universe which correspond to the largest scales. The first aspect is a consequence of the cosmological principle and the second aspect arises due to the notion of cosmic inflation which stretched out the largest scale modes of fluctuations at the earliest which were then frozen in time, and which reenter the causal horizon at the latest times today.

The rationale behind studying the CMB temperature anisotropy field for our objective is the following. Since we wish to assess the validity of the cosmological principle in tandem with that of cosmic inflation, hence, among the possible probes in Cosmology, we focus our attention on the ones which were generated and decoupled from the background primordial fluid at the earliest times. Such probes are (1) the Primordial Gravitational Wave (PGW) background created by the inflationary expansion, which permeates all of space, since these waves decoupled immediately after the Big Bang [163], (2) the Cosmic Neutrino Background (CνB), which decoupled about a second after the Big Bang [184] and (3) the CMB which decoupled about $380,000$ years after the Big Bang [99]. Direct and fairly accurate detections of (1) and (2) are active and challenging fields of research and we await their results. Thus currently the CMB is well understood and has been used widely to substantiate the Standard Model of Cosmology [136, 9]. This motivates a careful scrutiny of the CMB with regard to its isotropy for better understanding of cosmic inflation and the maximally symmetric background metric used to model the expansion of the universe during inflation. We focus on the temperature fluctuations of the CMB because they are stronger by at least an order of magnitude [144] and have considerably higher signal-to-noise ratio in the observed data as compared to polarisation signals [81, 45].

In the following two subsections we discuss about the notions of statistical isotropy (SI) and Gaussianity which are closely associated with those of large scale isotropy, and the null correlations between the different independent modes of fluctuations.

1.6.1 Gaussianity

In Fourier decomposition, the primordial curvature perturbation reads as,

$$\zeta(\vec{x},\tau) = \int \frac{d^3k}{(2\pi)^{3/2}} \left[\hat{a}_{\vec{k}} \zeta_{\vec{k}}(\tau) e^{i\vec{k}\cdot\vec{x}} + \hat{a}^{\dagger}_{\vec{k}} \zeta_{\vec{k}}(\tau)^* e^{-i\vec{k}\cdot\vec{x}} \right], \tag{1.58}$$

after being quantised and expanded in terms of the creation and annihilation operators, which satisfy $\left[\hat{a}_{\vec{k}}, \hat{a}^{\dagger}_{\vec{k}'}\right] = \delta(\vec{k} - \vec{k}')$, making these Fourier modes independent. Since the primordial curvature perturbations are described as sums of an infinite number of independent Fourier modes, they are expected to be Gaussian distributed due to the Central Limit Theorem [161]. Hence 2-point statistics suffice to describe them, as expected for ground-state quantum fluctuations. Further, each of the primordial fluctuations at any particular scale, i.e., the same wavelength, are expected to be correlated as they are Gaussian distributed with the same variance, and exit the cosmological horizon at the same time as and when cosmic inflation acts on them.

The temperature fluctuations which map the primordial curvature perturbations are therefore also Gaussian. Hence the angular power spectrum (APS) C_ℓ or the two-point angular correlation function $\langle \Delta T(\hat{n}_1) \Delta T(\hat{n}_2) \rangle$ for these fluctuations contain complete information of the same. In spherical harmonic basis, we know $\Delta T(\hat{n}) = \sum_{\ell m} a_{\ell m} Y_{\ell m}$, which entails that the $a_{\ell m}$'s must be Gaussian distributed, that is,

$$P(a_{\ell m}) = \frac{1}{\sqrt{2\pi C_\ell}} \exp\left(\frac{-a_{\ell m}^2}{2C_\ell}\right). \tag{1.59}$$

Herein lies an implicit assumption that the covariance matrix of the $a_{\ell m}$'s given by $\langle a_{\ell m} a^*_{\ell' m'}\rangle$ is diagonal and equal to the C_ℓ's which measure the strength of fluctuations at a given angular scale or multipole ℓ. This assumption is a consequence of SI, as we explain below.

1.6.2 Statistical Isotropy

Any anisotropy or preferred direction, especially at the largest scales is expected to be stretched beyond the cosmological horizon and hence must have no causal influence thereafter on the relatively smaller scale fluctuations. Hence when these larger scale fluctuations which were still outside the horizon at recombination reenter the horizon, their power spectrum should be essentially free from any directional preference and should have no bearing on the other relatively smaller scale fluctuations. Mathematically this manifests in the lack of correlations of the spherical harmonic coefficients ($a_{\ell m}$'s) of dissimilar multipoles for the temperature anisotropy field on the 2-sphere of observation. Thus only fluctuations of the same scale are correlated, which means that the individual variances of the $a_{\ell m}$'s are only dependent on the angular scale given by ℓ. The SI of the CMB encapsulates this notion.

Since SI upholds the absence of any preferred direction, hence mathematically it is enshrined in the rotational invariance of any n-point correlation function on the sky [161], i.e.,

$$\langle D\Delta T(\hat{n}_1)...D\Delta T(\hat{n}_{n-1})D\Delta T(\hat{n}_n)\rangle = \langle \Delta T(\hat{n}_1)...\Delta T(\hat{n}_{n-1})\Delta T(\hat{n}_n)\rangle, \tag{1.60}$$

where $D = D(\chi, \xi, \psi)$ is the Wigner rotation matrix with angles χ, ξ, ψ. Additionally , using $\Delta T(\hat{n}_i) = \sum_{\ell_i m_i} a_{\ell_i m_i} Y_{\ell_i m_i}(\hat{n}_i)$ and a harmonic representation of the Wigner-D matrix,

$$D(\chi, \xi, \psi) Y_{\ell m}(\hat{n}) = \sum_{\ell m'} D^{(\ell)}_{m' m} Y_{\ell m'}(\hat{n}), \tag{1.61}$$

where, $D^{(\ell)}_{m'm}(\chi, \xi, \psi)$ is the matrix element $\langle \ell, m'|D|\ell, m\rangle$ denoting a finite rotation of the state $|\ell, m\rangle$ to $|\ell, m'\rangle$, we can rewrite the equation (1.60) as

$$\sum_{m_1=-\ell_1}^{\ell_1}\sum_{m_1'=-\ell_1}^{\ell_1}...\sum_{m_n=-\ell_n}^{\ell_n}\sum_{m_n'=-\ell_n}^{\ell_n}\langle a_{\ell_1 m_1}...a_{\ell_n m_n}\rangle D^{(\ell_1')}_{m_1' m_1} Y_{\ell_1 m_1'}...D^{(\ell_n)}_{m_n' m_n} Y_{\ell_n m_n'}$$
$$= \sum_{m_1=-\ell_1}^{\ell_1}...\sum_{m_n=-\ell_n}^{\ell_n}\langle a_{\ell_1 m_1}...a_{\ell_n m_n}\rangle Y_{\ell_1 m_1}...Y_{\ell_n m_n}. \quad (1.62)$$

On the left hand side of this equation, m_i and m_i' are dummy indices (where $i = 1, ..., n$) and can hence be exchanged, after which we arrive at the following equation,

$$\sum_{m_1'}...\sum_{m_n'}\langle a_{\ell_1 m_1'}...a_{\ell_n m_n'}\rangle D^{(\ell_1)}_{m_1' m_1}...D^{(\ell_n)}_{m_n' m_n} = \langle a_{\ell_1 m_1}...a_{\ell_n m_n}\rangle. \quad (1.63)$$

This equation encapsulates the notion of SI for the angular power spectrum ($n = 2$), the bispectrum ($n = 3$), and so on. The covariance matrix of the $a_{\ell m}$'s is not necessarily diagonal, i.e., $\langle a_{\ell m} a^*_{\ell' m'}\rangle \neq f(\ell)\delta_{\ell\ell'}\delta_{mm'}$, without full sky coverage of the $\Delta T(\hat{n})$ and a rotationally invariant 2-point angular correlation function, i.e. (from (1.63)),

$$\langle a_{\ell_1 m_1} a^*_{\ell_2 m_2}\rangle = \sum_{m_1' m_2'}\langle a_{\ell_1 m_1'} a^*_{\ell_2 m_2'}\rangle D^{(\ell_1)}_{m_1' m_1} D^{(\ell_2)}_{m_2' m_2}. \quad (1.64)$$

The $a^*_{\ell_2 m_2}$ in the 2-point correlation function is used for conveniently expressing the same in terms of the estimator $\hat{C}_\ell$, and for ease in computing the products of the Wigner-D matrices.

If we assume that the angular covariance matrix of the $a_{\ell m}$'s is diagonal, say given by $\langle a_{\ell_1 m_1} a^*_{\ell_2 m_2}\rangle = \langle \hat{C}_{\ell_1}\rangle \delta_{\ell_1\ell_2}\delta_{m_1 m_2}$, then the above equation (1.64) reduces to

$$\begin{aligned}
\langle a_{\ell_1 m_1} a^*_{\ell_2 m_2}\rangle &= \langle \hat{C}_{\ell_1}\rangle \delta_{\ell_1\ell_2}\sum_{m_1' m_2'} D^{(\ell_1)}_{m_1' m_1} D^{(\ell_2)*}_{m_2' m_2}\delta_{m_1' m_2'} \\
&= \langle \hat{C}_{\ell_1}\rangle \delta_{\ell_1\ell_2}\sum_{m_1'} D^{(\ell_1)}_{m_1' m_1} D^{(\ell_1)*}_{m_1' m_2}, \\
\text{or,}\quad \langle a_{\ell_1 m_1} a^*_{\ell_2 m_2}\rangle &= \langle \hat{C}_{\ell_1}\rangle \delta_{\ell_1\ell_2}\delta_{m_1 m_2}, \qquad (1.65)
\end{aligned}$$

which proves that $\langle \hat{C}_\ell\rangle$ is rotationally invariant, thus manifesting in the diagonal covariance matrix of the $a_{\ell m}$'s. In the above deduction, we have used the orthogonality condition $\sum_k D^{(\ell)}_{k m_1} D^{(\ell)*}_{k m_2} = \delta_{m_1 m_2}$. Thus SI ensures that the $a_{\ell m}$'s and hence the temperature fluctuations are uncorrelated between different multipoles, or different angular scales.

1.7 Challenges in extracting the CMB

In order to accomplish our task of performing credible investigations into the isotropy of the CMB, we need observational data of the CMB in its most pristine form. However, there are several challenges in extracting the pure CMB from the observed data, categorised into: (1) astrophysical foregrounds, (2) systematic effects, and (3) statistical impediments.

1.7.1 Astrophysical foreground contamination

In a CMB experiment, the observed signal contains foregrounds, which must be separated out with the help of multi-frequency observations since the spectral shape of a foreground is different from that of the CMB. Their brightness temperatures are usually power laws of frequency raised to a spectral index. Some principal foregrounds [147] are explained as follows.

1. *Galactic synchrotron emission:* It is the synchrotron emission from cosmic ray electrons and positrons accelerated in the interstellar magnetic field. It is dominant at the frequency $\nu \sim 10$ GHz. The brightness temperature $T_b \propto \nu^{-\beta}$, with β being the spectral index which itself varies with frequency and spatial coordinates. The index β has an average value of 2.5 at radio frequencies, and 3.0 at $\nu \sim 10$ GHz. Since up to 70% of the synchrotron radiation is polarised, this interferes with the CMB polarisation signal. Its scale dependence $\sim \ell^{-3}$ means that it dominates at the largest of scales.

2. *Galactic free-free emission:* Thermal Bremsstrahlung emission emanating as hot electrons scatter off ions in the interstellar medium, is called free-free emission. The spectral index is $\simeq 2.15$. Relative to the synchrotron emission, free-free emission dominates at frequencies of $30 - 60$ GHz. It is composed of a diffuse and a discrete component. Hydrogen H-II is a principal source of discrete emission, whereas the H-α line corresponding to a wavelength of 6563 Å is a tracer of the diffuse form. Similar to synchrotron emission, free-free emission scales as $\sim \ell^{-3}$.

3. *Galactic thermal dust emission:* This emission is produced in the far infrared region,

due to the heating of dust grains such as graphites, silicates and PAHs (polycyclic aromatic hydrocarbons) by interstellar radiation. Its temperature depends on the intensity of the interstellar radiation heating the dust grains, efficiency of emission by the grains, not to mention the shapes, sizes, structures and chemical composition of the grains. Thermal dust emission occurs predominantly at frequencies $\gtrsim 70$ GHz. A global dust angular power spectrum scales as ℓ^{-3}, however, for higher galactic latitudes it is better denoted as $\ell^{-2.5}$, barring some spatial variations.

4. *Anomalous microwave emission (AME):* In addition to thermal dust, there is a spinning dust component which is an anomalous foreground emission at $\nu \sim 20 - 60$ GHz. A plausible candidate for this are PAHs spinning with some specific electric dipole moments. AME emanates from dense molecular gas and low density atomic gas regions. Another candidate for AME is magneto-dipole emission from strongly magnetised grains, the polarisation amplitude of which can go up to 40%.

5. *Carbon monoxide (CO) molecular clouds:* Rotational transitions of CO from its molecular clouds are a substantial contaminant, especially for ≥ 100 GHz band, as seen for the Planck satellite. For example, the first three transition lines ($J = 1 - 0, 2 - 1, 3 - 2$) at frequencies of 115 GHz, 230 GHz, and 345 GHz, feature in three of the high frequency observations made by the Planck satellite. The power spectrum of CO emissions is predominantly present at smaller angular scales of $\ell \gtrsim 10000$.

6. *Extragalactic sources:* Below and above 200 GHz, several populations of high frequency sources (like dusty galaxies) and radio sources (blazars, quasars, and the like) contribute to the extra-galactic region. Many such sources are very faint, making them difficult to be identified and removed compared to the brighter ones.

We note that galactic foreground contamination is predominant on large scales, and since our studies of the isotropy of the CMB focus mainly on the largest scale fluctuations, these foregrounds must be appropriately minimized before investigations are embarked on.

1.7.2 Systematic effects

Systematic effects [197] are a combination of astrophysical characteristics of the signal, the optical interface which determines the beam width and shape, the response of the instrument, and the environment which affects the thermal and electrical stability of the observational instrument, in addition to the pipelines of data extraction. Three prominent effects are as follows.

1. *$1/f$ noise and thermal effects:* Instrumental noise sources are shot noise, $1/f$ noise, Johnson (thermal) noise, temperature noise, and photon noise. Voltage fluctuations δv_f lead to Johnson noise whose power spectrum is white and varies directly with the circuit temperature and resistance. Shot noise has a white power spectrum and is seen in semiconductor parts like a transistor when an electrical charge crosses its p-n junction. Flicker noise $\propto 1/f^{\alpha}$ (f = frequency), is predominant below a 'knee' frequency, above which it is white noise like. Photon noise is caused by statistical fluctuations in the arrival and detection times of photons which causes their detected power to vary. Photon noise power is strongly proportional to temperature. Additionally, noisy lines at different frequencies are caused by periodic fluctuations in the thermal or the electrical environment of the instruments and the satellite.

2. *Optical and pointing effects:* Before the detector, the process of observation of the sky by an optical system introduces systematics. The telescope modifies the angular response of the feed (that couples the optical system and detectors) in order to conserve $(A_e \cdot \Omega_A)$, where A_e is the effective aperture of the feed or telescope, Ω_A is the beam solid angle given by $\Omega_A = \int_{4\pi} P_n(\theta,\phi)d\Omega$ and $P_n(\theta,\phi)$ is the normalised beam pattern of the feed or the telescope. For the telescope pointed in the direction θ_0, ϕ_0,

$$T_A(\theta_0,\phi_0) = \frac{\int_{4\pi} T_b(\theta,\phi) P_n(\theta-\theta_0,\phi-\phi_0) d\Omega}{\int_{4\pi} P_n(\theta,\phi) d\Omega}, \tag{1.66}$$

where T_A, T_b are the antenna and brightness temperatures. Thus an asymmetric $P_n(\theta,\phi)$ causes a smearing of the observed sky. These distortions in the beam (or observed portion of sky) degrade the angular resolution, decreasing the maximum accessible multipole, and increasing $\hat{C}_\ell$ estimation error. Moreover, stray-light variations $T_A^{(SL)}$ in the main beam antenna temperature T_A^{MB}, i.e., $T_A(\theta,\phi) = T_A^{MB}(\theta_0,\phi_0) + T_A^{SL}(\theta_0,\phi_0)$ may not be distinguishable from the CMB fluctuations measured by the main beam. Typically the error in pointing, σ_p is a very small fraction of the effective beam angular resolution (σ_{eff}), such that $\sigma_p \leq 0.1 \times \sigma_{eff}$. Since the beam convolved with the probability distribution of the pointing error gives the beam shape, the sky angular power spectrum at small scales or high multipoles gets affected.

3. *Data acquisition and handling:* After observations, the signals are sent as small volumes of data through telecommunication. The amount of data at a receiving station varies directly with the communication bandwidth and the time taken. Bandwidth optimisation is done using lossy and lossless strategies. The former focus on data quantisation, whereas the latter involve arithmetic compression algorithms. Lossy techniques introduce additional noise and systematics in the data stream. Additionally, the signal digitisation process introduces spurious noise in time-ordered-data (TOD) affecting non-Gaussianity studies of CMB maps. Corruption or loss of any of the data packets sent via telemetry may lead to data reduction errors. Besides, some small artifacts, introduced at the map-making stage, are described in the next subsection.

1.7.3 Statistical challenges

The two broad categories of statistical challenges are as follows.

1. *Intrinsic uncertainties:* The angular power spectrum C_ℓ is an ensemble average of the product of the spherical harmonic coefficients, but having only one universe to observe leads us to the problem of cosmic variance [290]. We know that,

$$\langle \hat{C}_\ell \rangle = \frac{1}{(2\ell+1)} \sum_{m=-\ell}^{\ell} \langle a_{\ell m}^* a_{\ell m} \rangle = C_\ell. \tag{1.67}$$

Thus the cosmic variance for $\hat{C}_\ell$ can be computed as,

$$\begin{aligned} \sigma^2_{\hat{C}_\ell} &= \langle \hat{C}_\ell \hat{C}_\ell \rangle - C_\ell^2 \\ &= \frac{1}{(2\ell+1)^2} \langle \left(\sum_{m=-\ell}^{\ell} a_{\ell m}^* a_{\ell m} \right) \times \left(\sum_{m'=-\ell}^{\ell} a_{\ell m'}^* a_{\ell m'} \right) \rangle - C_\ell^2 \end{aligned}$$

$$
\begin{aligned}
&= \frac{1}{(2\ell+1)^2}\sum_m\sum_{m'}\Big(\langle a^*_{\ell m}a_{\ell m}\rangle\langle a^*_{\ell m'}a_{\ell m'}\rangle+\langle a^*_{\ell m}a^*_{\ell m'}\rangle\langle a_{\ell m}a_{\ell m'}\rangle \\
&\quad +\langle a^*_{\ell m}a_{\ell m'}\rangle\langle a_{\ell m}a^*_{\ell m'}\rangle\Big)-{C_\ell}^2 \\
&= \frac{1}{(2\ell+1)^2}\sum_m\sum_{m'}\Big(C_\ell^2+2C_\ell^2\delta_{m,-m'}\Big)-C_\ell^2 \\
&= \frac{2}{(2\ell+1)}C_\ell^2. \qquad (1.68)
\end{aligned}
$$

Here we have implicitly used the Wick's theorem, and the fact that $\langle a_{\ell m}\rangle = 0$. Additionally, we use $a^*_{\ell m} = (-1)^m a_{\ell m}$ to obtain the terms of the form $C_\ell^2\delta_{m,-m'}$, that simply flips the summation for m, but $\sum_{m=+\ell}^{-\ell} = (2\ell+1)$, and hence the result is achieved. Thus the error is greatest at lowest of multipoles (ℓ's) and vice versa.

Besides, if a partial sky is observed, then the observed fraction of the sky (f_{sky}) increases the $\sigma_{\hat{C}_\ell}$. The variance due to noise and beam effects dominates at higher multipoles. Further the gravitational lensing of CMB photons converts the E modes into B modes, affecting the extraction of cosmological parameters from the CMB.

2. *Computational aspects:* The first challenge is to find an appropriate pixelisation scheme (such as HEALPix [117]) on a 2-sphere for storing CMB data, and strategising the manipulation of functions defined on the sphere, with minimal losses.

   Secondly we encounter computational challenges and losses at the level of map making [280]. For the TOD model $d = P(s+f)+n$, where, $s =$ CMB signal, $f =$ foregrounds and $P =$ Pointing matrix which encodes the optical processes and scanning methodology of the instrument. Using Bayes' theorem, the maximum likelihood estimate of $s+f$ is $\bar{m} = (P^TN^{-1}P)^{-1}P^TN^{-1}d$, and the noise covariance matrix $C_N = \langle\bar{m}\bar{m}^T\rangle = (P^TN^{-1}P)^{-1}$. For large datasets, the method is computationally expensive due to the size of the matrices ($\mathcal{O}(10^5-10^7)$). The assumption of symmetric beams also induces error as distorted beams and side lobes can produce spurious images of foregrounds.

   Thirdly, foreground separation methods are fairly involved. One method is to model various foregrounds for purging the maps. Another technique is of "blind separation", based on the statistical independence of the CMB and the foregrounds.

Fourthly, the likelihood estimation for $\hat{C}_\ell$ costs N_{pix}^3 operations (N_{pix} = number of pixels in a map). For the Planck satellite, $N_{pix} \sim 10^7$, so we need 10^{21} operations.

Lastly, the cosmological parameter estimation step requires exploration of the posterior density which varies over $10 - 20$ dimensions.

In the next Section 1.8, we discuss some state-of-the-art CMB isotropy investigation methods which are fairly robust against foreground and residual systematics, while minimising the computational aspects of statistical challenges discussed in this Section 1.7.

1.8 Existing probes of the isotropy of the CMB

Investigations of the isotropy of the CMB have been carried out meticulously by researchers over a considerable period of time, using diverse tools and techniques for the same. Further, any deviations from isotropy found in the CMB are made to undergo rigorous checks of robustness in order to reasonably eliminate possible systematic errors or minor foreground residuals introduced during the CMB extraction process, as possible causes of anisotropy. We categorise such techniques on the basis of possible entities probed, as follows.

(a) *Correlations* of the CMB anisotropies were studied in real or pixel space, and multipole or spherical harmonic space, to directly inspect the rotational invariance of the correlation functions for statistically isotropic CMB.

(b) *Power asymmetries:* The distribution of power based on geometry of the 2-sphere, or parity of the anisotropies were probed to assess possible power asymmetries.

(c) *Directional preferences:* Presence of preferred directions on the CMB which violate large scale isotropy were examined.

(d) *Local extrema or hot and cold spots of the CMB* were explored for assessing the isotropy of the CMB and its adherence to Gaussianity at small scales.

We discuss these categories of studies in the following subsections.

1.8.1 Correlations of the CMB anisotropies

We discuss two correlation based approaches: (a) in pixel space using the 2-point angular correlation function, and (b) in harmonic space with the bipolar spherical harmonics.

1.8.1.1 Pixel space two-point angular correlation function

In the work of [132], using COBE-DMR data, it was seen that there is near to negligible correlation of temperature fluctuations separated by angular distances of $\gtrsim 60°$. The 2-point angular correlation employed by the authors of this paper is

$$C(\alpha_{ij}) = \langle T_i T_j \rangle = \frac{1}{4\pi}\sum_{\ell}(2\ell+1)W_\ell^2 C_\ell P_\ell(\cos(\alpha_{ij})), \tag{1.69}$$

where, W_ℓ denotes the product of beam and pixel window functions as appropriate, P_ℓ is the Legendre polynomial, and C_ℓ is the expectation of the angular power spectrum. The correlation function defined for a fixed separation denoted by the angle α is given as

$$C(\alpha) = \frac{\sum_{ij} w_i w_j T_i T_j}{\sum_{ij} w_i w_j}, \tag{1.70}$$

where, the T_i's are temperature at i^{th} pixel, and w_i's are statistical weights of the same. The authors computed the correlation function (Equation (1.70)) for different bins of angular separations and plotted the same for combinations of CMB maps of different frequency channels. They additionally evaluated the cross correlations for maps from different channels. In each of these cases, the curves approach and stay close to zero beyond $60°$.

In the first year paper of WMAP [260], a number of discrepancies in the foreground-cleaned CMB (ILC) maps from observations were found relative to the standard (flat ΛCDM) model predictions, on small and large scales. The small scale discrepancies were alleviated with the use of a running spectral index, however those on the largest angular scales remained. Among these, the prominent deviation from predictions was that of the deficit of large angle correlations, as seen previously in COBE data. The flat ΛCDM model used by them was best fitted to both CMB and LSS data, before performing comparisons with observed data. The lack of power on these large angular scales was quantified with a 4-point statistic,

$$S_{1/2} = \int_{-1}^{1/2} [C(\theta)]^2 \, d(\cos(\theta)). \tag{1.71}$$

The upper and lower limits of $S_{1/2}$ were chosen a posteriori after looking at the unusual nature of the data in this region of the graph. Here, the form of the correlation function is:

$$C(\theta) = \frac{1}{4\pi}\sum_{\ell}(2\ell+1)W_{\ell}^{2}\hat{C}_{\ell}P_{\ell}(\cos(\theta)). \tag{1.72}$$

Upon comparing with the simulations from the standard model fitted to WMAP and 2dFGRS data, it was found that only 0.15% of the simulated maps had values of $S_{1/2}$ lower than that from WMAP data. This percentage improved only to 0.3% with a running spectral index.

In the work [65], the WMAP 1-year and 3-year ILC maps were used to study

$$\mathcal{C}(\theta) = \overline{T(\hat{n_1})T(\hat{n_2})}|_{\theta}, \tag{1.73}$$

which is defined for any two temperature fluctuations separated by an angular distance of θ. The over-bar denotes an average over all such pairs. The authors analysed the cut sky Q, V, W frequency band maps in addition to the full and partial sky ILC maps. In all of these cases, they found that $\mathcal{C}(\theta)$ is vanishingly small in the approximate range of angular separations $\in [60, 170]$, and above $\theta = 170$, there exists a small but peculiar anti-correlation whereas the standard model predicts a large positive correlation. In addition to the use of the $S_{1/2}$ statistic, the authors of this work used

$$S_{full} = \int_{-1}^{1}[C(\theta)]^{2}\, d(\cos(\theta)). \tag{1.74}$$

Upon comparisons of $S_{1/2}$ and S_{full} evaluated from the chosen real CMB maps, and those from simulated skies corresponding to the ΛCDM favoured by WMAP data, they found that only about $0.04\% - 0.15\%$ of the isotropic skies produce an $S_{1/2}$ value lower than than those of the 3-year cut sky WMAP Q, V, W maps, and for the 3-year cut sky WMAP ILC map, the p-value is 0.03%. Even when all angular scales are considered, the analysis with the S_{full} statistic reveals that the p-values are $\sim 1\%$. These clearly indicate a violation of SI which is more significant in the WMAP 3-year maps relative to the 1-year maps.

1.8.1.2 *Bipolar spherical harmonic power spectrum*

An interesting study in multipole or harmonic space was accomplished in the work of [123], where the following statistic was proposed for measuring the deviations from SI of the CMB.

$$\kappa_\ell = \int d\Omega \int d\Omega' \left[\frac{(2\ell+1)}{8\pi^2} \int d\mathcal{R}\chi_\ell(\mathcal{R}) C(\mathcal{R}\hat{q}, \mathcal{R}\hat{q}') \right]. \tag{1.75}$$

Here, $C(\mathcal{R}\hat{q}, \mathcal{R}\hat{q}')$ is the two-point correlation function of temperature fluctuations at $\mathcal{R}\hat{q}$ and $\mathcal{R}\hat{q}'$ which are position vectors obtained upon rotation of $\hat{q}$ and $\hat{q}'$ by the operator $\mathcal{R}$, an element of the 3D rotation group. The expected 2 point correlation function is given as,

$$C(\hat{q}, \hat{q}') = \frac{1}{8\pi^2} \int d\mathcal{R} C(\mathcal{R}\hat{q}, \mathcal{R}\hat{q}'). \tag{1.76}$$

The characteristic function $\chi_\ell = \sum_{M=-\ell}^{\ell} D^{\ell}_{MM}$, where D^{ℓ}_{MM} are the Wigner-D functions. The $d\mathcal{R}$ denotes the volume element of the 3D rotation group. For rotation by an angle $\omega \in [0, \pi]$, about the axis $\hat{r}(r, \theta, \phi)$, χ_ℓ and $d\mathcal{R}$ take the following forms

$$\chi_\ell(\mathcal{R}) = \chi_\ell(\omega) = \frac{\sin \frac{(2\ell+1)\omega}{2}}{\sin(\omega/2)}, \quad d\mathcal{R} = 4\sin(\omega/2) d\omega \sin(\Theta) d\Theta d\Phi. \tag{1.77}$$

With the use of the identity $\int d\mathcal{R}' \chi_\ell(\mathcal{R}') \chi_\ell(\mathcal{R}\mathcal{R}') = \chi_\ell(\mathcal{R})$, the expression for κ_ℓ reads

$$\kappa_\ell = \frac{(2\ell+1)}{8\pi^2} \int d\Omega \int d\Omega' C(\hat{q}, \hat{q}') \int d\mathcal{R}\chi_\ell(\mathcal{R}) C(\mathcal{R}\hat{q}, \mathcal{R}\hat{q}'). \tag{1.78}$$

For statistically isotropic temperature fluctuations, $C(\mathcal{R}\hat{q}, \mathcal{R}\hat{q}') = C(\hat{q}, \hat{q}')$, and hence, the above expression reduces to $\kappa_\ell = \kappa^0 \delta_{\ell 0}$, due to the orthonormality of $\chi_\ell(\omega)$. Thus, κ_ℓ is a measure of SI for the CMB. For computational simplicity, $C(\hat{q}, \hat{q}')$ is considered as a series expansion in the orthonormal basis of bipolar spherical harmonic (BipoSH) functions,

$$C(\hat{q}, \hat{q}') = \sum_{ll'\ell M} A^{\ell M}_{ll'} \{Y_l(\hat{q}) \otimes Y_l(\hat{q}')\}_{\ell M}, \tag{1.79}$$

where, $A^{\ell M}_{ll'}$ are coefficients of the expansion (BipoSH coefficients). The BipoSH functions form a basis in $S^2 \times S^2$ [274] and transform as ordinary $Y_{\ell m}(\hat{q})$'s under a rotation,

$$\{Y_l(\hat{q}) \otimes Y_l(\hat{q}')\}_{\ell M} = \sum_{m_1 m_2} \mathfrak{C}^{\ell M}_{l_1 m_1 l_2 m_2} Y_{l_1 m_1}(\hat{q}) Y_{l_2 m_2}(\hat{q}'), \tag{1.80}$$

where, $\mathfrak{C}^{\ell M}_{l_1 m_1 l_2 m_2}$ are the Clebsh-Gordon coefficients. It can be shown that,

$$A^{\ell M}_{ll'} = \sum_{mm'} \langle a_{lm} a^*_{l'm'} \rangle (-1)^{m'} \mathfrak{C}^{\ell M}_{lml'-m'}. \tag{1.81}$$

Due to cosmic variance, it is not possible to measure all of such BipoSH coefficients, hence analogous to the coefficients $a_{\ell m}$'s defined in S^2, where the angular power spectrum estimator $\hat{C}_\ell = \frac{1}{(2\ell+1)} \sum_{m=-\ell}^{\ell} |a_{\ell m}|^2$, the

$$\kappa_\ell = |A_{ll'}^{\ell M}|^2 \geq 0, \tag{1.82}$$

are the bipolar power spectrum estimators. And as we have seen that for the case of SI, $\kappa_\ell = 0$ for all $\ell > 0$, hence a non-zero κ_ℓ for such ℓ's will indicate a violation of SI. An intriguing aspect of κ_ℓ's is that they can help investigate some forms of non-trivial cosmic topology as described in [259]. The authors of this formalism computed the κ_ℓ for first-year data from WMAP (ILC map [33] and TOH map [271]) and found it to be consistent with zero, for a variety of window functions used to isolate different ranges of angular scales. Within a confidence interval twice that of the standard deviation, the authors reported no violation of SI for large angular scales such that $\ell \lesssim 60$ [124].

1.8.2 Symmetry based approaches to the power spectrum

We discuss three approaches to assess the CMB angular power spectrum, (a) a geometric approach, which involves ascertaining the power spectrum of two different hemispheres, (b) assessing parity, since neither symmetric or antisymmetric functional form of the CMB anisotropies must take precedence, (c) studying the symmetries of the eigenvectors of the power spectrum when the latter is defined in the generalised form of a power tensor.

1.8.2.1 Hemispherical power asymmetry

An asymmetric power distribution between two hemispheres of the CMB 2-sphere was observed by [92], and later by [128], which was based on a method of estimating the power spectrum from patches on the sky [127], using the concept of Gabor transforms. A Gabor transform [106] is known as a 'windowed Fourier transform' as it is the Fourier transform of a function $f(x)$ when it is multiplied by a Gabor window $G(x)$. This is useful when we would like to eliminate or weaken the effects of missing or noisy data at some $x = x_n$ by setting for example, $G(x_n) = 0$ and $G(x) = 1$ for other values of x. Additionally since standard likelihood methods used for power spectrum estimation utilise all the pixels or spherical harmonic coefficients of a CMB map, this leads to an $\approx N_{pix} \times N_{pix}$ sized correlation matrix, making it computationally expensive to invert.

In their work [127], the authors proposed to use the pseudo power spectrum as elements to define the data array in the likelihood, since the correlation function of the same scales as $\ell_{max} \times \ell_{max}$. Here ℓ_{max} is the highest multipole being probed. The pseudo $\tilde{C}_\ell$ and $\tilde{a}_{\ell m}$'s for a Gabor window $G(\hat{n})$ transformed map are given as,

$$\tilde{C}_\ell = \frac{1}{2\ell+1} \sum_m \tilde{a}^*_{\ell m} \tilde{a}_{\ell m}, \quad \tilde{a}_{\ell m} = \int d\hat{n} T(\hat{n}) G(\hat{n}) Y^*_{\ell m}(\hat{n}). \tag{1.83}$$

Here, $T(\hat{n})$ is the temperature fluctuation at $\hat{n}$. Considering $G(\hat{n})$ to be azimuthally symmetric about a point $\hat{n}_z$ such that the Gabor window can easily be expressed as a function of the angular separation given by $\cos\theta = \hat{n} \cdot \hat{n}_z$, we have the Legendre series expansion,

$$G(\theta) = \sum_\ell \frac{(2\ell+1)}{4\pi} g_\ell P_\ell(\cos\theta) = \sum_{\ell m} g_\ell Y_{\ell m}(\hat{n}) Y^*_{\ell m}(\hat{n}_z). \tag{1.84}$$

Moreover, as $T(\hat{n}) = \sum_{\ell m} a_{\ell m} Y_{\ell m}(\hat{n})$, hence the equation for $\tilde{a}_{\ell m}$ takes the form,

$$\begin{aligned} \tilde{a}_{\ell m} &= \sum_{\ell' m'} a_{\ell' m'} \sum_{\ell'' m''} g_{\ell''} Y^*_{\ell'' m''}(\hat{n}_z) \int d\hat{n} Y_{\ell m}(\hat{n}) Y_{\ell' m'}(\hat{n}) Y_{\ell'' m''}(\hat{n}) \\ &= \sum_{\ell' m'} a_{\ell' m'} \sum_{\ell'' m''} g_{\ell''} Y^*_{\ell'' m''}(\hat{n}_z) \sqrt{\frac{(2\ell+1)(2\ell'+1)(2\ell''+1)}{4\pi}} \\ &\quad \times \begin{pmatrix} \ell & \ell' & \ell'' \\ -m & m' & m'' \end{pmatrix} \begin{pmatrix} \ell & \ell' & \ell'' \\ 0 & 0 & 0 \end{pmatrix} (-1)^m. \end{aligned} \tag{1.85}$$

As for the transformation of the power spectrum, using the orthogonality of the Wigner-$3j$ symbols, and $\langle a_{\ell m} a^*_{\ell m} \rangle = C_\ell \delta_{\ell ell'} \delta_{mm'}$, we have

$$\langle \tilde{C}_\ell \rangle = \sum_{\ell'} C_{\ell'} K(\ell, \ell'), \quad \text{where, } K(\ell,\ell') = (2\ell'+1) \sum_{\ell''} g^2_{\ell''} \frac{2\ell''+1}{16\pi^2} \begin{pmatrix} \ell & \ell' & \ell'' \\ 0 & 0 & 0 \end{pmatrix}^2, \tag{1.86}$$

and the coefficients g_ℓ can be found by inverse Legendre transformation,

$$g_\ell = 2\pi \int_{\theta=0}^{\theta=\theta_c} G(\theta) P_\ell(\cos\theta) d\cos\theta. \tag{1.87}$$

Here, the cut-off angle θ_c denotes the angular value at which $G(\theta) \to 0$. For e.g., a Gaussian Gabor window is defined as $G(\theta) = e^{-\theta^2/(2\sigma^2)}$ for $\theta \leq \theta_c$, and $G(\theta) = 0$ for $\theta > \theta_c$. Further, g_ℓ is also independent of $\hat{n}_z$, like other terms in $K(\ell, \ell')$. This is an important result implying that the $\langle \tilde{C}_\ell \rangle$ will be the same regardless of where the Gabor window function is centred.

If a disc (or other such axisymmetric patch) on the observed sky is considered and multiplied by a Gabor window function, then the pseudo power spectrum can be inputted to a likelihood analysis to estimate the full sky power spectrum. For an axisymmetric patch, it is possible to analytically evaluate the sky signal correlations. We may assume that the $\tilde{C}_\ell$ are Gaussian distributed if the multipole ℓ is high enough. As an example, for a Gaussian Gabor window of full-width-at-half-maximum or FWHM $= 15°$, the $\ell \sim 100$. The likelihood ansatz chosen by the authors is,

$$\mathcal{L} = \frac{\left(-\frac{1}{2}d^T M^{-1} d\right)}{\sqrt{2\pi detM}}, \tag{1.88}$$

where, the data vector d contains elements of the form $d_i = \tilde{C}_{\ell_i} - \langle \tilde{C}^S_{\ell_i}\rangle - \langle \tilde{C}^N_{\ell_i}\rangle$. The $\tilde{C}_{\ell_i}$ is the observed pseudo power spectrum including noise. The other two terms are the expectation values of the pseudo power spectrum as in (1.86) corresponding to the signal and the noise for the patch, respectively. The matrix M given by

$$M_{ij} = \langle \tilde{C}_{\ell_i}\tilde{C}_{\ell_j}\rangle - \langle \tilde{C}_{\ell_i}\rangle\langle \tilde{C}_{\ell_j}\rangle = M^S_{ij} + M^N_{ij} + M^{SN}_{ij}, \tag{1.89}$$

denotes the correlations between the pseudo power spectrum coefficients, and $M^S_{ij}, M^N_{ij}, M^{SN}_{ij}$ represent the contributions due to the signal, the noise and the signal-noise cross-correlations. The noise correlations M^N_{ij} must be pre-computed using the specific noise model involved. Then the correlation matrices for the signal and the signal-noise mixing are given by,

$$M^S_{ij} = \sum_b \sum_{b'} D_b D'_b \chi(b,b',i,j), \quad M^{SN}_{ij} = \sum_b D_b \chi'(b,i,j). \tag{1.90}$$

Here, the expression for χ is as follows:

$$\begin{aligned} \chi(b,b',i,j) \quad &= \quad \frac{2}{(2\ell_i+1)(2\ell_j+1)} \times \sum_m \left[\sum_{\ell\in b} B^2_\ell \ell(\ell+1) h(\ell,\ell_i,m) h(\ell,\ell_j,m)\right] \\ &\times \left[\sum_{\ell\in b'} B^2_\ell \ell(\ell+1) h(\ell,\ell_i,m) h(\ell,\ell_j,m)\right], \end{aligned} \tag{1.91}$$

where, B_ℓ is the beam function in multipole space, and $h(\ell,\ell',m) = \sum_j G_j \lambda^j_{\ell m}\lambda^j_{\ell' m}\Delta_j$, such that the λ's are given by $Y_{\ell m}(\theta,\phi) = \lambda_{\ell m}(\theta)e^{-im\phi}$, Δ_j is the area of the j^{th} pixel, and G_j is the pixelised Gabor window function. Further, the expression for χ' is

$$\chi'(b,i,j) = \frac{2}{(2\ell_i+1)(2\ell_j+1)} \times \sum_m \left[\sum_{\ell \in b} B_\ell^2 \ell(\ell+1) h(\ell,\ell_i,m) h(\ell,\ell_j,m) \right] \times h'(\ell_i,\ell_j,m), \quad (1.92)$$

where, $h'(\ell,\ell',m) = \sum_i G_i^2 Y_{\ell m}^i Y_{\ell' m}^i \Delta_i^2 \sigma_i^2$ and σ_i is the noise variance in pixel i.

Due to limited information in each patch, the full sky power cannot be estimated for all ℓ's, and a binning procedure provides the power spectrum in N_{bin} bins. The log-likelihood optimisation causes the values of the estimated binned spectrum to be of a similar order of magnitude. Hence, the authors consider a parameterisation for the binned C_ℓ's,

$$C_\ell = \frac{D_b}{\ell(\ell+1)}, \quad \ell_b \leq \ell < \ell_{b+1}, \quad (1.93)$$

with ℓ_b being the first multipole of the b^{th} bin, and D_b is a parameter. Since these binned values are coupled, the covariance matrix becomes singular. In this regard, a choice of multipoles ℓ_i is made, N_i in number, such that the data vector d_i can be found. The required number of multipoles then depends on the coupling strength between the $\tilde{C}_\ell$'s, as dictated by the multipole widths of the kernel ($\Delta\ell_{ker}$) and the correlation matrix $\Delta\ell_{cor}$. This is because the correlation matrix after normalisation with the pseudo power spectrum varies with the window size like the kernel $K(\ell,\ell')$ width. The authors of the study noted that a small number of ℓ_i's, i.e, low N_i leads to larger error bars on the estimates, however a very high N_i may not altogether improve the same. Optimally, the maximum number of C_ℓ's that can be fit is equal to the number of $\tilde{C}_\ell$'s, which is N_i. Therefore, $N_{bin} \leq N_i$ is required.

With the likelihood analysis for a single axisymmetric circular patch on simulated skies, the authors found a high probability of the estimated $\tilde{C}_\ell$ being lower than the average $\langle \tilde{C}_\ell \rangle$, which is due to the assumption that $\tilde{C}_\ell$'s are Gaussian distributed. Thus, the bias can possibly be reduced when a larger area of the sky is available for the joint analysis of many patches to produce the full-sky power spectrum. With this forethought, the authors describe an extension of the method to tackle two major problems: (a) in a real experiment, the probability of observing a axisymmetric patch is very low, (b) the noise between any two pixels in the observed CMB map is usually correlated. Thus, the sky can be fragmented into several axisymmetric patches and the estimated $\tilde{C}_\ell$ from each patch can be utilised together for likelihood maximisation. However, it must be checked that the correlation of $\tilde{C}_\ell$'s from different patches (say patch A and patch B) is low. Usually the correlation between two widely separated patches approaches zero. An analytical form of such correlations is

$$\begin{aligned}\langle \tilde{C}_\ell^A \tilde{C}_{\ell'}^B \rangle &= \frac{1}{(2\ell+1)(2\ell'+1)} \sum_{mm'} \langle \tilde{a}_{\ell m}^{A*} \tilde{a}_{\ell m}^{A} \tilde{a}_{\ell' m'}^{B*} \tilde{a}_{\ell' m'}^{B} \rangle \\ &= \langle \tilde{C}_\ell^A \rangle \langle \tilde{C}_\ell^B \rangle + \frac{2\sum_{mm'} |\langle \tilde{a}_{\ell m}^{A*} \tilde{a}_{\ell' m'}^{B} \rangle|^2}{(2\ell+1)(2\ell'+1)}, \end{aligned} \tag{1.94}$$

where, $\langle \tilde{a}_{\ell m}^{A*} \tilde{a}_{\ell' m'}^{B} \rangle = \sum_{\ell''} C_{\ell''} d_{mm'}^{\ell''}(\Delta) h^A(\ell,\ell',m) h^B(\ell',\ell'',m')$ and Δ is the angle between the patch centres, while the Wigner-D coefficient is given by $D_{m'm}^{\ell}(\alpha,\beta,\gamma) = e^{im'\alpha} d_{m'm}^{\ell}(\beta) e^{im\gamma}$, with the property that $d_{m'm}^{\ell}(\beta) = d_{mm'}^{\ell}(-\beta)$. Using this analytical form of the correlation between $\tilde{C}_\ell$'s, and evaluating the same from Monte Carlo realisations, the authors concluded that off-block-diagonal correlations are ≈ 0, for non-overlapping patches. They found that on averaging the C_ℓ estimates from multiple non-overlapping patches, the mean estimate approaches the full power spectrum even at large angular scales or low ℓ's.

In the correlation matrix from such a joint analysis of several patches (N_{pat} in number), the block diagonal contains correlations for each individual patch and the log-likelihood is

$$L = \sum_{i=1}^{N_{pat}} d_i^T M_i^{-1} d_i + \sum_{i=1}^{N_{pat}} \ln\left(\det(M_i)\right), \tag{1.95}$$

where, the d_i is the i^{th} patch data vector, and M_i is its correlation matrix.

In the work [92], the authors have studied the asymmetric distribution of power in two hemispheres of the CMB 2-sphere. The authors note that despite the analytical form of the correlation matrix for axisymmetric patches (Equation (1.94)), the correlation matrix for a general sky patch (lacking any specific symmetry) must be computed from Monte Carlo simulations. They accomplished this task while simultaneously finding the maximum likelihood estimates for (1.88) to obtain the parameters D_b (equation (1.93)). With the help of this likelihood approach, they estimated the power spectra for 164 discs with radius $9^\circ.5$, which are selected uniformly on parts of the sphere outside the galactic cut obtained with the $Kp2$ mask of WMAP first-year data. The multipole range considered was $\ell \in [2,63]$. They compared the power spectra for discs from northern and southern hemispheres chosen by orientating the north-south axis in 82 different directions on the 2-sphere for coadded maps of WMAP V and W bands alongside 2048 simulated maps. The coadded map T_{ca} is obtained from maps at different channels (T_c) using inverse noise weighting,

$$T_{ca} = \frac{\sum_c T_c/\sigma_c^2}{1/\sigma_c^2}. \tag{1.96}$$

The procedure employed by them thereafter is as follows. They estimated the power spectrum in bins C_b of width $\Delta\ell = 3$, such that a multipole bin is $b \in \{\ell^b_{min}, \ell^b_{max}\}$, and $\ell_{min} = 2+3b$, $\ell_{max} = 4+3b$. The estimated bins in a given multipole range $[\ell_{min}, \ell_{max}]$ were added up for each of the 164 hemispherical contributions, to give $C_h = \sum_b C_b$, where $h = N, S$ for northern and southern hemispheres. The ratio of asymmetry between the spectra from the hemispheres was computed as $r = \max\left(\frac{C_N}{C_S}, \frac{C_S}{C_N}\right)$ for each of the 82 orientations, and the orientation corresponding to the largest r was recorded. The total number of discs is 164, since there are two discs per orientation, one in each hemisphere. The local power spectrum estimates for these slightly overlapping, 164 discs were compared to those from an ensemble of 6144 simulated maps, and it was seen that in the lowest multipole bin given by $\ell \in [2, 63]$, the amplitudes of the power spectra for the discs in the northern galactic hemisphere are generally lower in the WMAP data, than in the simulated maps, and that the opposite effect exists for the southern hemisphere.

Considering the ratio of the mean of the spectra in the northern to that of the southern hemisphere, the authors found that only 0.5% of the simulated maps furnish a ratio as small as that from WMAP data. After determining the coordinate frame that maximises the value of this ratio, they computed it for various multipole ranges. The authors found that the ratio value from WMAP data is larger than about 99% of the simulations. Additionally, they found that the asymmetry of power is concentrated about the northern galactic pole for low multipoles, whereas that of high multipoles ($5 < \ell < 40$) is maximised for an axis having its north pole at $(\theta, \phi) = (80°, 57°)$, in Galactic coordinates. When the same procedure was performed for the COBE-DMR data, after coadding maps from 53 and 60 GHz channels, for which the multipole range chosen was $\ell \in [2, 19]$, as the signal is dominant there, the axis of power asymmetry was found to be close to that of the WMAP data.

Similarly, in another work [128], the authors have employed the methods described earlier and computed the power spectrum estimates from individual discs as well as from a large sample containing combined estimates from several discs on Monte Carlo ensembles. Thereafter these estimates were compared with data from WMAP. In this work as well, 164 discs were used which are of radius $9^\circ.5$, chosen in observed regions outside the $Kp2$ mask. The results obtained from this analysis are similar to and hence corroborate those from [92].

1.8.2.2 Point parity asymmetry

For temperature anisotropies $\Delta T(\hat{n}) = \sum_{\ell m} a_{\ell m} Y_{\ell m}(\hat{n})$, when a point parity inversion is carried out, we obtain $\Delta T(-\hat{n}) = \sum_{\ell m} (-1)^\ell a_{\ell m} Y_{\ell m}(\hat{n})$. Effectively then, the spherical harmonic coefficients transform under parity as $a_\ell \to (-1)^\ell a_{\ell m}$. With this knowledge, one may construct the symmetric and antisymmetric forms of the temperature maps,

$$\Delta T^e(\hat{n}) = \frac{\Delta T(\hat{n}) + \Delta T(-\hat{n})}{2}, \quad \Delta T^o(\hat{n}) = \frac{\Delta T(\hat{n}) - \Delta T(-\hat{n})}{2}, \tag{1.97}$$

which have even and odd parity, respectively. Thus, in spherical harmonic decomposition,

$$\begin{aligned} \Delta T^e(\hat{n}) &= \sum_{\ell m} \frac{1+(-1)^\ell}{2} a_{\ell m} Y_{\ell m}(\hat{n}) = \sum_{\ell m} a_{\ell m} Y_{\ell m} \cos^2\left(\frac{\ell\pi}{2}\right), \\ \Delta T^o(\hat{n}) &= \sum_{\ell m} \frac{1-(-1)^\ell}{2} a_{\ell m} Y_{\ell m}(\hat{n}) = \sum_{\ell m} a_{\ell m} Y_{\ell m} \sin^2\left(\frac{\ell\pi}{2}\right). \end{aligned} \tag{1.98}$$

A distinctly preferential distribution of power for either ΔT^e or ΔT^o, indicating an asymmetric distribution of power for odd or even multipoles violates parity symmetry. The authors of [159] showed that for WMAP 3, 5 and 7-year data, the power spectrum for odd multipoles is higher than that for their neighbouring even multipoles. Since the Sachs-Wolfe plateau for low ℓ's ensures that $\frac{\ell(\ell+1)}{2\pi} C_\ell \sim$ constant, the authors considered the quantities,

$$P^e = \sum_{\ell=2}^{\ell_{max}} \cos^2\left(\frac{\ell\pi}{2}\right) \frac{\ell(\ell+1)}{2\pi} \hat{C}_\ell, \quad P^o = \sum_{\ell=2}^{\ell_{max}} \sin^2\left(\frac{\ell\pi}{2}\right) \frac{\ell(\ell+1)}{2\pi} \hat{C}_\ell, \tag{1.99}$$

where, the trigonometric factors ensure that only odd or even multipole powers are added for P^o or P^e, respectively, and ℓ_{max} denotes the upper limit of the multipole range. Thus a low value of the ratio $r_{eo} = \frac{P^e}{P^o}$, quantifies the odd-parity preference of data and vice versa.

They employed two masks, namely, the WMAP pre-processing mask for low multipole ranges ($\ell \in [2, 23]$) and the WMAP $KQ85$ mask for $\ell \in [2, 1024]$. The angular power spectrum was estimated by pixel based maximum likelihood methods for the low ℓ range maps and by the pseudo-C_ℓ approach for the higher ℓ range. Instrumental noise was ignored for multipoles $\ell \leq 100$. The ratio r_{eo} was computed for 10^4 simulated maps corresponding to the standard ΛCDM model, and WMAP maps from 7, 5 and 3 year data and compared, for different values of ℓ_{max}. It was seen that the fraction of simulated maps with $\frac{P^e}{P^o}$ as low as that from WMAP data is very low, clearly indicating the parity asymmetry of power. The lowest value of this fraction of simulated maps (p-value) is 0.0031 when $\ell_{max} = 22$.

An analysis of point parity asymmetry was carried out in [166] using the statistic,

$$S_p = \sum_{\ell=3}^{\ell_{max}} \frac{\ell(\ell+1)\hat{C}_\ell}{\ell(\ell-1)\hat{C}_{\ell-1}}. \tag{1.100}$$

In this study, the authors concluded that for several ranges of ℓ's considered, they could not find the probability of rejecting the null hypothesis of SI beyond the 97% confidence level.

In another work [19], the authors propose a different statistic (with $\mathcal{D}_\ell = \frac{\ell(\ell+1)}{2\pi}\hat{C}_\ell$):

$$Q(\ell_{odd}) = \frac{2}{\ell_{odd}-1}\sum_{\ell=3}^{\ell_{odd}} \frac{\mathcal{D}_{\ell-1}}{\mathcal{D}_\ell}. \tag{1.101}$$

The summation is over all the odd multipoles only. The estimator $Q(\ell_{odd})$ quantifies the mean deviation of the ratio of power in the even multipole, to the subsequent odd multipole from unity, and since $\ell(\ell+1)\hat{C}_\ell \sim$ constant for low ℓ, the value of $Q(\ell_{odd})$ is expected to fluctuate about one, just like r_{eo}. The authors of this work tested both the statistics $r_{eo}, Q(\ell_{odd})$, on WMAP 7-year CMB maps (cleaned using their own methods) against 10^4 simulated maps for a fiducial C_ℓ best fitted to the WMAP 7-year data, for multipoles defined by $\ell_{max} \in [3, 101]$. They reproduced the results of the [159] of lowest probability at $\ell_{max} = 22$, of 0.0013. Additionally they generated 800 simulations of foreground cleaned maps using ΛCDM realisations of the CMB, to which were added Planck Sky Model [22] foregrounds, which were then cleaned by applying the IPSE cleaning procedure ([271, 244]). The p-values were found to be slightly higher than those of the simulated SI obeying maps. With the analysis of these 800 maps, the authors concluded that the parity asymmetry is not due to over-subtraction of foregrounds, which was an idea posited due to the even-parity preference of foregrounds. Besides, the effect of noise is also negligible. The p-value obtained with these maps is 0.13%. In order to assess the effect of a low multipole cut-off, some low-ℓ

values were removed and the analysis was redone with the modified statistic:

$$Q(\ell_{odd}) = \frac{2}{\ell_{odd} - \ell_{cut} + 1} \sum_{\ell=\ell_{cut}}^{\ell_{odd}} \frac{\mathcal{D}_{\ell-1}}{\mathcal{D}_{\ell}}, \tag{1.102}$$

where the cut-off ℓ_{cut} is any odd $\ell > 3$. Similarly a lower ℓ cut-off was implemented for the r_{eo} statistic. The authors found that with $\ell \in [\ell_{cut}, 101]$, the p-values for the parity asymmetry recede from the critical regions completely on ignoring the multipoles $2, ..., 7$. This implies that the other low$-\ell$ anomalies and the parity asymmetry could share a common origin.

1.8.2.3 Mirror parity asymmetry

For the assessment of the symmetry of plane parity, we primarily refer to the work of [166]. A point parity inversion is defined by $\hat{n} \to -\hat{n}$, whereas a mirror parity inversion is given by

$$\hat{n} \to \hat{n} - 2(\hat{n}.\hat{p})\hat{p}, \tag{1.103}$$

where $\hat{p}$ is the normal to the plane ('mirror'). Given a parity inversion denoted by the operator P, such that the temperature fluctuations $\Delta T(\hat{n})$ transform as $P\Delta T(\hat{n}) = \Delta\tilde{T}(\hat{n})$ under parity, then two functions similar to case of point parity can be constructed,

$$\Delta T^{\pm}(\hat{n}) = \frac{\Delta T(\hat{n}) \pm \Delta\tilde{T}(\hat{n})}{2}. \tag{1.104}$$

For point parity inversions, the even or odd ℓ's contribute to the $\hat{C}_\ell$ in the $\Delta T^{+}(\hat{n})$ or $\Delta T^{-}(\hat{n})$ maps, respectively. However, for mirror parity inversion, modes with even or odd $(\ell + m)$ values contribute to $\hat{C}_\ell$'s of the respective $\Delta T^{+}(\hat{n})$ or $\Delta T^{-}(\hat{n})$ maps. Hence,

$$\hat{C}^{\pm}_{\ell}(\hat{n}_\ell) = \frac{1}{(2\ell+1)} \sum_m g^{\pm}_{\ell m} |a_{\ell m}|^2, \tag{1.105}$$

where, $g^{\pm}_{\ell m} = 0, 1$ for odd or even $\ell + m$, and $\hat{n}_\ell$ is the z-axis used for the expansion which changes with ℓ. A mirror handedness dictates the preference of $\hat{C}^{+}_{\ell}$ or $\hat{C}^{-}_{\ell}$ over the other. Moreover, the choice of $\hat{n}_\ell$ elucidates which m modes are preferred. The statistic used is,

$$r_\ell = \max_{m\vec{n}} \frac{\mathtt{C}_{\ell m}}{(2\ell+1)\hat{C}_\ell}, \quad \text{where, } \mathtt{C}_{\ell 0} = |a_{\ell 0}|^2, \text{ and } \mathtt{C}_{\ell m} = 2|a_{\ell m}|^2 \text{ for } m > 0, \tag{1.106}$$

since $m \neq 0$ contribute twice to $\mathtt{C}_{\ell m}$. Thus r_ℓ quantifies both statistical anisotropy and preference of any m mode, by helping find the direction $\hat{n}_\ell$ for which the highest value of r_ℓ

is obtained. The asymmetry between odd and even modes is given by,

$$r_\ell^{\pm} = \frac{\hat{C}_\ell^{+}(\hat{n}_\ell) - \hat{C}_\ell^{-}(\hat{n}_\ell)}{\hat{C}_\ell}, \tag{1.107}$$

where, the values of $\hat{C}_\ell^{\pm}$ are as in Equation (1.105), while those of $\hat{n}_\ell$ can be found using Equation (1.106). The authors considered various cleaned maps of WMAP [32, 271, 91] and found an even mirror parity preference ($r_\ell^+ > 0$). Further they found that the alignment of preferred axes of the quadrupole and octupole extends up to $\ell = 5$, and their preferred shapes unlike those of $\ell = 2,3$ is not planar. They found that $\approx 10\%$ of simulated maps are as unusual as the observed data for such a preferred $r_\ell^+ > 0$, in the range $\ell \in [2,5]$. However, the parity feature studied alongside the $\hat{n}_\ell$ alignments is highly significant at $\sim 99.99\%$ level. Since mirror parity and the alignment of $\hat{n}_\ell$ are independent effects, as seen through Monte Carlo simulations, their joint significance increases from 99.9% to 99.99%.

1.8.2.4 Rotational symmetry based statistics related to the power

In the paper [246], the authors develop new statistical tools based on considerations of rotational symmetry. They introduce two new measures of randomness, namely, the power entropy and the directional entropy. Assuming SI, tensor products constructed using $a_{\ell m}$'s must be isotropic. The focus of this work is on second rank tensors. Two quantities which can be defined are the isotropic power, and the power tensor, respectively,

$$\begin{aligned} A(\ell)\delta_{ij} &= \frac{1}{(2\ell+1)} \sum_{mm'} a^*_{\ell m}\delta_{ij}\delta_{mm'}a_{\ell m'}, \\ A_{ij}(\ell) &= \frac{1}{(2\ell+1)} \sum_{mm'} a^*_{\ell m}(J_iJ_j)_{mm'}a_{\ell m'}. \end{aligned} \tag{1.108}$$

Here, J_i's are the multipole representations of the angular momentum operators for Cartesian indices of $i = 1,,2,3$. SI dictates the following ensemble averages,

$$\langle A\rangle = C_\ell, \quad \langle A_{ij}(\ell)\rangle = \frac{C_\ell}{3}\delta_{ij}. \tag{1.109}$$

The authors note that the angular power spectrum is not the only rotationally invariant quantity, and that several other entities formed from the spherical harmonics are not examined as much as the $\hat{C}_\ell$'s are. In orders of $\ell \geq 2$, there exist three rotationally invariant eigenvalues of $A_{ij}(\ell)$. Since eigenvectors are independent and covariant quantities, under isotropy considerations, they must be randomly oriented. The sum of the eigenvalues of $A_{ij}(\ell)$ must equal the usual power spectrum C_ℓ, whereas two independent combinations for a given range of multipoles, can be used to form new invariants as follows.

If one considers a representation of the spherical harmonic coefficients, $a_{\ell m} = \langle \ell, m | a(\ell) \rangle$, using the Dirac notation for states (not ensemble averages), then the states $|\ell, m\rangle$ are eigenvectors of the angular momentum operators J^2 and J_z, with the eigenvalues of $\ell(\ell+1)$ and m. The temperature fluctuations being real valued, provide the constraint $a_{\ell m} = (-1)^m a^*_{\ell,-m}$. For a small rotation by an angle $\vec{\theta}$ that changes the state $|a(\ell)\rangle \to |a(\ell)\rangle'$, we have

$$|a(\ell)\rangle' = |a(\ell)\rangle + |\delta a(\ell)\rangle, \quad \text{where, } |\delta a(\ell)\rangle = -i\vec{\theta}\cdot\vec{J}|a(\ell)\rangle. \tag{1.110}$$

To assess the impact of the rotation, the authors compute the Hessian of the change,

$$\frac{\partial^2}{\partial\theta_i\partial\theta_j}\langle \delta a(\ell)|\delta a(\ell)\rangle = \langle a(\ell)|J^i J^j|a(\ell)\rangle = A^{ij}, \tag{1.111}$$

using which the Rayleigh-Ritz variation provides the understanding that the maximum rotation occurs along the eigenvectors of the tensor A_{ij}, which are naturally the principal axes of the spherical harmonic coefficients considered in multipole space. Further, using the notion of a linear map or a wavefunction [232], a vector factorisation,

$$\psi^k_m(\ell) = \frac{1}{\sqrt{\ell(\ell+1)}}\langle \ell, m|J^k|a(\ell)\rangle, \tag{1.112}$$

helps compare the various spin-1 representation factors of a vector across different multipoles. Thus the mapping between $\psi^k_m(\ell)$ and $a_{\ell m}$ can be obtained as,

$$\psi^k_m(\ell) = \frac{1}{\sqrt{\ell(\ell+1)}}\sum_{m'=\ell}^{\ell}\langle \ell, m|J^k|\ell, m'\rangle\langle \ell, m'|a(\ell)\rangle \quad = \sum_{m'=-\ell}^{\ell}\Gamma^k_{mm'}a_{\ell m'}, \tag{1.113}$$

where, the coefficient matrix,

$$\Gamma^k_{mm'} = \frac{1}{\sqrt{\ell(\ell+1)}}\langle \ell, m|J^k|\ell, m'\rangle, \quad \text{and,} \quad a_{\ell m} = \sum_{km'}\Gamma^{mm'}_k\psi^k_{m'}(\ell), \tag{1.114}$$

$$\text{such that,} \quad \Gamma^{mm'}_k = \frac{1}{\sqrt{\ell(\ell+1)}}\langle \ell, m|J^k|\ell, m'\rangle = \Gamma^k_{mm'}. \tag{1.115}$$

The behaviours of $\psi^k_m(\ell)$ and hence $a_{\ell m}$ under a rotation are

$$\psi^k_m \to \psi^{k'}_{m'} = R^{kk'}(1)R_{mm'}(\ell)\psi^k_m, \tag{1.116}$$

$$a_{\ell m} \rightarrow a'_{\ell m} = \Gamma_k^{mm'} R^{kk'}(1) R_{mm'}(\ell) \psi_m^k = R_{mm'}(\ell) a_{\ell m'}. \tag{1.117}$$

A standard invariant obtained from the product of ψ_m^k is $\sum_{mk} \psi_m^k \psi_m^{k*} = \sum_m a_{\ell m} a_{\ell m}^*$. The quantities ψ_m^k represent the decomposition of $a(\ell)$ as a unique sum of outer products of a basis vector e^α (spin-1 representation) with a basis multiplet u^α (spin-ℓ representation). The expansion can be written using singular value decomposition:

$$\psi_m^k(\ell) = \sum_{\alpha=1}^{3} e_k^\alpha \Lambda^\alpha u_m^{\alpha*}. \tag{1.118}$$

These angular values Λ^α are rotationally invariant with respect to the k and m indices. Additionally they are invariant under the higher order symmetry of independent rotations corresponding to the $SO(3) \times SO(3)$ group. Diagonalisation of the Hermitian matrices helps provide the requisite decomposition,

$$(\psi\psi^\dagger)^{kk'}(\ell) = \sum_m \psi_m^k(\ell) \psi_m^{k'*}(\ell) \quad = \sum_\alpha e_k^\alpha (\Lambda^\alpha)^2 e_{k'}^{\alpha*}, \tag{1.119}$$

$$(\psi\psi^\dagger)_{mm'}(\ell) = \sum_k \psi_m^{k*}(\ell) \psi_{m'}^k(\ell) \quad = \sum_\alpha u_m^\alpha (\Lambda^\alpha)^2 u_{m'}^{\alpha*}. \tag{1.120}$$

The orthonormality condition for these basis vectors is $\sum_k e_k^{\alpha*} e_k^\beta = \delta_{\alpha\beta}$, $\sum_m u_m^{\alpha*} u_m^\beta = \delta_{\alpha\beta}$. Moreover, as the $(\Lambda^\alpha)^2$ are eigenvalues of hermitian matrices, they are expected to be real and positive, and thus, one considers $\Lambda^\alpha > 0$ as the sign convention for e^α. The set of e^α and u^α form preferred frames for the vector components of ψ. In a preferred frame common to both these basis vectors, the matrix ψ_m^k can be seen to be diagonal in form with its three invariant singular eigenvalues being Λ^α, and hence $\Lambda\delta_{\alpha\beta}$ is known as the singular value matrix. For detection of violations of isotropy, the following matrix is considered (with Tr denoting trace),

$$\begin{aligned} A^{ij}(\ell) &= \frac{1}{\ell(\ell+1)} \mathrm{Tr}\left(J^i |a(\ell)\rangle\langle a(\ell)| J^j\right), \\ A^{ij} &= \sum_m \psi_m^i(\ell) \psi_m^{j*}(\ell) = \sum_\alpha e_i^\alpha(\ell) \left[\Lambda^\alpha(\ell)\right]^2 e_j^{\alpha*}(\ell). \end{aligned} \tag{1.121}$$

Assuming SI and using the orthogonality of the angular momentum operators, we arrive at

$$\langle A^{ij}(\ell)\rangle = \frac{C_\ell}{\ell(\ell+1)} \mathrm{Tr}\left(J^i J^j\right) = \frac{C_\ell}{3} \delta^{ij}. \tag{1.122}$$

The assumption of isotropy indicates that there must be no preferred eigenvector, and hence the eigenvalues must be closely spaced in value ($\equiv \sqrt{\frac{C_\ell}{3}}$). The most anisotropic case corresponds to that of a single preferred direction, with only one singular value carrying the full power, while the other two are zero. Then the $a_{\ell m}$'s can be written as the product of a vector $e^{(1)}$, and a multiplet $u^{(1)}$, thus forming a 'pure' state. However, if all the eigenvalues are degenerate (the isotropic case), then the matrix is a multiple of the unit matrix $\mathbb{I}$, given by the sum of outer products of the frame vectors, i.e., $\mathbb{I} = \sum_\alpha |e^\alpha\rangle\langle e^\alpha|$.

The tensor power entropy is defined in the following manner. Recognising that $\rho^{kk'} = (\psi\psi^\dagger)^{kk'}$ is proportional to a 3D-space density matrix, and that the proportionality constant itself is the power, the normalised form of the density matrix can be written as, $\tilde{\rho}^{kk'} = \frac{(\psi\psi^\dagger)^{kk'}}{\sum_j (\psi\psi^\dagger)^{jj}}$, and the associated entropy as originally given by von Neumann [279] for a normalised Hermitian matrix $\tilde{\rho}$ is

$$S = \mathrm{Tr}\,(\tilde{\rho}\log(\tilde{\rho})) = -\sum_\alpha (\tilde{\Lambda}^\alpha)^2 \log(\tilde{\Lambda}^\alpha)^2, \tag{1.123}$$

which provides the constraint, $0 \le S \le \log(3)$. The eigenvalues are also normalised to sum to one, as $(\tilde{\Lambda}^\alpha)^2 = \frac{(\Lambda)^2}{\sum_{\alpha'} (\Lambda^{\alpha'})^2}$, and hence, $\mathrm{Tr}(\tilde{\rho}) = 1$. Thus the entropy is zero for a pure state, and additionally, it adheres to the expectations of rotational invariance, positivity, and additiveness for independent subsystems under investigation.

Further, using the previously established formalism, the authors of this work explored the concept of alignment of the power tensor across different multipole classes, by using the principal eigenvector $\tilde{e}(\ell)$ corresponding to the largest eigenvalue for any ℓ. Following from Equation (1.122), we understand that the set of all the (normalised) principal frame vectors will symmetrically span a unit sphere due to isotropy. However, when anisotropy is present, these vectors will be preferentially directed along some axis, or will tend to lie in a certain preferred plane. To study such deviations, the following matrix is constructed,

$$X_{ij}(\ell_{max}) = \sum_{\ell=2}^{\ell_{max}} \tilde{e}_i^\ell \tilde{e}_j^\ell, \tag{1.124}$$

the eigenvalues of which help investigate the shape of such a bundle of principal eigenvectors, considered together for the multipole range $\ell \in [2, \ell_{max}]$. After constructing a density matrix from X, the equation for entropy (1.123) can be used to quantify the extent of adherence to isotropy. This directional entropy is independent of the the power entropy since it does not utilise the singular values extracted from the CMB data. Isotropy is confirmed only for $S_X \sim \log(3)$, whereas an unusually low value of S_X indicates a signature of anisotropy.

Another quantity formulated by the authors of this work is the traceless power tensor,

$$B^{ij} = A^{ij} - \frac{1}{3}\mathrm{Tr}\,(A(\ell))\,\delta^{ij} \tag{1.125}$$

which compares the alignment inclusive of the weights due to singular values from data. The eigenvectors of A and B are the same. A useful statistic associated with the tensor B is

$$Y(\ell,\ell') = \frac{\mathrm{Tr}\,(B(\ell)B(\ell'))}{\sqrt{\mathrm{Tr}\,(B(\ell)B(\ell))}\sqrt{\mathrm{Tr}\,(B(\ell')B(\ell'))}}, \tag{1.126}$$

which gives the correlation between two angular momentum classes. Hence in the isotropic case, the correlation between dissimilar modes should vanish or $Y(\ell,\ell') = \delta_{\ell\ell'}$.

On analysing the real CMB data, in the form the foreground cleaned CMB data of the WMAP-ILC map, the authors found that the power entropy for full sky case, is highly unlikely ($\lesssim 5\%$ of simulated maps exhibit such power entropy) for $\ell = 6, 16, 17, 30, 34, 40$. Additionally, the principal axes of the power tensor for $\ell = 3, 9, 16, 21, 40, 43$ align unusually (p-values $\lesssim 5\%$) with that of the quadrupole. Further, the principal axis of X matrix for $\ell \in [2, 50]$, is well aligned with the principal axes of the quadrupole and octupole from their power tensor matrices, and all of which are aligned in the direction of the Virgo supercluster. Thus the authors conclude that the alignment issues or violations of isotropy are not confined to low ℓ only but extend to a broader range of multipoles. A plot of the Y matrix describing correlations validate these findings. Moreover, the authors showed with a random CMB map to which was added simulated synchrotron contamination (at 23 GHz, and at 2% of the actual strength), that such a map produces a principal axis for X in the galactic plane, quite unlike the preferred directions of alignment observed in the WMAP-ILC map. This weakens the possibility of residual contamination being causative of the detected signals.

1.8.3 Finding preferred directions and alignments

Deviations from isotropy as discernible in the correlations of $\Delta T(\hat{n})$ or the asymmetries in power must have arisen from preference of directions in the CMB 2-sphere itself. Hence methods to directly detect the same warrant our attention. In this subsection, we review a few well known studies of unusual alignments and preferred directions in the real CMB.

1.8.3.1 Maximisation of angular momentum for largest scale modes

A technique developed in the work of [78] helps estimate the vector components of the preferred direction or axis for a given multipole. This was done to assess the quadrupole and octupole of the foreground cleaned CMB map from WMAP, because the authors of this work observed that the both the quadrupole and octupole components are very planar in structure, that is, the centres of their hot and cold spots seem to be highly aligned along some specific planes in either case. Further they noticed that the normals to these planes for $\ell = 2$ and $\ell = 3$ appear to be very well aligned with each other, whereas in the isotropic Gaussian random case of fluctuations, such specific alignments or planarity are not expected.

Expressing the temperature fluctuation as a wavefunction, i.e, $\Delta T(\hat{n}) = \psi(\hat{n})$, it is possible to find an axis $\hat{n}$, for which the angular momentum dispersion,

$$\langle\psi(\hat{n})|\left(\hat{n}\cdot\vec{L}\right)|\psi(\hat{n})\rangle = \sum_m m^2|a_{\ell m}(\hat{n})|^2, \tag{1.127}$$

can be maximised. The $a_{\ell m}(\hat{n})$ represents the spherical harmonic coefficients of a CMB map rotated to a coordinate system for which the $\hat{z}$-axis and $\hat{n}$ coincide. The procedure of maximisation is carried out as follows. Corresponding to maps at a HEALPix [117] resolution of $n_{side} = 512$, the expression (1.127) is evaluated for $\hat{n}$'s of all the pixel centres. The $\hat{n}$ for which the quantity is maximum to within a spacing of half a pixel ($\sim 0.06°$) is noted. As regards the rotation of the maps, alternatively, the $a_{\ell m}$'s are transformed to different coordinate systems by using the Wigner's formula. The values of the components corresponding to the preferred axes of the quadrupole and octupole are

$$\hat{n}_2 = (-0.1113, -0.5055, 0.8556), \quad \hat{n}_3 = (-0.2459, -0.3992, 0.8833), \tag{1.128}$$

each of which approximately point towards the Virgo supercluster with the value of $\hat{n}_2.\hat{n}_3 = 0.9849$. The statistical independence of the quadrupole and octupole $\hat{n}$'s dictates that $\hat{n}_2\cdot\hat{n}_3$ must be uniformly distributed in $[-1,-1]$, or that $|\hat{n}_2\cdot\hat{n}_3|$ is uniformly distributed in $[0,1]$. Hence the chance of occurrence of the observed alignment is once in $\frac{1}{1-0.9849} \approx 66$ times. The authors found that the planarity of the quadrupole is not as pronounced as that of the octupole. They quantified the statistical significance of the latter with help of the t statistic,

$$t = \max_{\hat{n}} \frac{|a_{3,-3}(\hat{n})|^2 + |a_{3,3}(\hat{n}|^2)}{\sum_{m=-3}^{3} |a_{3,m}(\hat{n})|^2}, \tag{1.129}$$

which estimates the amount of power of the octupole that can be ascribed to the contributions from $|m| = 3$. They found that for the WMAP cleaned map, $t = 94\%$. Besides, comparisons with a large number of simulated maps based on isotropic Gaussian random $a_{\ell m}$'s revealed that only 7% of such maps exhibit values of t larger than that from WMAP TOH [271] map. Another statistic , i.e., the angular momentum dispersion relative to the total power,

$$\psi_d = \frac{\langle\psi|(\hat{n}\cdot\vec{L})^2|\psi\rangle}{\langle\psi|\psi\rangle}, \tag{1.130}$$

provides a similar statistical significance of the effect of planarity of the octupole, whereas that of the quadrupole is rendered insignificant.

1.8.3.2 Multipole vectors

With the previous formalism, unusual features with respect to the quadrupole and octupole were identified. However, to extend such analyses to all multipoles, and to associate vectors with each of the multipoles, a novel mathematical approach was prescribed in the paper [63]. The authors of this work introduced ℓ vectors $\{\hat{\upsilon}^{\ell,i}|i = 1,...\ell\}$, and a scalar $A^{(\ell)}$ to characterise any multipole ℓ of the temperature fluctuations given by

$$f_\ell(\hat{n})\frac{\delta T_\ell(\hat{n})}{T_0} = \sum_{m=-\ell}^{\ell} a_{\ell m} Y_{\ell m}(\hat{n}). \tag{1.131}$$

Here, $f_\ell(\hat{n})$ can be represented by a symmetric and traceless rank-ℓ tensor $F_{i_1,\ldots,i_\ell}$ ($i_k = 1,2,3$), and can be formed using outer products of the proposed ℓ unit vectors $\hat{\upsilon}^{\ell,i}$ and the scalar $A^{(\ell)}$. These vectors being headless facilitate the absorption of any associated sign within the scalar $A^{(\ell)}$. The Cartesian representation of the dipole, $Y_{1,0} \to \hat{z}, \quad Y_{1,\pm 1} \to \mp\frac{1}{\sqrt{2}}(\hat{x} \pm \hat{y})$, helps express it in terms of a multipole vector as follows,

$$\begin{aligned}\sum_{m=-1}^{1} a_{1,m} Y_{1,m}(\hat{n}) &= A^{(1)}\left(\hat{\upsilon}_x^{(1,1)}, \hat{\upsilon}_y^{(1,1)}, \hat{\upsilon}_z^{(1,1)}\right) \cdot (\sin\theta\cos\phi, \sin\theta\sin\phi, \cos\theta) \\ &= A^{(1)}\hat{\upsilon}^{(1,1)} \cdot \hat{e}, \end{aligned} \tag{1.132}$$

where, the radial unit vector in spherical polar coordinates is given by $\hat{e}$. For a real valued function, the various components can be found out to be,

$$v_x^{(1,1)} = -\sqrt{2}a_{(1,1)}^{real}, \quad v_x^{(1,1)} = \sqrt{2}a_{(1,1)}^{imag}, \quad v_z^{(1,1)} = a_{(1,0)}, \quad A^{(1)} = |\vec{v}^{1,1}|. \tag{1.133}$$

Extending this procedure to higher multipoles, one may write,

$$\sum_{m=-\ell}^{\ell} = a_{\ell m}Y_{\ell m}(\hat{n}) \equiv A^{(\ell)}(\hat{v}^{(\ell,1)} \cdot \hat{e})....(\hat{v}^{(\ell,\ell)} \cdot \hat{e}). \tag{1.134}$$

Such a decomposition is justified on the grounds that after imposing the conditions of reality on the $a_{\ell m}$, the ℓ unit vectors and the scalar $A^{(\ell)}$ contain the same number of degrees of freedom as those of the $a_{\ell m}$, i.e., $(2\ell+1)$, considering that all the components of the right hand side of the previous equation (1.134) are not completely independent. Generally, the vectors are extracted one at a time from Equation (1.134) in a procedure elucidated as follows. A vector $\hat{v}^{(\ell,i)}$ (whose components are $\hat{v}_{i_1}^{(\ell,i)}$) must be found, alongwith a symmetric and traceless tensor with the rank-$(\ell-1)$. Here the index i_1 runs over three components x, y, z or $1, 0, -1$. Following this, a matrix of the form $a_{i_2,\ldots,i_\ell}^{\ell,1}$, having a shape of $3\times3\times3...\times3$ (taken $(\ell-1)$ times) can be constructed to represent $a^{(\ell,1)}$. To denote the degrees of freedom ($2\ell-1$ in number) for this quantity, the symbol used instead is $a_{\ell-1,m}^{(\ell,1)}$, with $m = -(\ell-1), ..., (\ell-1)$. In the next step, from the matrix denoted by $a^{(\ell,1)}$, the vector $\hat{v}^{(\ell,2)}$ and the symmetric traceless tensor $a^{(\ell,2)}$ (of rank $(\ell-2)$) are extracted. Thus, recursively, the method described is repeated on the remnant tensors which are symmetric and traceless, until the full set of ℓ vectors $\hat{v}^{(\ell,i)}|i = 1, ..., \ell$ have been ascertained. Thus, in the last step of such a procedure, when the penultimate vector is being extracted, namely $\hat{v}^{(\ell,\ell-1)}$, then the leftover symmetric and traceless tensor is $a^{(\ell,\ell-1)}$, which is the product of the scalar $A^{(\ell)}$ and the vector $\hat{v}^{(\ell,\ell)}$. The recursion relation used is

$$Y_{1,j}Y_{\ell-1}, m-j = C_j^{(\ell,m)}Y_{\ell,m} + D_j^{(\ell,m)}Y_{\ell-2,m}, \tag{1.135}$$

with j taking the values $-1, 0, 1$, and where the symbols $C_j^{(\ell,m)}, D_j^{(\ell,m)}$ are given by,

$$C_0^{(\ell,m)} = \sqrt{\frac{3}{4\pi}}\sqrt{\frac{(\ell-m)(\ell+m)}{(2\ell-1)(2\ell+1)}}, \quad C_{\pm1}^{(\ell,m)} = \sqrt{\frac{3}{8\pi}}\sqrt{\frac{(\ell\pm m-1)(\ell\pm m)}{(2\ell-1)(2\ell+1)}}, \tag{1.136}$$

$$D_0^{(\ell,m)} = \sqrt{\frac{3}{4\pi}}\sqrt{\frac{(\ell-m-1)(\ell+m-1)}{(2\ell-3)(2\ell-1)}}, \quad D_{\pm1}^{(\ell,m)} = \sqrt{\frac{3}{8\pi}}\sqrt{\frac{(\ell\mp m-1)(\ell\mp m)}{(2\ell-3)(2\ell-1)}}. \quad (1.137)$$

For a certain multipole, the vectors can be extracted using the relation,

$$\sum_{m=-\ell}^{\ell} a_{\ell,m}Y_{\ell,m} = \sum_{m'=-(\ell-1)}^{(\ell-1)}\sum_{j=-1}^{1}\hat{v}_j^{(\ell,1)}a_{(\ell-1,m')}^{(\ell,1)}Y_{1,j}Y_{\ell-1,m'} - \sum_{m''=-(\ell-2)}^{(\ell-2)} b_{m''}^{(\ell,1)}Y_{\ell-2,m''}, \quad (1.138)$$

given that $|\hat{v}^{(\ell,1)}| = 1$, and the sum over m'' ensures that the trace of the rank-$(\ell-1)$ matrix is subtracted off. With the help of the recursion relation (1.135), one obtains $(4\ell-1)$ quadratic equations which are coupled, and can be solved for $\hat{v}_j^{(\ell,1)}$, $a_{\ell-1,m-j}^{(\ell,1)}$ and $b_{m''}^{(\ell,1)}$ which constitute $4\ell-1$ unknowns. Consequently, one finds,

$$a_{\ell m} = \sum_{j=-1}^{1} C_j^{(\ell,m)}\hat{v}_j^{(\ell)}a_{\ell-1,m-j}^{(\ell,1)}, \quad b_{m''}^{(\ell,1)} = \sum_{j=-1}^{1} D_j^{(\ell,m'')}\hat{v}_j^{(\ell)}a_{\ell-1,m''-j}^{(\ell,1)}. \quad (1.139)$$

The above expressions for $a_{\ell m}$ and $b_{m''}^{(\ell,1)}$ constitute $(2\ell+1)$ and $(2\ell-3)$ equations, respectively, which must be solved along with one equation for $|\hat{v}^{(\ell)}| = 1$, thus giving us a total of $4\ell-1$ equations as before. These equations, as noted by the authors can be solved numerically. The components of $b_{m''}^{(\ell,1)}$ being functions of the $\hat{v}_{i_1}^{(\ell,1)}$ and $a_{\ell-1,m-i_1}^{(\ell,1)}$ are not independent. In conclusion, the general procedure for ascertaining these multipole vectors is as follows: firstly the $\hat{v}^{(\ell,1)}$ and $a_{\ell-1,m}^{(\ell,1)}$ are computed from a given $a_{\ell m}$, and this process is continued to obtain the $\hat{v}^{(\ell,2)}$ and $a_{\ell-2,m}^{(\ell,2)}$, and so on. A repetition of this sequence of steps ensures that finally, the $a_{2,m}^{(\ell,\ell-2)}$ will be found, along with the vectors $\hat{v}^{(\ell,\ell-1)}$ and $\hat{v}^{\ell,\ell}$.

Additionally, the authors of this work noted that pixel noise limits the accuracy of estimating these multipole vectors. It depends on the number of times a point in the sky is observed, and is given by $\sigma_{pix} \sim \frac{\sigma_0}{\sqrt{N_{obs}}}$ for WMAP , where σ_0 is the noise per observation, and per pixel number of observations are N_{obs}. Then, the full-sky noise covariance is

$$\langle a_{\ell m}a^*_{\ell' m'}\rangle = \hat{\Omega}_{pix}\sigma_{pix}^2\delta_{\ell\ell'}\delta_{mm'}. \quad (1.140)$$

Here the solid angle subtended by each pixel is assumed to be equal to $\hat{\Omega}_{pix}$. The authors considered the WMAP V-band map parameters as the standard for pixel noise given by $\sqrt{\hat{\Omega}_{pix}}\sigma_{pix} = 2.7\times10^{-4}$ mK. In order to ascertain the accuracy of estimation of the multipole vectors, they used Gaussian distributed noise with standard deviation $\sigma_{a_{\ell m}} = \sqrt{\hat{\Omega}_{pix}}\sigma_{pix}$, which was added to the statistically isotropic Gaussian random $a_{\ell m}$'s of maps conforming to the standard model of Cosmology. They found that the multipole vectors can be ascertained within $\pm 1^\circ$ order when noise was added to the map, which is within the order of the pixel noise. However, the authors noted that in the case of larger strength of noise ($\sigma_{a_{\ell m}} \gtrsim 10\sqrt{\hat{\Omega}_{pix}\sigma_{pix}}$), the deterioration in accuracy renders the multipole vectors inappropriate for representation of the CMB anisotropies. The effect is most pronounced for higher multipoles, since the number of vectors being estimated is large.

Considering the multipole vectors to be headless, the magnitudes of the following products were investigated by the authors for detecting violations of SI.

1. *"vector-vector" products:* These are dot products of vectors such as $\left|\hat{v}^{(\ell_1,i)} \cdot \hat{v}^{(\ell_2,j)}\right|$, where $\ell_1 \neq \ell_2$, and $\hat{v}^{(\ell_1,i)}$ is the i^{th} vector for ℓ_1, and $\hat{v}^{(\ell_2,j)}$ is the j^{th} vector for ℓ_2. They are $\ell_1\ell_2$ in number and quantify the orientation of the vectors.

2. *"vector-cross" products:* These are a total of $\ell_1\ell_2(\ell_2-1)/2$ dot products of the form
$$\frac{\left|\hat{v}^{(\ell_1,i)} \cdot \left(\hat{v}^{(\ell_2,j)} \times \hat{v}^{(\ell_2,k)}\right)\right|}{\left|\hat{v}^{(\ell_2,j)} \times \hat{v}^{(\ell_2,k)}\right|}, \quad \text{where, } j \neq k, \tag{1.141}$$
representing the orientation of a plane with a vector.

3. *"cross-cross" products:* As a total of $\ell_1\ell_2(\ell_1-1)(\ell_2-1)/4$ dot products of the form
$$\frac{\left|\left(\hat{v}^{(\ell_1,i)} \times \hat{v}^{(\ell_1,j)}\right) \cdot \left(\hat{v}^{(\ell_2,k)} \times \hat{v}^{(\ell_2,m)}\right)\right|}{\left|\left(\hat{v}^{(\ell_1,i)} \times \hat{v}^{(\ell_1,j)}\right)\right|\left|\left(\hat{v}^{(\ell_2,k)} \times \hat{v}^{(\ell_1,m)}\right)\right|}, \quad \text{where, } i \neq j, k \neq m, \tag{1.142}$$
these "cross-cross" products quantify the orientation of planes.

4. *"oriented area" products:* These are a total of $\ell_1\ell_2(\ell_1-1)(\ell_2-1)/4$ dot products representing the orientation of areas, and given by
$$\left|\left(\hat{v}^{(\ell_1,i)} \times \hat{v}^{(\ell_1,j)}\right) \cdot \left(\hat{v}^{(\ell_2,k)} \times \hat{v}^{(\ell_2,m)}\right)\right|, \quad \text{where, } i \neq j, k \neq m. \tag{1.143}$$
They are unnormalised versions of the previous "cross-cross" products.

In order to compare these statistics from WMAP data against Monte Carlo simulated maps, the authors considered rank-ordering of the products of each type. This is done because one does not specifically know which i^{th} vector of a certain ℓ_1 is obtained upon computation, and neither is such information carried in the dot products. They simulated 10^5 maps with isotropic, Gaussian random spherical harmonic coefficients, to which the inhomogeneous noise based on WMAP V-band data was added. After ascertaining multipole vectors for some ℓ_1 and ℓ_2, the N_d dot products corresponding to any one the categories above are computed, and rank ordered. Thus there will be N_d histograms with 10^5 elements each. Thereafter the likelihood corresponding to the WMAP map is

$$\mathcal{L}_{WMAP} = \Pi_{k=1}^{N_d} \frac{N_{k,WMAP}}{N_{k,max}}, \tag{1.144}$$

where, $N_{k,WMAP}$ is the value of the ordinate for the k^{th} histogram for the k^{th} product from WMAP after rank-ordering, and $N_{k,max}$ is the maximum value of the k^{th} histogram. Similarly, such likelihoods ((1.144)) are also computed for another set of 5×10^4 Gaussian random and statistically isotropic realisations of $a_{\ell_1 m}$ and $a_{\ell_2 m}$. Further their multipole vectors are computed and the product statistics are evaluated. Then the likelihood $\mathcal{L}_{WMAP}$ is rank-ordered among the 5×10^4 likelihoods from simulated maps to obtain the rank, R_{ℓ_1,ℓ_2} for WMAP, and the rank order as a fraction (for e.g., if the rank is 800 out of 1000, then the rank order is 0.9). This entire procedure is repeated for several such pairs of ℓ_1 and ℓ_2.

The rank quantifies the probability of the statistics being consistent with the null hypothesis of SI and Gaussianity. For obtaining the confidence level another test was considered, wherein the rank orders of various multipole pairs (N_r in number), were evaluated as u_i ($\in [0,1]$), arranged in descending order, and the following statistic was computed:

$$Q(u_1, ..., u_{N_r}) = N_r! \int_{u_1}^{1} dv_1 \int_{u_2}^{v_1} dv_2 ... \int_{u_{N_r}}^{v_{N_r - 1}} dv_{N_r}, \tag{1.145}$$

which represents the probability that the largest rank is greater than u_1, the second largest rank is greater than u_2 and so on, until the smallest rank is greater than u_{N_r}. The fraction of maps with Gaussian random $a\ell m$'s possessing a value of Q smaller than that from WMAP was computed. The authors found similar results for the TOH cleaned and Weiner filtered maps [271] and the WMAP-ILC [32] map, hence they presented those only for the WMAP-ILC map. The multipoles considered were only $\ell_1, \ell_2 \in [2, 8]$, and for the vector-cross products, both combinations (ℓ_1, ℓ_2) and (ℓ_2, ℓ_1) were taken care of since they are distinct entities.

Among the cross-cross ranks, they observed that for $\ell_1 = 3, \ell_2 = 8$, the rank order is 0.99988, which is highly significant. Further the previously known quadrupole-octupole alignment effect was corroborated with the new multipole vector analysis, using vector-cross products for $(2,3)$ and $(3,2)$, the cross-cross product for $(2,3)$, and the oriented area products, all of which had considerably low ranks ($\lesssim 0.05$). Additionally, ranks for some oriented areas showed unusual results, such as, out of 21 ranks, a total of 2 were > 0.99, 5 were > 0.9 and 8 are > 0.8. With respect to 10^4 simulated maps, the WMAP Q value was compared, and it was seen that only 107 of these maps possessed a Q value lower than that from WMAP.

Variations of the multipole range under scrutiny could have affected the findings. Hence the lower limit ℓ_{min} was increased and the change in probability for $\ell_{min} = 3,4$ were $1\%, 5.6\%$, respectively, indicating a slight weakening of the signals of statistical anisotropy. Similarly when ℓ_{max} was decreased, some diminution of the significance of the anomalies was seen, but not a complete disappearance. Further, increasing ℓ_{max} to 12 introduced more unusually high ranks. These indicate that the findings are not altogether dependent on the specific range of multipoles considered, but are definitely most visible in the range $\ell \in [2,8]$. Moreover, the authors corroborated the persistence of these unusual signals even when synthetic noise or small foreground contamination was added to the simulated CMB maps. Besides, this formalism, as noted by the authors is most suitable for full-sky maps, whereas for partial-sky maps [64] very large errors are introduced since multipole vectors are sensitive to the partial sky mode couplings intrinsic to the $a_{\ell m}$'s themselves, which may lead to weakening of correlations observed previously in the full sky case. Hence partial sky multipole vectors may be used primarily to assess consistency with full-sky results.

1.8.3.3 The axis of evil

The notion of a preferred direction, known as the "Axis of Evil" (AoE) was proposed by [167]. The authors of the work utilised the statistic r_ℓ defined in an earlier work (Equation (1.106)). The information provided by this statistic is three-fold: (a) the direction $\vec{n}_\ell$, (b) the shape of the power denoted by m_ℓ and (c) the ratio r_ℓ itself, which quantifies the power absorbed by the mode m_ℓ in the direction of $\vec{n}_\ell$. The statistic is unambiguous in determining these quantities, except when $\ell = 2$ has a planar structure, which corresponds to either $m = 2$ or $m = 1$ modes having their axis $\vec{n}_2$ rotated by $90°$. For this convention, the multipole and its azimuthal number are taken to be $\ell = 2, m = 2$. Additionally the authors studied the angles between any preferred axes of subsequent multipoles.

The authors analysed three maps: the power equalised map of [39], the WMAP ILC map [91], and the Wiener filtered map [271]. Using the cleaned and Wiener filtered maps, the authors reproduced the results of quadrupole-octupole alignment along the AoE which is $\approx (b,l) = (60,-100)$ in Galactic coordinates. They also observed that $\ell = 5$ is approximately concentrated as a mode of $m = 3$, aligned with the $(b,l) = (50,-91)$ axis. The multipole alignments seen for $\ell = 2,...,5$ do not extend towards higher ℓ's. Further, the authors examined the angles between various multipoles $\ell = 2,...,5$ and found that on an average these are never more than 20° apart. On comparing the same with Monte Carlo simulations obeying Gaussianity and SI, they could conclusively reject the null hypothesis of isotropy by 99.9% confidence for these angular scales. The authors found that r_ℓ is consistent with Gaussianity, and only some features like the power for $\ell = 3$ being concentrated in $m = 3$ mode appears to be anomalous at the 93% confidence level when one specifically probes the unusual planarity of the multipole. Otherwise the authors noted that a majority of simulated maps have power concentrated in a single m for a given ℓ. They conducted a scrutiny of the phase correlations and found that the $\ell = 3$ and $\ell = 5$ modes have a very close alignment of their phases rejecting isotropy at 94.5% confidence. This finding along with the unusual alignments for $\ell = 2,...,5$ increases the rejection confidence to about 99.995%.

1.8.3.4 Directions associated with features of parity

In their paper [208], the authors defined some statistics to compute preferred directions associated with the parity asymmetry feature of the CMB. To extract the symmetric and antisymmetric functions for $\Delta T(\hat{n})$, they considered the following,

$$\Delta T^{\pm}(\hat{n}) = \sum_{\ell} \sum_{m=-\ell}^{\ell} a_{\ell m} \Gamma^{\pm}(\ell) Y_{\ell m}(\hat{n}), \tag{1.146}$$

such that $\Gamma^{+}(\ell) = \cos^2 \frac{\pi \ell}{2}$ and $\Gamma^{-}(\ell) = \sin^2 \frac{\pi \ell}{2}$. We note that $Y_{\ell m}(\hat{n}) = (-1)^{\ell} Y_{\ell m}(-\hat{n})$. The theoretical two-point angular correlation function,

$$C^{th}(\Theta) = \langle \Delta T(\hat{n}) \Delta T(\hat{n}') \rangle = \sum_{\ell=\ell_{min}}^{\infty} \frac{(2\ell+1)}{4\pi} C_{\ell}^{th} P_{\ell}(\cos(\Theta)), \tag{1.147}$$

can be rewritten for the largest angular separation $\Theta = \pi$, as

$$C^{th}(\pi) = \sum_{\ell=\ell_{min}}^{\infty} \frac{(2\ell+1)}{4\pi} C_\ell^{th} (\Gamma^+(\ell) - \Gamma^-(\ell)). \tag{1.148}$$

Further, a ratio which helps estimate the contribution of even multipoles in the correlation function to that of odd multipoles is,

$$g(\ell) = \frac{\sum_{\ell'=\ell'_{min}}^{\ell} \frac{(2\ell'+1)}{4\pi} C_{\ell'} \Gamma^+(\ell')}{\sum_{\ell'=\ell'_{min}}^{\ell} \frac{(2\ell'+1)}{4\pi} C_{\ell'} \Gamma^-(\ell')}. \tag{1.149}$$

Here, ℓ'_{min} can be equal to 1 or 2. Thus, using this, the equation (1.148) can be recast as

$$C(\pi) = P^-(\ell)\left[g(\ell) - 1\right], \quad \text{where, } P^{\pm} = \sum_{\ell'=\ell'_{min}}^{\ell} \frac{(2\ell'+1)}{4\pi} C_{\ell'} \Gamma^{\pm}(\ell'), \tag{1.150}$$

which means that the correlation $C(\pi) = 0$, when $g(\ell) = 1$. By plotting the theoretical correlation function for a theoretical C_ℓ^{th}, and the function $C(\pi)$ for WMAP 7-year foreground cleaned map, the authors noted that generally, odd-parity is always favoured for $\ell'_{min} \leq 15$ in real CMB. Theoretically the chance to be parity asymmetric with $g(\ell) > 1$ when $\ell'_{min} = 2$, is favoured slightly, whereas there is minimal chance of $g(\ell) < 1$. However, for WMAP 7 year data, $C(\pi) < 0$ at 95% confidence level (C.L.). The statistically isotropic and Gaussian random $a_{\ell m}$'s ensure that the correlation function $C(\Theta)$ corresponding to the actual C_ℓ^{th} and pseudo-C_ℓ ($\hat{C}_\ell$) are both rotationally invariant. Therefore in order to identify the direction associated with the parity asymmetry, the authors formulate the statistic,

$$\hat{D}(\ell) = \frac{1}{(2\ell+1)} \sum_{m=-\ell}^{\ell} |a_{\ell m}|^2 (1 - \delta_{m0}). \tag{1.151}$$

Thus, the difference between the rotationally invariant and variant counterparts is

$$\Delta(\ell) = \frac{\hat{D}(\ell) - \hat{C}_\ell}{\hat{C}_\ell} = \frac{-a_{\ell 0}^2}{\sum_m |a_{\ell m}|^2}. \tag{1.152}$$

This difference is of the order $\sim \frac{1}{2\ell}$, hence it is most prominent for multipoles $\ell = 2, 3$ and the contributions would be lesser than 10% for $\ell \geq 5$.

If the Galactic coordinate system is rotated by Euler angles (χ, ξ, ψ), then the spherical harmonic coefficients $a_{\ell m}(\chi, \xi, \psi)$ in the rotated frame are given by

$$a_{\ell m}(\chi, \xi, \psi) = \sum_{m'=-\ell}^{\ell} a_{\ell m'} D_{mm'}^{(\ell)}(\chi, \xi, \psi). \tag{1.153}$$

The Galactic coordinate system corresponds to $(\chi, \xi, \psi) = (0, 0, 0)$, and $D_{mm'}^{(\ell)}$ is the Wigner rotation matrix. Using these $a_{\ell m}(\chi, \xi, \psi)$'s, one may define the corresponding rotationally variant power spectrum $\hat{D}(\ell; \chi, \xi, \psi)$. Additionally, since the $\hat{D}(\ell; \chi, \xi, \psi)$ are independent of the angle χ, a vector can be considered for the effective Euler angles $\hat{q} \equiv (\xi, \psi)$, as $\chi = 0$. The $\hat{q}$ vector labels the direction of the $z-$axis in the rotated coordinate system, such that in the Galactic coordinate system, the polar coordinates for this direction are (ξ, ψ). In order to define a rotationally variant parity parameter, the authors used

$$G(\ell, \hat{q}) = \frac{P^+(\ell) - X^+(\ell, \hat{q})}{P^-(\ell) - X^-(\ell, \hat{q})}, \text{ where, } X^{\pm}(\ell, \hat{q}) = \frac{1}{4\pi} \sum_{\ell'=2}^{\ell} a^2_{\ell' 0}(\hat{q}) \Gamma^{\pm}(\ell'),$$

$$a^2_{\ell 0}(\hat{q}) = \sum_{mm'} a_{\ell m} a^*_{\ell m'} D^{(\ell)}_{0m}(\hat{q}) D^{(\ell *)}_{0m'}(\hat{q}) = \frac{4\pi}{(2\ell+1)} \sum_{mm'} (-1)^{(m+m')} a_{\ell m} a^*_{\ell m'} Y^*_{\ell m}(\hat{q}) Y_{\ell m}(\hat{q}). \tag{1.154}$$

Hence the cross terms $a_{\ell m} a^*_{\ell m}$ provide the angular dependence of $G(\ell, \hat{q})$. The difference between this parity parameter in rotated coordinates, relative to the unrotated one (1.149) is,

$$\Delta_g(\ell) = \frac{G(\ell, \hat{q}) - g(\ell)}{g(\ell)} \simeq \frac{X^-(\ell, \hat{q}) - X^+(\ell, \hat{q})/g(\ell)}{P^-(\ell)}. \tag{1.155}$$

Since Equation (1.152) states that $\Delta(\ell) \sim \mathcal{O}(\frac{1}{2\ell})$, and it is known that $X^{\pm}(\ell, \hat{q}) \ll P^-(\ell)$, hence $\Delta_g(\ell) \ll 1$ for $\ell > 3$. Thus, $G(\ell, \hat{q})$ provides us with an amplitude very close to $g(\ell)$, but with the additional information of the preferred direction, due to its rotational variance.

On plotting the $G(\ell, \hat{q})$ for various $\ell \in [3, 22]$, as a function of the direction $\hat{q}$, the authors of this study found that the plots showed similar visual features for $\ell \geq 4$ in terms of directions $\hat{q}$ for which the parity parameter is minimised. The structural pattern of the $G(3, \hat{q})$ for the octupole is slightly different possibly due to its alignment with the quadrupole. An interesting finding is that the preferred directions $\hat{q}$ for which the violation of the parity symmetry is greatest, align very well with the direction of the kinematic dipole for the WMAP 7-year map. Moreover, the directions $\hat{q}$ for which the parity asymmetry is the least, are almost normal to the direction of the kinematic dipole. These results indicate a possible residual contamination of the WMAP maps with the kinematic dipole which causes the parity asymmetry to appear.

In a different paper [301], six types of statistics were designed to probe the directional associations of the parity asymmetry feature and the foreground-cleaned maps of SMICA, NILC, and SEVEM from Planck 2013 release [6] were analysed. The author compared the power spectra from these full-sky maps with that from a masked Planck Commander-Ruler (C-R) map, and showed that the biases affecting the low multipoles due to residual contamination in these maps is low. Moreover, the differences between these maps is small for low $\ell < 10$, but that the biases become relatively prominent for $\ell = 10$ and $\ell = 17$. Despite this observation the morphologies of the maps for these individual multipoles remains unaffected by residual contamination biases. To study the directional characteristics of the CMB parity, the author defined a new statistic for the rotationally variant power,

$$D_\ell = \frac{1}{2\ell} \sum_{m=-\ell}^{\ell} |a_{\ell m}|^2 (1 - \delta_{m0}), \tag{1.156}$$

such that for the Gaussian random $a_{\ell m}$'s, one notes that $\langle D_\ell \rangle = \langle \hat{C}_\ell \rangle = C_\ell^{th}$. Thus D_ℓ is also an unbiased estimator for C_ℓ^{th}. In its definition, the preferred axis is chosen to be the $z-$axis, because of the exclusion of $m = 0$ component. Similar to the previous paper [208], the definition of this statistic in a rotated coordinate system can be expressed as,

$$D_\ell(\hat{q}) = \frac{1}{2\ell} \sum_{m=-\ell}^{\ell} |a_{\ell m}(\hat{q})|^2 (1 - \delta_{m0}). \tag{1.157}$$

Another statistic for power estimation in a rotationally variant form can be written as,

$$\tilde{D}_\ell = \frac{1}{(2\ell+1)} \sum_{m=-\ell}^{\ell} m^2 |a_{\ell m}|^2, \tag{1.158}$$

which favours the higher m values, and is therefore useful in searching for planarity of these modes when $m = \pm\ell$, whereas the statistic D_ℓ contains the same weights for the modes $m \neq 0$. Further, the value of $\tilde{D}_\ell$ increases rapidly with the multipole number ℓ, due to the m^2 factor. Then this statistic in a general coordinate frame can be expressed as,

$$\tilde{D}_\ell(\hat{q}) = \frac{1}{(2\ell+1)} \sum_{m=-\ell}^{\ell} m^2 |a_{\ell m}(\hat{q})|^2. \tag{1.159}$$

Using these definitions, the six parity parameters or directional statistics are as follows.

1. The first parameter which describes parity asymmetry is

   $$g_1(\ell, \hat{q}) = \frac{\sum_{\ell'=2}^{\ell} \ell'(\ell'+1) D_{\ell'}(\hat{q}) \Gamma_{\ell'}^{+}}{\sum_{\ell'=2}^{\ell} \ell'(\ell'+1) D_{\ell'}(\hat{q}) \Gamma_{\ell'}^{-}}, \tag{1.160}$$

   since $g_1 < 1$ denotes an odd-parity preference, whereas $g_1 > 1$ denotes an even-parity preference. For any given ℓ, the sky map for this parameter can be constructed using the directions $\hat{q}$ corresponding to the various pixels of the CMB map in question.

2. The second parameter based on the correlation function estimator is,

$$g_2(\ell,\hat{q}) = \frac{\sum_{\ell'=2}^{\ell}(2\ell'+1)D_{\ell'}(\hat{q})\Gamma_{\ell'}^{+}}{\sum_{\ell'=2}^{\ell}(2\ell'+1)D_{\ell'}(\hat{q})\Gamma_{\ell'}^{-}},$$

$$\text{since, } C(\Theta=\pi,\hat{q}) = \sum_{\ell=2}^{\infty}\frac{(2\ell+1)}{4\pi}D_{\ell}(\hat{q})(\Gamma_{\ell}^{+}-\Gamma_{\ell}^{-}). \tag{1.161}$$

It measures the contribution of the even ℓ's to $C(\pi)$, relative to that of the odd ℓ's. Further, as $C(\pi) \propto g_2(\ell,\hat{q})-1$, hence $g_2 > 1$ indicates a positive correlation for the opposite directions, while $g_2 < 1$ accordingly represents an anti-correlation. Noticeably, the relative weights of the low ℓ's are higher in g_2 as compared to g_1.

3. The third parameter, similar to the one introduced in the work [19], is

$$g_3(\ell,\hat{q}) = \frac{2}{\ell_{odd}-1}\sum_{\ell'=3}^{\ell_{odd}}\frac{(\ell'-1))\ell' D_{\ell'-1}(\hat{q})}{\ell'(\ell'+1)D'_{\ell}(\hat{q})}, \tag{1.162}$$

with the summation is over odd multipoles only (and $\ell_{odd} \geq 3$). It measures mean deviation from unity, of the ratio of the even ℓ power to its subsequent odd ℓ power.

4., 5., 6. The fourth, fifth and sixth parameters are the same as the first, second and third parameters respectively, but with D_ℓ replaced with $\tilde{D}_\ell$:

$$g_4(\ell,\hat{q}) = g_1(\ell,\hat{q})|_{D_\ell\to\tilde{D}_\ell}, \quad g_5(\ell,\hat{q}) = g_2(\ell,\hat{q})|_{D_\ell\to\tilde{D}_\ell}, \quad g_6(\ell,\hat{q}) = g_3(\ell,\hat{q})|_{D_\ell\to\tilde{D}_\ell}. \tag{1.163}$$

The author applied the first three statistics to the data from SMICA, SEVEM and NILC maps of Planck, and found that for $\ell \in [3,21]$, and for the highest of odd multipoles, with directions $\hat{q}$, the $g_i < 1$ where, $i = 1,2,3$. Thus the odd-parity preference is seen to be independent of the choice of the parity parameters used. It is well understood that the $\tilde{D}_\ell$ is quite different from D_ℓ, and due to m^2 in $\tilde{D}_\ell$ the contribution from the higher $\ell \sim \ell_{max}$ takes precedence. Hence the author applied the last three statistics to $\ell < 10$ for which the parity asymmetry is most prominent. Again the author found that the $g_i(\ell,\hat{q}) < 1$ $(i = 4,5,6)$ for the three CMB maps under study, regardless of the direction $\hat{q}$. Thus the odd-parity preference is also independent of the change of the power spectrum estimator from D_ℓ to $\hat{D}_\ell$.

On generating sky maps for these statistics, the author found that the morphologies for the first three $g_i(\ell,\hat{q})$'s were very similar for $\ell > 3$, and the same was seen for the last three

$g_i(\ell,\hat{q})$. Further, the author computed the alignments of the preferred directions $\hat{q}$ with the kinematic dipole direction of the CMB, and found that the two axes are very close to each other, in all cases of the parity parameters. Further, the author noted that these directions are aligned towards the ecliptic plane. To assess if the parity asymmetry direction aligns with the axes of preference for the quadrupole and the octupole, the author used the statistic,

$$\langle|\cos\theta_{ij}|\rangle = \sum_{i,j=1,i\neq j}^{N} \frac{|\hat{r}_i\cdot\hat{r}_j|}{N(N-1)}, \tag{1.164}$$

where the number of directions being investigated is given by N, and the inner products $\hat{r}_i\cdot\hat{r}_j$ are evaluated for pairs of normalised preferred directions of the qudrupole, octupole, the kinematic dipole and those of the parity asymmetry. For assessing the significance of the alignments, the values of the statistics from actual CMB data and 10^5 simulated maps were compared. The author concluded that the parity asymmetry feature has a preferred direction which aligns closely with those of the kinematic dipole, quadrupole and the octupole, indicating that these anomalies may have a common origin.

In order to study the preference of parity asymmetry directions from masked CMB maps, the authors of [57] noted that the spherical harmonic coefficients ($\tilde{a}_{\ell m}$) can be expressed as

$$\tilde{a}_{\ell m} = \int \Delta T(\hat{n})W(\hat{n})Y_{\ell m}(\hat{n}), \quad \tilde{a}_{\ell m} = \sum_{\ell_1 m_1} a_{\ell_1 m_1} K_{\ell m \ell_1 m_1},$$

$$\begin{aligned} K_{\ell m\ell_1 m_1} &= \sqrt{\frac{(2\ell_1+1)(2\ell+1))}{4\pi}} \sum_{\ell_2 m_2} (-1)^m (2\ell_2+1) w_{\ell_2 m_2} \\ &\quad \times \begin{pmatrix} \ell_1 & \ell_2 & \ell \\ 0 & 0 & 0 \end{pmatrix} \begin{pmatrix} \ell_1 & \ell_2 & \ell \\ m_1 & m_2 & -m \end{pmatrix}. \end{aligned} \tag{1.165}$$

Here, $K_{\ell m\ell_1 m_1}$ is the coupling matrix, and $w_{\ell m} = \int W(\hat{n})Y^*_{\ell m}(\hat{n})d\hat{n}$ for the mask $W(\hat{n})$. Thus, the partial sky form of $\tilde{D}_\ell$ (1.156) and the unbiased estimator $\hat{\mathfrak{D}}_\ell$ for C_ℓ^{th} read,

$$\tilde{D}_\ell = \frac{1}{2\ell} \sum_{m=-\ell}^{\ell} \tilde{a}^*_{\ell m}\tilde{a}_{\ell m}(1-\delta_{m0}), \quad \hat{\mathfrak{D}}_\ell = \sum_{\ell'} N^{-1}_{\ell\ell'} \tilde{D}_{\ell'}, \tag{1.166}$$

where,

$$N_{\ell\ell'} = M_{\ell\ell'} - \frac{(2\ell'+1)}{2\ell} \sum_{\ell_2 \ell_2' m_1} \sqrt{\frac{(2\ell_2+1)(2\ell_2'+1)}{4\pi}} \times \begin{pmatrix} \ell' & \ell_2 & \ell \\ 0 & 0 & 0 \end{pmatrix} \begin{pmatrix} \ell' & \ell_2' & \ell \\ 0 & 0 & 0 \end{pmatrix}$$
$$\times \begin{pmatrix} \ell' & \ell_2 & \ell \\ m_1 & -m_1 & 0 \end{pmatrix} \times \begin{pmatrix} \ell' & \ell_2' & \ell \\ m_1 & -m_1 & 0 \end{pmatrix} w_{\ell_2 m_1} w_{\ell_2' m_1}, \tag{1.167}$$

$$M_{\ell\ell'} = (2\ell'+1) \sum_{\ell_2} \frac{(2\ell_2+1)}{4\pi} \begin{pmatrix} \ell' & \ell_2 & \ell \\ 0 & 0 & 0 \end{pmatrix}^2 \tilde{w}_{\ell_2}, \quad \tilde{w}_{\ell_2} = \frac{1}{(2\ell_2+1)} \sum_{m_2=-\ell_2}^{\ell_2} w^*_{\ell_2 m_2} w_{\ell_2 m_2} \tag{1.168}$$

Thus, the parity asymmetry statistic defined using Equation (1.166) is,

$$g(\ell, \hat{q}) = \frac{\sum_{\ell'=2}^{\ell} \ell'(\ell'+1) \hat{\mathfrak{D}}_{\ell'} \Gamma^+_{\ell'}}{\sum_{\ell'=2}^{\ell} \ell'(\ell'+1) \hat{\mathfrak{D}}_{\ell'} \Gamma^-_{\ell'}}. \tag{1.169}$$

When applying $g(\ell, \hat{q})$ on masked maps of the observed CMB, the authors note the several effects that are likely. For example, due to the loss of information from the masked region of a map, the unbiased estimator $\hat{\mathfrak{D}}_\ell$ and its uncertainties might be affected. Additionally the shape and positioning of the mask may influence how the directional preference manifests. However, the authors opine that these effects may be minimal if the mask itself is small. Using Planck 2015 [5] release maps of NILC, Commander, SMICA and SEVEM, the authors show that the preferred directions are very similar to those of the full-sky case, and they align closely with those of the kinematic dipole and the preferred axes of the quadrupole and octupole. Further, the authors conclude that there is negligible influence of residual contamination and masking on the lowest multipoles ($\ell_{max} \lesssim 21$) being considered.

In yet another study [20], the authors describe statistics related to the power tensor and the alignment tensor of Section 1.8.2.4. The power tensor defined by them,

$$A_{ij}(\ell) = \frac{1}{\ell(\ell+1)(2\ell+1)} \sum_{mm'm''} a_{\ell m} J^i_{mm'} J^j_{m'm''} a^*_{\ell m''}, \tag{1.170}$$

provides the notion of an ellipsoid as a map of each multipole with its different eigenvector strengths denoted by its eigenvalues. Thus, the concepts of axiality, planarity and isotropy of each multipole can be studied by assessing the ratio of the eigenvalues of this tensor, and any associated preferred eigenvector. The strength of the anisotropy or axiality of a multipole can be measured with the power entropy given as,

$$S_p = -\sum_{\alpha=1}^{3} \lambda_\alpha \ln(\lambda_\alpha), \tag{1.171}$$

where the λ_α are eigenvalues of the power tensor after normalisation by the sum of the eigenvalues. Perfect anisotropy or a single preferred direction is indicated by a value of $S_p \to 0$, whereas the case of SI is indicated by $\lambda_\alpha = 1/3$ for all α, i.e., $S_p \to \ln(3)$. If the eigenvectors are given by e^i_α (i denotes the vector components), and the principal eigenvector corresponding to the largest λ_α is $\tilde{e}^i$, then for $\ell \in [\ell_{min}, \ell_{max}]$, the alignment tensor is,

$$X_{ij}(\ell_{min}, \ell_{max}) = \sum_{\ell=\ell_{min}}^{\ell_{max}} \tilde{e}^i_\ell \tilde{e}^j_\ell, \tag{1.172}$$

where $\tilde{e}^i_\ell$ is the principal eigenvector of the power tensor for a certain ℓ. If the normalised eigenvalues and eigenvectors of $X_{ij}(\ell_{min}, \ell_{max})$ are ζ_α and f_α, respectively, then,

$$S_X = -\sum_{\alpha=1}^{3} \zeta_\alpha \ln(\zeta_\alpha), \tag{1.173}$$

is the alignment entropy. For uncorrelated principal eigenvectors over an ℓ range, the alignment tensor is $X_{ij} \sim \delta_{ij}$, and all the ζ_α become equal. Whereas, when all the principal eigenvectors are aligned along a single eigenvector for the whole ℓ range, then, except one eigenvalue, all $\zeta_\alpha \to 0$. Thus, similar to the power entropy, a completely uncorrelated case for SI is represented by $S_X \to \ln(3)$, while that of maximal correlation is represented by $S_X \to 0$. The principal eigenvector of the alignment tensor $X_{ij}(\ell_{min}, \ell_{max})$ represents the collective alignment vector for the set of multipoles under consideration, denoted by $\tilde{f}_\alpha$.

Further using the Planck 2015 CMB map cleaned with the Commander algorithm, the authors found that the collective alignment axes of the odd and even multipoles exhibit different behaviours. The odd-parity preferred anisotropy axes are not highly concentrated together, but definitely directional as indicated by low values of the alignment entropy. Whereas for the even parity multipole alignment axes, the authors note that those are well concentrated along the kinematic dipole direction. Further the alignment entropy S_X indicates uncorrelated isotropic distribution of the principal eigenvectors of even multipoles. Whereas, S_X is unusually low for odd multipoles $\lesssim 27$, beyond which the effect is insignificant. If a few of the low multipoles ($\ell \in [2, 7]$) are excluded, then the anomaly ceases to exist. When $\ell_{max} = 61$

is fixed, and ℓ_{min} is varied, the lowest $p-$ value for S_X occurs at $\ell \gtrsim 26$. Additionally, as the axes for $\ell > 27$ lie close to the Galactic plane, this indicates that residual Galactic bias could be causing the same. Moreover, the authors found that the axis for even mirror parity from Planck 2015 results [7] and the collective axes of even multipoles as computed by them for large angular scales point broadly towards the kinematic dipole. Whereas, the axes of odd mirror parity and that of the low odd multipoles associated with the hemispherical power asymmetry from Planck 2015 results lie closely within the region demarcated by odd multipole alignment axes computed by the authors. These findings illustrate a possible common origin of the various parity symmetry or asymmetry features of the CMB.

1.8.3.5 Preferred direction leading to the hemispherical power asymmetry

We have discussed about the hemispherical power asymmetry (HPA) in Section 1.8.2.1, as seen in the actual CMB, which is a prominent SI violating feature. In order to hypothesise a possible mechanism for the occurrence of features which spontaneously break isotropy in the CMB, the authors of the paper [116] suggested additive and multiplicative contributions to the temperature fluctuations. Of these, authors of the study [94] proposed the use of a dipole direction modulating the temperature fluctuations as a highly probably method to introduce the HPA. They performed both frequentist and Bayesian analyses to endorse their claims.

The model of the CMB temperature fluctuations used by the authors [94] is,

$$T_d(\hat{n}) = T_s(\hat{n})[1 + T_f(\hat{n})] + T_n(\hat{n}), \tag{1.174}$$

where the $T_s(\hat{n})$ denotes a Gaussian random SI obeying field with the power spectrum C_ℓ^{th}, the dipole modulation field is $T_f(\hat{n})$ which has a modulus less than one, and $T_n(\hat{n})$ is the instrumental noise. The $T_d(\hat{n})$ remains a Gaussian random field, with a covariance matrix,

$$\tilde{T}_s(\hat{n},\hat{m}) = [1 + T_f(\hat{n})]T_s(\hat{n},\hat{m})[1 + T_f(\hat{m})], \quad T_s(\hat{n},\hat{m}) = \frac{1}{4\pi}\sum_\ell (2\ell+1)C_\ell^{th} P_\ell(\hat{n}\cdot\hat{m}). \tag{1.175}$$

Considering both the instrumental noise and possible contamination from foregrounds, the complete covariance matrix and the log likelihood (up to an irrelevant constant) are,

$$C(\hat{n},\hat{m}) = \tilde{T}_s(\hat{n},\hat{m}) + N + F, \quad -2\log\mathcal{L} = T_d^T C^{-1} T_d + \log|C|, \tag{1.176}$$

respectively, and where N, F represent the noise and foreground covariance matrices that depend on the processing of data. Then the posterior distribution $P(\theta|d)$, where the θ are the set of all free parameters, needs to be quantified for the Bayesian approach. These parameters depend on either the isotropic or anisotropic modulation part of the CMB fluctuations. The isotropic component of the CMB is modelled as, $C_\ell^{th} = q\left(\frac{\ell}{\ell_0}\right)^n C_\ell^{fid}$. Here, the free amplitude is q and the tilt in the power spectrum is n, while the ℓ_0 is a pivot scale in ℓ space, and C_ℓ^{fid} is a fiducial model of the power chosen as per [134]. The modulation field itself is modelled in terms of a preferred direction $\hat{p}$, the amplitude A, $T_f(\hat{n}) = A(\hat{n}\cdot\hat{p})$. The authors choose $\hat{p}$ to be uniform over the $2-$sphere while using flat priors for all other parameters. The amplitude A was chosen to be ≤ 0.3, while q was taken $\in [0.5, 1.5]$, and the tilt was taken $\in [-0.5, 0.5]$. The choices, as noted by the authors, are sufficiently generous to include most of the non-zero portions within the likelihood. Thus, the posterior distribution is written as,

$$P(q,n,A,\hat{p}|T_d) \propto \mathcal{L}(q,n,A,\hat{p})P(q,n,A,\hat{p}), \tag{1.177}$$

which can be mapped out using the Markov Chain Monte Carlo (MCMC) process. The authors used a Gaussian proposal density for q, n, A, and a uniform one for $\hat{p}$. Thereafter, the mean likelihood over the prior volume, known as the Bayesian evidence,

$$E \equiv P(T_d|H) = \int P(d|\theta, H)P(\theta|H)d\theta, \tag{1.178}$$

estimates how good the model is. For two contesting models, H_0, and H_1, the difference, $\Delta\log(E) = \log(E_1) - \log(E_0)$ determines if the evidence for H_1 is substantial ($\Delta\log(E) > 1$), or strong ($\Delta\log(E) > 2.5$). Additionally, the authors computed the maximum likelihood estimate of parameters from isotropic simulated CMB maps for a frequentist analysis.

The authors analysed two versions of the WMAP 3-year release of data, namely, the template corrected frequency band maps of Q, V, W and the ILC map, at a resolution such that the pixel sizes were $\sim 3^\circ.6$, and for $\ell \lesssim 40$, since the maps were smoothed by a Gaussian beam of FWHM$= 9^\circ$. They used the WMAP $Kp2$ mask directly, and after extending it by 9° in all directions and manually removing some pixels near the galactic region if they are larger than noise in the difference maps between two channels. The former was used for the ILC map, and the latter for the other maps. The noise covariance is uniform, i.e, $N_{ij} = \sigma_n^2\delta_{ij}$.

The authors reported the best-fit dipole axis and its amplitude of modulation, in addition to the maximum likelihood difference and $\Delta \log(E)$ for both modulated and unmodulated models. The authors found that the best-fit dipole axis for modulation points towards $(l, b) = (225°, -27°)$, and its amplitude is 0.114, for the WMAP-ILC map. They assessed the probability of finding such a high modulation amplitude in the isotropic simulations, and found it to be $\sim 1\%$, with $\Delta \log(E) = 1.8$. They reported that these results are independent of the data set or the sky coverage, since the Q band map which is not very reliable given its relatively larger foreground residuals, provides a frequentist confidence of 98.7%, and $\Delta \log(E) = 1.5$. Further the authors showed that the dipole axis reported in [93], and those computed in their work, agree within 2σ, thus ensuring the stability of the findings against the method of statistical estimation, the data sets used, and the whole process of the analysis.

In a subsequent work, authors of [140] similarly analysed higher resolution maps of WMAP 5-year data, with pixel sizes $\sim 1°.8$, smoothed using a Gaussian beam of FWHM$=$ $4°.5$. The authors found that for $\ell \leq 64$ and the ILC map with a galactic cut as defined by the $KQ85$ mask, the amplitude of modulation is 0.072 ± 0.022 at $3.3.\sigma$, and the dipole axis points towards $(l, b) = (224°, -22°) \pm 24°$. All these results are consistent to within the confidence region of 1σ. Further, the Bayesian evidence difference is $\Delta \log(E) = 2.6$, which indicates a strong evidence for the anisotropic modulated feature.

A different technique [11] employs local variances of maps inside discs, since the dipolar structure manifests in a smaller resolution map of such local variances. The data used by authors of this work are the WMAP 9-year foreground-reduced and co-added maps from the V and W bands. As for Planck 2013 release, they presented results for SMICA and noted that consistent results exist for C-R, NILC, and SEVEM maps. They used the $KQ85$ mask for WMAP maps, and the $U73$ mask for Planck maps. For comparing with WMAP maps, they simulated 10^3 CMB-plus-noise maps based on the WMAP 9-year best fit to the ΛCDM power spectrum [136]. The Gaussian uncorrelated noise was ascertained by the number of observations per pixel. As for the Planck maps, they used 10^3 “Full Focal Plane” (FFP6) simulations from Planck, which include the instrument and noise characteristics besides lensing effects. On the original high resolution maps, the authors considered $n_{pix} = 3072$

discs corresponding to all pixels of an $n_{side} = 16$ map in HEALPix [117] nomenclature. Ignoring discs with more than 90% masked areas, the authors computed their variances, and assigned them to $n_{side} = 16$ maps. In order to subtract off the bias from the unmodulated part of the CMB, they computed the expected mean and variance inside each disc from an ensemble of simulations. Such a mean variance map was then subtracted from the observed real CMB maps and a simulated ensemble which was to be used for comparison. These local variance maps were then subject to the HEALPix routine "remove_dipole", with inverse variance weighting to determine the amplitude and direction of the dipole.

The authors demonstrated the usefulness of the method on simulated modulated and unmodulated data. The anisotropic simulations were generated using the amplitude 0.072 and direction $(l, b) = (224°, -22°)$ from [140]. Additionally they considered two sets of maps, one without smoothing, so that all the scales are modulated, and another with scales larger than $5°$ being modulated. They chose disc radii $\in [1°, 90°]$ and noted that for $\gtrsim 20°$, the simulated anisotropic maps tend to exhibit amplitudes overlapping with the isotropic case. This made them restrict the disc sizes to $[1°, 20°]$. This manner of ascertaining disc sizes before assessing the real data, mitigates the problem of a posteriori inference, and restriction to sensitive disc sizes alleviates the "looking elsewhere" criticism. The authors found that none of the 10^3 FFP6 simulated maps possess amplitudes of modulation larger than the SMICA map for discs $\in [6°, 12°]$ at $\approx 3.3.\sigma$. Histograms for local variances from unmodulated maps versus disc radii $\in [4°, 12°]$, with fitting of Gaussian distributions to the same, reveal that the real data carries a dipole modulation amplitude $\approx 4\sigma$ away from all such histograms. Similarly, in WMAP, the authors observed that albeit the trend of findings is similar to Planck, yet the significance could be capped up to $\sim 2.9\sigma$.

1.8.4 Local extrema or hot and cold spots

The shapes and arrangement of local maxima and minima of the temperature or polarisation anisotropy field on the $2-$sphere offer an important perspective to understand the CMB. Anisotropic distribution of local extrema could provide alternate mechanisms of relating previously known violations of isotropy. Considerable literature exists on the use of extrema statistics for non-Gaussianity detection. However, we will limit our discussion to some well known techniques of studying the hot and cold spots of the CMB to assess its isotropy.

1.8.4.1 Peak arrangement asymmetries

In the paper [169], the authors assessed one-point statistics (mean, variance, skewness, kurtosis and number) of peaks of the CMB temperature anisotropies using WMAP 1-year Q,V, and W frequency maps. The masks employed were $Kp0$, $Kp2$, $Kp12$, GN, GS, EN, and ES, with the first three from WMAP [33], while the rest extend $Kp0$ to discard the galactic (G) or ecliptic (E) northern (N) or southern (S) hemispheres, respectively. Gaussian skies at HEALPix $n_{side} = 512$ were simulated using WMAP best-fit power spectra, to which random Gaussian noise was added according to the noise characteristics of each frequency band [148]. Using the HEALPix subroutine "hotspot", the local extrema were computed on full sky maps, after which the maxima and minima inside the masked regions were discarded.

The authors found that generally the mean of WMAP temperature anisotropy extrema and the variance in a few cases, significantly differ from simulations, whereas the skewness, kurtosis, and the number of extrema statistics agree fairly well. However an ecliptic north-south asymmetry exists in the variance of the extrema. Further, none of the simulations with power law or running spectral index power spectra agree with mean extrema values, and the maxima are too cold, while the minima are too hot. The ecliptic north-south asymmetry is significantly discordant relative to simulations for all the four statistics.

In another work [24], the authors studied the WMAP 5-year maps for assessing the abundances of spots in the CMB. Their definition of a spot is as follows. The authors average over temperature fluctuations within the size of the anticipated spot, as demarcated using window functions $W(\theta, \phi)$,

$$\Delta T_{mean} = \int d\Omega \Delta T(\theta, \phi) W(\theta, \phi). \tag{1.179}$$

Thus, for a threshold $\Delta\mathbb{T}$, a hot spot should obey $\Delta T_{mean} \geq \Delta\mathbb{T}$, while a cold spot is expected for $\Delta T_{mean} \leq \Delta\mathbb{T}$. The scale for the mean temperature contrast is given as $\Delta_{rms} = \sqrt{\Delta T^2_{mean}}$. Thus, if the $\Delta\mathbb{T} \ll \Delta T_{mean}$, then the most of the regions will be characterised as spots, and vice versa. The window function could be a top hat circle or a square, and the authors demonstrated that the results are independent of the shape of $W(\theta,\phi)$, provided that the areas enclosed are the same. Such regions were identified as sectors within the intersections of rings of latitude and longitude, i.e, say, between θ_0, θ_1 and ϕ_0, ϕ_1. The equal area and equal boundary length criteria were imposed respectively, using

$$A = \int_{\mathcal{S}} d\Omega = \int_{\phi_0}^{\phi_1} d\phi \int_{\theta_0}^{\theta_1} \sin\theta d\theta, \quad (\phi_1 - \phi_0)\sin\theta_* = (\theta_1 - \theta_0), \tag{1.180}$$

where the $\theta_* = \theta_1$ on the northern hemisphere and $\theta_* = \theta_0$ in the southern hemisphere. For masked maps, the spots were selected for up to 5% masked regions within a sector. The real CMB maps analysed were the partial sky foreground-reduced WMAP Q, V and W band maps using the $KQ75$ mask, and the full sky WMAP-ILC map. The authors found that compared to the simulated maps of the ΛCDM model, there are significantly lesser number of spots in the cut-sky WMAP 5-year data. Additionally removing the quadrupole or simulating with the WMAP 5-year pseudo-C_ℓ weakens the discrepancies. Further only $0.16\% - 0.62\%$ of the simulated maps possess mean temperature fluctuations below that of the cut-sky WMAP data on angular scales of $4° - 8°$. On removing the quadrupole the significance decreases as this percentage increases to $2.5\% - 8\%$. Further, for full sky, the WMAP-ILC map agrees well with the simulations, however, outside the mask, there are very few spots, while inside the mask, the majority of the spots are present, clearly indicating the existing anisotropy.

1.8.4.2 Harmonic space characterisation of peaks

We primarily refer to the works [190, 191] for this discussion. The authors in the paper [190] shed light on expressing derivatives of a scalar field like the temperature anisotropy field on the 2-sphere, for evaluating peak positions, shapes, eccentricities and the like from second order derivatives which help determine the peaks. Spin raising and lowering operators are defined as $\eth$ and $\eth^*$, which are related to the Cartesian coordinate system of reference as $\eth \equiv -\partial_x - i\partial_y$, $\eth^* = -\partial_x + i\partial_y$. Thus the first and second derivatives of the $\Delta T(\theta,\phi) = \sum_{\ell m} a_{\ell m} Y_{\ell m}(\theta,\phi)$ are given by,

$$\eth^*(\Delta T) = \sum_{\ell=0}^{\infty} \sqrt{\frac{(2\ell+1)}{4\pi}} \sqrt{\frac{(\ell+1)!}{(\ell-1)!}} a_{\ell 1}, \quad (\eth^*)^2(\Delta T) = \sum_{\ell=0}^{\infty} \sqrt{\frac{(2\ell+1)}{4\pi}} \sqrt{\frac{(\ell+2)!}{(\ell-2)!}} a_{\ell 2},$$

$$\nabla^2(\Delta T) = \eth^* \eth(\Delta T) = \sum_{\ell=0}^{\infty} \sqrt{\frac{(2\ell+1)}{4\pi}} \frac{(\ell+1)!}{(\ell-1)!} a_{\ell 0}. \tag{1.181}$$

The quantities ΔT, $\nabla^2(\Delta T)$ are scalars, whereas, $\eth^*(\Delta T)$ is a vector and $(\eth^*)^2(\Delta T)$ is a spin-2 tensor. Under the assumption of isotropy, since these tensors of different ranks are statistically independent, the scalars ΔT and $\nabla^2(\Delta T)$ are correlated with each other, while the other two quantities $\eth^*(\Delta T)$ and $(\eth^*)^2(\Delta T)$ are uncorrelated. After normalising these four quantities by their appropriate variance weights, they can be represented in their harmonic decompositions respectively as,

$$\nu = \frac{\Delta T}{\sigma_\nu}, \quad \kappa = -\frac{\nabla^2(\Delta T)}{\sigma_\kappa}, \quad \eta = \frac{\eth^*(\Delta T)}{\sigma_\eta}, \quad \epsilon = \frac{(\eth^*)^2(\Delta T))}{\sigma_\epsilon}, \tag{1.182}$$

$$\nu = \sum_{\ell=0}^{\infty} \nu_\ell a_{\ell 0}, \quad \kappa = \sum_{\ell=0}^{\infty} \kappa_\ell a_{\ell 0}, \quad \eta = \sum_{\ell=0}^{\infty} \eta_\ell a_{\ell 1}, \quad \epsilon = \sum_{\ell=0}^{\infty} \epsilon_\ell a_{\ell 2}, \tag{1.183}$$

and in terms of their degrees of freedom they are described as follows:

1. Scalar ν denotes the height of the peak, or the value of the temperature at the extremum.

2. Scalar κ represents the local curvature in terms of the temperature field.

3. Vector η which is a complex number, encapsulates the geometric features of the peak, given as the gradient of the temperature fluctuation field. Ideally, for local extrema, the first derivative η must vanish, however the discretisation of the temperature field obviates $\eta = 0$. Nonetheless, η is considered to be very small, relative to σ_η.

4. Tensor or 2-spinor ϵ is a complex number with its modulus quantifying the eccentricity of the peak, while its phase provides the direction of the principal axes on the sky.

These peak variables, $\nu, \kappa, \eta, \epsilon$ help determine the minima and maxima. For a critical point, ideally, $\eta = 0$ and additionally for the extremum, the eigenvalues of the Hessian must be of the same sign, such that $|\epsilon| \leq \sqrt{a}|\kappa|$, and $a = \sigma_\kappa^2/\sigma_\epsilon^2$. If the $\kappa > 0$, then a maximum is found, and if $\kappa < 0$, then a minimum is found, while for $\kappa = 0$, the point is flat up to second order, but the probability of such an occurrence is null. Constraints on the extremum are provided by application of the probability of the peak degrees of freedom,

$$P(\nu, \kappa, \epsilon) d\nu d\kappa d^2\epsilon = \frac{2|\epsilon|}{2\pi\sqrt{1-\rho^2}} \exp\left(-\frac{\nu^2 - 2\rho\nu\kappa + \kappa^2}{2(1-\rho^2)} - |\epsilon|^2\right) d\nu d\kappa d|\epsilon| \frac{d\alpha}{\pi}, \tag{1.184}$$

where, the eccentricity is $\epsilon = |\epsilon|e^{2i\alpha}$. Here, ρ is the correlation quantity, and $\rho = \frac{\sigma_\eta^2}{\sigma_\nu \sigma_\kappa}$. Since ϵ itself is a Gaussian random number, $|\epsilon|$ is a Rayleigh distributed variable, and α is uniform in the range $[0,\pi]$. The expression (1.184), provides a way to compute the number density of the peaks, which in turn depends on the size of the peak, and is given as,

$$n(\nu,\kappa,\epsilon)d\nu d\kappa d^2\epsilon = \frac{1}{2\pi\theta_*^2}(a\kappa^2 - |\epsilon|^2)P(\nu,\kappa,\epsilon)d\nu d\kappa d^2\epsilon, \tag{1.185}$$

where the variable $\theta_*^2 = \frac{2\sigma_\eta^2}{\sigma_\epsilon^2}$. Upon integrating the number density $n(\nu,\kappa,\epsilon)$ over the complete space of ν and κ, while restricting the integration over ϵ to regions for which $|\epsilon| \leq \sqrt{a}\kappa$ (which guarantees the point to be an extremum), one obtains,

$$\langle N_{ext} \rangle = 2\left(1 + \frac{1}{\theta_*^2\sqrt{3+2\theta_*^2}}\right), \tag{1.186}$$

which is the expectation value of the total number of extrema. Using these, the authors produced curves of $\langle N_{ext} \rangle$ as a function of the peak size, and demonstrated that the flat approximation is violated for peaks having sizes $> 30^\circ$. They noted that since such peaks will be few, stacking of peaks may not be plausible to minimise cosmic variance. However, such large peaks are nonetheless useful for understanding properties of the large scale CMB.

The authors noted that expectation values of peak shapes depend on factors constraining the peak variables. For example, using thresholds for ν may induce bias in $\langle \nu \rangle$, making it non-zero. Similarly, the notion that $\langle \epsilon \rangle$ may possess a bias, with a ϕ dependence in the pattern of peaks on the sphere, must be accounted for. This was addressed by introducing "multipolar profiles". Since a field $X(\theta,\phi)$ can be represented in the basis of ϕ as

$$X(\theta,\phi) = \sum_{m=-\infty}^{\infty} X_m(\theta)e^{im\phi}, \tag{1.187}$$

the profile for $X(\theta,\phi)$ is $X_m(\theta)$. Such profiles contribute to a peak with different rotational symmetries. For a real field X, $X_m^*(\theta) = X_{-m}(\theta)$. Since peaks are determined using second order derivatives, the authors noted that profiles with spin $m > 2$ must equal zero. Additionally, the dipole profile ($m = 1$) is zero as the first order derivatives must also vanish. Thus, only the scalar ($m = 0$) and quadrupolar ($m = 2$) modes characterise these profiles.

For a qualitative study of peaks, the authors considered fixing ν to a given value, and analysed the pattern produced by such a peak. Both the temperature and polarisation fields can be studied with this formalism, and the monopolar profiles for these are

$$
\begin{aligned}
\langle \Delta T_0(\theta) \rangle &= \sum_{\ell=0}^{\infty} [b_\nu + b_\kappa \ell(\ell+1)] C_\ell^{TT} P_\ell(\cos\theta), \\
\langle Q_r 0(\theta) \rangle &= -\sum_{\ell=2}^{\infty} \frac{(2\ell+1)}{4\pi} \sqrt{\frac{(\ell-2)!}{(\ell+2)!}} [b_\nu + b_\kappa \ell(\ell+1)] C_\ell^{TE} P_\ell^2(\cos\theta), \\
\langle U_{r0}(\theta) \rangle &= \sum_{\ell=2}^{\infty} \frac{(2\ell+1)}{4\pi} \sqrt{\frac{(\ell-2)!}{(\ell+2)!}} [b_\nu + b_\kappa \ell(\ell+1)] C_\ell^{TB} P_\ell^2(\cos\theta).
\end{aligned}
\tag{1.188}
$$

Here, Q_r, U_r are the Stokes parameters in polar coordinates, with the origin placed at the centre of the extremum. The subscript r denotes that these Stokes parameters are rotated forms of the standard ones. The bias parameters b_ν, b_κ are evaluated from

$$
\begin{pmatrix} b_\nu \sigma_\nu \\ b_\kappa \sigma_\kappa \end{pmatrix} = \Sigma^{-1} \begin{pmatrix} \langle \nu \rangle \\ \langle \kappa \rangle \end{pmatrix},
\tag{1.189}
$$

where, the covariance matrix between κ and ν is Σ. Thus, for $\langle \epsilon \rangle \neq 0$, or that the peaks are oriented towards a particular direction, breaking isotropy, we have non-zero measures

$$
\begin{aligned}
\langle \Delta T_2(\theta) \rangle &= b_\epsilon \sum_{\ell=0}^{\infty} \frac{(2\ell+1)}{4\pi} C_\ell^{TT} P_\ell^2(\cos\theta), \\
\langle Q_{r2}(\theta) \rangle &= -2 b_\epsilon \sum_{\ell=0}^{\infty} \frac{(2\ell+1)}{4\pi} \sqrt{\frac{(\ell-2)!}{(\ell+2)!}} [C_\ell^{TE} P_\ell^+(\cos\theta) + i C_\ell^{TB} P_\ell(\cos\theta)], \\
\langle U_{r2}(\theta) \rangle &= 2 i b_\epsilon \sum_{\ell=0}^{\infty} \frac{(2\ell+1)}{4\pi} \sqrt{\frac{(\ell-2)!}{(\ell+2)!}} [C_\ell^{TE} P_\ell^-(\theta) + i C_\ell^{TB} P_\ell^+(\cos\theta)],
\end{aligned}
\tag{1.190}
$$

which represent the quadrupolar profiles. The bias parameter $b_\epsilon = \frac{\langle \epsilon \rangle}{\sigma_\epsilon}$, and,

$$
\begin{aligned}
P_\ell^+ &= -\left[\frac{(\ell-4)}{(1-x^2)} + \frac{1}{2}\ell(\ell-1) \right] P_\ell^2(x) + (\ell+2) \frac{x}{1-x^2} P_{\ell-1}^2(x), \\
P_\ell^-(x) &= -2 \left[(\ell-1) \frac{x}{1-x^2} P_\ell^2(x) - (\ell+2) \frac{1}{1-x^2} P_{\ell-1}^2(x) \right].
\end{aligned}
\tag{1.191}
$$

The authors in their formalism mentioned that these quadrupolar profiles being complex quantities possess phase angles which represent rotations of the system of reference, such that b_ϵ is real when the principal axes coincide with the xy axes. In case of polarisation, when the peak itself has non-zero eccentricity, the gradient and curl contributions will be mixed as the peak is elongated. Further a reduction of noise can be undertaken for better estimation of the orientation axes, by selecting principal axes in the inverse Laplacian of the temperature as done in [7].

Studies of peaks are intrinsically related to those of non-Gaussianity, such as the early work of [277], wherein a non-Gaussian Cold spot (NGCS) was discovered in the southern hemisphere of the CMB. The authors of this paper applied a technique using the spherical Mexican hat wavelet (SMHW) on WMAP 1-year combined Q-V-W map. They computed the skewness and kurtosis of the SMHW coefficients at various angular scales ranging from arcminutes to degrees. The NGCS was detected as a peak around an SMHW scale of 4°, with a size of $\approx 10^\circ$ on the sky, and a one-sided p-value of 0.1%. Additionally the authors found that the northern hemisphere obeys Gaussianity while the southern hemisphere does not. They found that their results were fairly independent of systematics and residual galactic foregrounds. The detection of the NGCS and other large scale peaks paved the way for the further scrutiny of their isotropy as is discussed in the following paragraphs.

In another work [191], the authors analysed temperature maps of the Planck 2015 data, in order to characterise large scale peaks based on the formalism of the paper [190] as discussed in this Section. They focused on five known large-scale peaks [192], which include two maxima, and two minima obtained by Gaussian filtering at angular scales (R) of 10°, and the fifth one is the NGCS, numbered $1, 2, 3, 4, 5$, respectively. For comparisons with simulated data, the fiducial model considered by them was determined using the Planck 2015 TT-low P best fit cosmological parameters. With a CMB map showing these five peaks, the authors noted that ellipses for the first four extrema ($R = 10^\circ$) are narrower than that for the NGCS ($R = 5^\circ$), since the correlation between κ and ν are dependent on the scale of peak selection, whereas for the eccentricity tensor, its one-point distribution does not depend on the scale R, and hence the contours of probability for all the peaks are the same.

The authors study the multipolar profiles for these five large scale peaks to assess their shapes. The profiles themselves can be expressed as an inverse of Equation (1.187),

$$\Delta T_m(\theta, \phi) = \frac{1}{2\pi} \int d\phi \Delta T(\theta, \phi) e^{-im\phi}, \tag{1.192}$$

where the θ, ϕ are radial and azimuthal coordinates centred at the location of the peak. With a conditioning of $\nu, \kappa, \eta, \epsilon$ with fixed values at the centre, the mean profiles are

$$\begin{aligned}
\langle \Delta T_0(\theta) \rangle &= \sum_{\ell=0}^{\infty} \frac{(2\ell+1)}{4\pi} [b_\nu + b_\kappa \ell(\ell+1)] b_\ell w_\ell C_\ell P_\ell(\cos\theta), \\
\langle \Delta T_1(\theta) \rangle &= b_\eta \sum_{\ell=0}^{\infty} \frac{(2\ell+1)}{4\pi} b_\ell w_\ell C_\ell P_\ell^1(\cos\theta), \\
\langle \Delta T_2(\theta) \rangle &= b_\epsilon \sum_{\ell=0}^{\infty} \frac{(2\ell+1)}{4\pi} b_\ell w_\ell C_\ell P_\ell^2(\cos\theta),
\end{aligned} \tag{1.193}$$

and $\langle \Delta T_m(\theta) \rangle = 0$ for $m \neq 0,1,2$. Here, the temperature field is assumed to have been filtered with a window function w_ℓ, and the profiles are computed from the field observed with a beam b_ℓ. The bias parameters $(b_\nu, b_\kappa, b_\eta, b_\epsilon)$ are determined with the derivatives at the centre. The authors compared the monopolar, dipolar, and quadrupolar profiles from the peaks in observed maps with those of simulated ones. To minimise adverse effects of galactic foregrounds, and isotropy violations due to masking, on profiles with $m > 0$, they used the inpainted Planck Commander map. The multipolar profiles were computed using Equation (1.192), while averaging the pixels within rings of width 1°, centred at various values of θ. They found that deviations for profiles ($m = 0,1,2$) of any of the peaks considered was well within 2σ. Additionally, the multipolar profiles of $m \leq 10$ were found to agree with ΛCDM at the 3σ level. As for the NGCS, the authors found that a conditioning of both ν and κ ensure an agreement of the monopolar profile with the standard model. However, if ν is fixed to the observed value, while κ is averaged over, then, the NGCS represents a profile which deviates by 4.7σ for angular scale $\theta < 10^\circ$, which makes it certain that the large discrepancy of the NGCS is caused primarily due to the large value of curvature κ at its centre.

Further, for an anisotropic random field, the CMB temperature $a_{\ell m}$'s may have phases which are non-uniformly distributed between 0 and 2π. The authors analysed these phases of the multipolar expansion centred at varying peak locations, using multipolar profiles $\Delta T_m(\theta)$ which elucidate how individual multipolar patterns contribute to the shape of the peak. For a certain m, the phases for $T_m(\theta)$ will not be independent due to correlations intrinsic to the field, which cause alignments of the multipoles. For comparing these correlations with theoretical predictions, a binning scheme is employed wherein the profiles are defined for independent bins in θ. So for n bins in the angle θ_i, the profiles computed are

$$\Delta\hat{T}_m(\theta_i) = \sum_{j=1}^{i} \lambda_{ij}^m [\Delta T_m(\theta_j) - \langle \Delta T_m(\theta_j)\rangle], \tag{1.194}$$

where the coefficients λ_{ij}^m are chosen in order to impose unit variance for $\Delta\hat{T}(\theta_i)$ and zero correlations between different i's. The mean field $\langle \Delta T_m(\theta_j)\rangle$ subtraction ensures that the peak degrees of freedom are removed from the phase analysis. Since $\Delta\hat{T}_m(\theta_i)$ has phases which are independent, they manifest in a Rayleigh random walk inside the complex plane defined for each m value. For the N^{th} time step, the random walk position is

$$\mathfrak{z}_N^m = \sum_{i=1}^{N} \frac{\Delta\hat{T}_m(\theta_i)}{|\Delta\hat{T}_m(\theta_i)|}. \tag{1.195}$$

If r be the distance between the origin and the random walk position at N^{th} step, then the probability density of the same and a precise formula for r are,

$$P_N(r) = \frac{2r}{N}\exp -\frac{r^2}{N}, \quad r_N^m = \sqrt{\left(1-\frac{1}{2N}\right)|\mathfrak{z}_N^m|^2 + \frac{|\mathfrak{z}_N^m|^4}{4N^2}}. \tag{1.196}$$

Thus, for correlated phases of $\Delta\hat{T}_m(\theta_i)$, the distances from random walks will be larger than those expected from Equation (1.196). The authors found using this approach that some correlation for the phases of $m = 8$ exists in peaks 2 and 4, whereas for peak number 3, and the NGCS, $m = 4, 5$ are most correlated. For the NGCS, maximum correlation is achieved at an angular scale of $15°$ corresponding to the hot ring which surrounds the NGCS.

1.8.4.3 Tensor Minkowski functionals

The authors of [59] introduced tensor Minkowski functionals (TMFs) for random fields on a 2-sphere, e.g., galactic foreground maps to assess their isotropy and Gaussianity. Further, in [107] the first application of TMFs was done to CMB temperature and polarisation maps to ascertain the net orientation of a set of structures, and their intrinsic anisotropies.

In the work [107], the authors explained that an excursion set K, having a smooth boundary ∂K can be simply connected (without a hole) or multiply connected (containing one or more holes). A hotspot is a connected region, whereas a coldspot is a hole, either of which is a structure. By convention, a hole is enclosed in the clockwise detection, whereas the contour for a hotspot is anticlockwise. The scalar Minkowski functionals (SMFs) are,

$$W_0(K) = \int_K d^2r, \quad W_i(K) = \frac{1}{2}\int_{\partial K} G_i dr, \tag{1.197}$$

where, i stands for $1,2$, such $G_1 = 1$, and $G_2 = \kappa$, which is the local curvature associated with each point in ∂K. Thus, W_0 and W_1 define the area and the boundary length for the connected region of K, while W_2 is the difference between the number of connected regions and the number of holes in K. For a single structure in $K_s \subset K$, the TMFs of rank $a+b \geq 0$ are constructed as a tensor product of a copies of the radial vector of position $\vec{r}$, and b copies of the unit normal $\hat{n}$ at each point on the contour ∂K,

$$W_0^{a,0}(K_s) = \int_{K_s} \vec{r}^a d^2r, \quad W_i^{a,b}(K_s) = \frac{1}{2}\int_{\partial K_s} \vec{r}^a \otimes \hat{n}^b G_i dr. \tag{1.198}$$

A tensor product can be written as $(\vec{A}\otimes\vec{B})_{ij} = \frac{(A_iB_j + A_jB_i)}{2}$. When $a+b=0$, then the Equation (1.198) gives three SMFs, whereas for $a=1, b=0$, one obtains three vectorial Minkowski functionals, and when $a+b=2$, one obtains the seven TMFs of rank 2. Being tensors, the TMFs vary under a coordinate transformation. Further, the quantities $W_1^{1,1}, W_1^{0,2} W_2^{1,1}, W_2^{0,2}$ are translation invariant. The authors specifically chose to study $W_2^{1,1}$, as the others are interrelated. The expression for $W_2^{1,1}$ in pixelised space is,

$$W_2^{1,1}(K_s) = \sum_{(i,j)} \frac{1}{2}|e_{ij}|^{-1}(e_{ij}\otimes e_{ij}), \tag{1.199}$$

such that the pair (i,j) is the edge of the polygon between the vertices i and j. The vector along the edge is $\vec{e}_{ij}$ with length $|e_{ij}|$. The tensor $W_2^{1,1}$ is a matrix of size 2×2, with two real eigenvalues λ_1 and λ_2, as $\lambda_1 \leq \lambda_2$. An average over all possible structures in a single map $\langle ... \rangle_s$, gives $\Lambda_1 \leq \Lambda_2$ as eigenvalues of the matrix $\langle W_2^{1,1}\rangle_s$, and the statistics

$$\alpha = \frac{\Lambda_1}{\Lambda_2}, \quad \beta = \left\langle \frac{\lambda_1}{\lambda_2} \right\rangle_s. \tag{1.200}$$

Generally the value of β is between 0 (anisotropy) and 1 (isotropy) for the shapes of the structures. Additionally, the orientation parameter $\alpha = 1$ for no preferred direction, otherwise $\beta \leq \alpha \leq 1$. For a single structure, or a set of structures which are arranged in some fixed pattern having an anisotropic shape, $\alpha = \beta$. The degree of alignment of the structures is,

$$\mathfrak{D} = \frac{1-\alpha}{1-\beta}. \tag{1.201}$$

For perfectly aligned structures, $\mathfrak{D}$ is 1, while that for zero net orientation, $\mathfrak{D} = 0$.

The α^T for CMB temperature (denoted by superscript ^{T}) simulations about threshold $\nu = 0$ appears symmetric, but for large $|\nu|$, there is a decrease in α^T, since the alignment in structures strengthens for fewer structures at higher $|\nu|$. As for β^T, the authors noted that the structures on an average exhibit an intrinsic anisotropy, and the mean value of β^T over various threshold values is ≈ 0.68. In case of the E mode field, denoted with superscript ^{E}, the mean β^E over thresholds is ≈ 0.69. Further, the curved portion of a generic contour can be approximated by a part of an ellipse using which they could subtract off the numerical error in $\beta^T = 0.68, \beta^E = 0.69$ for the case of elliptic polygons. The corrected values stand at $\beta^T = 0.62, \beta^E = 0.63$. Moreover, as the values of α^T, α^E are both close to 1, the authors noted that there is no need to correct for the numerical error in α.

The authors found for the Planck 2015 Commander, NILC, SMICA, and SEVEM temperature and E mode field maps, that the values of β are roughly $= 0.68$, and after application of the numerical error correction, they obtained $\beta = 0.62$. Both kinds of fields (T, E) from observed foreground-cleaned maps, possess structures that obey the ΛCDM model to within 2σ, except the NILC half mission 2 map which deviates by 2.1σ. As regards α, the temperature maps agree with those of the simulated ensemble. But for the E-mode field, the authors found 3σ deviations for all the datasets, apart from the SMICA full mission map. Besides, for all the methods of foreground cleaning, the half mission 1 maps have a significant alignment of the structure at 5σ level. The authors attributed statistical uncertainties of about 0.4% for β, and 0.7% for α, apart from pixelisation errors. They also confirmed that these deviations are not flukes arising due to the choice of stereographic projection, by considering other choices of projection planes, and finding similar results. However, there could be the effect of instrumental systematics and shape of beam detection devices, and noise in inducing spurious anisotropies. This is most likely in the case of E mode results, since the signal-to-noise ratio for the 44 GHz channel which is used for modelling the beam and noise characteristics, is well below unity.

1.9 Prelude to the subsequent chapters

In the previous Section 1.8, we discussed some existing state-of-the-art techniques which have been employed by several researchers to scrutinise the isotropy of the CMB. These methods are formalised mathematically in multipole or harmonic space of the CMB power spectrum, angular and pixel space for correlations, eigenspace of tensors like the power tensor or the tensor Minkowski functional, or with perspectives of determining preferred directions, through geometric and parity asymmetries, or by understanding the shape and distribution of local extrema in real and harmonic space, to name a few.

Thus, existing literature lends us considerable motivation to develop and assess new methods for studying the isotropy of the CMB. Additionally any statistical tools and techniques employed for studies of isotropy of the CMB must be robust against the presence of any remnants of foregrounds or other sytematics at different frequencies in the CMB maps, even after they have been minimised using sophisticated algorithms. In the subsequent chapters, we present three novel and robust approaches which we have explored in this thesis, brief descriptions of which are as follows.

1. Large angle correlation deficit [32, 67] and parity preference in power [159] of the CMB are known to us. We further explore a parity based study of correlations of the CMB angular power spectrum using the concept of level spacings.

2. Hot and cold spots in the CMB arose simultaneously with matter density perturbations, which were "seeds" of structure we see today. It is interesting to study the strength and shape of any deviation from isotropy of placement of these spots in the CMB.

3. Hemispherical power asymmetry [92] could have arisen due to dipolar modulation [116, 94, 260]. Intriguingly, we are able to train a machine to artificially develop intelligence for detecting such a dipolar modulation signal in actual CMB data.

CHAPTER 2

LEVEL CORRELATIONS OF THE CMB TEMPERATURE ANGULAR POWER SPECTRUM

2.1 Introduction

Large scale fluctuations in the CMB temperature potentially encode information about inflation [56], and hence any signatures that might have arisen primordially. These fluctuations are expected to be statistically isotropic since the power spectrum of the quantum perturbations is hypothesised to be rotationally invariant. This directly implies that the angular power spectrum (APS) measures are uncorrelated between different multipoles. A violation of the assumption of statistically isotropic CMB temperature field then manifests in the form of correlations in the APS measures [54, 237].

In this work, we propose a novel method, that has not been explored in existing literature, to study correlations among the temperature fluctuations of the CMB. The method investigates the spacings between the CMB APS measures, namely $\hat{C}_\ell$'s and $\mathcal{D}_\ell$'s ($= \frac{\ell(\ell+1)}{2\pi}\hat{C}_\ell$'s) [1]. Hereafter, we will drop the hat ($\hat{}$) from $\hat{C}_\ell$'s for simplicity, and denote $\langle \hat{C}_\ell \rangle = C_\ell^{th}$ or C_ℓ^{fid} as the ensemble average of the same. The principal objective of the work discussed in this chapter is to detect any signature of correlations in the angular power spectra of the foreground minimized CMB maps following the methodology of hypothesis testing. The null hypothesis corresponds to the assertion that the CMB angular power spectrum from the foreground cleaned CMB maps are uncorrelated. This is an important scientific question to ask since if the null hypothesis can be invalidated it may warrant new physics if the correlations are generated due to any small level of a primordial signal. If the correlations

[1] Here, apostrophes (') are used to denote plural forms.

are induced by the residual foregrounds or any other systematic effects present in the cleaned maps, then special care must be adopted in using these cleaned maps in cosmological parameter estimation for accurate interpretations of these variables. Some unknown systematics may creep in during the analysis pipeline of satellite data collection and/or during the map making process. These discussions illustrate the fundamental importance of the research work carried out in this work.

To motivate more into the focus of the current research work in the context of studies of CMB anisotropies we note that, in existing literature, the deficit of large angle correlation was seen for COBE-DMR four year maps [132] and subsequently for the WMAP first year data [32]. Thereafter, almost negligible correlation was seen above $60°$ for later WMAP and Planck releases [66, 65, 68], with increasing statistical significance. Hence it was argued to be a truly anomalous feature instead of being causative of a specific a posteriori choice of statistic [66]. In addition, this anomaly has recently been shown to exist in the latest Planck polarisation data [60]. Besides, parity asymmetry in the APS was found [156, 157] and it was shown that the anomaly disappears without the contribution from first six low multipoles ($\ell = 2, ..., 7$) [19]. Later [158] also showed that the parity asymmetry in the APS is phenomenologically equivalent to deficit of large angle correlation.

Thus, in literature, there are independent studies of (a) the deficit of large angle correlation and (b) its equivalence with odd-parity preference of the APS. However, there exist no investigations in the literature regarding whether there are any unusual correlations in either even or odd or both parities of multipoles of APS when their APS estimators (C_ℓ's and related $\mathcal{D}_\ell$'s) are separately considered instead of the two point angular correlation function. Further, the authors of [65] have noted that any covariance between C_ℓ's must be studied in addition to the two point angular correlation function. Besides, understanding correlations among the APS is important as these are directly used for cosmological parameter estimation. The nature of correlations among separate sets of odd multipole and even multipole APS as well as the complete set, can be captured by their respective average spacing estimators (Section 2.4) that we have devised as a novel statistic for our study.

Several studies can be found in existing literature that claim signatures of statistical anisotropy in the foreground cleaned CMB maps [77, 232, 247, 251, 246, 167, 301]. Besides, theoretically anisotropic models over large scales have been proposed to account for some of such observed statistically anisotropic signatures [4, 188, 258, 53, 177, 83]. In the past, analysis of CMB data unveiled many anomalies in the foreground minimized maps of WMAP [67] and Planck [253] satellite missions. This has entailed the study of anomalies in both WMAP and Planck maps to make departures more discernible if any such exist. Such anomalies include the north-south power asymmetry [37], which is relatively insignificant for all scales from Planck [229], high degree of octupole-quadrupole alignment [271, 78, 252] that strengthens on removing the frequency dependent kinetic Doppler quadrupole [211], quadrupole power deficit [32, 111] and planarity of the octupole [77], the power excess for lower odd multipoles [166], the non-Gaussian cold spot [277, 70, 72], unusually weak non-uniformity in the placement of CMB hot and cold spots [154], and the like.

Foreground cleaned CMB maps are obtained upon application of elaborate cleaning methods [6, 100, 50, 80, 31, 269, 49, 162, 242, 265, 294, 227] such as those of Gibbs sampling [95], Spectral Matching Independent Component Analysis [79], Internal linear combination (ILC) in needlet space [28], and ILC in pixel space [33] to the foreground contaminated maps of CMB radiation observed at different frequencies. In the case of foreground cleaned CMB maps, a breakdown of statistical isotropy may be caused due to primordial features which are unaccounted for in the concordance (ΛCDM) model of cosmology, or due to unaccounted agents between the surface of last scattering and the observer, or any possible residual foregrounds left over after cleaning, or due to some minor systematics that may have crept in during the analysis pipeline of satellite data collection and/or the map making procedure.

Our study here focuses on an effort to discover unusual signatures of correlations between consecutive multipole APS as manifested by their spacings. This chapter is organised as follows. In Section 2.2, we discuss about the statistics of Poisson and Wigner-Dyson in context of level spacings, and describe the basic variables, i.e, the APS spacings, used for our study. In Section 2.3 we elucidate level clustering and repulsion for CMB APS. Section 3.2 specifies the average spacing estimator as the novel statistic devised for our study of foreground cleaned CMB maps. Section 2.5 describes our way of testing consecutive multipole spacings with simulations. We report our primary results in Section 2.6 for all multipole and even/odd multipole spacings using the average spacing estimator. In Section 2.7 we establish the robustness of our findings with inpainted maps. And, in Section 2.8 we summarise these results and state our inferences.

2.2 Statistics and basic variables

In this section we review the relevant statistical distributions and the basic variables of our work. The analogue of 'level spacings' in the form of absolute differences of the consecutive multipole APS measures are given by,

$$\begin{aligned} \Delta C_\ell &= |C_{\ell_1} - C_{\ell_2}|, \\ \Delta \mathcal{D}_\ell &= \left| \frac{\ell_1(\ell_1+1)}{2\pi} C_{\ell_1} - \frac{\ell_2(\ell_2+1)}{2\pi} C_{\ell_2} \right|, \end{aligned} \tag{2.202}$$

where, ℓ_1, ℓ_2 are consecutive multipoles. Assuming statistical isotropy, C_ℓ's represent the unbiased APS estimators defined as [133],

$$C_\ell = \frac{1}{2\ell+1} \sum_{m=-\ell}^{\ell} |a_{\ell m}|^2, \tag{2.203}$$

and, the $a_{\ell m}$'s are coefficients of the expansion,

$$\Delta T(\hat{n}) = \sum_\ell \sum_{m=-\ell}^{\ell} a_{\ell m} Y_{\ell m}(\hat{n}). \tag{2.204}$$

$\Delta T(\hat{n})$'s are the temperature anisotropies relative to the uniform mean temperature of nearly $2.726K$ [103] of the CMB. Here $\hat{n}$ denotes a direction in the sky. The APS measures used in this work are of low multipoles ($\ell \in [2, 31]$) corresponding to large angular scales. For reference, we show the two natural APS measures, C_ℓ's and $\mathcal{D}_\ell$'s in Figure 2.1. As $\mathcal{D}_\ell$ fluctuates about a nearly constant curve over large scales, it is interesting to study spacings of the same in addition to C_ℓ's.

Since C_ℓ's arise from independent and uncorrelated Gaussian random $a_{\ell m}$'s (2.203), they should be uncorrelated. As $\mathcal{D}_\ell$'s differ from C_ℓ's only by a multiplicative factor of $\frac{\ell(\ell+1)}{2\pi}$, they are expected to be uncorrelated as well. Therefore, low spacings (level clustering) for the C_ℓ's and $\mathcal{D}_\ell$'s may be favoured because of Poisson statistics [38], which holds for

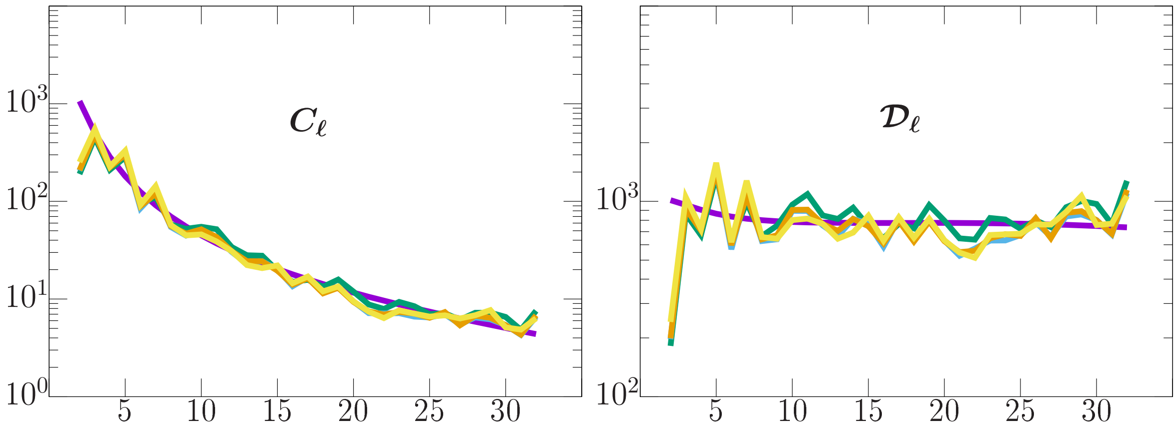

Figure 2.1: C_ℓ and $\mathcal{D}_\ell$ versus ℓ: the subfigures compare the theoretical APS best fit to Planck 2018 data (purple) with estimated APS from COMM (green), NILC (light blue), SMICA (ochre) and WMAP (yellow) maps used here. The monopole and dipole have been excluded in this figure. The vertical axis is in log-scale.

i.i.d. variables. However, there will be some deviations from purely Poisson nature for spacings of statistically isotropic realisations of the CMB having uncorrelated APS, since they are constrained by cosmic variance, and are not identically distributed [2]. If the observed C_ℓ's were specially correlated, the Wigner-Dyson statistics [42] which favour level repulsion could effectively describe these spacings, and preclude the possibility of consecutive C_ℓ's and $\mathcal{D}_\ell$'s being arbitrarily close.

It is known that Poisson statistics (describing a possibly integrable underlying system) and Wigner-Dyson statistics (describing those with classically chaotic or non-integrable counterparts) can be represented as in equation (2.205) for a spacing s between two consecutive eigenvalues of the associated random matrix, with a probability distribution $p(s)$ [196].

$$
\begin{aligned}
p(s) &\propto e^{-s} \quad \text{(Poisson statistics)},\\
p(s) &\propto s^{\alpha} e^{-b_\alpha s^2} \quad \text{(Wigner-Dyson statistics)},
\end{aligned}
\tag{2.205}
$$

(where, $\alpha > 0$). There can be a large class of random matrices, which may have i.i.d entries extracted from distributions other than those of the standard Gaussian ensembles. It has been seen for such matrices [126, 89] as well that their eigenvalue spacings obey some appropriate Wigner-Dyson form in the presence of correlations. This is the concept of universality [120],

[2] Each C_ℓ is a χ^2 variable but with $2\ell+1$ degrees of freedom. Thus the closest to nearly identical distributions for any two C_ℓ's can be considered by taking spacings of consecutive multipoles, as done here. This minimizes the difference between the distributions of the two C_ℓ's in a spacing to that of $(2(\ell+1)+1)-(2\ell+1)=2$ degrees of freedom.

which we seek to explore in the context of the APS measures.

Due to the parity inversion property of spherical harmonics [3], the temperature anisotropy field can be reconstructed as a sum of a symmetric and an anti-symmetric function [159]. These functions are of even and odd parity, respectively and the power for a multipole range can be rewritten as a sum of contributions from the even and odd multipole APS. Hence, we study nearest neighbour spacings of separate sets of even and odd multipole APS measures in addition to an analysis of APS spacings without a parity distinction. This may help us find if any parity preference of spacings exist, which can indicate deviations from the assumed isotropy of the universe on large scales.

2.3 Level clustering and level repulsion in CMB APS

In this section, we discuss how the transition between level clustering (Poisson statistics) and level repulsion (Wigner-Dyson statistics) for the CMB angular power spectrum (APS) may occur, due to introduction of correlations in otherwise uncorrelated CMB APS of statistically isotropic CMB maps. We demonstrate how the respective phenomena of level clustering and level repulsion are also applicable in the context of CMB APS. Level clustering occurs when the APS is uncorrelated between multipoles for statistically isotropic CMB. Whereas level repulsion takes place when the APS gets correlated on introduction of statistical anisotropy.

To illustrate clustering and repulsion between 'levels' of the CMB APS at different multipoles, we utilised some typical foregrounds to introduce correlations in otherwise statistically isotropic CMB maps. However, we must note that there can be several mechanisms by which correlations may be introduced in the CMB APS, such as a small statistically anisotropic primordial signal, any minor residual foregrounds, or other systematics left over due to the analysis pipeline followed in satellite data collection and/or the algorithms used for preparing foreground cleaned CMB maps. Thus, introduction of statistical anisotropy in the CMB APS by addition of foreground contamination is only one of various possible mechanisms, and has been chosen solely as a representative example for demonstrating level clustering in correlated CMB APS. This helps benchmark our methodology and also provides important

[3] Under a parity transform, i.e., $\hat{n} \to -\hat{n}, Y_{\ell m}(\hat{n}) \to Y_{\ell m}(-\hat{n}) = (-1)^{\ell} Y_{\ell m}(\hat{n}) \implies a_{\ell m} \to (-1)^{\ell} a_{\ell m}$

insights regarding the classification of possible nature of correlations that are detected on the foreground cleaned CMB maps.

Statistically isotropic (SI) CMB maps can be generated as Gaussian random realisations based on the concordance (ΛCDM) model. Foregrounds introduce statistical anisotropy in the SI CMB realisations. Thus, an addition of foregrounds to SI CMB maps is expected to enhance correlations between C_ℓ's that may cause the level spacing distributions to obey an appropriate deviation from level clustering. To quantify such a departure, the gap ratio introduced by [212], is:

$$r_\ell = \frac{\min(\Delta_\ell, \Delta_{\ell-1})}{\max(\Delta_\ell, \Delta_{\ell-1})}. \tag{2.206}$$

Here, Δ_ℓ can be either of ΔC_ℓ or ΔD_ℓ. The ensemble average of this ratio has standard values for various distributions. For Poisson, $\langle r \rangle \simeq 0.38$, for GOE (Gaussian Orthogonal Ensemble), $\langle r \rangle \simeq 0.5295$. Further, [23] calculated the same for GUE (Gaussian Unitary Ensemble) and GSE (Gaussian Symplectic Ensemble), as $\langle r \rangle \simeq 0.60266,\ 0.67617$, respectively. The advantage of using the mean gap ratio is that we need not concern ourselves with unfolding, to remove effects of local densities of the variables being investigated for their spacing distribution. Besides, the mean gap ratios may help us assign the appropriate distributions to these spacings, and give a measure of the how chaotic the underlying system is.

As our APS measures C_ℓ's and D_ℓ's are not i.i.d., we may expect slightly deviated forms from the Poisson and Wigner-Dyson behaviours given by their gap ratios of consecutive spacings. We have generated 10^4 realisations of SI CMB maps based on the theoretical APS best fitted to Planck 2018 data [9]. To these, three typical foregrounds (synchrotron, thermal dust and free-free emission maps obtained by the Commander cleaning algorithm of the Planck Legacy archive [98]) were added after being extrapolated at $100\,\mathrm{GHz}$, to obtain 10^4 statistically anisotropic (SA) CMB maps.

From these realisations, we find that $\langle r \rangle = 0.41702294,\ 0.67770755$, respectively for SI and SA CMB C_ℓ's. For spacings of C_ℓ's, we can say that roughly Poisson statistics is followed by SI CMB ΔC_ℓ's, whereas for SA CMB, the GSE form of Wigner-Dyson statistics may be appropriate. It is well known that the GSE form is obeyed by underlying systems that do not have rotational symmetry, and the value of the mean gap ratio found for ΔC_ℓ's may

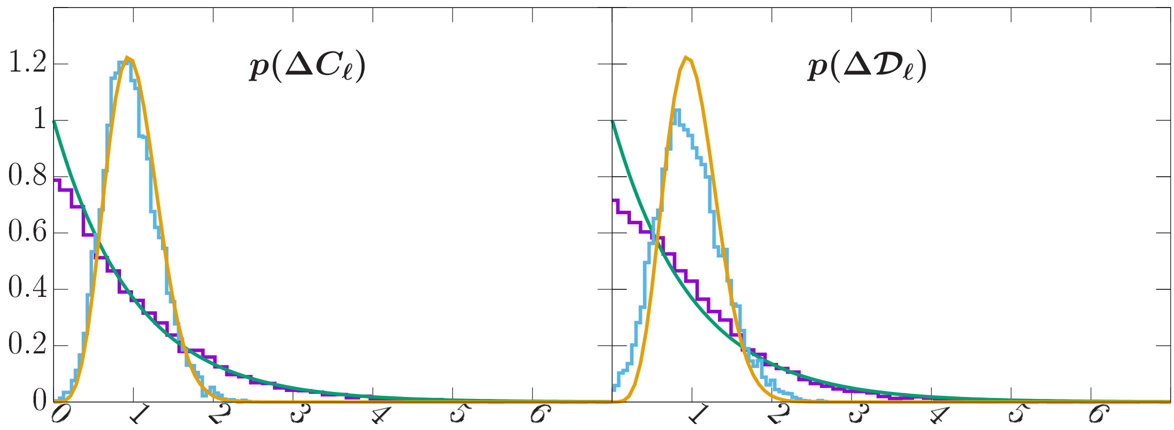

Figure 2.2: Left panel: Distribution of the ΔC_ℓ spacing from SI CMB maps without any foreground addition (in purple) and with addition of three foregrounds (in light-blue), i.e, synchrotron, thermal dust, and free-free emission extrapolated at $100\,\mathrm{GHz}$. There is a clear departure from nearly Poisson ($p(s) = \mathrm{e}^{-s}$, green curve) to Wigner-Dyson form of GSE ($p(s) = \frac{2^{18}}{3^6\pi^3} s^4 \mathrm{e}^{-\frac{64}{9\pi}s^2}$, orange curve) for SA CMB maps. Right panel: Distribution of the $\Delta \mathcal{D}_\ell$ spacing from SI (purple) and SA (light-blue) CMB maps. Again a departure from approximately Poisson to some appropriate level repulsion statistics is seen.

be related with the lack of rotational symmetry for SA CMB maps. Likewise, for $\Delta \mathcal{D}_\ell$'s we find $\langle r \rangle = 0.45045788, 0.82103559$ for SI and SA CMB, respectively. These higher values of $\langle r \rangle$ are indicative of additional dependence among $\mathcal{D}_\ell$'s as $\frac{\ell(\ell+1)}{2\pi}\langle C_\ell \rangle \simeq constant$ for low ℓ's. In the first panel of Figure 2.2 we have plotted the probability distribution of ΔC_ℓ to illustrate the change in the spacing distribution from approximately Poisson to GSE form of Wigner-Dyson statistics. In the second panel of Figure 2.2, we see that the curves for $\Delta \mathcal{D}_\ell$'s are not easily classifiable into the standard forms given by Poisson or Wigner-Dyson statistics. However, the subfigure shows the transition between level clustering to level repulsion. This is in agreement with the values of mean gap ratios for $\Delta \mathcal{D}_\ell$'s which show a departure from very low to high correlations, for SI and SA CMB maps.

2.4 Level correlation estimator

We propose a novel estimator for probing correlations among the APS of the foreground cleaned CMB temperature maps. For the range of multipoles $[2, 31]$, the spacings between consecutive C_ℓ's and $\mathcal{D}_\ell$'s are estimated. Say, such consecutive multipole spacings are $[\Delta_1, \Delta_2, \ldots]$, then the average spacing estimator is

$$avg_i = \frac{\Delta_1^i + \Delta_2^i + \ldots}{N}. \tag{2.207}$$

Here, $i = a, o, e$, where a, o, e stand for all, odd and even multipoles, and N = number of spacings for the given range of ℓ's.

This estimator helps characterise behaviours of APS spacings and hence large angle correlations in an easily quantifiable way. Besides, the choice of this estimator is a priori. The behaviour of all, even and odd multipole spacings for simulated SI and SA CMB maps, is shown in Figure 2.3. These have been obtained from 10^4 realisations of SI CMB to which foregrounds were added to obtain 10^4 SA CMB maps, as described in Section 2.3. The overall effect of addition of foregrounds to statistically isotropic CMB realisations is to shift the average estimator to higher values. Thus it may be highly unlikely to attribute unusually low mean spacings in foreground cleaned CMB maps to any residual foregrounds. The advantage of using this estimator is that we can consider the mean spacing from many statistically isotropic CMB realisations to compare with that from foreground cleaned CMB data. Otherwise, with entities like the gap ratio, any individual spacing, or the Pearson's correlation coefficient, we need an ensemble of realisations, while we have only one universe to observe.

2.5 Methodology

We have compared values of the average spacing estimator for foreground cleaned CMB APS with those of the theoretical APS (Planck 2018 best fit [9]). With the help of the HEALPix [117] package, we generate 10^4 statistically isotropic CMB maps of the theoretical temperature APS to account for statistical fluctuations.

CMB maps used here for probing APS spacings are full-sky foreground cleaned maps of WMAP 9 year ILC and 2018 release full mission Planck Commander (COMM), NILC and SMICA maps from latest sources, i.e., [209] and [98], respectively. These have been downgraded with the help of HEALPix [117] software facilities to a HEALPix $n_{side} = 16, n\ell_{max} = 32$ (hence, an appropriate pixel-window) with no beam smoothing (fwhm_arcmin= 0.0) and the statistically isotropic CMB maps are obtained using the same resolution. With all foreground cleaned and simulated statistically isotropic CMB maps thereof on an equal footing, we have proceeded with the analysis. We have excluded multi-

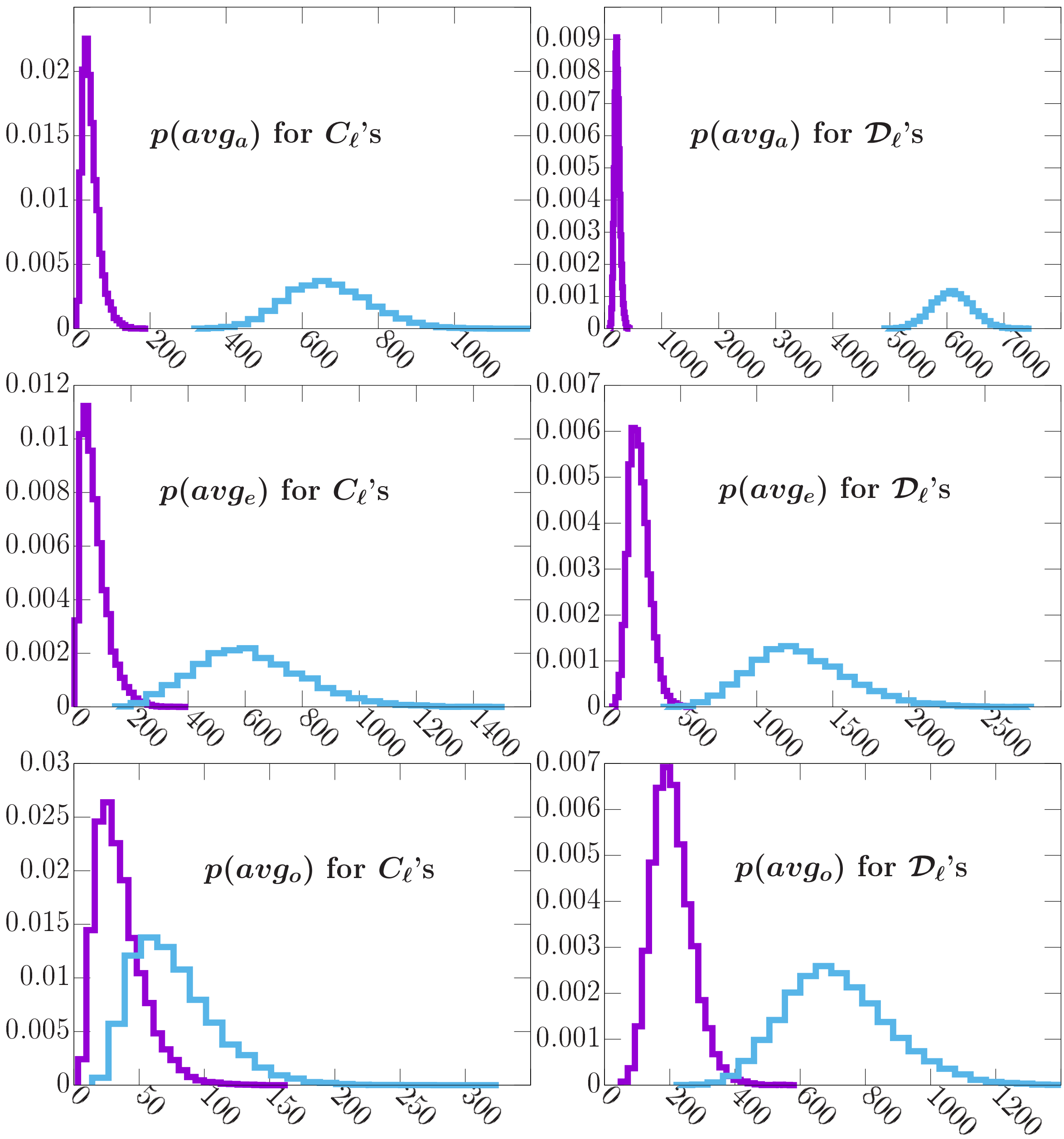

Figure 2.3: Probability distributions of avg_a, avg_e, and avg_o from 10^4 statistically isotropic (purple) and anisotropic (light-blue) CMB maps for C_ℓ's and $\mathcal{D}_\ell$'s. Foreground impurities added to statistically isotropic CMB maps enhance correlations between consecutive multipole APS and cause average spacings to be larger.

poles $\ell = 0, 1$ as these correspond respectively to the monopole of uniform CMB temperature ($\approx 2.726K$) [103], and the dipole which arises due to our peculiar motion relative to the CMB rest frame [47]. In addition, we have ignored contributions from noise, as it is not expected to be significant at the large scales studied here [270].

We have taken the average (avg_i) spacing (2.207) of C_ℓ's and $\mathcal{D}_\ell$'s for consecutive multipoles firstly without any parity distinction and later separately for odd and even multipoles. For example, for the 6 multipoles in the range $[2, 7]$ for C_ℓ's, we have 5 spacings with no parity based distinction namely, $|C_2 - C_3|, |C_3 - C_4|, ..., |C_6 - C_7|$. Whereas for even and odd multipoles taken distinctly, in the same range, we have 2 spacings each for even and odd multipoles i.e., $|C_2 - C_4|, |C_4 - C_6|$ and $|C_3 - C_5|, |C_5 - C_7|$ respectively. Thus avg_a is the mean value of 5 spacings, while avg_e, avg_o are mean values of 2 spacings each. Average spacings for consecutive $\mathcal{D}_\ell$'s are found in a similar fashion. The range of multipoles used for our study is $\ell \in [2, 31]$. With this chosen range of multipoles (i.e, $\ell \in [2, 31]$), we are able to consider an equal number of odd and even multipole spacings.

For characterising the extent to which the average spacing from foreground cleaned CMB maps may be different from statistically isotropic realisations of the CMB in a quantitative way, we define the probability $P^t(avg_i)$. Here, $i = a, o, e$ which stand for all (no parity based distinction), odd and even multipoles respectively. The fraction $P^t(avg_i)$ is calculated by counting the number of statistically isotropic CMB simulations having the value of the avg_i estimator greater than the foreground cleaned CMB map and dividing the number by the total number of simulations, that being 10^4 for the work presented in this chapter.

2.6 Results

We have computed the probabilities $P^t(avg_i)$ and report those which feature below 5% or above 95%, corresponding to departures from the 5%–95% confidence range of hypothesis testing methodology [40, 101, 210].

From the left panel of Figure 2.4, we see that the average spacings of C_ℓ's for all and odd multipoles are well within our confidence range. For even multipoles, however, all the four maps exhibit unusually low average spacings. From the right panel of Figure 2.4, again, we

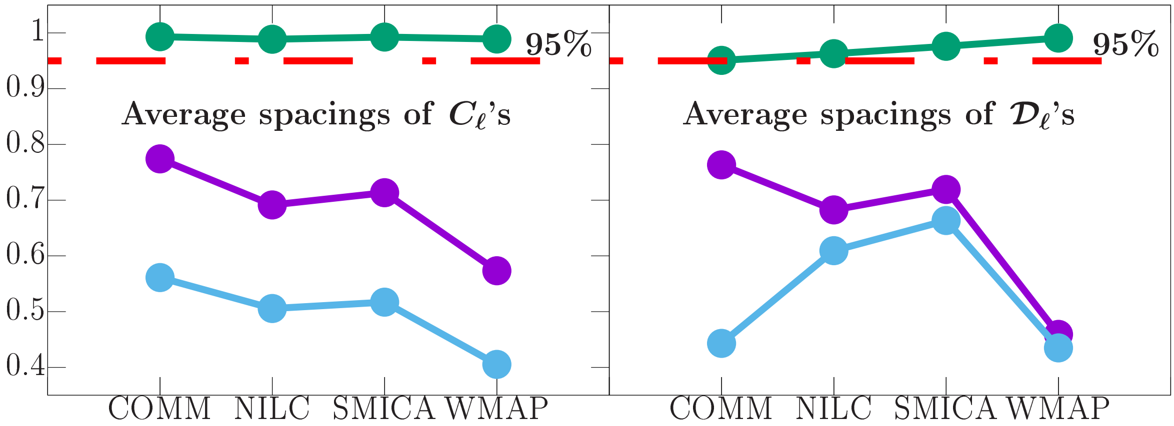

Figure 2.4: Left panel: Probabilities $P^t(avg_a)$ (purple), $P^t(avg_e)$ (green), $P^t(avg_o)$ (light-blue) for C_ℓ's. Right panel: P^t of average spacings of $\mathcal{D}_\ell$'s. Red dashed lines indicate 95% C.L. The average spacings of even multipoles from cleaned CMB maps are unusually low.

Table 2.1: Values of $P^t(avg_e)$ for four maps, for C_ℓ's and $\mathcal{D}_\ell$'s.

Map	for C_ℓ's	for $\mathcal{D}_\ell$'s
COMM	99.33%	95.07%
NILC	98.86%	96.27%
SMICA	99.26%	97.61%
WMAP	98.90%	99.08%

see that the average spacings of $\mathcal{D}_\ell$'s for all and odd multipoles are as expected, but those for even multipoles are unusually low for all the four maps. The values of P^t for even multipoles are in Table 2.1.

Overall, we see that the multipole spacings of even multipoles are unusually low relative to those based on the ΛCDM concordance model, and rejected at $\gtrsim 95\%$ C.L. for all the four foreground cleaned CMB maps. This may mean that the unexpected signal is either truly characteristic of the CMB sky or that it has been left over due to a generic systematic error or a similar foreground residual in all the maps, despite the use of different cleaning methods. In either case, such occurrences must be further checked for their robustness. In the next section, we subject our findings to rigorous checks of robustness with the help of an inpainting method based on constrained Gaussian realisations with two kinds of galactic masks. In addition, we mask the non-Gaussian cold spot (NGCS) and inpaint over the same. Thus, evaluating the average spacing estimator for the foreground cleaned inpainted CMB maps helps us explore any variations of the signal with respect to (a) possibly minor foreground residuals in the galactic region, and (b) the NGCS.

2.7 Robustness with inpainted realisations

The unusually low valued estimator (avg_e) found in the previous section albeit is seen consistently for all four maps, yet, the result could be due to foreground residuals or other unresolved systematics. To distinguish the occurrence of unusual patterns as being characteristic of the CMB sky as opposed to residual uncertainties, we use masks for the galactic region and some extragalactic point sources. Since foreground residuals in and around the galactic region may cause such unexpected signatures. The $KQ75$ mask of WMAP, and a product of the temperature confidence masks of COMM, NILC, SEVEM, and SMICA of Planck, referred to as the $U73$ mask, are used here. These are shown in Figure 2.5.

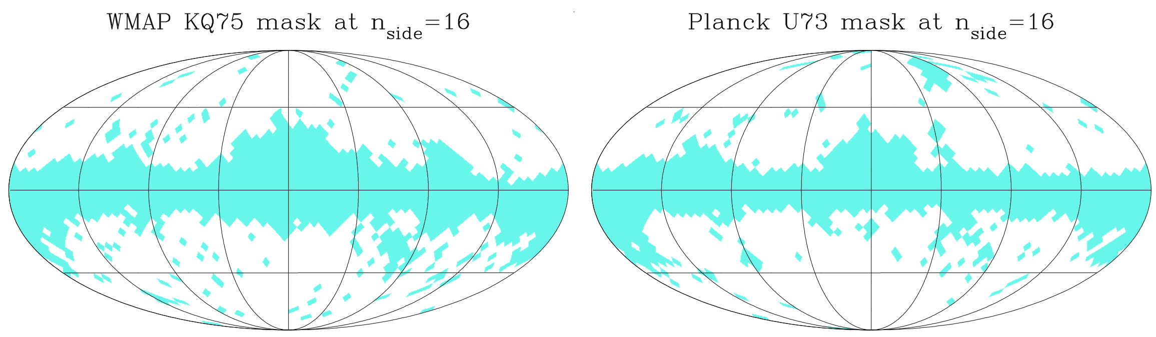

Figure 2.5: Low resolution (HEALPix $n_{side} = 16$) versions of WMAP's $KQ75$ and Planck's $U73$ masks. Masked regions are indicated in cyan.

To obtain these low resolution (HEALPix $n_{side} = 16$) masks, we downgrade the available high resolution masks and apply a threshold of $x = 0.85$ to the $KQ75$ mask and that of $x = 0.98$ to the $U73$ mask. This implies that after downgrading, we set all pixels with value $\leq x$ to 0, and the others to 1. Being a conservative mask, $KQ75$ includes a wider galactic cut and many point sources relative to the $U73$ mask. Choices for the thresholds are based on [14], and help us keep a considerable sky fraction (62.9% for $KQ75$ and 67.5% for $U73$) while masking regions with dominant foreground sources at large scales [270]. Hence the analysis for avg_e is repeated on full sky inpainted realisations of the masked CMB maps.

2.7.1 Mathematical framework for inpainting

The inpainting method we use is that of local constrained Gaussian realisations (CGRs) in pixel space in regions of the sky that are masked. The mathematical framework behind this algorithm of generating the CGR of the map pixels in the masked region can be understood in the following manner. Consider the complete covariance matrix of the map $m = \begin{pmatrix} p \\ q \end{pmatrix}$, as

$$\mathcal{C} = \begin{pmatrix} \mathcal{C}_{pp} & \mathcal{C}_{pq} \\ \mathcal{C}_{qp} & \mathcal{C}_{qq} \end{pmatrix}. \tag{2.208}$$

We suppose that p_{cg} are pixels of the map as required in the form of a CGR, which is constrained by a covariance matrix $\mathcal{C}pp$ corresponding to a fiducial angular power spectrum C_ℓ^{fid}. For convenience, we drop the subscripts from p,q and concern ourselves with only the maximum likelihood estimate (MLE) of the masked region pixels. The Gaussian probability distribution for the map can be written as:

$$P(m) = \frac{1}{\sqrt{2\pi\det(\mathcal{C})}} \exp\left(-\frac{1}{2}m^T\mathcal{C}^{-1}m\right). \tag{2.209}$$

Equivalently, the log-likelihood for the vector array p given the pixel values of q can be defined as:

$$\log\mathcal{L} = \text{constant} - \frac{1}{2}\left(p^T(\mathcal{C}^{-1})_{pp}p + p^T(\mathcal{C}^{-1})_{pq}q + q^T(\mathcal{C}^{-1})_{qp}p\right), \tag{2.210}$$

where, we have absorbed terms that are independent of p in the constant. If we denote $E = (\mathcal{C}^{-1})_{pp}, F = (\mathcal{C}^{-1})_{pq}, G = (\mathcal{C}^{-1})_{qp}$, then,

$$\log\mathcal{L} = \text{constant} - \frac{1}{2}\left(p_iE_{ij}p_j + p_iF_{ij}q_j + q_iG_{ij}p_j\right), \tag{2.211}$$

in Einstein's summation convention. If we take the first derivative of the log-likelihood with respect to p and equate it to zero, we get the MLE of p. Hence,

$$\begin{aligned} \frac{\partial(\log\mathcal{L})}{\partial(p_k)} &= E_{kj}p_j + p_jE_{jk} + F_{kj}q_j + q_jG_{jk} \\ &= Ep + p^TE + Fq + q^TG = 0. \end{aligned} \tag{2.212}$$

The solution to this equation is $p = p_{ml} = -E^{-1}Fq$, which is the MLE. With this information, we can rewrite the expression (2.209) for the probability distribution of p given the complete covariance matrix ($\mathcal{C}$) of the map m, as

$$P(p|q) \propto \exp\left(-\frac{1}{2}(p-p_{ml})^T(\mathcal{C}^{-1})_{pp}(p-p_{ml})\right). \tag{2.213}$$

Thus, in order to accomplish the task of generating the pixels p when pixels of q are known, has reduced to creating a realisation of pixels, say $p_r = (p - p_{ml})$ knowing from (2.213) that p_r must follow a covariance matrix $((\mathcal{C}^{-1})_{pp})^{-1}$. However, this task is fairly non-trivial, since we would need to find the equivalent of a square root of the covariance matrix, which can be computationally expensive. Instead we utilise the technique first given by [139] and extended by [48] which is as follows.

Consider the block decomposition relation [185] for the inverse of the covariance matrix:

$$\begin{pmatrix} \mathcal{C}_{pp} & \mathcal{C}_{pq} \\ \mathcal{C}_{qp} & \mathcal{C}_{qq} \end{pmatrix}^{-1} =$$

$$\begin{pmatrix} (\mathcal{C}_{pp}-\mathcal{C}_{pq}(\mathcal{C}_{qq})^{-1}\mathcal{C}_{qp})^{-1} & -(\mathcal{C}_{pp}-\mathcal{C}_{pq}(\mathcal{C}_{qq})^{-1}\mathcal{C}_{qp})^{-1}\mathcal{C}_{pq}(\mathcal{C}_{qq})^{-1} \\ -(\mathcal{C}_{qq}-\mathcal{C}_{qp}(\mathcal{C}_{pp})^{-1}\mathcal{C}_{pq})^{-1}\mathcal{C}_{qp}(\mathcal{C}_{pp})^{-1} & (\mathcal{C}_{qq}-\mathcal{C}_{qp}(\mathcal{C}_{pp})^{-1}\mathcal{C}_{pq})^{-1} \end{pmatrix}. \tag{2.214}$$

Hence, the covariance matrix that p_r must follow is $((\mathcal{C}^{-1})_{pp})^{-1} = \mathcal{C}_{pp} - \mathcal{C}_{pq}(\mathcal{C}_{qq})^{-1}\mathcal{C}_{qp}$.

With a random realisation of a full sky map, we can denote the map pixels as $m^T = (p^T \quad q^T)$, which obeys the full sky covariance matrix (2.208) . If we suppose that a linear transformation of p which takes it to a variable p' is given by

$$p' = p - Aq, \tag{2.215}$$

then p' will obey the covariance matrix

$$\begin{aligned} \mathcal{C}_{p'p'} &= \langle p'p'^T \rangle \\ &= \langle (p-Aq)(p-Aq)^T \rangle \\ &= \langle pp^T \rangle - \langle pq^T \rangle A^T - A\langle qp^T \rangle + A\langle qq^T \rangle A^T \\ &= \mathcal{C}_{pp} - \mathcal{C}_{pq}A^T - A\mathcal{C}_{qp} + A\mathcal{C}_{qq}A^T. \end{aligned} \tag{2.216}$$

This relation holds for any general linear transformation with a matrix A. Analogically, if $p' = p_r$, then $A = -((\mathcal{C}^{-1})_{pp})^{-1}(\mathcal{C}^{-1})_{pq}$. Using (2.214), we get,

$$A = \mathcal{C}_{pq}(\mathcal{C}_{qq})^{-1}. \tag{2.217}$$

Hence using (2.216) and (2.217), we arrive at

$$\mathcal{C}_{p_r p_r} = \mathcal{C}_{pp} - \mathcal{C}_{pq}(\mathcal{C}_{qq})^{-1}\mathcal{C}_{qp} = ((\mathcal{C}^{-1})_{pp})^{-1}, \tag{2.218}$$

which is the correct covariance matrix as required for p_r. Thus, when a full sky Monte Carlo realisation is generated using the fiducial power spectrum, and the masked region pixels from this map are taken, they are expected to obey the correct covariance matrix structure.

2.7.2 Algorithm for inpainting

This algorithm is based on [48, 35] and can be outlined in the following steps:

1. Consider the entire set of pixels of an foreground cleaned CMB full sky map, as $m = \begin{pmatrix} p_{obs} \\ q_{obs} \end{pmatrix}$, where, p_{obs} represents the set of pixels in a masked region, and q_{obs} represents those of the unmasked region that will be used to constrain the pixels in the masked region.

2. With a fiducial power spectrum C_ℓ^{fid}, a full sky Gaussian random realisation is generated given by $m_r = \begin{pmatrix} p_r \\ q_r \end{pmatrix}$. Here C_ℓ^{fid} is the theoretical best fit to Planck 2018 data.

3. Set $q_{in} = q_{obs} - q_r$

4. Calculate covariance matrices $\mathcal{C}_{pq}, \mathcal{C}_{qq}$ of pairs of masked-unmasked and unmasked-unmasked pixel sets, respectively, determined from random Gaussian realisations based on a theoretical (ΛCDM model, say) power spectrum best fitted to some data (here, Planck 2018 data). A simpler method to calculate these covariance matrices, as used here is by considering the expression for elements of the CMB covariance matrix

$\mathcal{C}$ [264] :

$$\begin{aligned}\mathcal{C}_{ij} &= \sum_{\ell=2}^{n\ell_{max}} \frac{2\ell+1}{4\pi} C_\ell^{fid} B_\ell^2 P_\ell^2 \mathcal{P}_\ell(\cos(\gamma_{ij})), \\ \cos(\gamma_{ij}) &= \cos(\theta_i)\cos(\theta_j) \\ &\quad + \sin(\theta_i)\sin(\theta_j)\cos(\phi_i - \phi_j), \end{aligned} \tag{2.219}$$

where, (θ_i, ϕ_i) are the spherical polar angles for the i^{th} pixel, B_ℓ, P_ℓ are the beam and pixel window functions, respectively, and $\mathcal{P}_\ell$ is the Legendre polynomial.

5. Set $p_{ml} = \mathcal{C}_{pq}\mathcal{C}_{qq}^{-1} q_{in}$. The inverse can be found using the Moore-Penrose generalised pseudo inverse [87, 218, 264].

6. Set $p_{cg} = p_{ml} + p_r$. Thus p_{cg} corresponds to pixels of a local constrained Gaussian realisation.

7. The set of pixels for the complete inpainted map are given by $m_{cg} = \begin{pmatrix} p_{cg} \\ q_{obs} \end{pmatrix}$

To demonstrate the efficacy of the inpainting algorithm employed here, we consider a statistically isotropic CMB realisation map and its inpainted version. The inpainting is done on the partial sky map obtained with a mask which is a product of the $KQ75$ and $U73$ masks, and hence a more conservative mask relative to either of the two. Beside the inpainted map, we present a Mollweide projection of their difference. Say, for the original map, given by m, and its inpainted version given by m_{ip}, the difference map is $m_d = m_{ip} - m$. So m, m_{ip} and m_d, for a statistically isotropic CMB map are shown in Figure 2.6.

2.7.3 Results from inpainting over *KQ75* and *U73* masks

After separately applying the $KQ75$ and $U73$ masks to cleaned CMB maps, we generated 10^3 inpainted realisations of each of those, and have shown normalised counts ($\mathcal{N}$) of the avg_e estimator. This quantity $\mathcal{N}(avg_e)$ is the number of realisations with a value of avg_e in a certain bin, divided by the total number of realisations. Notably, these curves for both C_ℓ's and $\mathcal{D}_\ell$'s have very small spreads. Hence these resemble nearly vertical lines when shown along with $\mathcal{N}(avg_e)$ from statistically isotropic CMB realisations. We calculated $P^t(avg_e)$

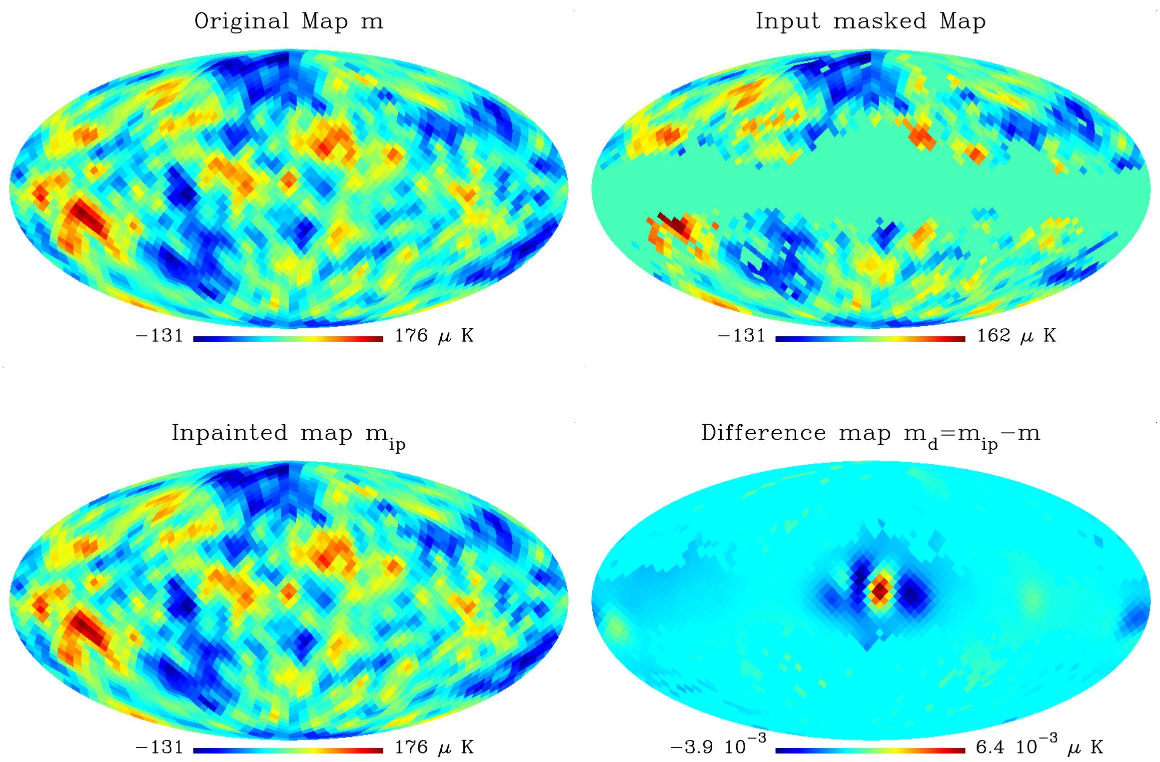

Figure 2.6: Top left panel: Original statistically isotropic CMB map m; top right panel: Map m after masking; bottom left panel: map m_{ip} after inpainting over the masked region; bottom right panel: difference between the original and inpainted maps. The difference map has values of order 10^{-3}. This helps demonstrate the efficacy of the inpainting method used, which is that of a local constrained Gaussian realisation.

for each of the 10^3 inpainted realisations of a particular map and for a certain mask. We found that the values for all realisations of each of the four respective cleaned maps are the same as those in Table 2.1, regardless of the mask used.

In the first row of Figure 2.7, from left to right, the four subfigures correspond to $\mathcal{N}(avg_e)$ of C_ℓ's from inpainted realisations of COMM, NILC, SMICA and WMAP using the $KQ75$ mask (dark-green). Vertical red lines indicate values of avg_e from the four originally cleaned full sky maps. The second row shows the same curve of $\mathcal{N}(avg_e)$ (in dark-green) along with that from 10^4 statistically isotropic CMB realisations (in cyan). The third and fourth rows show the same curves as the first and second rows, respectively but with the use of the $U73$ mask.

The fifth and sixth rows of Figure 2.7 follow the same pattern as the first and second rows, but for $\mathcal{D}_\ell$'s. The curves of $\mathcal{N}(avg_e)$ for $\mathcal{D}_\ell$'s from 10^3 inpainted realisations using the $KQ75$ mask are shown in orange, while that from 10^4 statistically isotropic CMB maps is shown in pink. The seventh and eighth rows follow the same pattern as the fifth and sixth rows, but with the $U73$ mask.

From these subfgures we see that the spreads of $\mathcal{N}(avg_e)$ from inpainted realisations are very small and closely centred around the red lines from the full sky foreground cleaned CMB maps. Besides, some curves of $\mathcal{N}(avg_e)$ from inpainted realisations that are shifted significantly tend to favour lower values of avg_e compared to these red lines (for e.g., fifth-row-first-column and seventh-row-fourth-column subfigures of Figure 2.7). Again relative to the curve from statistically isotropic CMB maps, these confirm that they lie on the leftmost unlikely regions, as seen before (Table 2.1). Thus inpainting over the two masks indicates that the signal of anomalously low avg_e persists for both C_ℓ's and $\mathcal{D}_\ell$'s of $\ell \in [2, 31]$, robustly for four different cleaning methods and two different masks. This makes it difficult to attribute the same to foreground residuals.

2.7.4 Effect of the non-Gaussian cold spot (NGCS)

The NGCS [71, 194, 276, 36] approximately centred at $(\theta, \phi) = -57$**??**jnltextdegree$, 209$**??**jnltextdegree was shown to be correlated with the north-south power asymmetry [37, 229, 11, 92, 93, 94].

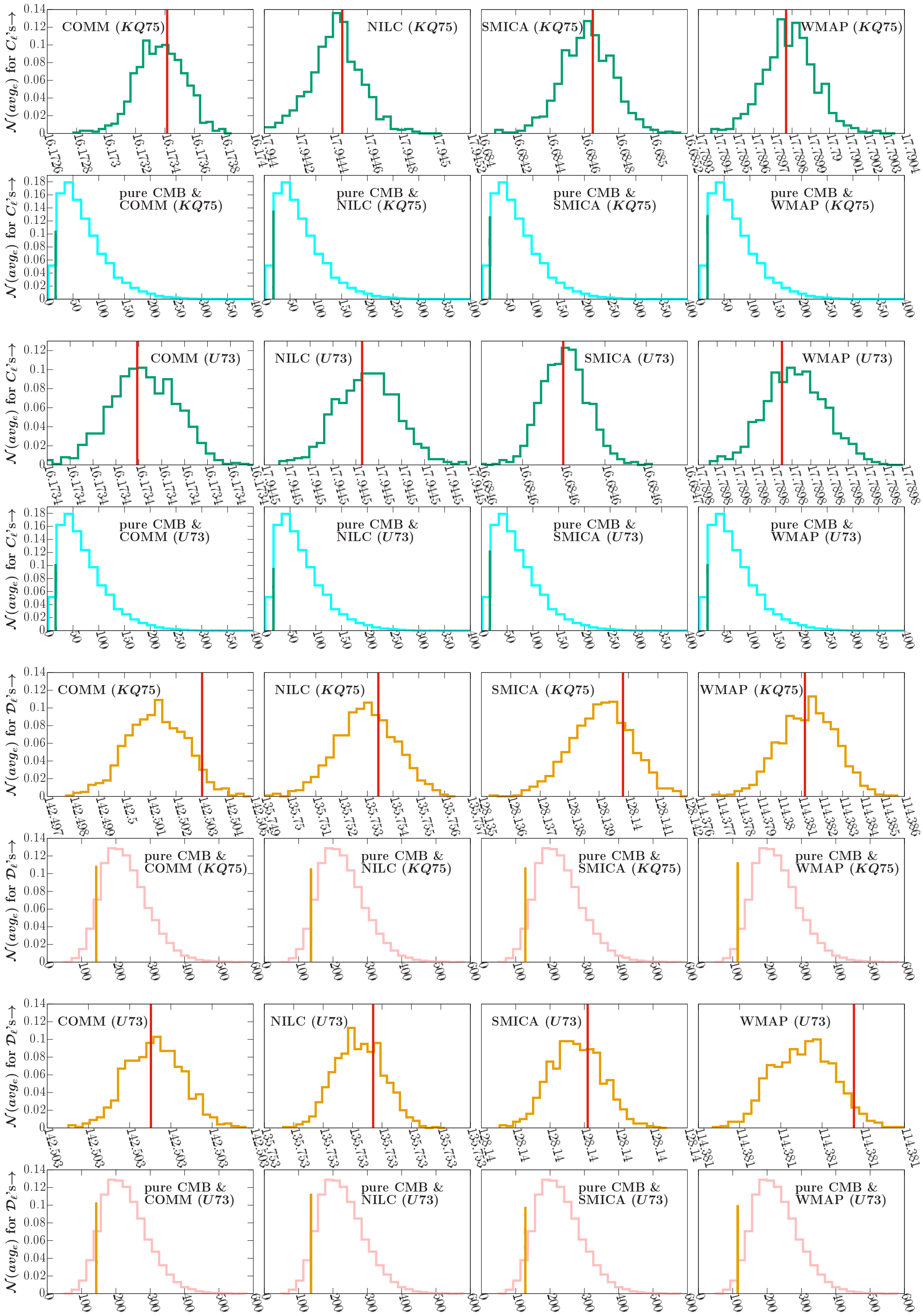

Figure 2.7: First row: Normalised counts $\mathcal{N}(avg_e)$ for C_ℓ's using 10^3 inpainted realisations of COMM, NILC, SMICA, WMAP with the $KQ75$ mask. Second row: $\mathcal{N}(avg_e)$ as in first row, along with that from 10^4 statistically isotropic CMB realisations. Third, fourth row: Same as first and second rows, but with the $U73$ mask. Fifth row: $\mathcal{N}(avg_e)$ for $\mathcal{D}_\ell$'s using 10^3 inpainted realisations of COMM, NILC, SMICA, WMAP with the $KQ75$ mask. Sixth row: $\mathcal{N}(avg_e)$ as in fifth row, along with that from 10^4 statistically isotropic CMB realisations. Seventh, eighth row: Same as first and second rows, but with the $U73$ mask. Vertical red lines indicate values from full sky cleaned maps.

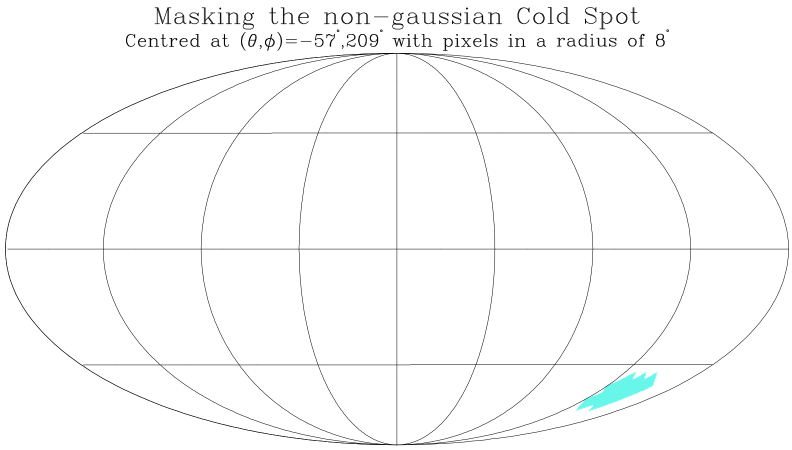

Figure 2.8: The non-Gaussian cold spot (NGCS) mask: the NGCS is shown in cyan; the unmasked region is in white.

However, the significance of this effect was seen to be low for low resolution [215] maps at HEALPix $n_{side} = 16$. Nevertheless, a study of its relation with the deficit of large-angle correlations has not been investigated. We therefore generate a mask for the NGCS by setting all pixels in a radius of 8**??**jnltextdegree from its center to zero, as shown in Figure 2.8. We utilise this mask in union with the $KQ75$ and $U73$ masks (referred to as the $KQ75-CS$ and $U73-CS$ masks) and redo the analysis with such inpainted realisations of the four foreground cleaned CMB maps.

In the first row of Figure 2.9, from left to right, the four subfigures correspond to $\mathcal{N}(avg_e)$ of C_ℓ's from inpainted realisations of COMM, NILC, SMICA and WMAP using the $KQ75-CS$ mask (in green). Vertical red lines indicate values of avg_e from the original cleaned full sky maps. The second row shows the same $\mathcal{N}(avg_e)$ along with that from 10^4 statistically isotropic CMB realisations (in cyan). The third and fourth rows show the same curves as the first and second rows, respectively but with the use of the $U73-CS$ mask. The fifth and sixth rows follow the same pattern as the first and second rows, but for $\mathcal{D}_\ell$'s. The seventh and eighth rows follow the same pattern as the third and fourth rows for $\mathcal{D}_\ell$'s.

The values of $P^t(avg_e)$ for these inpainted realisations are again the same as those of their respective full sky cleaned maps as in Table 2.1, regardless of the mask used. Thus, inpainting over the union masks, $KQ75-CS$ and $U73-CS$ indicates that the signal is

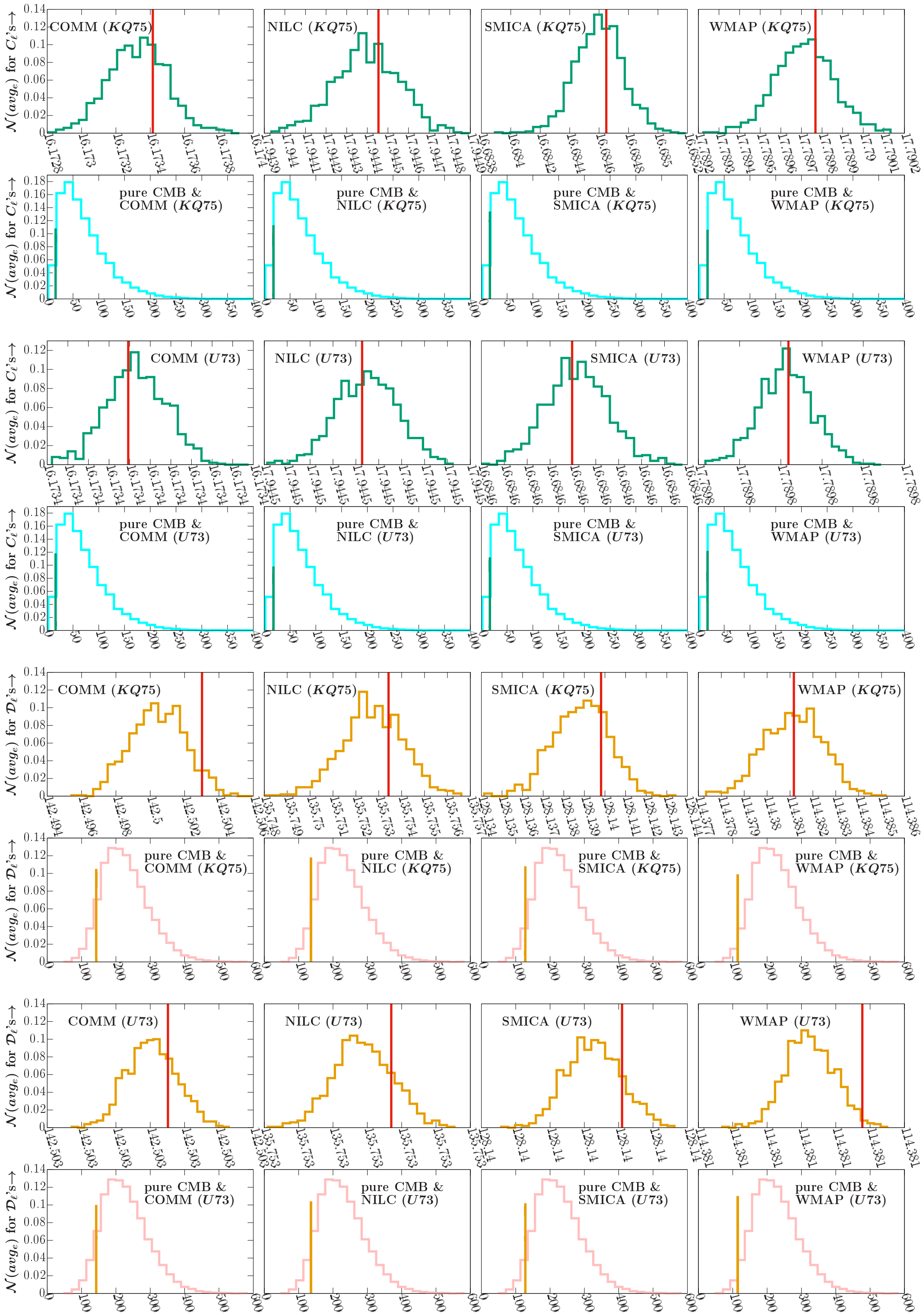

Figure 2.9: First row: Normalised counts $\mathcal{N}(avg_e)$ for C_ℓ's using 10^3 inpainted realisations of COMM, NILC, SMICA, WMAP with the $KQ75-CS$ mask. Second row: $\mathcal{N}(avg_e)$ as in first row, along with that from 10^4 statistically isotropic CMB realisations. Third, fourth row: Same as first and second rows, but with the $U73-CS$ mask. Fifth row: $\mathcal{N}(avg_e)$ for $\mathcal{D}_\ell$'s using 10^3 inpainted realisations of COMM, NILC, SMICA, WMAP with the $KQ75-CS$ mask. Sixth row: $\mathcal{N}(avg_e)$ as in fifth row, with that from 10^4 statistically isotropic CMB realisations. Seventh, eighth row: Same as first and second rows, but with the $U73-CS$ mask. Vertical red lines indicate values from full sky cleaned maps. We have omitted the suffix '$-CS$' due to lack of space in the subfigures.

independent of the NGCS. Thus a significantly low mean spacing of even multipole APS exists which is robust against four different cleaning methods, two different masks, and the presence or absence of the NGCS.

2.8 Summary and conclusion

Level spacings of eigenvalues of random matrices have been studied before to classify the change of correlations between integrable and chaotic systems. Integrable systems are those for which the energy eigenvalues show level clustering (Poisson statistics) as they are uncorrelated, while those of chaotic systems show level repulsion (Wigner-Dyson statistics) due to presence of correlations.

Within the framework of the concordance model of cosmology, we expect the CMB to be statistically isotropic. This implies that the angular power spectrum (APS) of CMB is uncorrelated between different multipoles. Since foreground cleaned CMB maps are obtained from observed CMB radiation after application of various state of the art foreground cleaning methods, these maps are expected to be representative of the actual CMB sky, which is hypothesised to have no correlations in its APS measures. Thus it is interesting to probe the nature of any possible correlations in the APS of foreground cleaned maps to ascertain if the principle of statistical isotropy is obeyed. We note that a breakdown of statistical isotropy could be due to several possible mechanisms. These include the presence of a statistically anisotropic primordial signal, or some minor residual foregrounds, or any unaccounted agents between the source and the observer, or due to any minuscule systematics left over as a result of the analysis pipeline employed during satellite data collection and/or the map making procedure.

The presence or absence of correlations can be concretely established with the help of the mean gap ratio, which avoids the problem of unfolding. We show that in the context of simulated statistically isotropic CMB maps, the mean gap ratio closely corresponds to that for Poisson statistics, whereas, on introduction of statistical anisotropy in the maps, we see a shift towards some appropriate level repulsion statistics. The mean gap ratio is obtained by averaging over an ensemble of CMB realisations, similar to how quantities like the correlation coefficients are ascertained. Since we have only one CMB sky to observe instead of an ensemble, therefore we devise a novel estimator which computes the average APS spacing of a set of low multipoles ($\ell \in [2, 31]$). We show that such an estimator can distinguish between statistically isotropic and anisotropic CMB, and hence is useful in categorising the nature of correlations present in foreground cleaned CMB maps. This estimator is computed for even and odd multipole spacings in addition to all multipoles taken together.

Without any parity distinction, for all multipoles, the spacings are seen to be in good agreement with theoretical expectation. Parity based distinction reveals that the average spacing of even multipoles (avg_e) is anomalously low for both C_ℓ's (at $\geq 98.86\%$ C.L.) and $\mathcal{D}_\ell$'s (at $\geq 95.07\%$ C.L.). Since all four maps, namely, COMM, NILC, SMICA, and WMAP, are obtained with the help of different foreground cleaning algorithms, the amounts of foreground residuals in these maps are different [170, 6, 91]. These systematic differences are distinctly visible if we consider any two of these maps at low resolution and subtract one from the other. Hence we perform further studies with inpainted realisations of masked CMB maps, to establish whether the observed anomalously low avg_e spacings are due to foreground residuals, and we find that the signal persists in all the foreground cleaned inpainted CMB maps. We conclude that this signal of unusually low average even multipole spacings is robust against

(a) the use of two different galactic masks,

(b) data from two different instruments, i.e, WMAP and Planck satellites,

(c) consideration of maps obtained from four different cleaning methods, namely those of Gibbs sampling for COMM, Spectral Matching Independent Component Analysis for SMICA, Internal linear combination (ILC) in needlet space for NILC, ILC in pixel space for WMAP, and

(d) the presence or absence of the non-Gaussian cold spot.

Thus, we find a robust signal of low average spacing for $\ell \in [2, 31]$ with even multipoles of C_ℓ's and $\mathcal{D}_\ell$'s which seems unlikely due to foreground residuals in the galactic region of cleaned maps. This finding is in agreement with previous findings of the deficit of large-angle correlation and its equivalence with the odd-parity preference of the APS. However, our findings may additionally indicate that correlations between odd multipole APS are not anomalous, as opposed to those of even multipole APS. This accounts for a possibly unusual level clustering of even multipole APS or a spacing distribution that favours low even multipole spacings. The unusually low average even multipole spacing hints at possible breakdown of statistical isotropy which is primordial in origin. For instance, there could be the possibility of an anisotropic Finsler spacetime model [53] with a correction term that lowers even multipole C_ℓ's. A theoretical model that alters the correlations of primordial fluctuation modes [298], could inspire some alternate work to shed light on the low even multipole APS correlation.

CHAPTER 3

ISOTROPY STATISTICS OF CMB HOT AND COLD SPOTS

3.1 Introduction

The anisotropies of the CMB temperature field play a fundamental role behind the formation of large scale structure of the universe. Over large angular scales these anisotropies are believed to have originated dominantly due to quantum fluctuations of the inflaton field present in the very early universe. The primordial curvature perturbation power spectrum contains snapshots of these fluctuations at the time of horizon crossing. Under the assumption of rotational invariance of this power spectrum, the observable CMB is expected to be statistically isotropic without picking up any preferred direction in the radiation field. However, in recent literature there are discussions [125, 259, 92, 233, 156, 20, 157, 19, 63] and claims of the presence of preferred direction [77, 232, 247, 251, 246, 167, 301] in the CMB field or breakdown of rotational invariance of the primordial power spectrum [128, 11, 129]. These indicate possible hints towards new fundamental physics [4, 188, 258, 53, 177, 83]. Apart from the cosmological origin of any possible anisotropic signal in the CMB, a question of equal importance is whether the foreground minimized CMB maps may have any residual systematics, e.g., residual foreground contamination which may potentially induce a breakdown from rotational invariance of the field and consequently give rise to a preferred direction. Needless to mention, if the presence of such residuals are not taken care of, cosmological parameters estimated from the CMB maps will be potentially biased or contain inaccurate confidence intervals on their estimated values. Thus, for proper and accurate extraction of cosmological information from CMB maps it is utmost essential to analyse from as many different perspectives as possible, if the observed maps contain any signal of breakdown of statistical isotropy.

In this chapter, we use a new method to investigate the isotropy of the anisotropy pattern of the CMB radiation field. The local maxima (hot spots) and minima (cold spots) of the CMB are uniformly distributed over the surface of a two-sphere if the field is isotropic and does not contain any preferred direction. A breakdown from uniformity of the distributions of either or both of these types of spots then needs to be investigated to validate the null hypothesis of isotropy. We use the concept of the orientation matrix introduced by Watson (1965) [285] and Scheidegger (1965) [249], to probe any violations of uniformity of the distributions of hot and cold spots over the CMB sky. The method is unique in its nature, since if there is any non-uniformity present in the data, it provides a geometric description of the non-uniformity in terms of clustering or girdling (ring structure) and an additional measure of the magnitude of such a deviation from uniformity in terms of the so-called strength parameter.

In earlier literature, the distribution of hot and cold spots of the CMB maps have been shown to encapsulate topological properties of the temperature field [281]. Apart from possible primordial or residual systematic effects present in the cleaned CMB maps, any unusual features such as clustered or girdled spots in cleaned maps may indicate presence of organised collections of structures or voids [267] between the source and observer. In addition, a higher signal-to-noise ratio at the hot spots [248, 43] as noted by [169], makes them favourable to study.

A statistical analysis of such hot and cold spots on the pixelised sphere using the orientation matrix has some other practical advantages as well. This reduces the large data set of numerous hot and cold spots to their respective eigenbases [149]. For accurate estimation of properties of the CMB sky, sometimes one analyses partial sky CMB maps, which are obtained by masking out the foreground dominated regions near the plane of the Milky Way [147]. Our study can easily be applied to partial CMB skies, without bothering about the complications that may arise due to multipole mode couplings on masked CMB maps [138] or due to any subtle biases introduced due to inpainting methods [234] when an underlying statistically isotropic CMB theoretical angular power spectrum is assumed while trying to reconstruct the lost sky region due to masking.

Previously, authors of [169] have studied one-point statistics such as the number, mean and variance of local extrema and demonstrated that on an average the hot (cold) spots of the observed CMB data are not hot (cold) enough. Further with the help of two-point statistics it was shown that possibly unusual properties associated with large angular scale structures are related with the behaviour of hot and cold spots of the CMB [142]. Since the initial density fluctuations are assumed to be Gaussian, a 3D Gaussian field model [26] was extended to address the 2D Gaussian CMB temperature field [43]. Notable works that have followed thereafter have dealt with the number density, shapes, separation distances and peak-peak correlation functions for spots [223, 62, 272]. The discovery of the non-Gaussian cold spot [277, 70, 72] and the theoretical frameworks for hot and cold spots of a 2D Gaussian field as presented in [43, 223, 62] have inspired further research to probe non-Gaussianity [272, 58, 199].

This chapter is organised as follows. In Section 3.2 we define the estimators for the shape and strength of non-uniformity used in our study. In Section 3.3 we analyse the behaviour of the chosen estimators on two toy model maps to illustrate clustering or girdling of spots. In Section 3.4, we discuss the application of these estimators to observed CMB maps. In Section 2.6 we present our results for any non-uniformity of spots in the observed CMB. In Section 3.6, we assess if the results obtained may be related with low CMB variance. In Section 3.7 we consider the composite set of both hot and cold spots and assess their uniformity. In Section 3.8 we form general conclusions and summarise our findings.

3.2 Estimators

One can study the distribution of spherical data as an analogue of unit mass points on the surface of a 2-sphere with the help of a unit-mass orientation matrix [286, 292, 102],

$$T = \begin{pmatrix} \sum_i {x_i}^2 & \sum_i x_i y_i & \sum_i x_i z_i \\ \sum_i x_i y_i & \sum_i {y_i}^2 & \sum_i y_i z_i \\ \sum_i z_i x_i & \sum_i z_i y_i & \sum_i {z_i}^2 \end{pmatrix}, \tag{3.220}$$

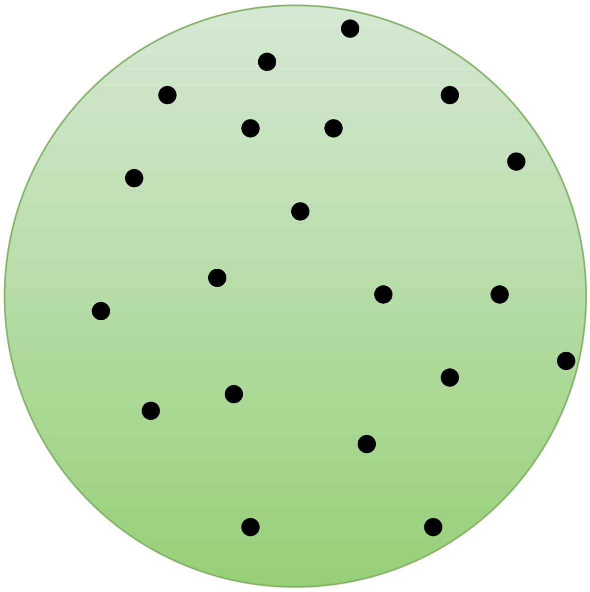

Figure 3.1: A 2-sphere for which all its data points or spots are considered to contribute equally to the orientation matrix, such that these points can be assigned unit masses.

where, $(x_1, y_1, z_1)...(x_n, y_n, z_n)$ are the direction cosines of unit mass points labelled with index $i = 1, ..., n$. Scheidegger (1965) [249] used the principal eigenvector of the normalised unit-mass orientation matrix (i.e, T/n) to find a 'mean' axis, while Watson (1965) [285] used the eigenvalues of T to classify non-uniform placements of data points on a 2-sphere. Woodcock (1977) [293] defined two kinds of eigenvalue ratios to quantify the shape and strength of such non-uniformity.

The CMB has a nearly uniform background temperature of $T_0 = 2.726K$ [103]. However there exist small directionally dependent differences of the order of a few hundred μK relative to T_0, which are called anisotropies. The hot and cold spots of the CMB temperature anisotropy field can therefore be treated as data points on a 2-sphere and their placements can be studied with the help of the orientation matrix.

In [102], the authors treat all data points on the sphere as equivalent in magnitude and ascribe unit masses to the same, such as the sphere shown in Figure 3.1, containing all spots in the same colour (black), to highlight their equivalent contribution to the orientation matrix. However, in the case of the CMB temperature field, as various extrema are offset differently relative to T_0 (illustrated in Figure 3.2), we extend the concept to include 'non-unit masses', i.e, peak values of the hot spots or cold spots, and express an orientation matrix $\mathcal{T}^{(s)}$ as,

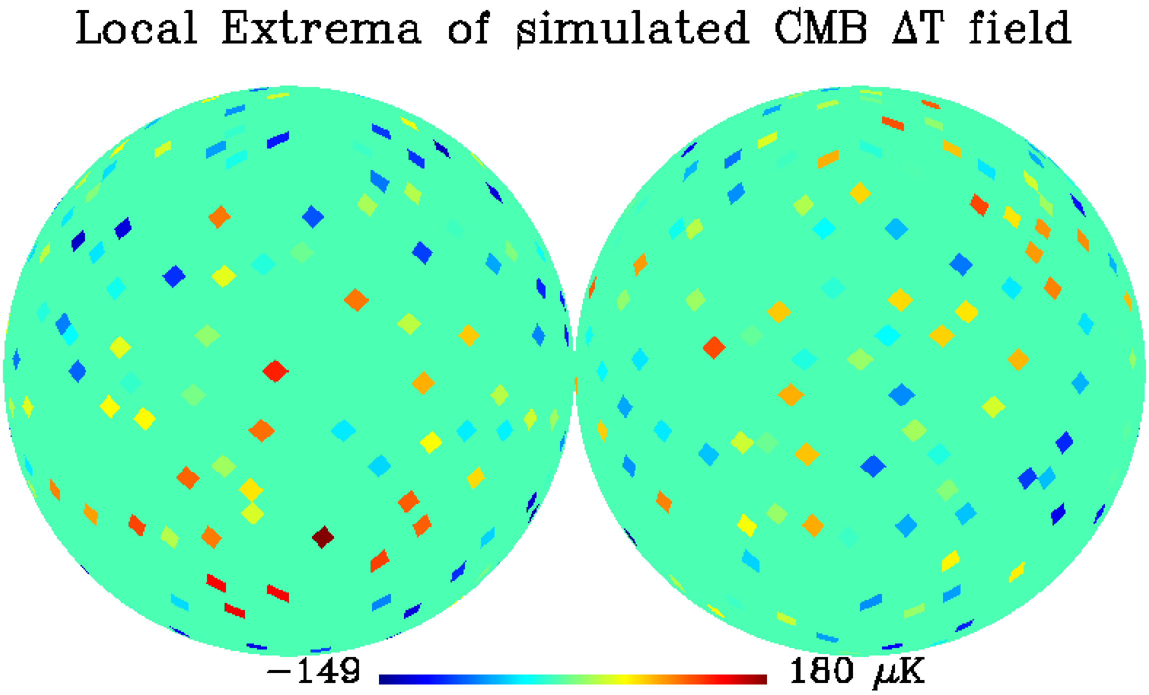

Figure 3.2: For the CMB temperature anisotropy field, its local extrema or spots contribute in varying degrees of magnitude to the orientation matrix, as shown by their lightness or darkness of colour. Hence we associate non-unit masses with these spots. Here, the CMB 2-sphere is shown in an orthographic projection.

$$\mathcal{T}^{(s)} = \frac{\sum_i m_i^{(s)} \tau_i^{(s)}}{\sum_i m_i^{(s)}} \tag{3.221}$$

where,

$$\tau_i^{(s)} = \begin{pmatrix} {x_i^{(s)}}^2 & x_i^{(s)} y_i^{(s)} & x_i^{(s)} z_i^{(s)} \\ x_i^{(s)} y_i^{(s)} & {y_i^{(s)}}^2 & y_i^{(s)} z_i^{(s)} \\ z_i^{(s)} x_i^{(s)} & z_i^{(s)} y_i^{(s)} & {z_i^{(s)}}^2 \end{pmatrix}. \tag{3.222}$$

Here, the superscript $^{(s)}$ stands for $s = h, c$, for hot or cold spots, respectively. For the i^{th} s-spot, $x_i^{(s)}, y_i^{(s)}, z_i^{(s)}$ are its direction cosines. Its non-unit mass weight is $m_i^{(s)} = |\Delta T_i^{(s)}| = |T_i^{(s)} - T_0|$, which is the magnitude of its temperature relative to T_0. The normalisation by the non-unit mass weights in equation (3.221) ensures that the sum of the three eigenvalues of the non-unit mass orientation matrix ($\mathcal{T}^{(s)}$) used by us becomes unity, as it was in the case of the normalised unit-mass orientation matrix (T/n) [102].

The principal advantage of using non-unit masses is that it helps take into consideration the additional randomness from peak values of the spots along with the randomness that comes from eigenvector directions. In the case of perfect uniformity in the placement of spots, there can be no preferred eigenvector directions, and hence all eigenvalues of the orientation matrix must be equal. Inequalities of eigenvalues therefore indicate the presence of non-uniformity. We note that each spot on the CMB sphere may contribute differently in terms of its mass weights ($|\Delta T_i^{(s)}|$) to determine the magnitudes of eigenvalues and hence the preference of any eigenvector direction. Thus the inclusion of non-unit mass weights is crucial for an accurate detection of non-uniformity in the arrangement of spots. In Section 3.3, we further elucidate this using two toy maps.

The orientation matrix is positive definite by construction, and thus all its eigenvalues ($\lambda_i^{(s)}$ for $i = 1, 2, 3$) are positive and its eigenvectors are mutually orthogonal. Considering the three eigenvalues arranged in ascending order, i.e., $0 \leq \lambda_1^{(s)} \leq \lambda_2^{(s)} \leq \lambda_3^{(s)}$, one can quantify the manner and extent of non-uniformity in placements of hot and cold spots about their respective eigenvectors. Isotropic or completely uniform distributions of spots on the CMB sphere correspond to $\lambda_1^{(s)} = \lambda_2^{(s)} = \lambda_3^{(s)}$; for planar girdles of spots that are evenly placed in great circles, $\lambda_1^{(s)} < \lambda_2^{(s)} \simeq \lambda_3^{(s)}$; whereas linear clusters manifest as $\lambda_1^{(s)} \simeq \lambda_2^{(s)} < \lambda_3^{(s)}$. Thus, the following ratios,

$$
\begin{aligned}
\gamma^{(s)} &= \frac{\log \frac{\lambda_3^{(s)}}{\lambda_2^{(s)}}}{\log \frac{\lambda_2^{(s)}}{\lambda_1^{(s)}}}, \\
\zeta^{(s)} &= \log \frac{\lambda_3^{(s)}}{\lambda_1^{(s)}}, \qquad (3.223)
\end{aligned}
$$

can help us to study the nature of placement of spots on the CMB sphere. These are known as the shape and strength parameters, respectively. By definition both these parameters take positive values. The shape parameter describes the arrangement of spots on the sphere, in terms of girdling ($\gamma^{(s)} < 1$) as opposed to clustering ($\gamma^{(s)} > 1$) and transitions ($\gamma^{(s)} \to 1$) between these two shapes of arrangement. The strength parameter quantifies the degree of non-uniformity, starting from a value of zero which corresponds to the case when each of the three eigenvalues are equal to $1/3$ and the distribution of spots is absolutely uniform or

Table 3.1: Value-based interpretations of isotropy estimators: The shape parameter categorises non-uniformly placed spots into clusters or girdles (rings). The strength parameter tells us how weak or strong is the extent of this non-uniformity. Here, $^{(s)}$ can be replaced by $s = h, c$ for hot spots or cold spots, respectively.

Isotropy estimators	Ranges	Interpretations
Shape $\gamma^{(s)}$	$0 \leq \gamma^{(s)} \lesssim \infty$	Girdling for $\gamma^{(s)} \in [0,1)$; Clustering for $\gamma^{(s)} \in (1,\infty)$; Cluster-girdle transitions for $\gamma^{(s)} \to 1$.
Strength $\zeta^{(s)}$	$0 \leq \zeta^{(s)} \lesssim \infty$	Perfect uniformity for $\zeta^{(s)} = 0$; Perfect non-uniformity for $\zeta^{(s)} \to \infty$.

isotropic. We present the ranges of values of these estimators and associated interpretations in Table 3.1. This table may be helpful as a quick reference to categorise the ways in which hot and cold spots are placed on the celestial sphere of the CMB.

Further, to estimate the distributions of values of these estimators, we obtain 10^4 full sky statistically isotropic Gaussian random realisations of the pure CMB using the ΛCDM concordance model based on the Planck 2018 best-fit theoretical angular power spectrum [9]. All pure CMB maps are at a HEALPix [117] resolution of $n_{side} = 16$ with $\ell_{max} = 32$. We identify the hot and cold spots of the pure CMB maps with the help of the HEALPix F90 facility called 'hotspot'. The probability densities of isotropy estimators for these full sky pure CMB maps are shown in Figure 3.3. From the left panel of Figure 3.3, we see that pure CMB realisations exhibit a wide range of values of the shape parameter ($\gamma^{(s)}$) and the probability densities of $\gamma^{(s)}$ for both hot and cold spot placements behave similarly. From the right panel of Figure 3.3, we see that probability density functions of strengths of non-uniformity ($\zeta^{(s)}$) of both hot and cold spots are also similar in behaviour as expected.

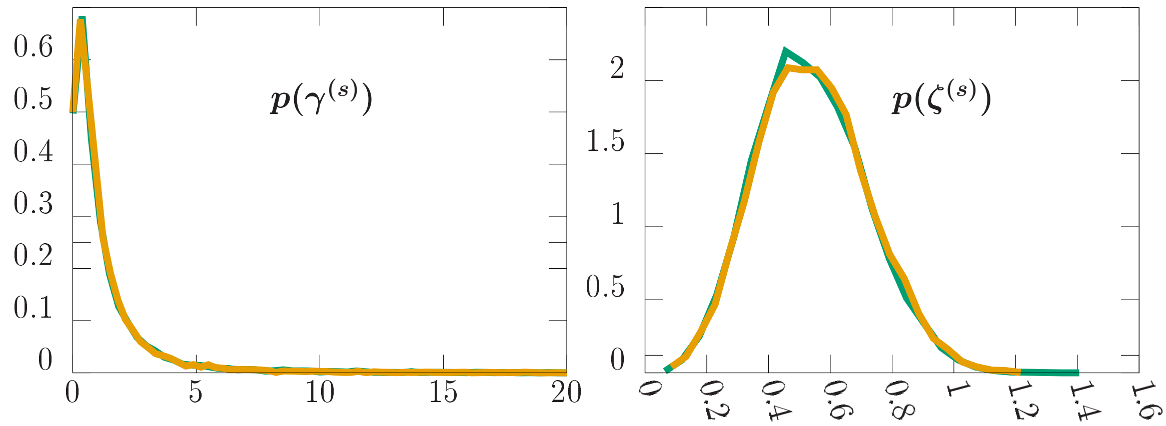

Figure 3.3: Left panel: Probability density functions of the shape parameter ($\gamma^{(s)}$) for hot spots (green) and cold spots (orange) from 10^4 full sky pure CMB maps at HEALPix resolution of $n_{side} = 16$. The horizontal axis has been clipped at $\gamma^{(s)} = 10$, else it ranges up to an order of 10^2. Both curves show qualitatively similar behaviour. Right panel: Probability density functions of the strength parameter ($\zeta^{(s)}$) for hot spots and cold spots. Both $p(\zeta^{(h)})$ and $p(\zeta^{(c)})$ behave similarly.

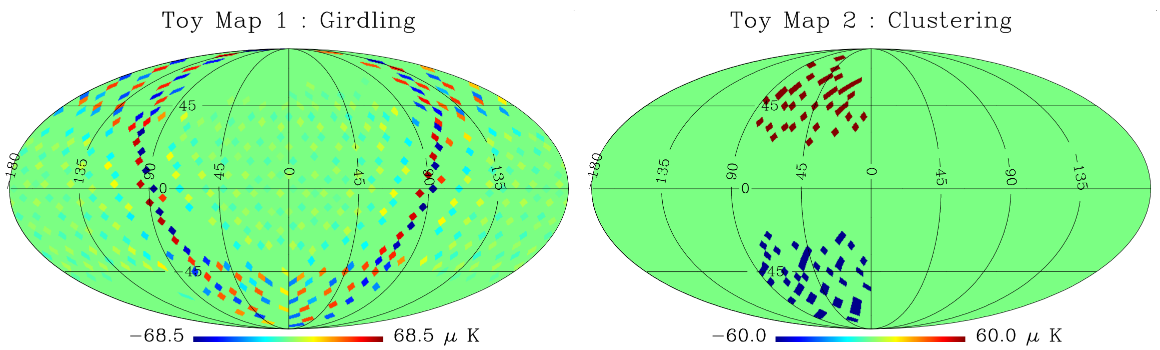

Figure 3.4: Two toy model maps of hot spots and cold spots, to show their girdled and clustered distributions, respectively, with different extents of non-uniformity or anisotropy.

3.3 Analysis of toy models

We test our estimators with two toy CMB maps which have been constructed to illustrate girdling and clustering of spots. Each of the toy maps have different strengths of non-uniformity. We use HEALPix for constructing and analysing these maps. The maps are at a resolution of $n_{side} = 16$.

We form the first toy map (TM1) by constraining its spherical harmonic coefficients ($a_{\ell m}$) in the harmonic space. For this purpose, we randomly set the $a_{\ell m}$ for $\ell = 8$ to a value of 6 and for $\ell = 28$ to to a value of -6 for both real and imaginary parts. Rest of the spherical harmonic coefficients are set to zero. We then convert these $a_{\ell m}$ coefficients to HEALPix

Table 3.2: Values of the isotropy estimators for toy model maps. For the first toy map (TM1), $\gamma^{(s)} < 1$ indicates girdled hot and cold spots, with strengths of $\zeta^{(s)} > 1$. The second toy map (TM2) is more non-uniform with $\zeta^{(s)} > 2$, and has clusters as $\gamma^{(s)} > 1$.

Toy Map	Spots(s)	$\gamma^{(s)}$	$\zeta^{(s)}$
1	h	0.12690120	1.2989503
1	c	0.12694086	1.1855485
2	h	7.1326062	2.7095464
2	c	8.4651048	2.5985995

map at $n_{side} = 16$.

We construct the second toy map (TM2) in the following manner. To assign clustered hot and cold spots, we specify some positive and negative values for two groups of neighbouring pixels of a map array (say m_a) while setting other pixels to a value of zero. We also consider a randomly generated map m_b. Then TM2 is a linear combination of these maps, given by $m_a + \lambda \times m_b$. Here λ is a very small fraction which highly suppresses spots from the randomly generated part (m_b), making them almost invisible.

We show the maps TM1 and TM2 with their hot spots and cold spots in a standard Mollweide projection in Figure 3.4. From the left panel of Figure 3.4 we see that TM1 contains an approximately girdled distribution of spots. Since the non-uniformity of spots in TM1 is distinctly visible, the strength parameter should definitely be greater than zero but it may not be very high due to the presence of several weak (lightly coloured) hot and cold spots in the map. In the right panel of Figure 3.4 we see that the hot and cold spots of TM2 in the northern and southern hemispheres are quite clustered, and their non-uniformity is stronger relative to TM1.

The values of the estimators ascertained from these two toy maps are given in Table 3.2. Clearly, the strength of non-uniformity for TM1 is lower than that of TM2. The values of $\gamma^{(s)}$ for TM1 are lesser than unity, indicating girdles, and those for TM2 indicate clusters as those are greater than unity.

Both maps TM1 and TM2 contain several faint hot and cold spots which have low peak values. Despite being faint, some of these spots are visible for TM1 but for TM2 they are highly suppressed. These spots are numerous and their overall distributions are reasonably free from any signal of girdling or clustering. If such faint spots are considered on an equal footing with the dark coloured spots which have higher peak values, our estimators may not be able to correctly recover the signal of non-uniformity. This would be the case when all spots are treated as unit masses. On such a treatment, we find that

(a) shape parameters of TM1 are $\gamma^{(h)} = 1.2926231$, $\gamma^{(c)} = 1.5587367$, neither of which correspond to girdles.

(b) For TM2, we have $\gamma^{(h)} = 0.98292051$, $\gamma^{(c)} = 0.47354657$, neither of which correspond to clusters.

(c) Strength parameters of TM1 are $\zeta^{(h)} = 0.34948347$, $\zeta^{(c)} = 0.38412180$, which indicate very weak non-uniformity.

(d) For TM2, the strengths are $\zeta^{(h)} = 0.19635766$, $\zeta^{(c)} = 0.17391740$, which indicate nearly uniform placement of spots.

These estimator values obtained with unit-mass weights are markedly insensitive to the visible signatures of non-uniformity of spots. Hence, the use of non-unit mass weights in the orientation matrix for CMB spots is indispensable for a reliable recovery of signals of non-uniformity.

3.4 Application on foreground-minimized CMB maps

We simulate 10^4 pure CMB maps using the Planck 2018 best-fit theoretical angular power spectrum [9] at $n_{side} = 16$ with $\ell_{max} = 32$. All these maps contain pixel smoothing corresponding to the pixel resolution $n_{side} = 16$. The advantage of pixel window smoothing is two fold. First, if the maps are not smoothed by the window function unwanted errors in the characterization of peaks may occur. Secondly, since the HEALPix pixel tessellation does not follow an isotropic distribution, systematics can be introduced in the shape and strength parameters if the maps are not smoothed by the pixel window functions. For the observed CMB maps we downgrade them from $n_{side} = 2048$ (for Planck) or $n_{side} = 512$ (for WMAP) to $n_{side} = 16$ using ‘ud_grade’ facility. Therefore, these low resolution data maps also correctly contain pixel window smoothing effects. We convert the pixel smoothed data maps to spherical harmonic coefficients and reconstruct the actual data maps for our analysis by taking multipoles between $\ell = 2$ to 32. In addition, any existing beam smoothing effects are removed from observed CMB maps. Thus similar to pure CMB maps, the observed maps are not convolved with any beam window function.

We exclude multipoles $\ell = 0, 1$ from our analysis since these correspond respectively, to the monopole of uniform CMB temperature [103] and the dipole due to our motion relative to the CMB rest frame [47]. We neglect noise in the analysis, as it is expected to be insignificant for the low multipole range maps analysed here [270], as these correspond to large angular scales. We utilise the F90 facility 'hotspot' of HEALPix for finding the hot and cold spots for simulated as well as observed CMB maps.

We compute the values of the shape and strength parameters, denoted by x for each of the observed and simulated maps. Then the fraction $P^t(x)$ for each observed data map can be calculated by counting the number of simulations which have a value of x_{sim} greater than that from observed data (x_{data}) and dividing the same by the total number of simulations. Conventionally, x_{data} for which $P^t(x)$ are found outside the confidence interval bounded by the probability values 0.05 and 0.95 are considered unlikely relative to pure CMB realisations. Thus for $P^t(x) < 5\%$, this would imply that x_{data} is unusually high, whereas x_{data} becomes unusually low for $P^t(x) > 95\%$.

In the following Sections 3.4.1 and 3.4.2, we describe the observed CMB maps and masks used for the analysis. We first choose to include the galactic region in the analysis along with the other parts of the sky. In this case, our study concerns two cases. First we use the entire sky and secondly we exclude only the region corresponding to the non-Gaussian cold-spot (NGCS). Thereafter, we exclude the galactic regions from the analysis. The inclusion and exclusion of the galactic regions in two different analyses help us understand effects of any (minor) residual foregrounds that may be present in the galactic regions even after performing foreground minimization. We present the results for isotropy statistics in Section 2.6.

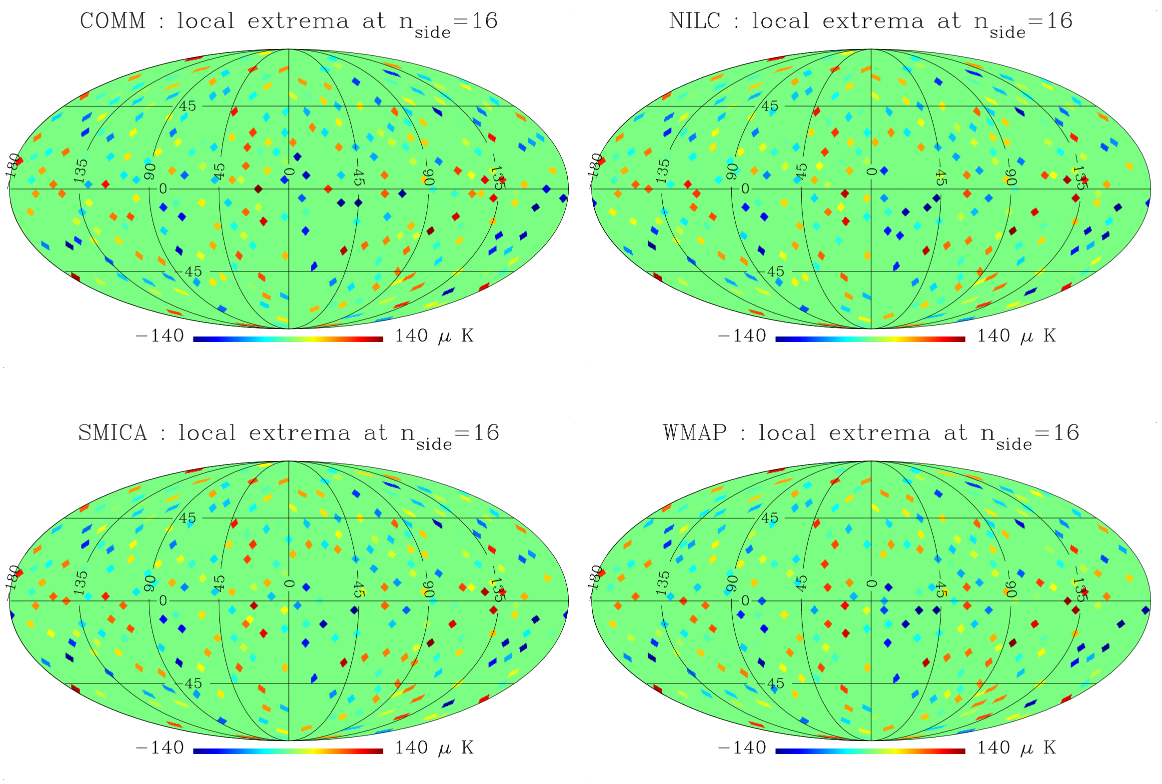

Figure 3.5: Mollweide projections of hot spots and cold spots for the four full sky cleaned CMB maps, i.e., COMM, NILC, SMICA, and WMAP at a HEALPix resolution of $n_{side} = 16$. These subfigures illustrate how hot and cold spots are placed on observed full sky CMB maps.

3.4.1 Case I: Without galactic masks

3.4.1.1 Input maps

We use four cleaned maps, namely, those of the 2018 release [12] of Planck's Commander (COMM), NILC, and SMICA, and WMAP's 9 year ILC [34] (hereafter referred to as WMAP) for the full sky analysis. We present Mollweide projections showing hot and cold spots of these four individual full sky maps in Figure 3.5 to illustrate how the spots are scattered on the observed full sky CMB.

3.4.1.2 NGCS mask

The non-Gaussian Cold spot (NGCS) [71, 194, 276] is a well established anomaly, centred at $(\theta, \phi) = -57$**??**jnltextdegree$, 209$**??**jnltextdegree. The north-south power asymmetry [37, 229, 11, 92, 93, 94] was seen to be correlated with the NGCS [36], the significance of which effect was seen to be low for low resolution [215] maps at HEALPix $n_{side} = 16$. In order to

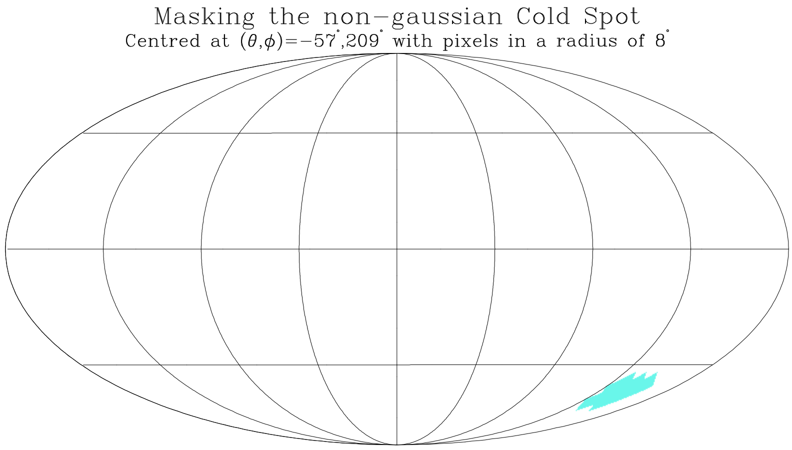

Figure 3.6: The non-Gaussian cold spot (NGCS) mask at a HEALPix resolution of $n_{side} = 16$: the masked region is in cyan; the white region is unmasked.

check for any correlation between the isotropy estimators and the NGCS, we mask out the map pixels in a radius of 8**??**jnltextdegree from the cold spot center. This mask is shown in Figure 3.6. This mask is used independently for the four cleaned maps and all pure CMB maps described above, and later along with two galactic masks for nine observed maps as mentioned below.

3.4.2 Case II: With galactic masks

3.4.2.1 Input maps

In addition to the four cleaned CMB maps (COMM, NILC, SMICA, and WMAP 9 year ILC), we use WMAP's foreground reduced Q, V and W frequency maps and Planck's 'fgsub-sevem' $70\,\mathrm{GHz}$ and $100\,\mathrm{GHz}$ frequency maps. These five frequency maps will hereafter be referred to as freqQ, freqV, freqW, freq70, and freq100, respectively.

3.4.2.2 Masks

Foreground residuals predominantly in the galactic region of cleaned CMB maps may cause certain unusual patterns to manifest in the observed data when it is analysed relative to pure CMB realisations. The use of a mask for the galactic region and some extra-galactic point sources is required to check if such unusual patterns are truly characteristic of the CMB or due to residual systematics.

We utilise low resolution versions of the $KQ75$ mask of WMAP 9 year data and the $U73$ mask of Planck 2018 data, which is a product of the temperature confidence masks associated with COMM, NILC, SEVEM, and SMICA. The two masks are shown in Figure 3.7. The $KQ75$ mask is very conservative in the sense that it comprises a wider galactic cut and conceals a larger number of point sources as compared to the $U73$ mask.

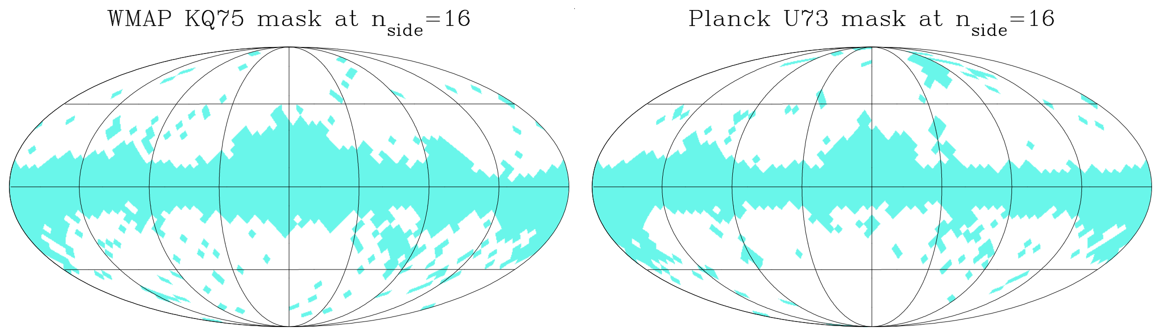

Figure 3.7: $KQ75$ and $U73$ masks at a HEALPix resolution of $n_{side} = 16$: the masked region is in cyan; the white region is unmasked.

These low resolution masks are obtained by downgrading their high resolution variants to HEALPix $n_{side} = 16$ and applying thresholds of 0.85 and 0.98 for the $KQ75$ and $U73$ masks, respectively. A threshold of y entails setting all pixels with values $\leq y$ to 0, and the rest to 1, after a mask is downgraded. The resulting sky fractions for the $KQ75$ and $U73$ masks are 62.9% and 67.5%, respectively. The thresholds chosen here are a bargain between a good sky fraction of the CMB for signal detection vis a vis any dominant foreground sources at the large scales [270] considered here. The choices for thresholds are not altogether arbitrary, but inspired from [14]. Additionally, we consider the union masks of $KQ75$ and $U73$ with the NGCS mask, referred to as $KQ75-CS$ and $U73-CS$, respectively.

We apply these galactic masks one by one, simultaneously to the four cleaned CMB and five foreground reduced frequency maps and 10^4 pure CMB maps. The partial sky analysis with the nine input maps of observed CMB using galactic masks provides checks of robustness of any detected signal, against the following:

Table 3.3: Values of the isotropy estimators for observed full sky CMB maps: Strengths $\zeta^{(h)}$ and $\zeta^{(c)}$ are low, indicating mostly uniform placements of hot spots and cold spots.

Data Map	$\gamma^{(h)}$	$\zeta^{(h)}$	$\gamma^{(c)}$	$\zeta^{(c)}$
COMM	1.5660	0.2137	1.5079	0.3479
NILC	1.5811	0.1849	0.7978	0.2800
SMICA	1.0435	0.2089	0.5460	0.2367
WMAP	0.4239	0.2148	2.4463	0.3408

1. Different galactic masks ($KQ75$ and $U73$),
2. Various methods of foreground cleaning (Planck's COMM, NILC, and SMICA, and WMAP's ILC) and reduction (foreground template model reduction [134, 34] for freqQ, freqV, freqW and SEVEM [100, 172] for fgsub-sevem freq70 and freq100 maps),
3. Several frequencies (Q, V, W bands and $70\,\mathrm{GHz}, 100\,\mathrm{GHz}$),
4. Presence or absence of the NGCS when the galactic region is masked out, and
5. Different instruments (WMAP and Planck's Low Frequency [15] and High Frequency Instruments [10]).

3.5 Results and analysis

We present results from the analysis of foreground minimized CMB maps with and without galactic masks. Without galactic masks, we analyse four cleaned CMB maps, firstly, for the full sky, and secondly after masking the NGCS. With galactic masks, we analyse nine observed CMB maps.

3.5.1 Case I: Without galactic masks

For the four full sky cleaned CMB maps used, we tabulate the values of the estimators in Table 3.3. We see that mostly uniform placements of hot spots and and cold spots can be inferred from the values of the strength parameter.

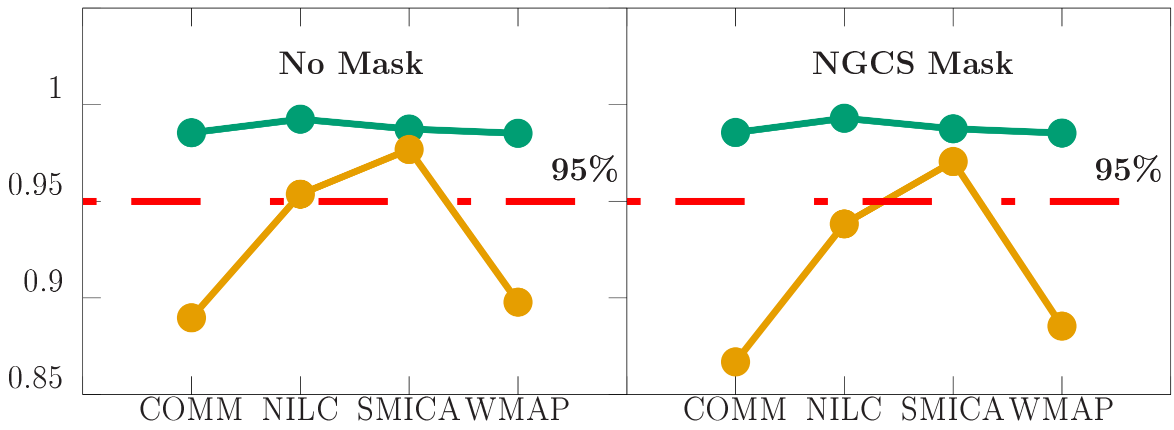

Figure 3.8: Left panel: $P^t(\zeta^{(h)})$ (green) and $P^t(\zeta^{(c)})$ (orange) are shown; for the four full sky maps, unusual uniformity of hot spots is seen for all maps, and that of cold spots is seen for NILC and SMICA. Right panel: for the four maps with the NGCS mask, unusual uniformity of hot spots persists for all maps, but that of cold spots is seen for SMICA.

In Figure 3.8, we show P^t for the four cleaned CMB maps, without galactic masks. On the left panel of Figure 3.8, results from the full sky maps are presented. We find that the strength parameters $\zeta^{(h)}$ and $\zeta^{(c)}$ are relatively lower than those from pure CMB simulations, as $P^t(\zeta^{(h)})$ ranges between 98.52%–99.25% and $P^t(\zeta^{(c)})$ ranges between 88.97%–97.68%. Thus, we see robustly low $\zeta^{(h)}$ for all the four cleaning methods. The lowest value of $\zeta^{(h)} = 0.1849$ with $P^t(\zeta^{(h)}) = 99.25\%$ is seen for NILC. Low $\zeta^{(c)}$ for NILC and SMICA are seen, of which the lowest $\zeta^{(c)} = 0.2367$ with $P^t(\zeta^{(c)}) = 97.68\%$ is seen for SMICA.

On the right panel of Figure 3.8, results from the four maps after masking the NGCS are shown. We find that $P^t(\zeta^{(h)})$ ranges between 98.53%–99.30%, and $P^t(\zeta^{(c)})$ lies between 86.69%–97.06%. Thus removal of the NGCS very slightly increases the significance of low $\zeta^{(h)}$ while decreasing the significance of low $\zeta^{(c)}$ relative to pure CMB realisations. Robustly low $\zeta^{(h)}$ for all the four cleaned maps is seen with the NGCS mask, and the lowest value of $\zeta^{(h)} = 0.1849$ with $P^t(\zeta^{(h)}) = 99.30\%$ occurs for NILC. Low $\zeta^{(c)}$ is seen for SMICA with $\zeta^{(c)} = 0.2516$ and $P^t(\zeta^{(c)}) = 97.06\%$.

Thus, unusually weak non-uniformity of hot spots in all four maps is seen for full sky as well as for partial sky outside the NGCS mask. However, the shape parameters $\gamma^{(h)}, \gamma^{(c)}$ are in good agreement with pure CMB realisations. Unusually low strength of non-uniformity of cold spots is seen for NILC and SMICA for full sky. Interestingly, after masking the galactic regions, this signal spreads over several cleaned maps. We discuss this in detail in the subsequent section.

3.5.2 Case II: With galactic masks

In Figure 3.9, we show P^t for the nine observed partial sky CMB maps, with galactic masks. On the top left panel of Figure 3.9, results obtained with the use of $KQ75$ mask are shown. Significantly low $\zeta^{(c)}$ is seen for all the maps, except SMICA and freq100. Lowest $\zeta^{(c)} = 0.4007$ with $P^t = 96.75\%$ is seen for freqW, without the NGCS mask. On the top right panel of Figure 3.9, we again obtain robust results of anomalously low $\zeta^{(c)}$ for the $KQ75 - CS$ mask for all maps, except SMICA and freq100. Lowest $\zeta^{(c)} = 0.3924$ with $P^t = 97.03\%$ is seen for freqW.

On the bottom left panel of Figure 3.9, results obtained with the use of $U73$ mask are shown. Again, an unusually low $\zeta^{(c)}$ is seen robustly for various maps. Significantly low $\zeta^{(c)}$ is seen for all maps except freq100. Lowest value of $\zeta^{(c)} = 0.2446$ occurs for freqW with $P^t(\zeta^{(c)}) = 99.37\%$ without the NGCS mask. From the bottom right panel of Figure 3.9, for $U73 - CS$ mask, we see significantly low $\zeta^{(c)}$ for all maps except freq100. Lowest value of $\zeta^{(c)} = 0.2432$ with $P^t = 99.44\%$ occurs for freqW.

We have presented the numerical values of $P^t(\zeta^{(c)})$ in Table 3.4. These numerical values indicate that the unusually weak non-uniformity of cold spots is more significant with the use of the less conservative $U73$ and $U73 - CS$ masks. The values of P^t in Table 3.4 reveal that the the absence of the NGCS slightly complements the unusual nature of $\zeta^{(c)}$ with the $KQ75$ mask.

Thus, unusually low strength of non-uniformity of cold spots is seen for all maps, except SMICA and freq100 when $KQ75$ mask is applied with and without the NGCS mask. Again, such weak non-uniformity of cold spots is seen for all maps, but with the exception of freq100, when $U73$ mask is applied with and without the NGCS mask. Strength of non-uniformity of hot spots ($\zeta^{(h)}$) is also low, but the effect is not significant relative to pure CMB realisations. A single instance of an unusual ring structure of hot spots for freqQ (not shown in Figure 3.9) is seen with $P^t(\gamma^{(h)}) = 99.32\%$ for the $U73$ mask and $P^t(\gamma^{(h)}) = 99.33\%$ for the $U73 - CS$ mask. But no significantly unusual $\gamma^{(h)}$ was seen with the more conservative $KQ75$ and

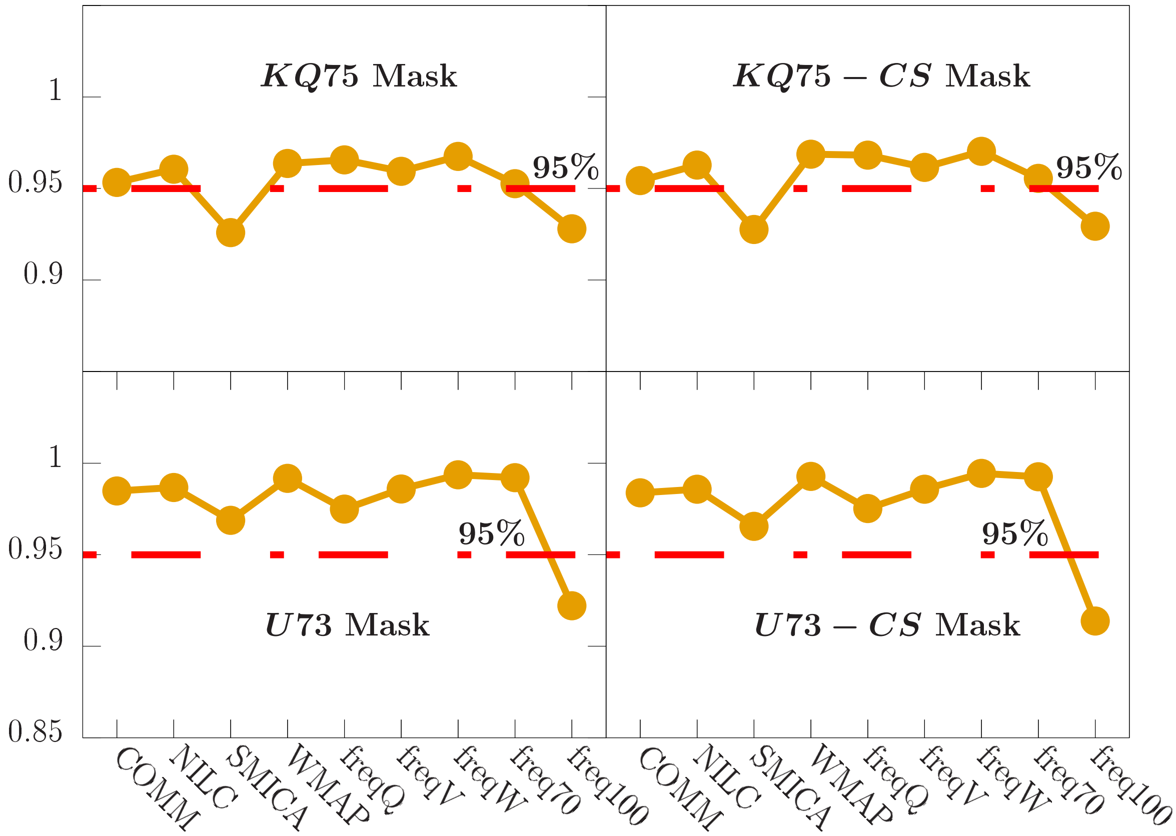

Figure 3.9: Top left panel: $P^t(\zeta^{(c)})$ is in orange; $\zeta^{(c)}$ is significantly low for all maps except SMICA and freq100. Top right panel: unusual uniformity of cold spots is seen for all maps except SMICA and freq100. Bottom left panel: similarly unusual uniformity of cold spots is seen for all maps except freq100. Bottom right panel: again, $\zeta^{(c)}$ is significantly low for all maps except freq100.

Table 3.4: Numerical values of $P^t(\zeta^{(c)})$ for partial sky analysis with galactic masks. A very high P^t entails that the value of the estimator from observed data is unusually low, and vice versa. Hence, we see anomalously low $\zeta^{(c)}$ for several maps, albeit with different P^t values for different masks. Significant values of P^t are in boldface.

Map	$KQ75$	$KQ75 - CS$	$U73$	$U73 - CS$
COMM	**0.9533**	**0.9543**	**0.9848**	**0.9838**
NILC	**0.9605**	**0.9628**	**0.9867**	**0.9858**
SMICA	0.9259	0.9276	**0.9688**	**0.9655**
WMAP	**0.9637**	**0.9687**	**0.9917**	**0.9928**
freqQ	**0.9656**	**0.9682**	**0.9749**	**0.9752**
freqV	**0.9594**	**0.9615**	**0.9859**	**0.9858**
freqW	**0.9675**	**0.9703**	**0.9937**	**0.9944**
freq70	**0.9526**	**0.9555**	**0.9921**	**0.9926**
freq100	0.9280	0.9294	0.9221	0.9138

$KQ75-CS$ masks. This implies that the ring structure of hot spots for freqQ could be due to some foreground residuals when the $U73$ and $U73-CS$ masks are applied. Apart from this occurrence, no other unusual clustering or girdling is seen for any of the maps with the four masks.

3.6 Is anomalously weak non-uniformity due to low variance?

It has been seen before that on an average hot and cold spots of the observed CMB have unexpectedly low peak values [169]. Besides, the variance of the CMB temperature anisotropy field is anomalously low [202]. Therefore such low variance in addition to low mean values of local extrema entails that the peak values when measured will turn out to be lower than expected from statistically isotropic Gaussian random fluctuations of the temperature field. Since peak values of spots are incorporated as non-unit mass weights in the orientation matrix, our novel isotropy statistics carry this information. Further, the low variance anomaly was seen to be confined to the northern ecliptic hemisphere. Any such directional preference is additionally manifested in the relative magnitudes of eigenvalues, which is encapsulated by the strength of non-uniformity ($\zeta^{(s)}$). Thus it is important to check if the signal of anomalously low strength of non-uniformity as seen for hot spots on full sky and partial sky with the NGCS mask, or that for cold spots on partial sky outside galactic masks are correlated with the low CMB variance anomaly. Another interesting question to consider is that of how the shape and strength parameters behave on different scales. We can understand this behaviour by analysing CMB maps containing different ranges of multipoles.

Thus, we seek to investigate the following:

(a) whether the signal of anomalously weak non-uniformity is correlated with low CMB temperature variance, and

(b) how the isotropy statistics behave on different scales.

Since the CMB low variance anomaly disappears when the quadrupole and octupole are excluded [73], therefore both these questions can be addressed by excluding the quadrupole and octupole which correspond to two of the largest scales.

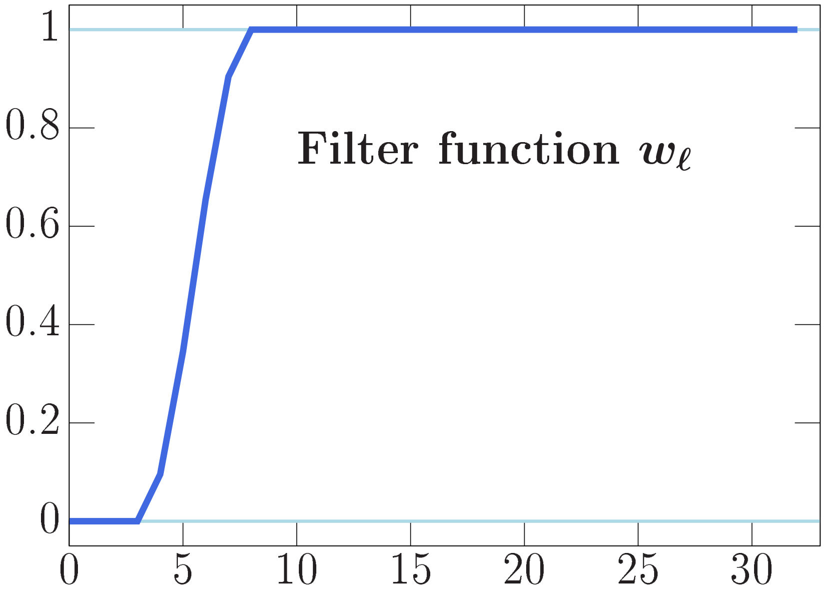

Figure 3.10: The cosine filter function which is multiplied with the spherical harmonic coefficients of CMB maps to study how quadrupole-octupole contributions and hence low CMB variance may affect the strength of non-uniformity of hot and cold spots.

Thus we reconstruct all pure and observed CMB maps after multiplying their spherical harmonic coefficients by a cosine filter,

$$
\begin{aligned}
w_\ell &= 0 \quad \text{for } \ell \in [0,3], \\
w_\ell &= \frac{1}{2}\left[1-\cos\left(\frac{\pi(\ell-3)}{5}\right)\right] \quad \text{for } \ell \in [4,7], \\
w_\ell &= 1 \quad \text{for } \ell \in [8,32].
\end{aligned} \tag{3.224}
$$

This filter function (shown in Figure 3.10) excludes the quadrupole and octupole and smoothly suppresses low multipoles upto $\ell = 7$. We perform the same analysis as in Section 3.5 for the new maps and find that:

1. without galactic masks, the signal robustly disappears across all cleaned maps for the full sky and with NGCS mask. This is reflected in the values of P^t, which range between 48.68%–90.92% for $\zeta^{(h)}$ and 30.12%–94.01% for $\zeta^{(c)}$.

2. However, with galactic masks, the signal does not persist in any of the foreground minimized maps except maps of freqQ (with $U73$ mask) and freqV (with $KQ75, KQ75-CS$ masks) for which $\zeta^{(c)}$ is unusually low. Thus we see that $P^t(\zeta^{(h)})$ ranges between 31.22%–81.59% whereas $P^t(\zeta^{(c)})$ lies between 47.93%–97.02%.

Since the signal of weak non-uniformity robustly disappears across all cleaned maps for full and partial sky coverage, this indicates that the signal could potentially be related with low CMB variance and quadrupole-octupole contributions, and these may share a common origin. Besides, the loss of robustness in disappearance of the signal occurs only for freqQ and freqV maps outside the galactic region. This strongly suggests that some foreground residuals in these two maps contribute to the signal.

3.7 Some other considerations

In our work we have considered separate sets of hot spots and cold spots. Further we have taken into account the peak values of spots relative to the mean CMB temperature, in the form of non-unit mass weights. In Section 3.3, we have demonstrated for two toy maps how the use of unit mass weights is insufficient to accurately recover any signal of non-uniformity of spots. However, for pure and observed CMB maps, one may be curious to consider:

(a) The use of unit masses for the hot and cold spots,

(b) The composite set of hot and cold spots taken together.

We attempt at shedding light on the consequences of these choices by analysing both types of spots together, using a single orientation matrix,

$$\mathcal{T}^{(h+c)} = \frac{\sum_i m_i^{(h)} \tau_i^{(h)} + \sum_j m_j^{(c)} \tau_j^{(c)}}{\sum_i m_i^{(h)} + \sum_j m_j^{(c)}}, \tag{3.225}$$

for two cases, i.e, with unit and non-unit masses. Here, the superscript $^{(h+c)}$ denotes the composite set including both hot and cold spots.

When both kinds of spots are taken together, we expect a more uniform (isotropic) placement of the spots from pure CMB realisations, compared to the case when they are considered separately. Thus we expect low strength of non-uniformity ($\zeta^{(h+c)}$) for most of the pure CMB maps. A low $\zeta^{(h+c)}$ corresponds to very closely spaced eigenvalues, so that there are almost no preferred directions for any non-uniform placements of the spots.

We know that with the choice of non-unit masses as opposed to unit masses, we are introducing the randomness which is attributable to the peak values of spots in the system. This is in addition to the randomness associated with the eigenvector directions. Hence performing a comparative study of unit ($m_i^{(h)}, m_i^{(c)} = 1$) and non-unit masses will help elucidate the advantage of considering non-unit masses to corroborate the expected isotropy of eigenvalues. We show the probability distributions of the shape and strength parameters for simulated pure CMB maps in Figure 3.11 and those for the three eigenvalues ($\lambda_1^{(h+c)} \leq \lambda_2^{(h+c)} \leq \lambda_3^{(h+c)}$) in Figure 3.12. We use the colour magenta for the case of unit-mass weights and cyan for the case of non-unit mass weights.

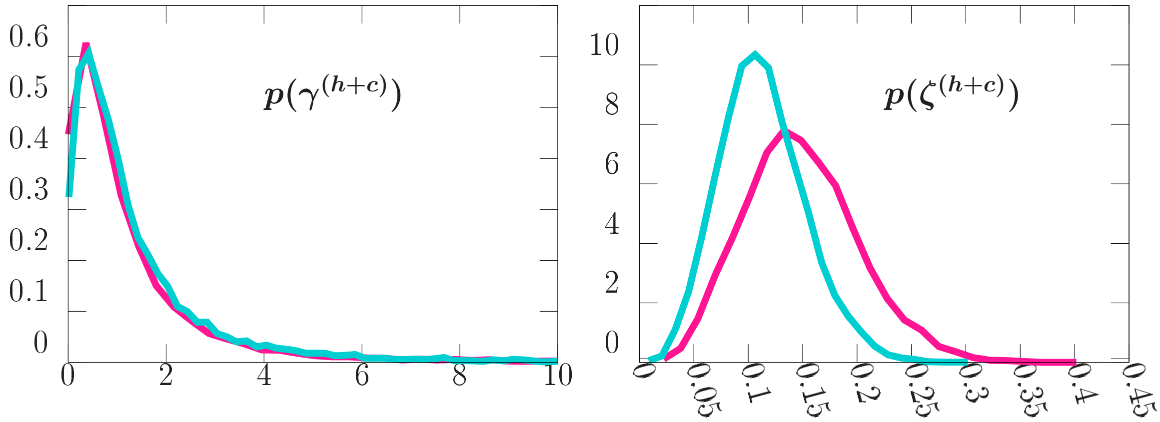

Figure 3.11: Left panel: Probability density functions of the shape parameter ($\gamma^{(h+c)}$) obtained from Monte-Carlo simulations are shown for unit masses (magenta) and for non-unit masses (cyan). The horizontal axis is clipped at 10, else it ranges up to an order of 10^2. Both the densities show qualitatively similar behaviour. Right panel: Probability density functions of the strength parameter ($\zeta^{(h+c)}$) for unit-mass and non-unit mass weights are shown. For non-unit mass case $p(\zeta^{(h+c)})$ peaks at lower values of $\zeta^{(h+c)}$.

The left panel of Figure 3.11 shows that the distributions for unit and non-unit masses behave similarly for the shape parameter $\gamma^{(h+c)}$. From the right panel of Figure 3.11, for $\zeta^{(h+c)}$ with non-unit masses, the range of values is more constricted relative to that with unit-masses, and the peak of the $p(\zeta^{(h+c)})$ curve is at lower values of $\zeta^{(h+c)}$ for non-unit mass weights, hence corresponding to greater uniformity. From subfigures of Figure 3.12, we see that the expectations of uniformity are adhered to for unit and non-unit masses. However, in the case of non-unit masses, the most probable eigenvalues are definitely closer in magnitude to each other and to $1/3$. Further, the spread in the probability distributions of the eigenvalues is smaller for non-unit mass weights.

As for observed CMB maps, we find that when both types of spots are taken together with unit masses, the observed data is in good agreement with the concordance model. But we see some unusual estimator values when non-unit masses are considered, as shown in

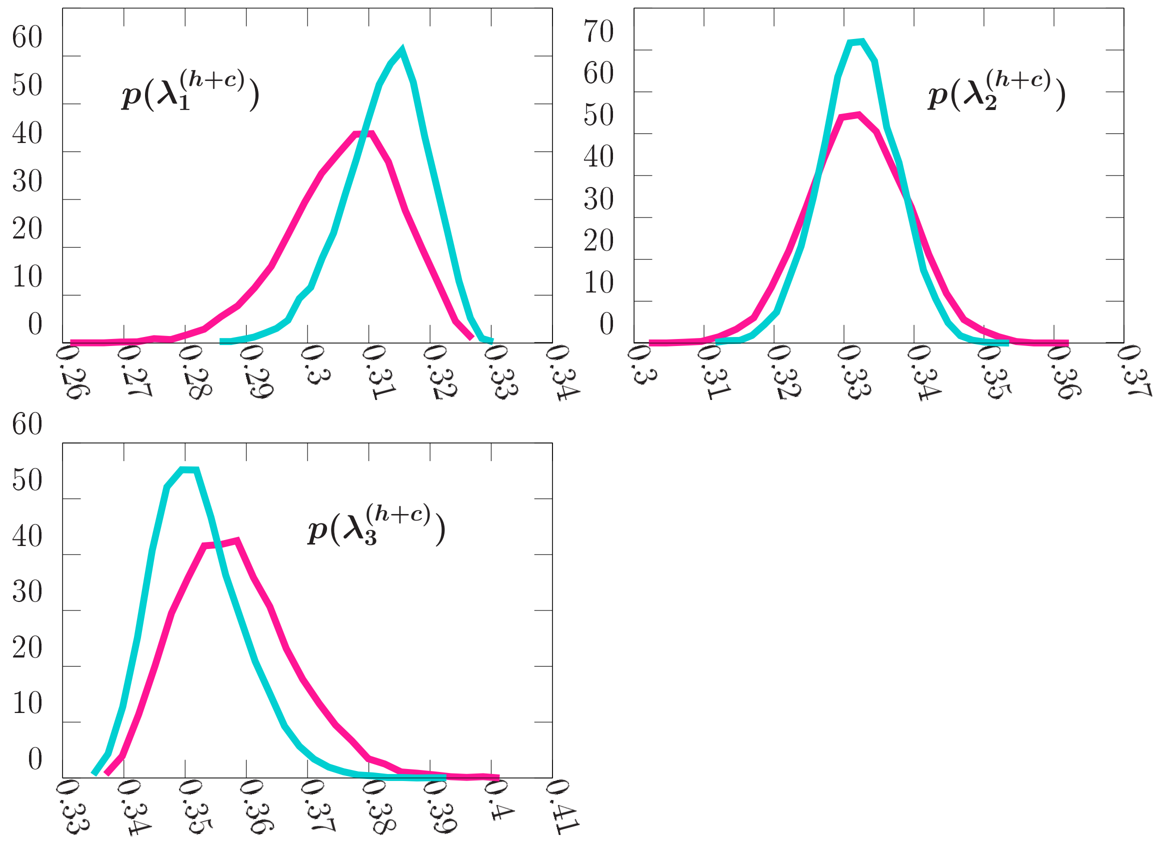

Figure 3.12: Top left panel shows probability density functions of the smallest eigenvalue ($\lambda_1^{(h+c)}$) in magenta for unit masses, and in cyan for non-unit masses. Top right panel shows the density functions of the intermediate eigenvalue ($\lambda_2^{(h+c)}$). Bottom panel shows the density functions of the largest eigenvalue ($\lambda_3^{(h+c)}$). All three density functions for non-unit mass weights have a smaller spread. The most probable values of $\lambda_1^{(h+c)}$, $\lambda_2^{(h+c)}$, $\lambda_3^{(h+c)}$ for non-unit masses are closer to each other and to $1/3$ as opposed to those for unit-masses. This is due to the additional randomness introduced into the orientation matrix while using non-unit mass weights.

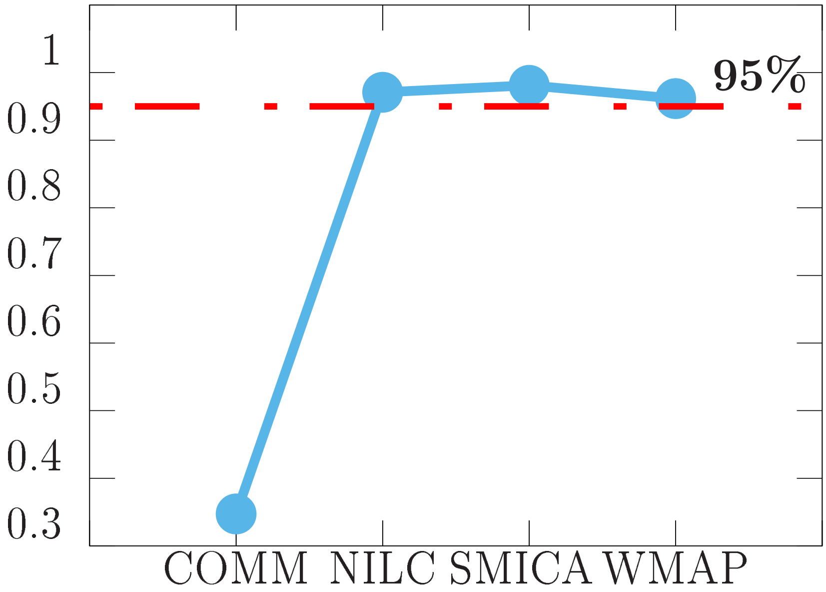

Figure 3.13: For non-unit mass weights, the fraction $P^t(\zeta^{(h+c)})$ is shown in light-blue. The observed full sky maps of NILC, SMICA and WMAP have unusually low values of $\zeta^{(h+c)}$.

Figure 3.13. From this figure we notice that for non-unit masses $\zeta^{(h+c)}$ is unusually low for NILC, SMICA and WMAP. The robustness of this signal is violated only for COMM which has a higher value of $\zeta^{(h+c)}$ compared to the other three cleaned maps. All the cleaned maps are representative of the same CMB signal, possibly barring some minor foreground residuals that differ among these maps. Such residuals could be causative of the differences in values of $\zeta^{(h+c)}$ between COMM and the other maps. We will study the cause of such differences in detail in a future work. In addition we find that the value of $\gamma^{(h+c)}$ is unusually high for NILC and WMAP, and low for SMICA (not shown in Figure 3.13). Hence, this analysis illustrates how the use of non-unit masses is sensitive to any of the signals that could arise from the randomness of the peak values of hot spots and cold spots, as well as that from their eigenvector directions. This makes the use of non-unit masses in the orientation matrix a more general and inclusive approach. Hence, treating hot and cold spots separately with non-unit masses provides us with an opportunity to explore their distinct behaviours regarding isotropy.

3.8 Summary and conclusion

The principal property of isotropy of the distributions of hot spots and cold spots of the CMB is an important facet that needs to be studied by performing detailed investigations using foreground minimized CMB maps. An unusual observed property could give insights into new physics as regards the existence of any structure in the early universe. In this chapter, we presented a modified form of the orientation matrix to account for magnitudes of the data points on a 2-sphere. Eigenvalues of this matrix can be used to construct the so-called shape ($\gamma^{(s)}$) and strength ($\zeta^{(s)}$) parameters, where the superscript s can be replaced with h or c to denote hot or cold spots, respectively. We employed these parameters as estimators to analyse distributions of hot and cold spots on the CMB maps at low resolution. The shape parameter helps distinguish clusters or girdles (rings) of the spots, and the strength parameter quantifies how strongly non-uniform (anisotropic) is their placement on the celestial sphere. Large scale homogeneity and isotropy can be investigated quantitatively with the help of these estimators. We demonstrated this with the help of two toy model CMB maps. The estimators were also evaluated for observed CMB maps and compared with those from pure CMB maps, which are Monte-Carlo simulations of statistically isotropic realisations of the CMB obtained using the ΛCDM concordance model.

In our study we consider analysis over both full sky and partial sky CMB maps. For full sky analysis we use four foreground cleaned CMB maps, i.e., Commander (COMM), NILC and SMICA from Planck's 2018 data-release, and WMAP's 9 year ILC map (WMAP). For partial sky analysis we use several masks. These include non-Gaussian cold spot (NGCS) mask, WMAP $KQ75$ and Planck $U73$ masks. We also use two union masks which are determined by the pairs of masks $KQ75$, NGCS and $U73$, NGCS. For partial sky analysis with galactic masks, in addition to the four foreground cleaned maps mentioned above, we use WMAP's foreground reduced Q, V, W frequency band maps (freqQ, freqV, freqW), and Planck's foreground subtracted 'fgsub-sevem' 70, 100 GHz maps (freq70, freq100) respectively, resulting in a set of nine foreground minimized CMB maps for this case. A summary of important observations stemming out from the work presented in this chapter is mentioned below.

Employing isotropy statistics over full sky we find

(i) that the hot spots of all four cleaned maps exhibit highly uniform distributions. These correspond to consistently low values of $\zeta^{(h)}$ ($> 95\%$ C.L.) when compared with pure CMB maps.

(ii) The values of $\zeta^{(c)}$ are small. The distributions of cold spots are consistent with pure CMB realisations except for NILC and SMICA.

(iii) Since the distributions of hot spots and that of cold spots tend to be uniform, neither type of spots for the cleaned maps show any signature of a ring or clustering nature.

(iv) Masking the NGCS only slightly increases the significance of low $\zeta^{(h)}$ for the four maps, while slightly reducing that of low $\zeta^{(c)}$ for SMICA and washing out the signal of low $\zeta^{(c)}$ for NILC. However, the conclusion of point (iii) above remains unchanged with respect to the NGCS mask.

Analysing isotropy statistics over the $KQ75$ masked sky we find

(i) that the signal of highly uniform placement of hot spots as seen for the full sky disappears. Instead, the cold spots for all nine maps tend to be very uniform. They are significantly uniform (at $> 95\%$ C.L.) for all the partial sky CMB maps except SMICA and freq100 maps.

(ii) The significance of the above findings slightly increases after applying the NGCS mask.

(iii) We do not find any clustering or girdling (ring) structure of either of hot or cold spots, as in the full-sky case.

Instead of the $KQ75$ mask if we apply the $U73$ mask,

(i) the distribution of cold spots becomes even more uniform, pushing the probability of observation of such high degree of uniformity compared to pure CMB realisations further into the critical region for all the partial sky CMB maps, except freq100.

(ii) However, unlike the case of the KQ75 mask, when the NGCS mask is applied, the significance of the results slightly decrease for COMM, NILC, SMICA, freqV, and increase for WMAP, freqQ, freqW, and freq70.

(iii) No specific signature of girdling or clustering is observed for hot or cold spots, except with freqQ for which some ring structure exists with and without the NGCS.

Thus, with the analysis of partial sky outside galactic masks, very low $\zeta^{(c)}$ is found to be anomalous for most of the nine maps. This result is robust despite the use of two different masks (KQ75 and U73), data from different instruments (WMAP and Planck's HFI and LFI) and at various frequencies, and masking of the NGCS. Exceptions to such robustness are SMICA and freq100 with the $KQ75$ mask and freq100 with the $U73$ mask. However the low values of $\zeta^{(c)}$ for these two maps are still close to being unlikely at $> 91\%$ C.L.

The strength of non-uniformity for hot spots ($\zeta^{(h)}$) is seen to be robustly low for all the cleaned maps (COMM, NILC, SMICA, and WMAP's ILC) on the full sky and on the partial sky outside the NGCS mask. As for the partial sky analysis with galactic masks, we find that the low values of $\zeta^{(h)}$ are no longer significantly unexpected. This could mean that some galactic foreground residual common to all the four cleaned CMB maps is causative of the unusually low $\zeta^{(h)}$ when the galactic region is included for the analysis. Irrespective of its actual nature of origin, a washout of this signal is probable due to masking of the galactic region.

The use of galactic masks may not completely rule out any unknown foreground residuals or other systematic errors creeping in from the unmasked region of the sky. However, the simultaneous application of masks to both pure and observed CMB maps rules out a cut-sky effect as a causative agent of the anomalies observed.

The average peak values of hot spots and cold spots and the CMB temperature variance are known to be anomalously low. Since we consider peak values for studying non-uniformity of spots, therefore the signal of low strength of non-uniformity may be related with the low CMB temperature variance. The low variance anomaly is seen to vanish when the quadrupole and octupole are removed. Hence we perform our analysis again after using a cosine filter which excludes the quadrupole and octupole. A robust disappearance of the signal occurs across all cleaned maps, indicating that the low variance anomaly and the unusually weak non-uniformity of spots are potentially related. The robustness is lost on the partial sky outside galactic masks only for freqQ and freqV maps, which strongly suggests that some foreground residuals in these two maps contribute to the signal.

The source of the signals observed in this work remains uncertain at present. Further investigation will be necessary for understanding the possible origin of the signals observed in this work. The robustness of the uniform signal of hot spots on the full sky and sudden spill over of the cold spot signal over most of the cleaned CMB maps (obtained from two different satellite missions, several different frequencies, detectors and foreground removal algorithms) excluding galactic regions, raises a significant curiosity as to whether the signals may be related to a cosmological origin. Additionally, both these signals are seen to be independent of the presence or absence of the non-Gaussian cold spot. However, we find that the signals of anomalously weak non-uniformity of spots could share a common origin with the low CMB temperature variance and anomalous contributions of the quadrupole and octupole.

CHAPTER 4

DETECTION OF DIPOLE MODULATION IN CMB TEMPERATURE ANISOTROPY MAPS FROM WMAP AND PLANCK USING ARTIFICIAL INTELLIGENCE

4.1 Introduction

Departures from Statistical Isotropy (SI) of the Cosmic Microwave Background (CMB) temperature field may indicate limitations or errors in measurement of the CMB despite the use of highly precise instruments for observation, if not due to an actual breakdown of the rotational invariance of the primordial power spectrum. However, by means of appropriate statistical methods, systematic effects or foreground residuals may be considerably eliminated as possible causes of deviations from SI.

Several such departures from SI have been studied by authors in existing literature. These include the unusually low cosmic quadrupole [32, 111, 77], and planarity of the cosmic octupole and the quadrupole-octupole alignment as investigated by [77, 271, 78, 252]. The quadrupole-octupole alignment was seen to get strengthened on removal of the frequency dependent kinetic Doppler quadrupole [211]. The low multipole regime was studied by [251] with the help of multipole vectors and found to be consistently anomalous with respect to multipole aligments. Further, [167] showed that a mysterious correlation exists between azimuthal phases of the third and fifth multipole moments. A significant power asymmetry between the two hemispheres of the CMB was found by [92, 128, 94] and further corroborated by [37].

A power excess for odd multipoles was studied in the work of [166]. This parity asymmetry in the CMB angular power spectrum (APS) was confirmed by [156, 157] and the anomaly was seen to disappear without the contribution of the first six low multipoles [19]. Using symmetry-based methods of power and directional entropy statistics, [246, 247] showed that the departures from SI extend to higher multipoles as well. For scales above 60°, nearly negligible correlation was seen by [65, 66, 68] with various CMB data releases. [158] showed that the occurrence of parity asymmetry in the APS is equivalent to this deficit of large angle correlation. Further, on the basis of behaviours of level clustering and repulsion for uncorrelated and correlated values, [153] showed that only the level correlations between even multipoles is anomalously low. [301] studied a directional dependence of the parity asymmetry and suggested a common origin of the low multipole anomalies.

Additionally [169] showed that the mean values of hot and cold spots of the CMB are unexpectedly low, while [202] found that the variance of the CMB temperature anisotropy field is also anomalously low. The low CMB variance anomaly was seen to vanish when the quadrupole and octupole were excluded from the CMB maps under investigation [73]. Using novel statistics to measure the strength and shape of distribution of CMB local extrema, [154] found a strikingly weak non-uniformity in the distribution of hot and cold spots on the CMB, which is due to the low CMB temperature variance and anomalous contributions of the quadrupole and octupole.

It is important to investigate any CMB anomaly from as many perspectives as possible to assess its significance and role in cosmological parameter estimation. For example, the direction associated with CMB parity asymmetry aligns at about 45° from a best-fit dipole form for various cosmological parameters [296]. Besides, a directional variation of the cosmological parameters on the CMB sky was found to be significantly anisotropic and this finding is corrrelated with the preferred direction for the hemispherical power asymmetry anomaly [104]. Since these works report a correlation between these departures from SI of the CMB and the anisotropic directional dependence of cosmological parameters, hence it becomes difficult to disregard the violations of SI as mere statistical fluctuations [21].

These departures from SI were found to be robust against masking of the CMB sky, instruments used for observation, foreground cleaning methods, periods of observation, bands of frequencies at which the CMB is observed, and the like. Further, checks of robustness help reduce the possibility that the significant results can be attributed to look-elsewhere effects. Many such independently conducted findings of deviations from SI also weaken the inference that the consequent signal detection could have happened solely due to the nature of estimators which were designed by hand 'a posteriori' [34, 235] to focus on some unusual features.

However, despite the high statistical significance of most of such departures from SI, they are ascertained to be fairly within the underlying probability distribution given by the ΛCDM model. Thus we can have either of two possible conclusions: (a) we may say that we happen to inhabit a rare realisation of the universe given by the ΛCDM standard model, or (b) we inhabit a reasonably probable realisation of a different model. The latter case then warrants contemplation of new physics beyond the Standard Model of Cosmology.

One of such departures from SI which has been robustly observed, is the hemispherical power asymmetry [92, 94]. It was hypothesised to be engendered by the addition of a dipolar modulation to otherwise statistically isotropic CMB temperature anisotropy fluctuations $\Delta T_0(\hat{n})$, which we will denote as $T_0(\hat{n})$ for simplicity. Thus, the net temperature anisotropies in this scenario are

$$T(\hat{n}) \quad = \quad T_0(\hat{n})\left(1 + A\hat{\lambda}\cdot\hat{n}\right) \quad , \tag{4.226}$$

where, the amplitude of modulation is denoted by A, and the preferred direction is given by the unit vector $\hat{\lambda}$ and $\Delta T(\hat{n})$ is denoted simply by $T(\hat{n})$. In harmonic space, the temperature fluctuations $T_0(\hat{n})$ are decomposed as:

$$T_0(\hat{n}) \quad = \quad \sum_{l=0}^{\infty}\sum_{m=-\ell}^{\ell} a_{\ell m} Y_{\ell m}(\hat{n}) \quad . \tag{4.227}$$

These $T_0(\hat{n})$ are expected to be Gaussian random and generated from a rotationally invariant primordial power spectrum. Hence there are no preferred directions in the standard model that may couple modes of these temperature fluctuations in harmonic space. This notion of SI is encapsulated in the relation

$$\langle a_{\ell m} a^*_{\ell' m'} \rangle \quad = \quad C_\ell \delta_{\ell\ell'} \delta_{mm'} \quad . \tag{4.228}$$

Thus the spherical harmonic coefficients $a_{\ell m}$ are uncorrelated between different multipoles. However, if the dipole modulated $T(\hat{n})$ are similarly decomposed in spherical harmonics, the corresponding $a_{\ell m}$ will contain correlations between multipoles ℓ and $\ell+1$ [237], indicating a violation of SI.

As an entirely novel approach towards understanding the possible presence of a dipolar modulation in CMB temperature anisotropy data, we employ Artificial Neural Networks (ANNs). ANNs are computer based analogs of networks of biological neurons, and constitute an important machinery with decision making and parameter estimation capabilities, that falls under the umbrella of Artificial Intelligence (AI). We use deep learning techniques to train the ANNs on a mixed set containing equal numbers of simulated SI obeying (unmodulated) and SI violating (dipole modulated) CMB maps, which is inclusive of a large number of possibilities of the presence or absence of the signal. Thus our trained ANNs can make a self-guided and robust estimation of the presence of the signal of dipolar modulation, quantified with the value of the amplitude. The rationale behind using the amplitude for this purpose is that CMB maps that obey SI will have zero amplitude for such modulation, whereas those that contain the modulation will have non-zero values of the amplitude. As a realistic approach, we design an ANN with partial sky coverage in addition to one that works for full sky coverage, since we may not always have completely reliable full sky observations. Besides, we are able to compute the directions of the modulation with the help of the trained ANNs. Thus our method serves as an independent investigation to establish or reject the existence of the dipolar modulation signal as seen in existing literature.

Previously, statistics or estimators have been devised to ascertain the amplitude and direction of a possible dipolar modulation in the CMB. Estimators can be constructed in pixel or harmonic space, as per the requirements of the studies that undertake the same. For example, since the amplitude of the modulation has been shown to be dependent on the scale [140] and hence the multipole range under consideration, studying estimators in multipole space helps estimate this scale dependence [189, 236]. Whereas, an analysis in pixel space can be immensely useful so as to avoid subtle biases introduced due to masking of the sky that causes extraneous couplings in multipole space [138], or those caused due to inpainting of partial sky maps [262]. In this work, we train ANNs with normalised or re-scaled local variance maps [11] in pixel space, which serve as important input features containing direct information of the amplitude and directions of the dipolar modulation in the form of scalar products. This method helps us eschew the complex task of constructing statistics for detection of the signal. The ANNs are designed to work on scales of observation corresponding to the range of multipoles $\in [2, 256]$. We defer a study of the scale dependence of A to future work.

The implementation of ANNs for detecting previously studied features in the CMB could revolutionise perspectives towards understanding CMB anomalies as opposed to classical fitting or regression methods and traditional frequentist approaches. ANN architectures can 'learn' signal detection capabilities by being introduced to a training set of samples. Once trained, the ANN can then be fed observed foreground-cleaned CMB data to predict a possible signal in the same.

A comprehensive review of the preliminary use of ANNs in Astronomy and Astrophysics can be found in the article by [200] with regard to telescope optics, object classification and filtering of detector events. Further [268, 284, 84, 55] describe the growth of ANN based algorithms to perform time series analysis, detection of noise, and data mining in addition to classification and identification of astrophysical objects such as new stars, galaxies or even dark matter.

In Cosmology, use of ANNs has ushered in a new era of numerical frameworks to ease computations and analyses. They were used by [183] for generating dynamics of inflationary trajectories in a multi-field scenario. [82] used ANNs to reconstruct late-time expansion and LSS cosmological parameters. [282] used them to estimate quantities such as the Hubble parameter and luminosity distance as a function of redshift of Type Ia supernovae. [122] modelled ANNs with Bayesian inference to calculate the likelihood function and reduce computation time for cosmological parameter estimation. [96] provided a combined Bayesian and Recurrent neural network approach to ascertain confidence regions for parameters from dark energy models. Besides, ANNs can be designed for estimation of parameters using the 21 cm signal from the epoch of reionization [256, 61]. A general overview of ANNs and their applications in analysis of cosmological data can be found in the article by [76].

Recent applications of ANNs specific to CMB data analysis can be found in the following works. [1] implemented an appreciable full-sky foreground cleaning of the observed CMB, while [283] were able to recover CMB signals from foreground contaminated maps using Convolutional neural networks (CNNs). [52] applied ANNs to successfully recover full sky CMB temperature APS from a low resolution masked or partial sky CMB map, while [217] designed ANNs for such estimation of full sky CMB temperature power spectrum with higher resolution partial sky CMB maps. Using CNNs [216] reconstructed the full sky power spectra of CMB E and B modes for such high resolution CMB maps, while minimising the leakage between the two modes. [118] implemented Bayesian inference algorithms to make ANNs learn the likelihood function and estimate cosmological parameters from CMB data. [205, 141] trained ANNs to mimic mixing of Markov chains (MCs) and parameterization of Monte Carlo MC proposals. [261] developed ANN based estimators to compute the matter and CMB power spectra as a replacement of Boltzmann codes suited for both LSS and CMB surveys.

We have organised this chapter as follows. In Section 4.2 we present a mathematical proof of how dipole modulation violates SI, and the underlying formalism behind normalised local variance maps which can be directly used as input features for training a neural network. In Section 4.3, we briefly describe the internal structures of ANNs and the algorithms with which they function as trainable artificial analogs of biological neural networks. We elucidate our procedure for obtaining mixed sets of unmodulated and modulated CMB maps, and using them for training the ANNs in Section 4.4. Following this, we discuss the specific structure of our ANNs and regularization methods used to train the same for both full and partial sky maps in Section 4.5. The analysis of test sets and observed foreground-cleaned CMB maps are presented in Section 4.6, after application of our trained ANNs to those. In Section 4.7, we summarise our work, and enumerate the key findings of the same.

4.2 Formalism

The effect of dipole modulation can be extracted in both harmonic and pixel or real space. Therefore, in the following subsections, we present (a) a rigorous proof of how a dipole modulation couples spherical harmonic coefficients of a CMB map, and (b) how normalised local variances of such a map can be used to ascertain its modulated portion ($A\hat{\lambda}\cdot\hat{n}$). We employ the latter for detection of the dipole modulation signal in real CMB maps.

4.2.1 Dipole modulation in harmonic space

For the modulated temperature fluctuations in a spherical harmonic decomposition given by $T(\hat{n}) = \sum_{\ell m} \tilde{a}_{\ell m} Y_{\ell m}(\hat{n})$, we present a mathematical demonstration of how the covariance matrix of the $\tilde{a}_{\ell m}$'s digresses from the statistically isotropic expectation (Equation (4.228)) by coupling adjacent modes. Considering that the spherical harmonic coefficients of the anisotropic temperature fluctuations are expressed as,

$$\tilde{a}_{\ell m} = \int d\Omega T(\hat{n}) Y^*_{\ell m}(\hat{n}) = \int d\Omega T_0(\hat{n}) \left(1 + A\hat{\lambda}\cdot\hat{n}\right) Y^*_{\ell m}(\hat{n}), \tag{4.229}$$

where, the integration is over the solid angle Ω, we can write the covariance matrix of these $\tilde{a}_{\ell m}$'s in the following manner,

$$\begin{aligned}\langle \tilde{a}_{\ell_1 m_1} \tilde{a}^*_{\ell_2 m_2} \rangle &= \int\int d\Omega_1 d\Omega_2 \langle T(\hat{n}_1) T^*(\hat{n}_2) \rangle Y^*_{\ell_1 m_1}(\hat{n}_1) Y_{\ell_2 m_2}(\hat{n}_2) \\ &= \mathcal{I}_1 + \mathcal{I}_2 + \mathcal{I}_3 + \mathcal{I}_4,\end{aligned} \tag{4.230}$$

where, $\langle\rangle$ represents an ensemble average and,

$$\mathcal{I}_1 = \int\int d\Omega_1 d\Omega_2 \langle T_0(\hat{n}_1) T_0^*(\hat{n}_2) \rangle Y^*_{\ell_1 m_1}(\hat{n}_1) Y_{\ell_2 m_2}(\hat{n}_2), \tag{4.231}$$

$$\mathcal{I}_2 = \int\int d\Omega_1 d\Omega_2 \langle T_0(\hat{n}_1) T_0^*(\hat{n}_2) A\hat{\lambda}\cdot\hat{n}_1 \rangle Y^*_{\ell_1 m_1}(\hat{n}_1) Y_{\ell_2 m_2}(\hat{n}_2), \tag{4.232}$$

$$\mathcal{I}_3 = \int\int d\Omega_1 d\Omega_2 \langle T_0(\hat{n}_1) T_0^*(\hat{n}_2) A\hat{\lambda}\cdot\hat{n}_1 \rangle Y^*_{\ell_1 m_1}(\hat{n}_2) Y_{\ell_2 m_2}(\hat{n}_2), \tag{4.233}$$

$$\mathcal{I}_4 = \int\int d\Omega_1 d\Omega_2 \langle T_0(\hat{n}_1) T_0^*(\hat{n}_2) A^2 (\hat{\lambda}\cdot\hat{n}_1)(\hat{\lambda}\cdot\hat{n}_2) \rangle Y^*_{\ell_1 m_1}(\hat{n}_2) Y_{\ell_2 m_2}(\hat{n}_2). \tag{4.234}$$

Since the amplitude is assumed to be negligibly small at second order, we will focus primarily on $\mathcal{I}_1, \mathcal{I}_2, \mathcal{I}_3$ which introduce couplings between ℓ and $\ell+1$, and discuss $\mathcal{I}_4$ towards the end of this subsection.

For, $\mathcal{I}_1$, we consider the spherical harmonic decomposition of $T_0(\hat{n})$ (Equation (4.227)), and the condition of SI on the $a_{\ell m}$'s (Equation (4.228)). Thus,

$$\begin{aligned}\mathcal{I}_1 &= \int\int d\Omega_1 d\Omega_2 \langle \sum_{\ell' m'} a_{\ell' m'} Y_{\ell' m'}(\hat{n}_1) \sum_{\ell'' m''} a^*_{\ell'' m''} Y^*_{\ell'' m''}(\hat{n}_2) \rangle Y^*_{\ell_1 m_1}(\hat{n}_1) Y_{\ell_2 m_2}(\hat{n}_2) \\ &= \int\int d\Omega_1 d\Omega_2 \left(\sum_{\ell_3 m_3} C_{\ell_3} Y_{\ell_3 m_3}(\hat{n}_1) Y^*_{\ell_3 m_3}(\hat{n}_2) \right) Y^*_{\ell_1 m_1}(\hat{n}_1) Y_{\ell_2 m_2}(\hat{n}_2). \qquad (4.235)\end{aligned}$$

Further, using the orthonormality of spherical harmonic functions, i.e, $\int d\Omega Y_{\ell' m'} Y_{\ell'' m''} = \delta_{\ell' \ell''} \delta_{m' m''}$, we have,

$$\mathcal{I}_1 = C_{\ell_1} \delta_{\ell_1 \ell_2} \delta_{m_1 m_2}. \qquad (4.236)$$

Similarly, we can simplify $\mathcal{I}_2$ and $\mathcal{I}_3$ as,

$$\mathcal{I}_2 = A C_{\ell_2} \int d\Omega_1 Y_{\ell_2 m_2}(\hat{n}_1)(\hat{\lambda} \cdot \hat{n}_1) Y^*_{\ell_1 m_1}(\hat{n}_1), \qquad (4.237)$$

$$\mathcal{I}_3 = A C_{\ell_1} \int d\Omega_2 Y^*_{\ell_1 m_1}(\hat{n}_2)(\hat{\lambda} \cdot \hat{n}_2) Y_{\ell_2 m_2}(\hat{n}_2). \qquad (4.238)$$

For evaluating $\mathcal{I}_2$ and $\mathcal{I}_3$, we note the following. The preferred direction $\hat{\lambda}$ can be expressed as,

$$\begin{aligned}\hat{\lambda} &= \lambda_x \hat{x} + \lambda_y \hat{y} + \lambda_z \hat{z} \\ &= \lambda_+ \hat{\lambda}_+ + \lambda_- \hat{\lambda}_- + \lambda_0 \hat{\lambda}_0 \qquad (4.239)\end{aligned}$$

where,

$$\lambda_+ = \left(\frac{\lambda_x - i\lambda_y}{\sqrt{2}} \right), \quad \lambda_- = \left(\frac{\lambda_x - i\lambda_y}{\sqrt{2}} \right), \quad \lambda_0 = \lambda_z, \qquad (4.240)$$

and,

$$\hat{\lambda}_+ = \left(\frac{\hat{x} + i\hat{y}}{\sqrt{2}} \right), \quad \hat{\lambda}_- = \left(\frac{\hat{x} - i\hat{y}}{\sqrt{2}} \right), \quad \hat{\lambda}_0 = \hat{z}. \qquad (4.241)$$

In the basis of spherical polar coordinates, we can rewrite these vectors as,

$$\begin{aligned}
\hat{\lambda}_+ &= \frac{e^{i\phi}}{\sqrt{2}}\left[(\sin\theta)\hat{r}+(\cos\theta)\hat{\theta}+i\hat{\phi}\right], \\
\hat{\lambda}_- &= \frac{e^{-i\phi}}{\sqrt{2}}\left[(\sin\theta)\hat{r}+(\cos\theta)\hat{\theta}-i\hat{\phi}\right], \\
\hat{\lambda}_0 &= (\cos\theta)\hat{r}-(\sin\theta)\hat{\theta}.
\end{aligned} \tag{4.242}$$

Thus, representing $\hat{n}=\hat{r}(r,\theta,\phi)$, we can recognise the scalar product $\hat{\lambda}\cdot\hat{n}$ as

$$\begin{aligned}
\hat{\lambda}\cdot\hat{n} &= \lambda_+\frac{e^{i\phi}}{\sqrt{2}}(\sin\theta)+\lambda_-\frac{e^{-i\phi}}{\sqrt{2}}(\sin\theta)+\lambda_0(\cos\theta) \\
&= \sqrt{\frac{4\pi}{3}}\left[-\lambda_+Y_{1,1}(\hat{n})+\lambda_-Y_{1,-1}(\hat{n})+\lambda_0Y_{1,0}(\hat{n})\right].
\end{aligned} \tag{4.243}$$

Using this form of the scalar product and equations (4.237) and (4.238), we can express $\mathcal{I}_2$ and $\mathcal{I}_3$ as follows,

$$\mathcal{I}_2=\sqrt{\frac{4\pi}{3}}AC_{\ell_2}\int d\Omega_1 Y_{\ell_2 m_2}(\hat{n}_1)\left[-\lambda_+Y_{1,1}(\hat{n}_1)+\lambda_-Y_{1,-1}(\hat{n}_1)+\lambda_0Y_{1,0}(\hat{n}_1)\right]Y^*_{\ell_1 m_1}(\hat{n}_1), \tag{4.244}$$

$$\mathcal{I}_3=\sqrt{\frac{4\pi}{3}}AC_{\ell_1}\int d\Omega_2 Y^*_{\ell_1 m_1}(\hat{n}_2)\left[-\lambda_+Y_{1,1}(\hat{n}_2)+\lambda_-Y_{1,-1}(\hat{n}_2)+\lambda_0Y_{1,0}(\hat{n}_2)\right]Y_{\ell_2 m_2}(\hat{n}_2). \tag{4.245}$$

We will make use of the identity for products of two spherical harmonic functions,

$$\begin{aligned}
Y_{\ell_1 m_1}(\hat{n})Y_{\ell_2 m_2}(\hat{n}) &= \frac{\sqrt{(2\ell_1+1)(2\ell_2+1)}}{\sqrt{4\pi}}\sum_{\ell' m'}(-1)^{m'}\sqrt{(2\ell'+1)} \\
&\quad\times\begin{pmatrix}\ell_1 & \ell_2 & \ell' \\ m_1 & m_2 & -m'\end{pmatrix}\begin{pmatrix}\ell_1 & \ell_2 & \ell' \\ 0 & 0 & 0\end{pmatrix}Y_{\ell' m'}(\hat{n}).
\end{aligned} \tag{4.246}$$

The conditions for this product to not vanish are the following:

1. $m_1+m_2-m'=0$.
2. $|\ell_1-\ell_2|\le\ell'\le\ell_1+\ell_2$.
3. $m_1\in[-|\ell_1|,+|\ell_1|]$, $m_2\in[-|\ell_2|,+|\ell_2|]$, $m'\in[-|\ell'|,+|\ell'|]$.
4. $\ell_1+\ell_2+\ell'$ is an integer.
5. Additionally, for $\begin{pmatrix}\ell_1 & \ell_2 & \ell' \\ 0 & 0 & 0\end{pmatrix}$ to be non-zero, we must have $\ell_1+\ell_2+\ell'=$ an even

integer only.

Each of $\mathcal{I}_2$ and $\mathcal{I}_3$ can be broken up into three terms (say, $\mathcal{I}_{21},\mathcal{I}_{22},\mathcal{I}_{23}$, and $\mathcal{I}_{31},\mathcal{I}_{32},\mathcal{I}_{33}$) which are functions of the spherical harmonic functions $Y_{1,1},Y_{1,-1},Y_{1,0}$, respectively. We will initially focus on $\mathcal{I}_2$, for which, the first term is

$$\begin{aligned}\mathcal{I}_{21} &= -\left(\sqrt{\frac{4\pi}{3}}A\lambda_+ C_{\ell_2}\right)\int d\Omega_1 Y_{\ell_2 m_2}(\hat{n}_1)Y_{1,1}(\hat{n}_1)Y^*_{\ell_1 m_1}(\hat{n}_1)\\ &= \left(\sqrt{\frac{4\pi}{3}}A\lambda_+ C_{\ell_2}\right)\sum_{\ell' m'}\frac{\sqrt{(2\ell_2+1)(3)(2\ell'+1)}}{\sqrt{4\pi}}(-1)^{m'+1}\\ &\quad\times\begin{pmatrix}\ell_2 & 1 & \ell'\\ m_2 & 1 & -m'\end{pmatrix}\begin{pmatrix}\ell_2 & 1 & \ell'\\ 0 & 0 & 0\end{pmatrix}\int d\Omega_1 Y^*_{\ell_1 m_1}(\hat{n}_1)Y_{\ell' m'}(\hat{n}_1)\\ &= A\lambda_+ C_{\ell_2}(-1)^{m_1+1}\sqrt{(2\ell_1+1)(2\ell_2+1)}\begin{pmatrix}\ell_2 & 1 & \ell_1\\ m_2 & 1 & -m_1\end{pmatrix}\begin{pmatrix}\ell_2 & 1 & \ell_1\\ 0 & 0 & 0\end{pmatrix}.\end{aligned} \tag{4.247}$$

Using the conditions outlined earlier (4.2.1), we realise that the permissible values are $m_2=m_1-1$ and $\ell_2=\ell_1-1$ or, $\ell_2=\ell_1+1$. Thus, we need to evaluate the Wigner-$3j$ symbols in the above expression for two cases, namely $\delta_{m_2,m_1-1}\delta_{\ell_2,\ell_1-1}$ and $\delta_{m_2,m_1-1}\delta_{\ell_2,\ell_1+1}$. The products of the Wigner-$3j$ symbols computed for these two cases are thus,

$$\begin{pmatrix}\ell_1-1 & 1 & \ell_1\\ m_1-1 & 1 & -m_1\end{pmatrix}\begin{pmatrix}\ell_1-1 & 1 & \ell_1\\ 0 & 0 & 0\end{pmatrix} = \frac{(-1)^{m_1}}{\sqrt{2}}\sqrt{\frac{(\ell_1+m_1-1)(\ell_1+m_1)}{(2\ell_1-1)(2\ell_1+1)}}, \tag{4.248}$$

$$\begin{pmatrix}\ell_1+1 & 1 & \ell_1\\ m_1-1 & 1 & -m_1\end{pmatrix}\begin{pmatrix}\ell_1+1 & 1 & \ell_1\\ 0 & 0 & 0\end{pmatrix} = \frac{(-1)^{1-m_1}}{\sqrt{2}}\sqrt{\frac{(\ell_1-m_1+1)(\ell_1-m_1+2)}{(2\ell_1+1)(2\ell_1+3)}}. \tag{4.249}$$

such that the complete term $\mathcal{I}_{21}$ can be written as,

$$\begin{aligned}\mathcal{I}_{21} &= \frac{A\lambda_+}{\sqrt{2}}\delta_{m_2,m_1-1}\left[C_{\ell_1+1}\delta_{\ell_2,\ell_1+1}\sqrt{\frac{(\ell_1-m_1+1)(\ell_1-m_1+2)}{(2\ell_1+1)(2\ell_1+3)}}\right.\\ &\quad\left.-C_{\ell_1-1}\delta_{\ell_2,\ell_1-1}\sqrt{\frac{(\ell_1+m_1-1)(\ell_1+m_1)}{(2\ell_1-1)(2\ell_1+1)}}\right].\end{aligned} \tag{4.250}$$

Similarly, we can evaluate the other two terms to yield

$$\begin{aligned}\mathcal{I}_{22} &= \frac{A\lambda_-}{\sqrt{2}}\delta_{m_2,m_1+1}\Bigg[C_{\ell_1-1}\delta_{\ell_2,\ell_1-1}\sqrt{\frac{(\ell_1-m_1-1)(\ell_1-m_1)}{(2\ell_1-1)(2\ell_1+1)}} \\ &\quad -C_{\ell_1+1}\delta_{\ell_2,\ell_1+1}\sqrt{\frac{(\ell_1+m_1+1)(\ell_1+m_1+2)}{(2\ell_1+1)(2\ell_1+3)}}\Bigg], \qquad (4.251)\end{aligned}$$

$$\begin{aligned}\mathcal{I}_{23} &= A\lambda_0\delta_{m_2,m_1}\Bigg[C_{\ell_1-1}\delta_{\ell_2,\ell_1-1}\sqrt{\frac{(\ell_1-m_1)(\ell_1+m_1)}{(2\ell_1-1)(2\ell_1+1)}} \\ &\quad +C_{\ell_1+1}\delta_{\ell_2,\ell_1+1}\sqrt{\frac{(\ell_1-m_1+1)(\ell_1+m_1+1)}{(2\ell_1+1)(2\ell_1+3)}}\Bigg]. \qquad (4.252)\end{aligned}$$

Considering the expression for $\mathcal{I}_3$ (Equation (4.238)), we show the computation of its first term $\mathcal{I}_{31}$,

$$\begin{aligned}\mathcal{I}_{31} &= -\left(\sqrt{\frac{4\pi}{3}}A\lambda_+C_{\ell_1}\right)\int d\Omega_2 Y^*_{\ell_1m_1}(\hat{n}_2)Y_{1,1}(\hat{n}_2)Y_{\ell_2m_2}(\hat{n}_2) \\ &= \left(\sqrt{\frac{4\pi}{3}}A\lambda_+C_{\ell_1}\right)\sum_{\ell'm'}\frac{\sqrt{(2\ell_2+1)(3)(2\ell'+1)}}{\sqrt{4\pi}}(-1)^{m'+1} \\ &\quad \times\begin{pmatrix}1 & \ell_2 & \ell' \\ 1 & m_2 & -m'\end{pmatrix}\begin{pmatrix}1 & \ell_2 & \ell' \\ 0 & 0 & 0\end{pmatrix}\int d\Omega_2 Y^*_{\ell_1m_1}(\hat{n}_2)Y_{\ell'm'}(\hat{n}_2) \\ &= A\lambda_+C_{\ell_1}(-1)^{m_1+1}\sqrt{(2\ell_1+1)(2\ell_2+1)}\begin{pmatrix}1 & \ell_2 & \ell_1 \\ 1 & m_2 & -m_1\end{pmatrix}\begin{pmatrix}1 & \ell_2 & \ell_1 \\ 0 & 0 & 0\end{pmatrix}. \qquad (4.253)\end{aligned}$$

Here, using the conditions for non-zero products of the Wigner-$3j$ symbols, the permissible cases are $\delta_{m_2,m_1-1}\delta_{\ell_2,\ell_1-1}$ and $\delta_{m_2,m_1-1}\delta_{\ell_2,\ell_1+1}$. Thus the term now reads,

$$\begin{aligned}\mathcal{I}_{31} &= \frac{A\lambda_+}{\sqrt{2}}C_{\ell_1}\delta_{m_2,m_1-1}\Bigg[\delta_{\ell_2,\ell_1+1}\sqrt{\frac{(\ell_1-m_1+1)(\ell_1-m_1+2)}{(2\ell_1+1)(2\ell_1+3)}} \\ &\quad -\delta_{\ell_2,\ell_1-1}\sqrt{\frac{(\ell_1+m_1-1)(\ell_1+m_1)}{(2\ell_1-1)(2\ell_1+1)}}\Bigg]. \qquad (4.254)\end{aligned}$$

A similar approach to compute the other two terms results in the following expressions,

$$\begin{aligned}\mathcal{I}_{32} &= \frac{A\lambda_-}{\sqrt{2}}C_{\ell_1}\delta_{m_2,m_1+1}\Bigg[\delta_{\ell_2,\ell_1-1}\sqrt{\frac{(\ell_1-m_1-1)(\ell_1-m_1)}{(2\ell_1-1)(2\ell_1+1)}} \\ &\quad -\delta_{\ell_2,\ell_1+1}\sqrt{\frac{(\ell_1+m_1+1)(\ell_1+m_1+2)}{(2\ell_1+1)(2\ell_1+3)}}\Bigg], \qquad (4.255)\end{aligned}$$

$$
\begin{aligned}
\mathcal{I}_{33} &= A\lambda_0 C_{\ell_1}\delta_{m_2,m_1}\left[\delta_{\ell_2,\ell_1-1}\sqrt{\frac{(\ell_1-m_1)(\ell_1+m_1)}{(2\ell_1-1)(2\ell_1+1)}}\right.\\
&\left.-\delta_{\ell_2,\ell_1+1}\sqrt{\frac{(\ell_1-m_1+1)(\ell_1+m_1+1)}{(2\ell_1+1)(2\ell_1+3)}}\right].
\end{aligned} \tag{4.256}
$$

Thus, considering that $\mathcal{O}(A^2)\to 0$, we have the following expression for the covariance matrix of the $\tilde{a}_{\ell m}$'s,

$$
\langle \tilde{a}_{\ell_1 m_1}\tilde{a}^*_{\ell_2 m_2}\rangle = C_{\ell_1}\delta_{\ell_1\ell_2}\delta_{m_1 m_2}+\mathcal{I}_{21}+\mathcal{I}_{22}+\mathcal{I}_{23}+\mathcal{I}_{31}+\mathcal{I}_{32}+\mathcal{I}_{33}, \tag{4.257}
$$

where the forms of $\mathcal{I}_{21},\ldots,\mathcal{I}_{33}$ are given in Equations (4.250), (4.251), (4.252), (4.250), (4.254), (4.255), (4.256), respectively. Further we have seen from these equations that couplings between consecutive multipoles have been introduced, clearly leading to a violation of SI.

As regards the last term $\mathcal{I}_4$ (Equation (4.234)) which is of the second order in A, we see that it can be written as,

$$
\mathcal{I}_4 = \sum_{\ell_3 m_3} C_{\ell_3}A^2\int d\Omega_1 Y_{\ell_3 m_3}(\hat{n}_1)(\hat{\lambda}\cdot\hat{n}_1)Y^*_{\ell_1 m_1}(\hat{n}_1)\int d\Omega_2 Y^*_{\ell_3 m_3}(\hat{n}_2)(\hat{\lambda}\cdot\hat{n}_2)Y_{\ell_2 m_2}(\hat{n}_2). \tag{4.258}
$$

We notice that the first and second integrals on the right hand side of this equation resemble the forms of $\mathcal{I}_2$ and $\mathcal{I}_3$ as in Equations (4.237) and (4.238). If we focus solely on the multipole number ℓ, this leads us to recognise that first integral will provide conditions such as δ_{ℓ_3,ℓ_1-1} and δ_{ℓ_3,ℓ_1+1}, while the second integral will furnish conditions of δ_{ℓ_2,ℓ_3-1} and δ_{ℓ_2,ℓ_3+1}. Thus, the product of these two integrals will help remove the summation ($\sum_{\ell_3 m_3}$) by enabling couplings of the form δ_{ℓ_2,ℓ_1-2} and δ_{ℓ_2,ℓ_1+2}, in addition to the statistically isotropic forms $\delta_{\ell_1\ell_2}$. We must note that there will be couplings between the azimuthal numbers as well. In conclusion, the term $\mathcal{I}_4$ introduces quadrupolar couplings, i.e, couplings between second nearest neighbour multipoles, and since this effect is assumed to be negligible due to the smallness of A^2, we invariably refer to the modulation studied in this chapter as a dipolar modulation, i.e, one between adjacent multipoles.

4.2.2 Normalised local variances

For the CMB temperature anisotropy field defined on the 2-sphere of observation, we can compute its variances inside different local regions of the sphere. We consider these regions to be discs of equal area spanning the 2-sphere. In this section, we present the formalism of how such local variances, after appropriate re-scaling are equivalent to the amplitude times a scalar product of the constant unit vector of modulation and the mean direction of the local disc, as first utilised in the work of [11].

In HEALPix [117] notation, the parameter n_{side} characterises the pixel resolution of a CMB map. For convenience, we denote the n_{side} of a high resolution CMB map by n_h and that of a lower resolution CMB map by n_l. We consider a disc of radius r_h, on the map at resolution n_h. We then calculate the local mean and variance of temperature fluctuations within the disc. Thus the mean of modulated disc temperature fluctuations from equation (4.226) is,

$$\langle T\rangle_d \;\; = \;\; \langle T_0\rangle_d + \langle AT_0\hat{\lambda}\cdot\hat{n}\rangle_d \;\; , \tag{4.259}$$

where $\langle\rangle_d$ denotes expectation value over the disc. Let us consider the second term in the equation above where A is a constant. The statistically isotropic Gaussian random fluctuations T_0 are approximately independent of and uncorrelated with the variations of $\hat{\lambda}\cdot\hat{n}$, if the disc is sufficiently small enough so that the $\hat{\lambda}\cdot\hat{n}$ term is slowly varying. Hence, the expression (4.259) reads:

$$\langle T\rangle_d \;\; = \;\; \langle T_0\rangle_d + A\langle T_0\rangle_d\langle\hat{\lambda}\cdot\hat{n}\rangle_d \;\; . \tag{4.260}$$

The local variance within the disc is

$$\sigma_d^2 \;\; = \;\; \langle (T-\langle T\rangle_d)^2\rangle_d \;\; . \tag{4.261}$$

Expanding out, the expression for the disc variance becomes

$$
\begin{aligned}
\sigma_d^2 &= \langle\Big[(T_0-\langle T_0\rangle_d)+A\Big(T_0\hat{\lambda}\cdot\hat{n}-\langle T_0\rangle_d\langle\hat{\lambda}\cdot\hat{n}\rangle_d\Big)\Big]^2\rangle_d \\
&= \langle(T_0-\langle T_0\rangle_d)^2\rangle_d \\
&\quad +2A\langle(T_0-\langle T_0\rangle_d)\times\Big(T_0\hat{\lambda}\cdot\hat{n}-\langle T_0\rangle_d\langle\hat{\lambda}\cdot\hat{n}\rangle_d\Big)\rangle_d \\
&\quad +\mathcal{O}(A^2) \\
&= \sigma_{0d}^2+2A\Big[\langle T_0^2\hat{\lambda}\cdot\hat{n}\rangle_d-\langle T_0\langle T_0\rangle_d\langle\hat{\lambda}\cdot\hat{n}\rangle_d\rangle_d \\
&\quad -\langle T_0\langle T_0\rangle_d\hat{\lambda}\cdot\hat{n}\rangle_d+\langle T_0\rangle_d^2\langle\hat{\lambda}\cdot\hat{n}\rangle_d\Big]+\mathcal{O}(A^2) \\
&= \sigma_{0d}^2+2A\left[\langle T_0^2\rangle_d-\langle T_0\rangle_d^2\right]\times\langle\hat{\lambda}\cdot\hat{n}\rangle_d+\mathcal{O}(A^2)\ ,
\end{aligned}
\tag{4.262}
$$

where σ_{0d}^2 stands for the disc variance in the absence of a modulation. We can replace the term $\langle\hat{\lambda}\cdot\hat{n}\rangle_d$ with $\hat{\lambda}\cdot\langle\hat{n}\rangle_d$, since $\hat{\lambda}$ for any particular CMB map is constant. Further, as the average of position vectors $\hat{n}$ is over a disc, $\langle\hat{n}\rangle_d=\hat{N}$, where $\hat{N}$ is the centre of the disc. Hence,

$$
\frac{\sigma_d^2-\sigma_{0d}^2}{\sigma_{0d}^2} \simeq 2A\hat{\lambda}\cdot\hat{N}\ . \tag{4.263}
$$

However, evaluating σ_{0d}^2 from a single Gaussian random realisation may give a biased estimate. Instead, we will compute $\langle\sigma_{0d}^2\rangle_e$ and use that in our expression above. This expectation $\langle\rangle_e$ is over an ensemble of statistically isotropic realisations. Thus finally we arrive at the following normalised local variance (NLV),

$$
\boxed{\frac{\sigma_d^2-\langle\sigma_{0d}^2\rangle_e}{\langle\sigma_{0d}^2\rangle_e}\simeq 2A\hat{\lambda}\cdot\hat{N}}\ , \tag{4.264}
$$

which shall be used in all analyses hereafter.

Several discs on the n_h map are considered and their NLVs computed. These NLV values are then assigned to corresponding pixels of another map at a lower resolution n_l. Thus to construct an NLV map, the total number of discs to be considered $=12\times n_l^2$. The centre of any particular disc on the n_h map is taken to be the same as the position vector of the pixel of the n_l resolution map to which the NLV of that disc is assigned. With this information, we can calculate the approximate number of pixels (n_{pd}) of the n_h map inside each disc of

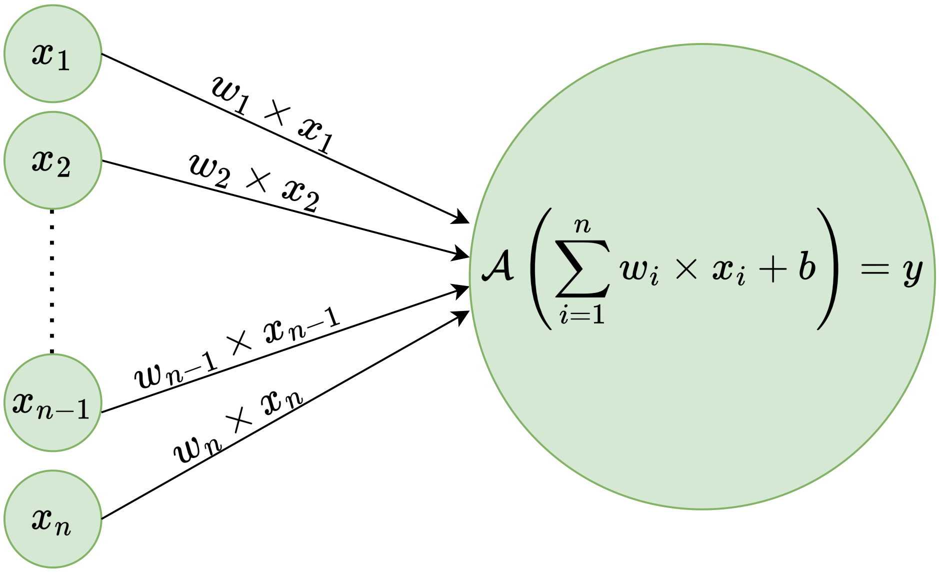

Figure 4.1: An artificial neuron is the building block of an ANN. Its structure comprises inputs x_i's which are weighted with w_i's, summed over and added to a bias b, the resultant of which is acted on by an activation function $\mathcal{A}$ to give the output y.

given radius r_h (in degrees). This is expressed as

$$\begin{aligned} n_{pd} &= \frac{\text{Area of the disc}}{\text{Area of a pixel in } n_h} \\ &= \pi\left(\frac{r_h \times \pi}{180}\right)^2 \Big/ \frac{4\pi}{12 \times n_h^2} \,, \end{aligned}$$

$$\boxed{n_{pd} = 3 \times \left(\frac{n_h \times r_h \times \pi}{180}\right)^2} \,. \tag{4.265}$$

We can calculate the approximate number of pixels in possibly overlapping regions as follows. For $n_{pl} = 12 \times n_l^2$ discs, the total number of pixels taken is $n_{pt} = n_{pl} \times n_{pd}$. Thus if $n_{pt} > n_{ph}$, then there are $n_{pt} - n_{ph}$ number of pixels which are present in overlapping regions of discs, and vice versa. Here, $n_{ph} = 12 \times n_h^2$.

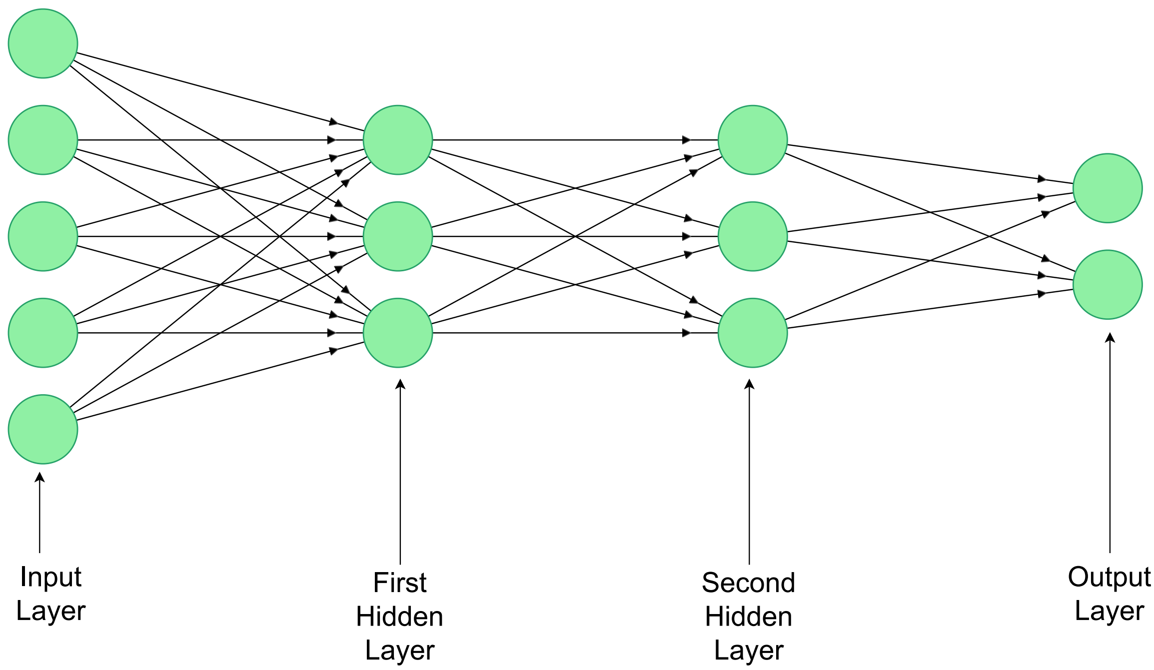

Figure 4.2: An example of an ANN architecture, containing 5 inputs, two hidden layers with 3 nodes each, and 2 outputs. Each layer after the input layer has nodes which are densely connected to those of the preceding layer.

4.3 How does an ANN work?

An artificial neuron is the building block of an ANN, which is inspired from the concept of the biological neuron [195, 240]. It combines a weighted sum of several inputs, adds a bias to that sum to give a preliminary output. Since this preliminary output is a linear mapping, no matter how many neurons are interconnected to form a network, the mapping from initial inputs to the last output can always be described as a linear mapping [186]. In reality, the complex relations between inputs and expected outputs may never be reducible to a linear mapping. Hence using activation functions [88] to introduce non-linearity becomes pertinent. Thus a modern day artificial neuron can be represented by the example in Figure 4.1, which shows how inputs x_i are weighted by w_i and summed together along with an offset or bias b. An activation function $\mathcal{A}$ acts on this sum to give the subsequent output y.

The initial inputs x form a layer of nodes called the 'input layer'. Several such outputs y can be formed from these initial inputs, using different weights and biases. All these y are then a new set of nodes that constitute the first 'hidden layer'. The second hidden layer can be formed by considering y's from the first hidden layer as inputs, and so on. A small ANN may have one or two hidden layers, whereas a larger ANN could comprise several such hidden layers. The last layer of any ANN consists of the final outputs and is called the 'output layer'. The number of nodes in this layer is equal to number of expected outputs that the ANN is being trained for. Due to the presence of hidden layers that are densely connected to their preceding layers, the method of training such ANNs is referred to as 'deep learning' [90].

The activation function used to obtain the outputs usually differs from the choices in other hidden layers. For example, while the $ReLU$ or $LeakyReLU$ activation functions can be used for hidden layers, for the output layer, the respective activation used could be a $sigmoid$ or $softmax$ for binary or multi-class classification problems, or $linear$ for regression problems [173]. To illustrate the arrangement of a neural network, we show an example ANN in Figure 4.2. For all layers apart from the input layer, each node is fully connected to all the nodes in the previous layer.

Beginning with the input layer as the 0^{th} layer, we can successively number the other layers. Consider the i^{th} node in the $(l-1)^{th}$ layer, which is connected to the j^{th} node in layer l. The associated weight and bias will be $w_{ij}^{(l)}$ and $b_j^{(l)}$. Thus the value taken by the j^{th} node in layer l is:

$$y_j^{(l)} = \mathcal{A}\left(\sum_i w_{ij}^{(l)} \times y_i^{(l-1)} + b_j^{(l)}\right). \tag{4.266}$$

If $l = 1$, then $y_j^{(l)}$ represents a node in the first hidden layer and $y_i^{(l-1)} = x_i$ corresponds to that of the input layer. The 2D weight matrix between layers $(l-1)$ and l is given by $[W^{(l)}]_{ij} = w_{ij}^{(l)}$, while the bias column vector is $[B^{(l)}]_j = b_j^{(l)}$. To begin with, the weights and biases for the ANN can be chosen randomly.

In the process of assigning values to nodes in subsequent layers, a forward propagation in the ANN is achieved. To verify if the final outputs are as expected, a loss function is computed for the outputs generated [115]. Since in this chapter, we are dealing with a regression problem, we will consider the loss function as the mse or mean squared error, given as

$$mse = \frac{1}{N} \times \sum (y_{true} - y_{pred})^2 , \tag{4.267}$$

where the summation is over a total number of output values N. Thus mse is the average of squared differences between the predicted outputs (y_{pred}) from the ANN and the true values (y_{true}). To train the ANN effectively, we must perform back-propagation [241], in which the weights and biases associated with the different layers are updated iteratively so as to minimize the mse loss function. The rate or step-size for updating in this process is known as the learning rate σ. Thus the basic relations which describe the process of back-propagation for a loss function H are,

$$
\begin{aligned}
W^{(l)} &\rightarrow W^{(l)} - \sigma \times \nabla_{W^{(l)}} H \ , \\
B^{(l)} &\rightarrow B^{(l)} - \sigma \times \nabla_{B^{(l)}} H \ .
\end{aligned}
\tag{4.268}
$$

These relations correspond to the algorithm of gradient descent. However, such an algorithm when applied to the whole data-set can be computationally expensive. Thus the data set is divided into several batches [112] randomly, and the above algorithm is applied. A batch represents the number of samples from the data-set which are used during a part of an iteration for updating the parameters of weights and biases. A complete iteration during which the whole data-set is made to undergo the algorithm for optimization is called an epoch. Due to the random subdivision of the training set into batches, some stochasticity is introduced into the loss function. For our problem of regression of the amplitude and directions of any possible dipolar modulation, we have considered the $Adam$ (adaptive moment estimation) optimizer [160], which incorporates adaptive estimates of the gradients and their squares. In this method, the parameters (weights and biases) are updated as follows.

1. A step-size or learning rate σ is specified.

2. Exponential decay rates for the moment estimates are $\gamma_1, \gamma_2 \in [0, 1)$.

3. Stochastic loss function $H(\delta)$ is given.

4. Parameters δ are initialised randomly.

5. The first moment vector m_0, second moment vector v_0 and time-step t are initialised to zero.

6. The time step is updated as $t \to t+1$.
7. Gradient $g_t = \nabla_\delta H_t(\delta_{t-1})$.
8. $m_t = \gamma_1 \times m_{t-1} + (1-\gamma_1) \times g_t$.
9. $v_t = \gamma_2 \times v_{t-1} + (1-\gamma_2) \times g_t^2$.
10. Bias correction for first moment estimate: $\hat{m}_t = m_t/(1-\gamma_1^t)$.
11. Bias correction for second moment estimate: $\hat{v}_t = v_t/(1-\gamma_2^t)$.
12. Updating of parameters: $\delta_t = \delta_{t-1} - \sigma \times \hat{m}_t/(\sqrt{\hat{v}_t} + \epsilon)$.
13. Steps 6–12 are repeated until δ_t converges.
14. Resulting parameters are δ_t .

Here, values of $\gamma_1 = 0.9$, $\gamma_2 = 0.999$, and $\epsilon = 10^{-7}$. Superscripts t in γ_1^t, γ_2^t, denote that those are raised to the power of t. The algorithm described above for the $Adam$ optimizer is run for each of the batches within an epoch so that the ANN trains with the entire data set during one epoch itself. Several epochs may be required for the ANN to become fully trained.

At the end of an epoch, the ANN evaluates the final loss function from the set on which it is being trained. To infer whether or not an ANN is fully trained, i.e, if it is able to generalise its knowledge to sets on which it has not been trained, another data-set for validation is simultaneously considered at every epoch. The ANN acts on this set and generates the corresponding loss value. Depending on the nature of the loss function, the optimization of the same may either correspond to that of minimisation or maximisation. We consider the case of mse as the loss function, which must be minimized. Thus, over a considerable number of epochs, if the training loss does not appear to minimize, then the ANN is said to be ‘under-fitting’ and usually a more complex network architecture can help resolve the issue. On the other hand, if the training loss adequately reaches its minimum, while that of validation does not, then the ANN is said to be ‘over-fitting’. This can be seen from the loss curves, where the validation loss curve is always above the training loss, whereas the training loss has converged to an appropriate minimum. The condition of over-fitting indicates that the weights and biases in the ANN are very well suited for the training set, but those are not optimal for the ANN to make appropriate predictions for new data sets that it has not 'seen' before.

Over-fitting can be resolved using regularization methods [297] such as those of the $L1$ or $L2$ penalty or with the help of a 'dropout'. In designing our ANNs for estimation of dipolar modulation parameters, we have used kernel regularizers with $L1$ and $L2$ penalties in addition to a dropout. Kernel regularizers penalise the loss function of the training set by adding to it a strength factor ($\mathcal{S}$) times the penalty $\mathcal{P}$, which is formed from entries in the weight matrices. In case of the $L1$ kernel regularizer, $\mathcal{P}$ is the sum of absolute values of the weights, whereas for the $L2$ regularizer, it is the sum of the squares of the weights. On the other hand, if a dropout [137] is applied before a layer, a fraction of the inputs from the previous layer are randomly dropped out, i.e, set to zero. This fraction is known as the rate of dropout and its value lies $\in [0, 1]$.

4.4 Methodology

We have considered a mixed set of 5×10^4 randomly generated CMB realisations of maps at $n_h = 128$. Half of these are statistically isotropic, and the other half are dipole modulated versions of the same.

The statistically isotropic CMB temperature maps at $n_h = 128$ are obtained by choosing the spherical harmonic coefficients $a_{\ell m}$ as Gaussian random variables with zero mean and variance given by the theoretical CMB temperature APS best fit to Planck 2018 data. Thus, we generate 2.5×10^4 SI obeying maps with different seed values.

In order to obtain 2.5×10^4 dipole modulated counterparts of the SI obeying maps at $n_h = 128$, we utilise equation (4.226). We pick A from a uniform random distribution in accordance with the order of magnitude of reported values from observed foreground-cleaned data. We have further considered a wide range given by $A \in [0.03, 0.15]$ so as to sufficiently accommodate a large number of possible values of amplitude. This further helps minimize the epistemic uncertainty [145] of the ANN.

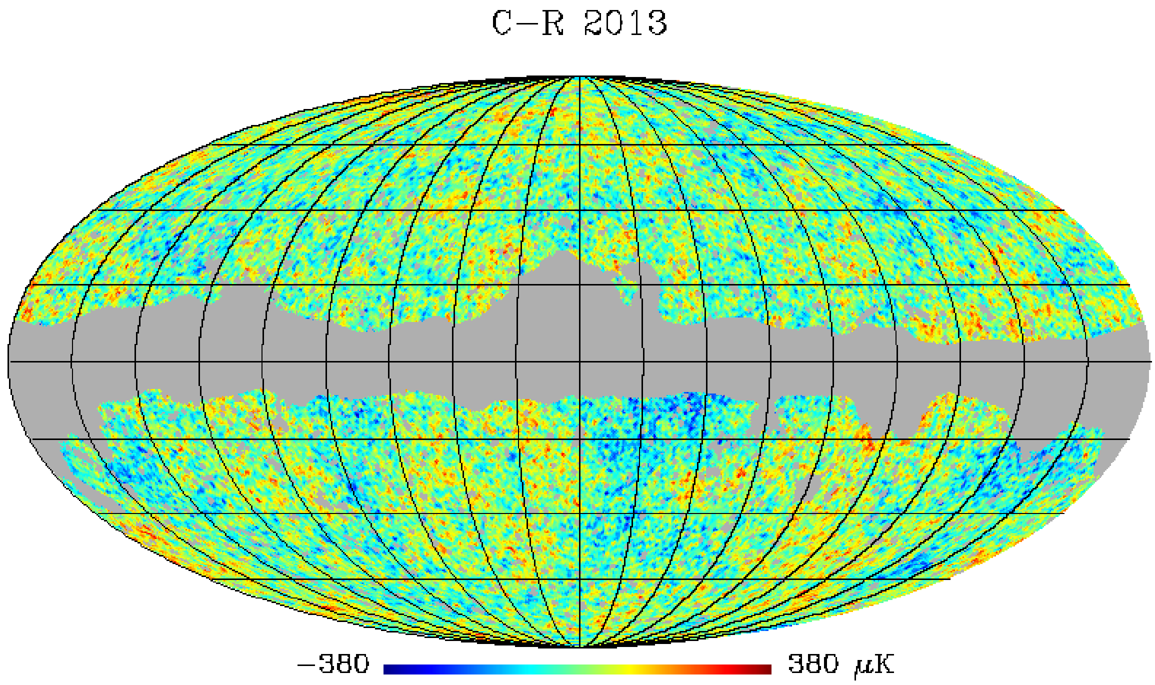

Figure 4.3: As an example of partial sky coverage, we present the Planck 2013 Commander-Ruler (C-R) map at resolution $n_h = 128$ after application of the Planck 2013 $U73$ mask. The masked regions are shown in grey colour. The CMB fluctuations are shown in thermodynamic temperature units of μK.

The direction of the dipole for modulation ($\hat{\lambda}$) is chosen in the following manner. For three different seed values, we generate three random numbers from a normal distribution with a mean of zero and standard deviation equal to one. The numbers are chosen such that the sum of their squares are non-zero. They are then normalised by the square root of the sum of their squares. Thus the three resulting numbers form components of the randomly chosen unit vector $\hat{\lambda}$, which gives the preferred direction of dipolar modulation for a particular realisation. The rationale behind choosing the components as random normal numbers is to take into account all possible directions on the sphere [207], since other choices such as those of random uniform numbers restrict the randomness in directionality of the modulation.

The NLV maps at $n_l = 16$ are constructed using discs of radius $= 6°$. Thus inside each disc, the approximate number of pixels at $n_h = 128$ over which the local variances are computed is approximately 540, according to equation (4.265), for which it can be shown that there are about 1459237 pixels in overlapping regions of discs.

The manually adopted choice of $r_h = 6°$ is an optimal one due to the following reasons.

Local variance estimates over smaller disks will have relatively higher contributions from Monte Carlo noise due to lower number of pixels contained by them, which must be avoided. Besides, very small radii such as $r_h \lesssim 4^\circ$ are subject to non-negligible contributions from the Doppler dipole [8]. However, choosing large radii weakens the assumption of a slow variation of $\hat{\lambda} \cdot \hat{n}$ inside the disc (Section 4.2), and can cause results to concur with statistically isotropic maps [11] for very large r_h. Hence, we choose $r_h = 6^\circ$ which is sufficiently small, and reasonably free from contributions of the Doppler dipole and Monte Carlo noise.

In order to construct the NLV maps, we require a mean variance map containing $\langle \sigma^2_{0d} \rangle_e$ values. This mean variance map is obtained using an ensemble of 1×10^5 local variance maps at $n_l = 16$, which were extracted from the same number of corresponding SI obeying realisations of maps at $n_h = 128$. Of the total mixed set of 5×10^4 NLV maps, 2×10^4 maps are used for training the ANNs, 10^4 are used for validation, and the remaining 2×10^4 are used for testing the trained ANN.

We consider two cases of sky coverage, i.e, full and partial sky. In both cases of sky coverage and for both simulated and observed foreground-cleaned CMB maps at $n_h = 128$, the multipole range under consideration is $[2, 256]$. This is because the monopole (which corresponds to the uniform temperature of the CMB) and the dipole (containing contributions from the Doppler shift due to solar motion) must be disregarded for cosmological inferences. For the observed foreground-cleaned full sky CMB map (m_i) at resolution n_h in harmonic space, we set the spherical harmonic coefficients corresponding to the monopole and dipole to zero. With the new set of spherical harmonic coefficients, we generate the corresponding full sky CMB map (m_f) which is devoid of the monopole and dipole.

Further, since the simulated maps are devoid of any beam smoothing effects, therefore any existing beam smoothing in all the observed foreground-cleaned CMB maps is removed as well. In order to deconvolve beam effects from the observed foreground-cleaned CMB map, we consider the map m_i in harmonic space. We divide all the spherical harmonic coefficients ($a_{(\ell m)i}$'s) of the map by the beam window function ($B_{(\ell)i}$) of the respective observational instrument. With these new spherical harmonic coefficients ($a_{(\ell m)f}$) we construct the full sky map m_f which is devoid of beam smoothing effects. Hence,

$$a_{(\ell m)f} \quad = \quad a_{(\ell m)i} \times \frac{B_{(\ell)f} \times P_{(\ell)f}}{B_{(\ell)i} \times P_{(\ell)i}}. \tag{4.269}$$

Here, the initial beam window function $B_{(\ell)i}$ corresponds to a full-width at half-maximum (FWHM) $= 5'$ for Planck maps, or $= 60'$ for WMAP maps. The final beam window function $B_{(\ell)f}$ corresponds to an FWHM $= 0'$ for both Planck and WMAP maps. The initial pixel window function $P_{(\ell)i}$ corresponds to an $n_{side} = 2048$ for Planck maps or $n_{side} = 512$ for WMAP maps. The final pixel window function $P_{(\ell)f}$ corresponds to an $n_{side} = 128$ for both Planck and WMAP maps.

Firstly we consider the case of full sky CMB maps, for which we directly use map m_f to compute the NLVs inside the discs of radius r_h and assign them to pixels of a map at resolution n_l. In this case, an ANN is modelled to be trained with $12 \times 16^2 = 3072$ input features. The observed foreground-cleaned CMB maps tested in this case are all the available inpainted ones from Planck 2013 [6] and 2018 [12] data releases. The application of the ANN to NLV maps obtained from these inpainted maps makes it unlikely to attribute the findings to any minor residual foreground contamination from the galactic region.

Secondly, we consider partial sky CMB maps, obtained after masking with the $U73$ mask from Planck 2013 release [6], which sufficiently excludes the galactic region in addition to extragalactic point sources. The use of a mask helps minimize contributions from any minor foreground residuals. This $U73$ mask at $n_h = 128$ is obtained after downgrading the original binary mask and setting all pixels with values ≥ 0.8 to one and the rest to zero. Thus for the case of partial sky coverage, we take a map m_f and apply the $U73$ mask, for example in Figure 4.3. We calculate the NLVs only for discs which are not masked beyond 90% of their area, following the strategy of [11]. We then assign these NLVs to the map at resolution n_l. Thus for partial sky coverage, the ANN architecture is designed to work with 2652 input features, which are the remaining pixels in the $n_l = 16$ map, after obeying this criterion for disc rejection. We test the ANN on NLV maps obtained from the observed foreground-cleaned partial sky CMB maps from all releases of Planck (2013-2021) [6, 5, 9, 13], and WMAP (1yr-9yr) [33, 134, 135, 113, 34].

4.5 Training the neural networks

We have two ANNs, one for each of the full and partial sky cases. The input features used for training the ANNs are values of the NLV map arrays. Both the ANNs are similar in structure, save the difference in the number of input features and hyper-parameters associated with regularization methods. The ANNs are trained on realisations with the same seed values, but with different sky coverage.

Since $\hat{\lambda}$ is a unit vector, the degrees of freedom in ascertaining the components of $\hat{\lambda}$ are only two. Another degree of freedom in constructing the dipole modulated map is that of A. Thus, there are three degrees of freedom in total. Therefore we utilise the three components of the vector $A \times \hat{\lambda}$ as the associated training labels. For SI obeying CMB maps, these three labels are always zero, whereas for SI violating ones, they are non-zero. We choose the training labels in this manner since any other choices of training labels such as those of (A, θ, ϕ) or $(A, \lambda_1, \lambda_2)$ and the like cannot be unambiguously defined for SI obeying maps.

For the training set from simulated data, we compute the mean and standard deviation of the input features (denoted by μ_{in}, σ_{in}) as well as those of the training labels (denoted by μ_{out}, σ_{out}). We re-scale both the inputs and labels by subtracting their respective means from the entire set and dividing the resultant by their respective standard deviations. For similarly re-scaling the validation and test sets for simulated data, we use the previously computed means (μ_{in}, μ_{out}) and standard deviations (σ_{in}, σ_{out}) from the training set. Further this scaling is appropriately taken care of for the test set from observed foreground-cleaned CMB data.

A schematic flowchart to describe the ANN architecture common to both full and partial sky cases is shown in Figure 4.4. The differences between the two cases in the input layer and regularization parameters such as the rates of dropout and strengths of penalty for kernel regularizers are mentioned accordingly. We describe the two cases in further detail as follows.

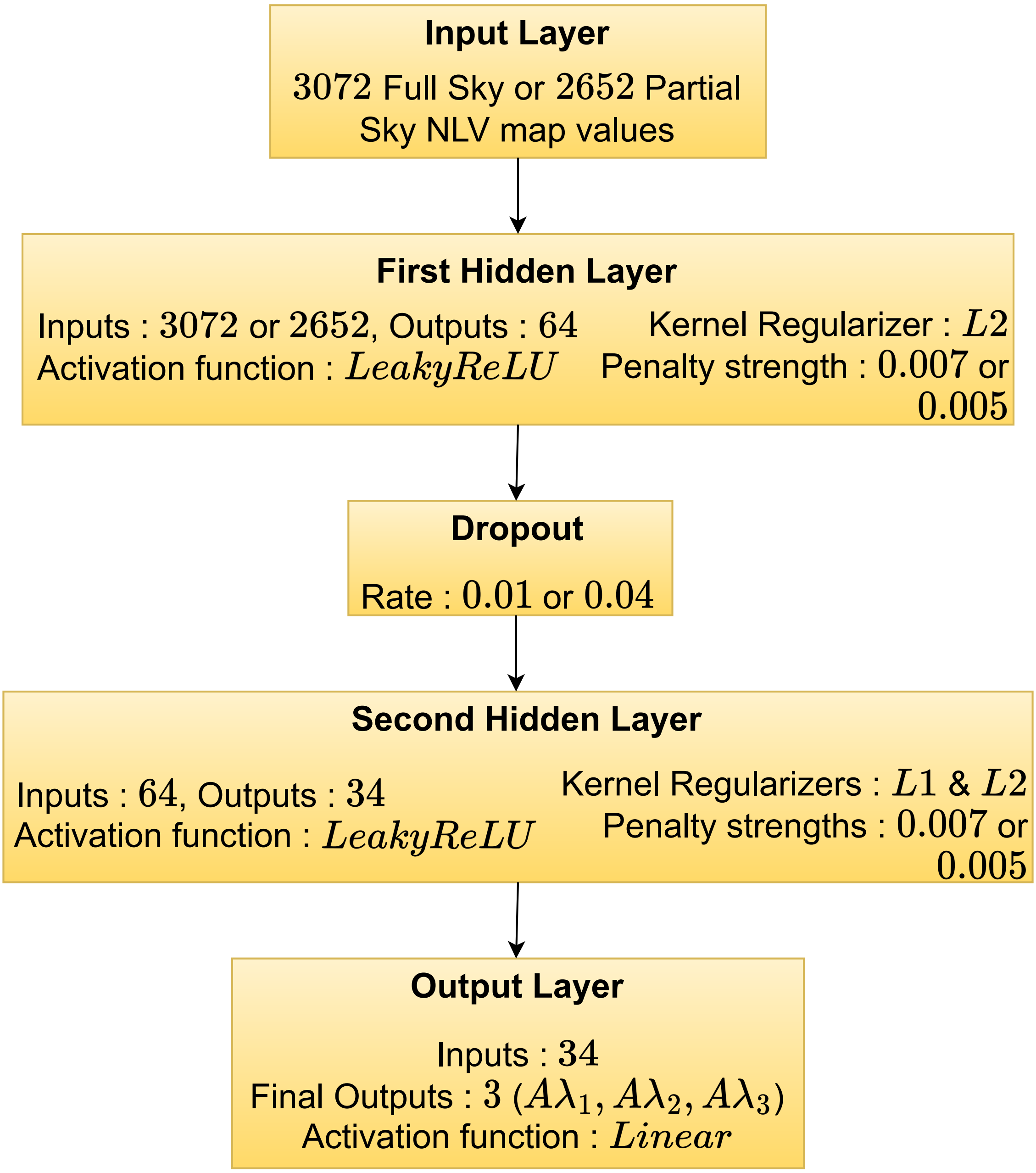

Figure 4.4: A schematic diagram of the common ANN architecture for detecting the dipolar modulation signal. The differences between full and partial sky cases are mentioned with 'or'. All layers after the input layer are densely connected to their preceding layers. The dropout implemented after the first hidden layer has a rate of 0.01 for full sky or 0.04 for partial sky. Additionally, the kernel regularizers used are $L2$ in the first hidden layer and both $L1$ and $L2$ in the second hidden layer with strengths of 0.007 each for the full sky case and 0.005 each for the partial sky case.

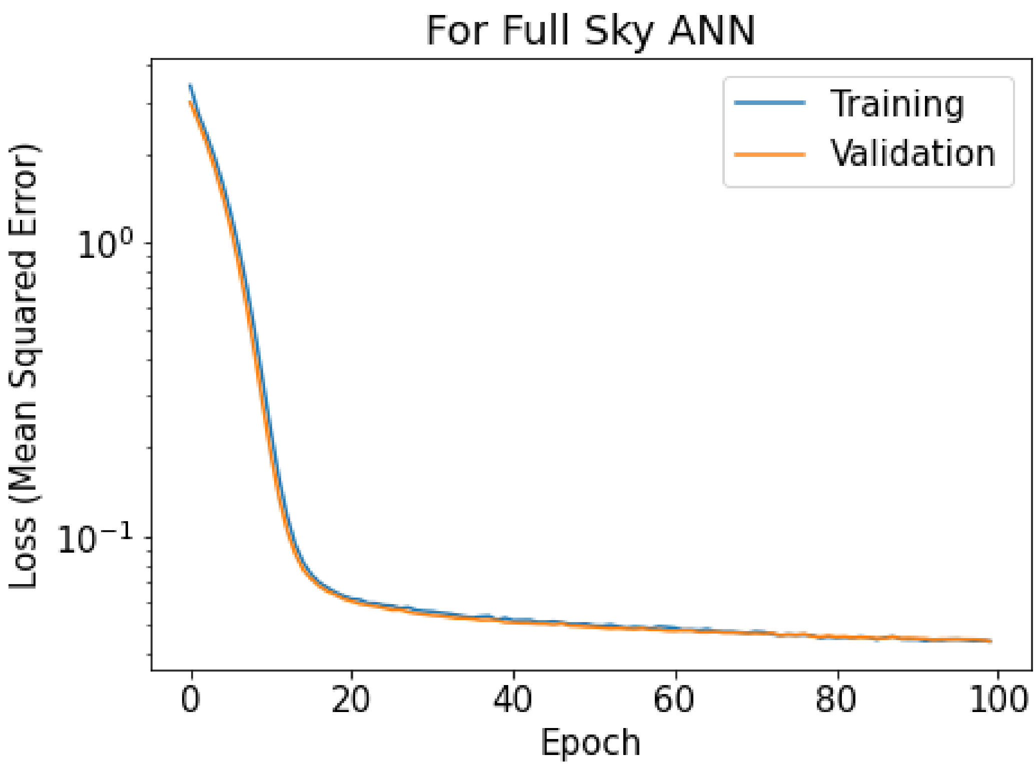

Figure 4.5: Loss curves for the ANN modelled using full sky CMB maps. The stabilisation around 80 epochs and beyond indicates that the ANN is trained.

4.5.1 Full sky ANN

In the full sky case, we consider 3072 features in the input layer, which is followed by two hidden layers having 64 and 34 nodes each. The first hidden layer has an $L2$ kernel regularizer with strength of penalty $= 0.007$. There is a dropout at a rate of 0.01 after this layer. In the second hidden layer, we have both $L1$ and $L2$ kernel regularizers each with strength of penalty values $= 0.007$. The output layer has three nodes corresponding to the three components of $A \times \hat{\lambda}$. The activation function used in each of the hidden layers is $LeakyReLU$ whereas that in the output layer is $linear$.

For training the ANN, we use mse as the loss function, while we use $Adam$ for optimization purposes with a learning rate of 10^{-4}. We see from Figure 4.5 that the training is accomplished by the end of approximately 80 epochs, when training with a batch size of 64. The time taken for a complete run of 100 epochs is 263.18 seconds, or ~ 4.4 minutes on an ordinary CPU.

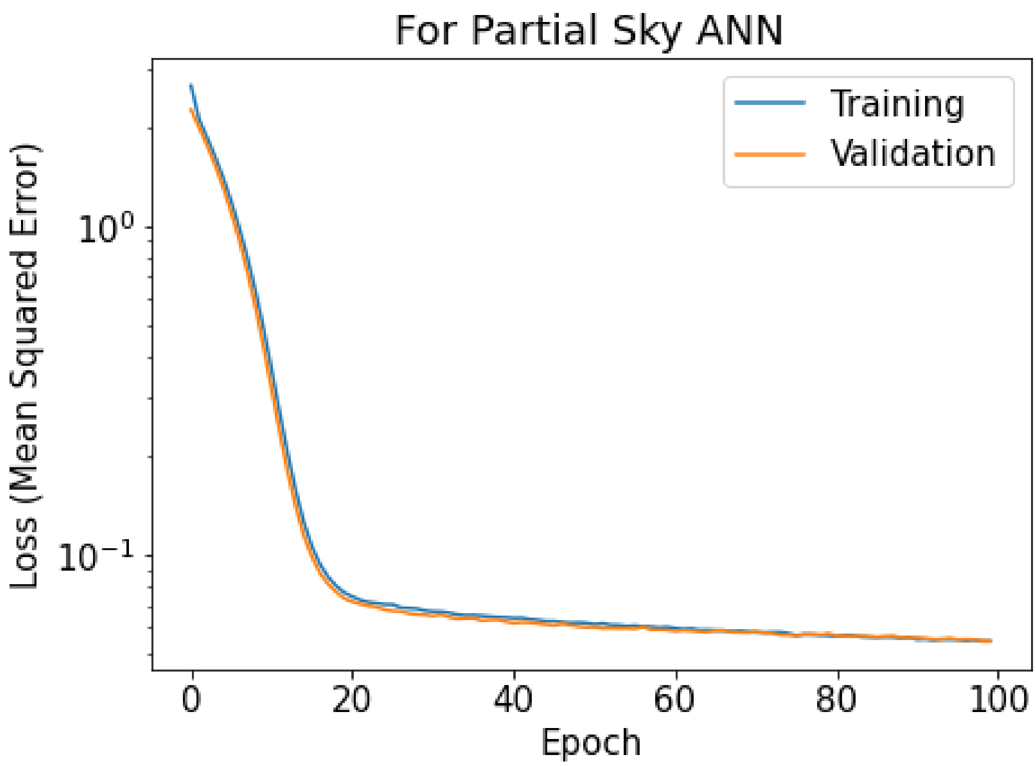

Figure 4.6: Loss curves for the ANN modelled using partial sky CMB maps. The stabilisation occurs around 80 epochs and beyond, indicating that the ANN is trained.

4.5.2 Partial sky ANN

Similar to the full sky case, we have two hidden layers of 64 and 34 nodes each. The input layer however takes 2652 features, which are the remnant pixels on the partial sky NLV map. In this case, the dropout rate used after the first hidden layer is 0.04. The kernel regularizers have strengths of penalty of 0.005 for $L2$ at the first hidden layer and 0.005 for both $L1$ and $L2$ at the second hidden layer. The output layer as usual has three nodes. The activation function is $LeakyReLU$ for both hidden layers, while that for the output layer is $linear$. Again, the mse is used as the loss function, and the optimizer is $Adam$ with a learning rate of 10^{-4}. The loss curves for training and validation sets are stabilised by 80 epochs, as seen in Figure 4.6, when the batch size is 64. For a complete training run of 100 epochs, the time taken is 254.85 seconds or ~ 4.25 seconds on an ordinary CPU.

4.6 Analysis and results

First we present the analysis of test samples with the trained ANNs for the two cases of sky coverage. We specify the goodness of fit for the same with the help of R^2 scores for each of the three outputs of $A\lambda_1, A\lambda_2, A\lambda_3$. Mathematically, R^2 score can be expressed as

$$R^2 \quad = \quad 1 - \frac{\sum \left(y_{true} - y_{pred}\right)^2}{\sum \left(y_{true} - \overline{y_{true}}\right)^2}, \tag{4.270}$$

where the summations are over all the samples of the set for which the outputs are predicted. It ranges between 0 and 1, where $R^2 = 1$ indicates a perfect fit or the notion that all variations in the predicted data can be explained by the intrinsic dispersion of the actual values.

Of the total 2×10^4 test samples, half are SI obeying (unmodulated) and the rest are SI violating (modulated) maps. So we can separate them and calculate their respective modulation amplitudes from the predicted outputs as $A = \sqrt{(A\lambda_1)^2 + (A\lambda_2)^2 + (A\lambda_3)^2}$. We expect the spread of values in amplitude for the unmodulated maps to be very close to zero, and that of modulated maps to closely follow the range $[0.03, 0.15]$ in which we have randomly chosen the amplitude.

In the following subsections, we present the respective probability densities of amplitude for unmodulated and modulated maps. Despite our expectation that A from unmodulated maps must be equal to zero, there is a very small non-zero spread in the values of A. This is attributable to the fact that the goodness of fit can not be achieved to be exactly equal to one, and is due to the underlying aleatoric uncertainty [289] of the realisations in question. Hence when we compute A for the observed foreground-cleaned CMB maps, we can say within the confidence defined by this uncertainty, as to whether the predicted value of A from an observed foreground-cleaned CMB map corresponds to a signal of modulation. The significance of detection of the signal is thus quantified with p-values of predicted A for observed foreground-cleaned maps versus the null hypothesis prediction for test samples of unmodulated maps.

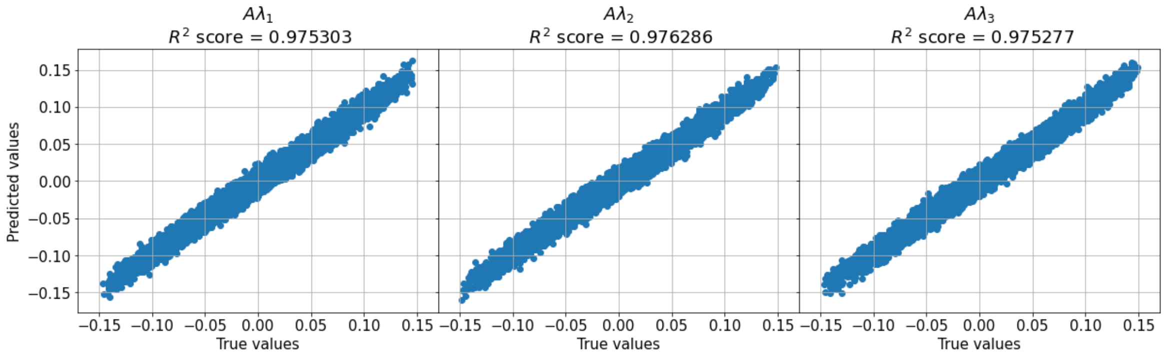

Figure 4.7: Predicted $A\hat{\lambda}$ components for the test set versus their true values, obtained using the full sky ANN. The predicted values present a good fit to their actual counterparts, as given by $R^2 > 0.97$.

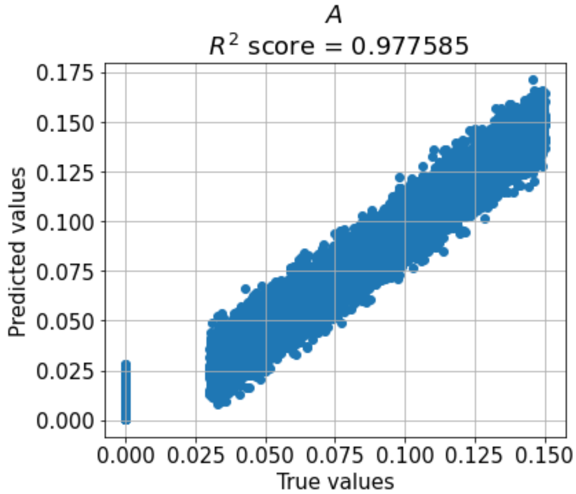

Figure 4.8: Predicted A for the test set versus their true values, obtained using the full sky ANN. The predicted values present a good fit to their actual counterparts, as given by $R^2 > 0.97$. The amplitude from unmodulated case are isolated on the left of the figure with a dispersion intrinsic to the reconstruction power of the ANN.

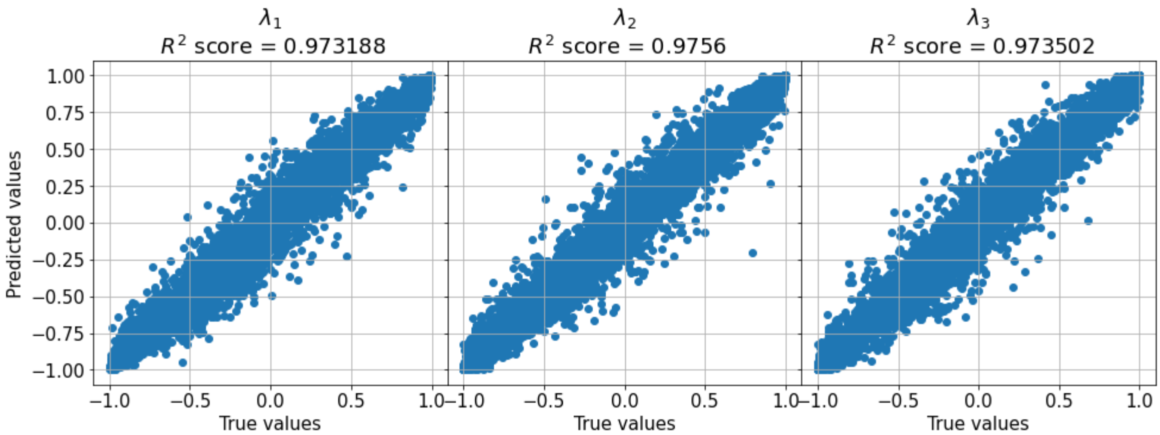

Figure 4.9: Predicted $\hat{\lambda}$ components for the modulated maps of the test set versus their true values, obtained using the full sky ANN. The predicted values present a good fit to their actual counterparts, as given by $R^2 > 0.97$. The $\hat{\lambda}$ components for unmodulated maps are not shown since they are undefined.

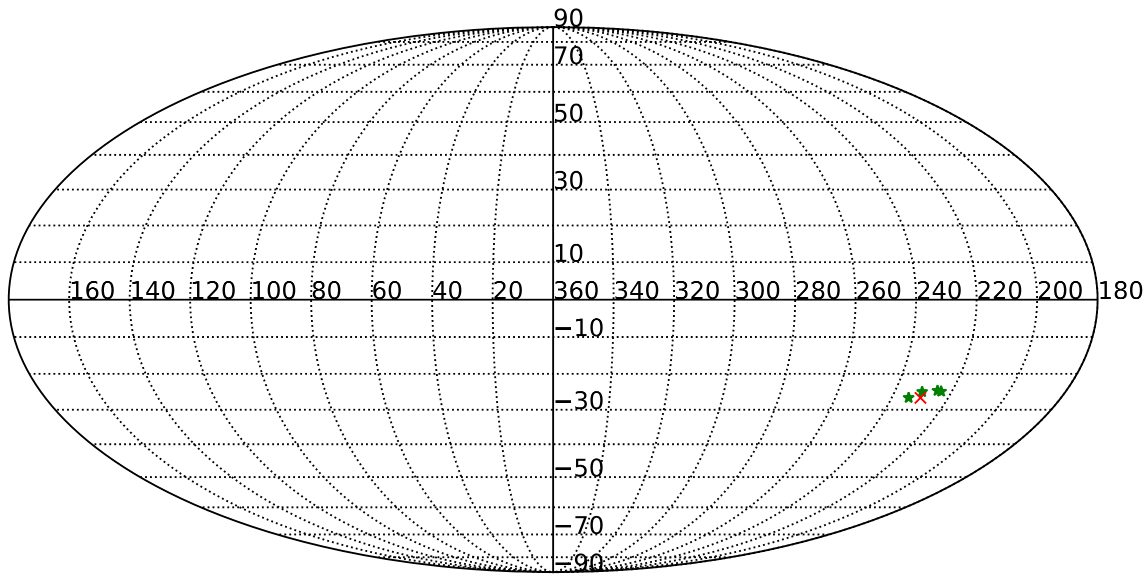

Figure 4.10: The preferred directions causing a dipolar modulation in the 5 inpainted observed CMB maps we have investigated with full sky coverage. For the Planck 2013 release inpainted NILC map, the direction is indicated with a red $\times$, while the same for each of the Planck 2018 inpainted CMB maps are shown with a green $\star$. Directions of dipolar modulation in these maps are fairly consistent with each other.

Map	$A\lambda_1$, $A\lambda_2$, $A\lambda_3$	A	Direction (l, b)	p-value
COMM 2018	-0.009961 , -0.012024 , -0.007281	0.0172	$230.3609°$, $-25.0006°$	1.19%
NILC 2013	-0.009646 , -0.011421 , -0.007509	0.0167	$229.8179°$, $-26.6688°$	1.35%
NILC 2018	-0.012476 , -0.011948 , -0.008014	0.019	$223.7628°$, $-24.8865°$	0.62%
SMICA 2018	-0.011885 , -0.01196 , -0.007744	0.0186	$225.1796°$, $-24.6688°$	0.74%
SEVEM 2018	-0.007996 , -0.011014 , -0.006827	0.0152	$234.0216°$, $-26.6376°$	2.79%

Table 4.1: Predictions for observed foreground-cleaned CMB maps using the full sky ANN. Both amplitudes and directions for all the maps are similarly valued, and the detection of the dipolar modulation signal is statistically significant.

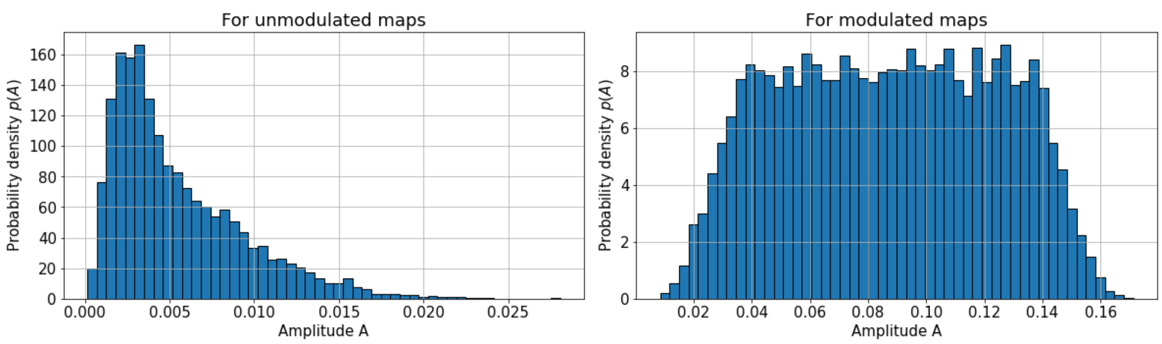

Figure 4.11: Probability densities of predicted amplitudes $p(A)$ for unmodulated and modulated maps from the test set using the full sky ANN. The histograms closely follow expected ranges of values for unmodulated and modulated maps.

4.6.1 Full sky

We test the trained full sky ANN on the 2×10^4 test samples and note the predictions of the ANN for the three components of $A\hat{\lambda}$. These results for the test set are shown along with their goodness of fit scores in Figure 4.7. The R^2 scores are > 0.97 indicating that the predicted components of $A\hat{\lambda}$ fit the expected true values quite well. In addition we present the scatter graphs of predicted versus true values of the amplitude (A) for the mixed set of unmodulated and modulated maps in Figure 4.8. We show amplitudes for both the unmodulated and modulated maps, and the former can be seen on the left corner of the graph with some dispersion. The scatter graphs of the direction given by the three components of $\hat{\lambda}$ are shown in Figure 4.9, only for modulated maps, since they are undefined for unmodulated maps.

The observed foreground-cleaned CMB maps considered in the full sky case are all the available inpainted maps, namely, NILC from Planck 2013 release, and Commander (COMM), NILC, SMICA and SEVEM from Planck 2018 release. We have evaluated the directions for each observed foreground-cleaned CMB map in the following manner. Firstly we normalise the predicted $A\hat{\lambda}$ vector by its respective A to get $\hat{\lambda}$. We then compute $\theta = \cos^{-1}(\lambda_3)$ and the galactic coordinate $b = 90^\circ - \theta$. A general procedure to obtain Galactic l can be outlined as follows:

1. We must find $\phi = \tan^{-1}\left(\frac{|\lambda_2|}{|\lambda_1|}\right)$.
2. If $\lambda_1 > 0, \lambda_2 > 0$, then $l = \phi$.
3. If $\lambda_1 < 0, \lambda_2 > 0$, then $l = 180^\circ - \phi$.
4. If $\lambda_1 < 0, \lambda_2 < 0$, then $l = 180^\circ + \phi$.
5. If $\lambda_1 > 0, \lambda_2 < 0$, then $l = 360^\circ - \phi$.

The consistency of the preferred directions given by $\hat{\lambda}$ or (l, b) for these five inpainted observed foreground-cleaned CMB maps can be illustrated by plotting the same in a Mollweide map, as shown in Figure 4.10.

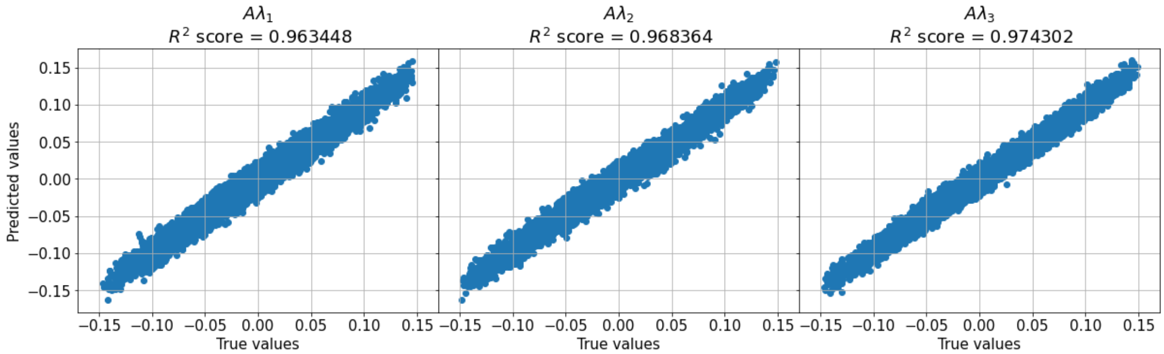

Figure 4.12: Predicted $A\hat{\lambda}$ components for the test set versus their true values, obtained using the partial sky ANN. The predicted values present a good fit to their actual counterparts, as given by $R^2 > 0.96$.

Additionally, we present the probability densities of the amplitudes computed from the predicted vector components for the 10^4 unmodulated and modulated maps of the test set in Figure 4.11, which show that the spread in predicted values closely obeys expectations. However, the ANN does not predict a perfect zero for the amplitude in the case of all the 10^4 unmodulated maps in the test set. Hence, we must gauge the possibility that the ANN predicts a non-zero value for these modulation amplitudes, even if there was no modulation in the observed foreground-cleaned CMB. This is given by a p-value which is computed as the percentage of predicted amplitudes from 10^4 unmodulated maps of the test set that lie above the predicted amplitude for an observed foreground-cleaned CMB map.

In Table 4.1, we present the results obtained for these inpainted maps, which lists the direct outputs ($A\hat{\lambda}$ components) from the ANN, the derived values of the amplitude and direction which are consistent across maps, and the p-values which indicate a significant detection of the dipolar modulation signal for all the maps.

4.6.2 Partial sky

For the case of partial sky coverage, we apply the corresponding trained ANN on the test set and then on available foreground cleaned CMB maps from all the releases of Planck and WMAP satellites.

In Figure 4.12, we present the scatter graph of predicted values of the components of the $A\hat{\lambda}$ vector with respect to the true values, along with their respective R^2 scores. Despite the fact that the goodness of fit scores are > 0.96, we notice that they are lower than those in the

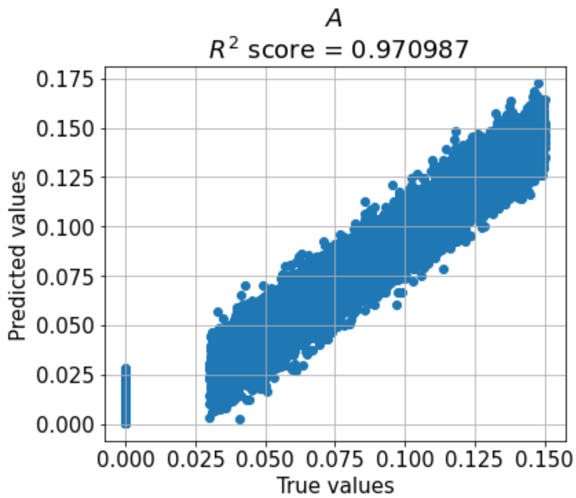

Figure 4.13: Predicted A for the test set versus their true values, obtained using the partial sky ANN. The predicted values present a good fit to their actual counterparts, as given by $R^2 > 0.97$. The amplitude from unmodulated case are isolated on the left of the figure with a dispersion intrinsic to the reconstruction power of the ANN.

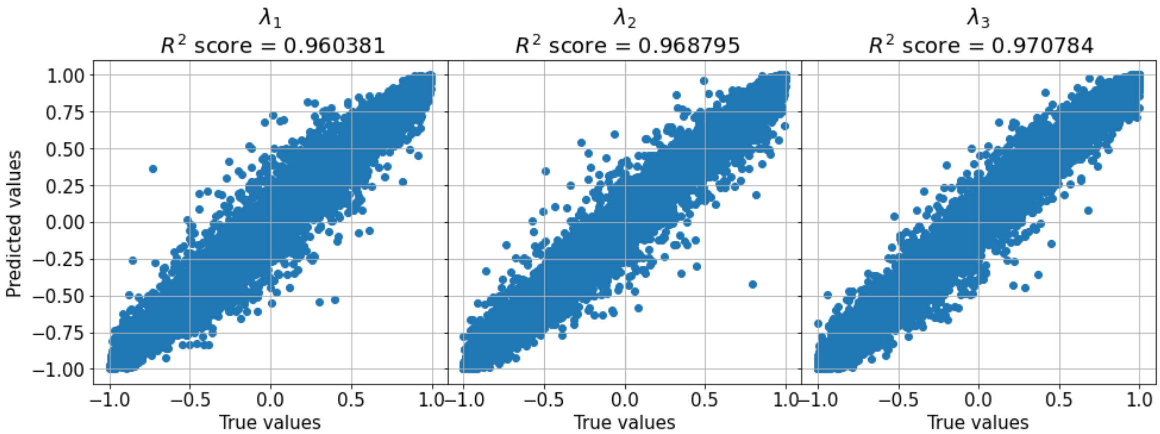

Figure 4.14: Predicted $\hat{\lambda}$ components for the modulated maps of the test set versus their true values, obtained using the partial sky ANN. The predicted values present a good fit to their actual counterparts, as given by $R^2 > 0.96$. The $\hat{\lambda}$ components for unmodulated maps are not shown since they are undefined.

Map	$A\lambda_1$, $A\lambda_2$, $A\lambda_3$	A	Direction (l, b)	p-value
C-R 2013	-0.022411 , -0.012969 , -0.008142	0.0271	$210.0573°$, $-17.4566°$	0.04%
COMM 2015	-0.022461 , -0.013471 , -0.006697	0.027	$210.9529°$, $-14.342°$	0.04%
COMM 2018	-0.022416 , -0.013744 , -0.007312	0.0273	$211.5149°$, $-15.5412°$	0.04%
NILC 2013	-0.022881 , -0.014141 , -0.006798	0.0277	$211.7163°$, $-14.1835°$	0.02%
NILC 2015	-0.021521 , -0.013196 , -0.007197	0.0263	$211.5149°$, $-15.9114°$	0.1%
NILC 2018	-0.022742 , -0.013616 , -0.00725	0.0275	$210.9099°$, $-15.2974°$	0.02%
SMICA 2013	-0.023005 , -0.014293 , -0.006445	0.0278	$211.8531°$, $-13.3859°$	0.02%
SMICA 2015	-0.022912 , -0.013846 , -0.006701	0.0276	$211.1449°$, $-14.0539°$	0.02%
SMICA 2018	-0.022649 , -0.013983 , -0.006931	0.0275	$211.6895°$, $-14.5946°$	0.02%
SEVEM 2013	-0.022908 , -0.014313 , -0.00661	0.0278	$211.9983°$, $-13.7514°$	0.02%
SEVEM 2015	-0.021601 , -0.013769 , -0.007109	0.0266	$212.5148°$, $-15.5113°$	0.07%
SEVEM 2018	-0.021764 , -0.013886 , -0.007099	0.0268	$212.54°$, $-15.376°$	0.06%
SEVEM 2021	-0.02145 , -0.013833 , -0.007017	0.0265	$212.8182°$, $-15.371°$	0.07%
WMAP 1yr	-0.039227 , -0.019561 , -0.00865	0.0447	$206.5035°$, $-11.1626°$	0.0%
WMAP 3yr	-0.027934 , -0.015285 , -0.009217	0.0331	$208.6861°$, $-16.1434°$	0.0%
WMAP 5yr	-0.022598 , -0.012087 , -0.00881	0.0271	$208.1404°$, $-18.971°$	0.04%
WMAP 7yr	-0.020355 , -0.012319 , -0.008	0.0251	$211.1818°$, $-18.5848°$	0.17%
WMAP 9yr	-0.014497 , -0.00986 , -0.007313	0.019	$214.2221°$, $-22.6406°$	1.66%

Table 4.2: Predictions for observed foreground-cleaned CMB maps using the partial sky ANN. Overall, both amplitudes and directions across all maps are consistent. Additionally, the detection of the signal of dipolar modulation in all the maps is statistically significant.

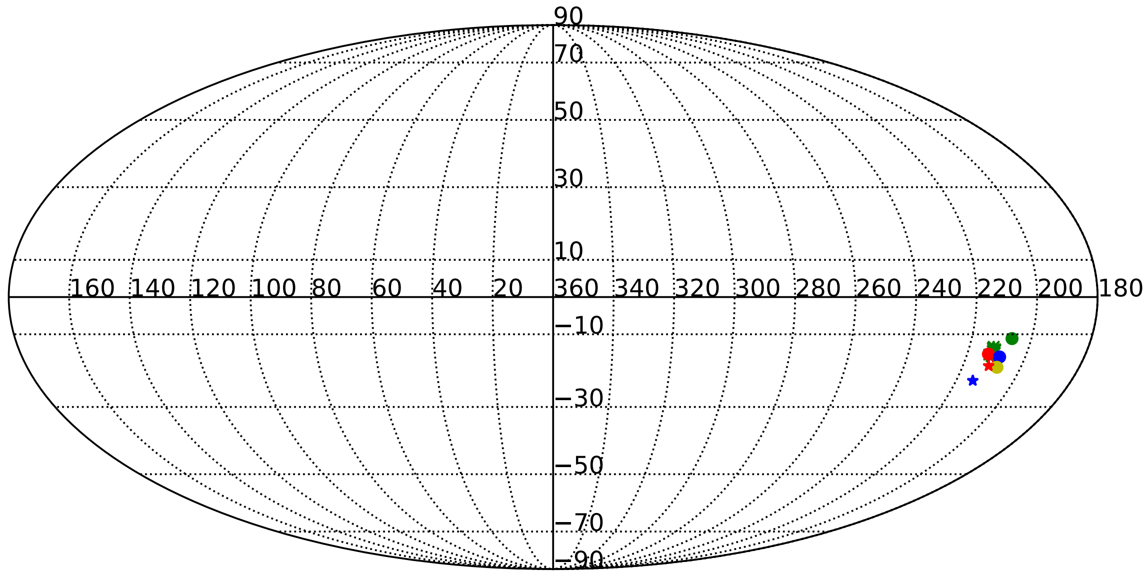

Figure 4.15: The preferred directions causing a dipolar modulation in the 18 observed foreground-cleaned CMB maps we have investigated with partial sky coverage. Preferred dipole direction in observed foreground-cleaned partial sky CMB maps from Planck releases of 2013, 2015, 2018, and 2021 are indicated with red $\times$'s, green $\times$'s, green $\star$'s and a red $\bullet$, respectively. Those for each of WMAP 1yr, 3yr, 5yr maps are shown with a green, blue and yellow $\bullet$, and directions for WMAP 7yr and 9yr are shown with a red and a blue $\star$. The figure shows that the directions are mostly consistent over all these variously procured maps.

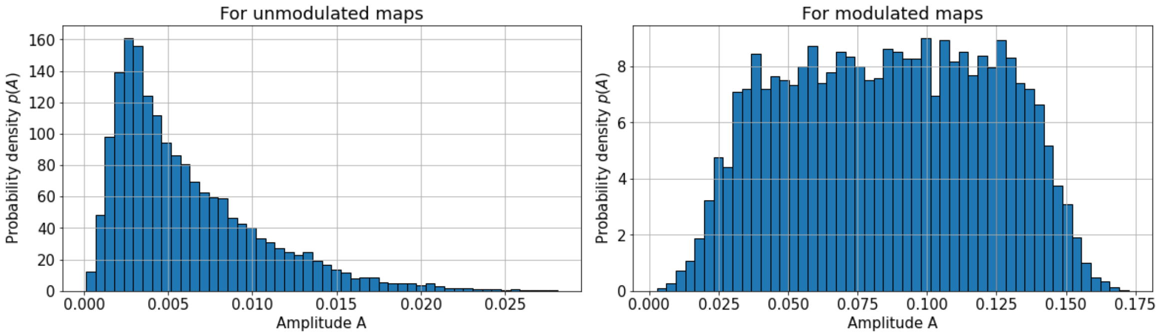

Figure 4.16: Probability densities of predicted amplitudes $p(A)$ for unmodulated and modulated maps from the test set for the partial sky ANN. The range of predicted amplitudes appropriately follow zero and non-zero values for unmodulated and modulated maps.

full sky case. This is due to the increased variations that cannot be explained by a similar dispersion in the true values, obviously caused by the use of a mask in this case. Further, since the $U73$ mask primarily conceals galactic sources, it is somewhat symmetric about the z-axis, and hence the R^2 score for $A\lambda_3$ is not as compromised as those of $A\lambda_1$ and $A\lambda_2$. This is in contrast with the full sky case, for which the goodness of fit values of all the three components were similar (about 0.975).

Further we show the scatter graphs of the amplitude (A) for the test set in Figure 4.13. We present amplitudes for both the unmodulated and modulated maps, and the former shows some dispersion for the unmodulated case on the left corner of the figure. Similar to the case of full sky coverage, the three components of $\hat{\lambda}$ are undefined for unmodulated maps. Hence, the scatter graphs for the direction are shown in Figure 4.14 only for modulated maps.

When the partial sky ANN is applied to NLV maps of the partial sky observed foreground-cleaned CMB, we see a very consistent amplitude and direction of dipolar modulation across all the maps from Planck and WMAP releases ranging from Planck 2013-2021 data and WMAP 1yr-9yr data. The consistency of the preferred directions given by $\hat{\lambda}$ or (l, b) for the 18 observed foreground-cleaned CMB maps can be inferred from a plot of the same in a Mollweide map, as presented in Figure 4.15.

Following our approach in the full sky case, we estimate the amplitudes from predicted $A\hat{\lambda}$'s and present their probability densities for the 10^4 unmodulated and modulated maps from the test set in Figure 4.16. On finding the minimum and maximum values of predicted amplitudes for these two types of maps, we see that there is a very subtle increase in their spreads (of the orders of 10^{-4} for unmodulated maps, and 10^{-3} for modulated maps), compared to the full sky case. Nonetheless, these histograms are qualitatively similar to those obtained for the case of full sky coverage, and the predicted amplitudes for unmodulated maps are again not exactly zero. Thus we can quantify the significance of detection for the dipolar modulation signal in the observed foreground-cleaned partial sky CMB maps. We represent this significance with the p-value which is computed as the percentage of 10^4 unmodulated maps for which the predicted amplitudes are larger than those from the observed foreground-cleaned CMB maps.

We finally present all the findings from the partial sky analysis in Table 4.2, which shows the partial sky ANN outputs for the three $A\hat{\lambda}$ components, the computed values of the amplitudes and directions which are consistent across maps, and the p-values which correspond to a significant detection of the signal of dipolar modulation for all the maps.

4.7 Summary and conclusion

The CMB temperature fluctuations are expected to obey statistical isotropy (SI) according to the Standard (ΛCDM) model of Cosmology. This entails that there must be no preference of a direction in the CMB. However, the hemispherical power asymmetry as seen by many authors in existing literature indicates a departure from the Standard Model. This departure is significant given the reported magnitudes of the p-values, and the sheer volume of such findings obtained with independent methods. An underlying dipolar modulation is suggested as a possible cause of this power asymmetry, the strength of which is known to vary with the scale at which it is estimated.

For the first time, we use deep learning with Artificial Neural Networks (ANNs) to probe the existence of a possible dipolar modulation signal. This provides a novel approach towards validating or rejecting evidence for such a signal in previous literature. Employing ANNs for studying features in the CMB may introduce a paradigm shift in interpretation of signals of SI violation, relative to traditional methods of regression or fitting associated with the frequentist approach. This is because ANN architectures can ‘learn’ how to detect a signal when presented with a set of samples for training. Upon adequate training the ANN develops the artificial intelligence to act on observed foreground-cleaned CMB data and consequently estimate a possible signal in such data.

We consider normalised local variance (NLV) maps which are very useful as input features to train ANNs. We build two ANN architectures namely, for the full and partial sky cases. To obtain partial sky maps, we use the Planck $U73$ mask released in 2013. The key findings of this work are as follows.

1. With full sky coverage,
   (a) generally consistent values of amplitude and direction of the modulation are seen across all available observed foreground-cleaned full sky inpainted maps from all releases of Planck (COMM 2018, NILC 2013, NILC 2018, SMICA 2018, SEVEM 2018).
   (b) The detected signal is significant (at $97.21\% - 99.38\%$ C.L.) for all these 5 maps.
2. With partial sky coverage,
   (a) we find reasonably consistent values of amplitude and direction of the modulation across all observed foreground-cleaned partial sky maps from all releases of Planck (2013-2021) and WMAP (1yr-9yr).
   (b) The detected signal is significant at $99.9\% - 99.98\%$ C.L. for all the 13 Planck maps, and at $98.34\% - 100.0\%$ C.L. for all the 5 WMAP maps.
3. These results are therefore robust against sky coverage, observational instruments, periods of observation, and foreground cleaning and inpainting methods.

In the following paragraphs, we discuss two criticisms that have been posited against the manner in which any possibly anisotropic signals in the CMB are probed, and address how our method is able to mitigate those effects further.

Firstly the look-elsewhere effect occurs when a signal is detected purely by chance and is attributable to the large sample size for which it becomes more favourable to see some random fluctuations that are statistically significant. It is additionally the result of a constant approach of ‘looking elsewhere’ to find a significant signal, while disregarding any previously insignificant findings. In this work, we are able to weaken the look-elsewhere effect (a) with the robustness of the detection, and (b) by adding to existing literature an independent method like the one in this work, which also detects a significant signal, thus strengthening the repeatability of the initial findings.

Secondly, the concept of a posteriori statistical inference is based on devising estimators to shift our focus to visually anomalous features. However, (a) since the method of deep learning to distinguish unmodulated maps from modulated ones (quantified with the magnitude of the modulation) is distinct from the process of devising an estimator which focuses on a search for such a signal after looking at the data, and (b) as we use a wide range of amplitudes and directions to train the ANN so that it is not focused at detection of amplitude and directions specific to the observed foreground-cleaned data and can be used to probe unseen data, we are able to alleviate the criticism of an a posteriori choice of statistics.

In conclusion, we can say that our findings agree quite closely with those in existing literature. Further, assuming that no unknown residual systematics are commonly present in all the observed foreground-cleaned CMB maps considered here, this entails that either our universe is a rare realisation of the Standard Model, or that we live in a statistically anisotropic universe which could be a rather common realisation of a different model.

CHAPTER 5

DISCUSSION AND CONCLUSION

The evolution of the universe is expected to have arisen from a period of cosmic inflation, based on a homogeneous and isotropic background metric for expansion, with some perturbations to act as seeds for structure formation in due course of time. Such an assumption of large scale homogeneity and isotropy coupled with the notion that inflation uniformly expands the space fabric, leads to the expectation that there must be no directional preference in the placement of perturbations on the largest scales which correspond approximately to the size of the causal horizon. This is known as Statistical Isotropy (SI), which mathematically asserts that the two-point correlation function of the primordial perturbations is rotationally invariant.

Several violations of SI have been found and studied by authors in existing literature, such as the hemispherical power asymmetry, the quadrupole-octupole alignment, the parity asymmetry, large angle correlation deficit, and so on. The signals observed in each of these works is significant and robust against various sky coverages, instruments and periods of observation, frequency bands, foreground reduction or cleaning algorithms and the like. Hence, we have two possible conclusions: either the CMB and hence the universe we live in is an unusual realisation of the concordance (ΛCDM) model of Cosmology, or that possible corrections need to be made to accommodate our universe as a more common realisation of a different model. The latter case therefore warrants the need for more exotic physics of evolution of the early universe. Possibilities for such exotic physics include non-trivial cosmic topology or anisotropic spacetimes, modulation of the primordial power spectrum of perturbations to incorporate rotational variance, to mention a few.

Hence it becomes imperative to study the large scale temperature fluctuations in the

CMB, firstly because the CMB happens to be one of the earliest sources of radiation from the primordial universe, and secondly because the large-scale fluctuations carry pristine information from the conditions prevalent at the time of inflation. The gravitational perturbations transform into imprints on the temperature of the CMB causing these fluctuations called temperature anisotropies. Therefore, in this thesis, we scrutinised the largest scale CMB temperature anisotropies for a holistic understanding of the isotropy of the universe we live in, and hence our assumptions regarding the inflationary era in the evolution of the universe. We analysed foreground-minimized CMB temperature fluctuation data from Planck and WMAP to ascertain the presence of departures from its theoretically expected SI with traditional frequentist methods and Machine Learning (ML). For both frequentist and ML approaches we additionally used simulated CMB maps for comparison or training purposes, respectively. The three works that we explored are as follows.

Firstly, since the temperature anisotropy field of the CMB can be expressed as a sum of a symmetric and an antisymmetric function, they equivalently carry with them the information of an even parity and odd parity respectively. Further, SI of the universe dictates that there must be no such symmetry or antisymmetry which reflects in the CMB. We established a connection between the correlations of the angular power spectrum (APS) of the CMB temperature anisotropy field and the parity associated with it, by studying the correlations between APS measures at different multipoles. We devised a novel average level spacing estimator inspired from the respective concepts of level clustering and level repulsion for uncorrelated and correlated eigenvalues of random matrices. Our estimator is able to distinguish correlations between APS measures with or without parity distinction. Thus we considered three cases, namely, with all, even and odd multipole spacings of the APS. We found using traditional frequentist methodology, that there exists an even parity biased correlation deficit in the observed foreground-cleaned CMB, which manifests as an unusually low value of the even multipole mean spacing. To understand if any known galactic foregrounds, or the non-Gaussian cold spot (NGCS) could be contributing to the signal, we used galactic masks in union with a mask for the NGCS. Since we worked in multipole space, partial sky coverage cannot be dealt with sans introduction of some correlations due to the pseudo-C_ℓ

method. Thus, we eschewed this problem and demonstrated the robustness of the results by inpainting over several masked observational CMB data, using the technique of constrained Gaussian realisations. Existing literature contains works describing (a) an anomalous odd parity preference of the CMB APS [156], and (b) an unusual deficit of large angle correlation in the CMB [67] which is equivalent to (a) [158]. Our work augments these works with the finding that on an average over large angular scales, consecutive even multipole APS measures tend to stay unusually close together, suggesting that the manner in which they are correlated does not agree with theoretical predictions. Further, since the large scale angular correlation deficit has already been associated with the odd-parity preference of power, a future study may help shed light on whether the possibly peculiar correlations in even parity APS measures primarily contribute to the lack of large angular scale correlations.

Secondly, we studied the local extrema (hot and cold spots) of the CMB since they reflect the local extrema of matter density perturbations at last scattering. Besides, SI entails that the CMB spots must be isotropically distributed. Thus, it is important to investigate if there is any significant non-uniformity in the placement of spots of the observed CMB, since the presence or absence of the same dictates how LSS forms. We utilised the orientation matrix which is defined for a study of data points on the surface of a 2-sphere and modified it by incorporating weights of the temperature extrema values to encapsulate the randomness attributable to both the magnitudes of the temperature intensities as well as their directions. From the eigenvalues of the weighted orientation matrix we could construct two parameters: (a) to quantify the strength of the non-uniformity, and (b) to denote the shape of the clumping of spots in terms of clustering or girdling. We found a significant and robust signal of an anomalously weak non-uniformity in the placement of hot and cold spots of various foreground-cleaned CMB maps and foreground-reduced CMB maps at different frequency bands, with full and partial sky coverage, which is independent of the NGCS. Further, we found that intriguingly the signal vanishes without the anomalous contributions of the quadrupole and octupole and hence it must be related with the low CMB temperature variance anomaly.

In our third work, we investigate the notion that due to SI, there should exist no large scale anisotropy or preferred direction to have a direct bearing on the smaller scale fluctuations, as the former must have been washed out of the cosmological horizon, thus having no causal influence on sub-horizon evolution of fluctuations. However, the hemispherical power asymmetry [92] as noted in the observed CMB indicates a violation of SI. A dipole modulation of the CMB temperature anisotropy field was posited [94, 116, 260] to explain this power asymmetry. Such a dipolar modulation introduces off-diagonal correlations between spherical harmonic coefficients corresponding to adjacent multipoles, thus breaking SI. Hence, we employed Artificial Neural Networks (ANNs) as a representative example of Artificial Intelligence (AI) to detect the presence of a dipolar modulation in the CMB temperature field. Since we utilised modulated and unmodulated simulations of CMB maps for training the ANNs, the machine could equip itself with the capability to make a self guided detection of the signal, while also providing us the magnitude of the dipole and its direction in terms of the three vector components. We used normalised local variance maps [11] at a lower resolution obtained from a corresponding higher resolution modulated or unmodulated CMB map to train the ANNs. Since a large variety of amplitudes and directions were used to train the ANNs to learn how to detect the signals, we were able to mitigate the criticism of a posteriori inference. With this novel and independent approach we obtained robust signals of the modulation at high confidence, consistent with existing literature. We found the signal to persist with values of the amplitude and direction consistent over foreground-cleaned and/or inpainted CMB temperature maps from all releases of Planck and WMAP satellites, over both full and partial sky coverages. The robustness of this independent method of detection of the signal additionally alleviates look-elsewhere effects.

In conclusion, we explored and found the following. (I) Measures of the CMB temperature APS of adjacent even multipoles stay unusually close to each other on an average over large scales, suggesting that these have a peculiar nature of correlations. (II) A strikingly weak non-uniformity in placement of hot and cold spots which shares a common origin with the low temperature variance anomaly and anomalous contributions of the quadrupole and octupole. (III) A significant detection of the dipolar modulation signal with consistent values of amplitude and direction across observed CMB maps using ANNs, thus weakening the criticism of look-elsewhere effects and a posteriori inferences. In all of these works, we found significant signals of anomalous features, which are robust against different sky coverages, various observation instruments, frequency bands, foreground reduction and/or cleaning algorithms, periods of observation, inpainting methods, and the like, as the case may be. Hence, it becomes difficult to attribute these signals to systematics or known foreground residual sources. So we either happen to live in an unlikely realisation of the universe, or some exotic physics unaccounted for in the concordance model is at play, unless these effects are completely free from some unknown residuals common to all the foreground-minimized CMB maps considered.

In the future, given that observations of the CMB polarisation will be characterised by a considerably higher signal-to-noise ratio, we shall be able to thus suitably modify the tools and techniques developed for CMB temperature anisotropy data, for an application of those on CMB polarisation data. This will essentially help corroborate the findings of yesteryears with regard to violations of SI. Additionally, we will assess LSS data along with CMB data in cross-correlation studies for a better understanding of violations of SI which must evolve according to the Einstein-Boltzmann equations and leave imprints in the formation of structure. A notable aspect of the results we have obtained, especially from our works on the level correlations, and on isotropy of local extrema, is that these are independent of the NGCS, while the excess isotropy of spots as seen by us is characterised by the anomalous contributions of the quadrupole and octupole components. Such investigations to find common origins and to unify statistically anisotropic features in the CMB will help expedite efforts in finding a common solution. Thus, with these aims in the future, we shall be able to exploit the full potential of upcoming cosmological observations at our disposal.

References

[1] M. A. Petroff et al. Full-sky Cosmic Microwave Background Foreground Cleaning Using Machine Learning. *The Astrophysical Journal*, 903(2):104, nov 2020. doi: 10.3847/1538-4357/abb9a7. URL https://dx.doi.org/10.3847/1538-4357/abb9a7.

[2] G. Aad et al. Observation of a new particle in the search for the Standard Model Higgs boson with the ATLAS detector at the LHC. *Physics Letters B*, 716(1):1–29, 2012. ISSN 0370-2693. doi: 10.1016/j.physletb.2012.08.020. URL https://www.sciencedirect.com/science/article/pii/S037026931200857X.

[3] L. Abbott et al. Particle production in the new inflationary cosmology. *Physics Letters B*, 117(1):29–33, 1982. ISSN 0370-2693. doi: 10.1016/0370-2693(82)90867-X. URL https://www.sciencedirect.com/science/article/pii/037026938290867X.

[4] L. Ackerman et al. Imprints of a primordial preferred direction on the microwave background. *Phys. Rev. D*, 75:083502, April 2007.

[5] R. Adam et al. Planck 2015 results - IX. Diffuse component separation: CMB maps. *A&A*, 594:A9, 2016. doi: 10.1051/0004-6361/201525936. URL https://doi.org/10.1051/0004-6361/201525936.

[6] P. A. R. Ade et al. Planck 2013 results. XII. Diffuse component separation. *A&A*, 571:A12, 2014. doi: 10.1051/0004-6361/201321580. URL https://doi.org/10.1051/0004-6361/201321580.

[7] P. A. R. Ade et al. Planck 2015 results - XVI. Isotropy and statistics of the CMB.

A&A, 594:A16, 2016. doi: 10.1051/0004-6361/201526681. URL https://doi.org/10.1051/0004-6361/201526681.

[8] S. Adhikari. Local variance asymmetries in Planck temperature anisotropy maps. *Monthly Notices of the Royal Astronomical Society*, 446(4):4232–4238, 12 2014. ISSN 0035-8711. doi: 10.1093/mnras/stu2408. URL https://doi.org/10.1093/mnras/stu2408.

[9] N. Aghanim et al. Planck 2018 results. VI. Cosmological parameters. *Astronomy and Astrophysics*, 641:A6, Sept. 2020. doi: 10.1051/0004-6361/201833910.

[10] N. Aghanim et al. Planck 2018 results - III. High Frequency Instrument data processing and frequency maps. *A&A*, 641:A3, 2020. doi: 10.1051/0004-6361/201832909. URL https://doi.org/10.1051/0004-6361/201832909.

[11] Y. Akrami et al. POWER ASYMMETRY IN WMAP AND PLANCK TEMPERATURE SKY MAPS AS MEASURED BY A LOCAL VARIANCE ESTIMATOR. *The Astrophysical Journal Letters*, 784(2):L42, mar 2014. doi: 10.1088/2041-8205/784/2/L42. URL https://dx.doi.org/10.1088/2041-8205/784/2/L42.

[12] Y. Akrami et al. Planck 2018 results - IV. Diffuse component separation. *A&A*, 641:A4, 2020. doi: 10.1051/0004-6361/201833881. URL https://doi.org/10.1051/0004-6361/201833881.

[13] Y. Akrami et al. Planck intermediate results - LVII. Joint Planck LFI and HFI data processing. *A&A*, 643:A42, 2020. doi: 10.1051/0004-6361/202038073. URL https://doi.org/10.1051/0004-6361/202038073.

[14] Y. Akrami et al. Planck 2018 results - VII. Isotropy and statistics of the CMB. *Astronomy & Astrophysics*, 641:A7, Sept. 2020. ISSN 0004-6361, 1432-0746. doi: 10.1051/0004-6361/201935201. URL https://www.aanda.org/articles/aa/abs/2020/09/aa35201-19/aa35201-19.html.

[15] Y. Akrami et al. Planck 2018 results - II. Low Frequency Instrument data processing. *A&A*, 641:A2, 2020. doi: 10.1051/0004-6361/201833293. URL https://doi.org/10.1051/0004-6361/201833293.

[16] A. Albrecht and P. J. Steinhardt. Cosmology for Grand Unified Theories with Radiatively Induced Symmetry Breaking. *Phys. Rev. Lett.*, 48:1220–1223, Apr 1982. doi: 10.1103/PhysRevLett.48.1220. URL https://link.aps.org/doi/10.1103/PhysRevLett.48.1220.

[17] A. Albrecht et al. Reheating an Inflationary Universe. *Phys. Rev. Lett.*, 48:1437–1440, May 1982. doi: 10.1103/PhysRevLett.48.1437. URL https://link.aps.org/doi/10.1103/PhysRevLett.48.1437.

[18] G. Altarelli and S. Forte. *The Standard Model of Electroweak Interactions*, pages 35–81. Springer International Publishing, Cham, 2020. ISBN 978-3-030-38207-0. doi: 10.1007/978-3-030-38207-0_3. URL https://doi.org/10.1007/978-3-030-38207-0_3.

[19] P. K. Aluri and P. Jain. Parity asymmetry in the CMBR temperature power spectrum. *Monthly Notices of the Royal Astronomical Society*, 419(4):3378–3392, 01 2012. ISSN 0035-8711. doi: 10.1111/j.1365-2966.2011.19981.x. URL https://doi.org/10.1111/j.1365-2966.2011.19981.x.

[20] P. K. Aluri et al. Alignments of parity even/odd-only multipoles in cmb. *Monthly Notices of the Royal Astronomical Society*, 472(2):2410–2421, August 2017.

[21] P. K. Aluri et al. Is the Observable Universe Consistent with the Cosmological Principle?, 2022. URL https://arxiv.org/abs/2207.05765.

[22] M. Ashdown et al. PSM: Planck Sky Model. Astrophysics Source Code Library, record ascl:1208.005, Aug. 2012.

[23] Y. Y. Atas et al. Distribution of the Ratio of Consecutive Level Spacings in Random Matrix Ensembles. *Phys. Rev. Lett.*, 110:084101, Feb 2013. doi:

10.1103/PhysRevLett.110.084101. URL https://link.aps.org/doi/10.1103/PhysRevLett.110.084101.

[24] Y. Ayaita et al. Too few spots in the cosmic microwave background. *Phys. Rev. D*, 81: 023507, Jan 2010. doi: 10.1103/PhysRevD.81.023507. URL https://link.aps.org/doi/10.1103/PhysRevD.81.023507.

[25] J. M. Bardeen et al. Spontaneous creation of almost scale-free density perturbations in an inflationary universe. *Phys. Rev. D*, 28:679–693, Aug 1983. doi: 10.1103/PhysRevD.28.679. URL https://link.aps.org/doi/10.1103/PhysRevD.28.679.

[26] J. M. Bardeen et al. The Statistics of Peaks of Gaussian Random Fields. *The Astrophysical Journal*, 304:15, May 1986. doi: 10.1086/164143.

[27] J. G. Bartlett. The standard cosmological model and CMB anisotropies. *New Astronomy Reviews*, 43(2):83–109, 1999. ISSN 1387-6473. doi: 10.1016/S1387-6473(99)00007-X. URL https://www.sciencedirect.com/science/article/pii/S138764739900007X.

[28] S. Basak and J. Delabrouille. A needlet internal linear combination analysis of WMAP 7-year data: estimation of CMB temperature map and power spectrum. *Monthly Notices of the Royal Astronomical Society*, 419(2):1163–1175, 12 2011. ISSN 0035-8711. doi: 10.1111/j.1365-2966.2011.19770.x. URL https://doi.org/10.1111/j.1365-2966.2011.19770.x.

[29] M. Bauer and J. D. Shergold. Limits on the cosmic neutrino background. *Journal of Cosmology and Astroparticle Physics*, 2023(01):003, jan 2023. doi: 10.1088/1475-7516/2023/01/003. URL https://dx.doi.org/10.1088/1475-7516/2023/01/003.

[30] T. W. Baumgarte and S. L. Shapiro. *Numerical Relativity : Solving Einstein's Equations on the Computer*. Cambridge University Press, 2010.

[31] L. Bedini et al. Separation of correlated astrophysical sources using multiple-lag data covariance matrices. *EURASIP Journal on Applied Signal Processing*, 2005: 2400–2412, Aug. 2005. doi: 10.1155/ASP.2005.2400. URL https://ui.adsabs.harvard.edu/abs/2005EJASP2005.2400B.

[32] C. L. Bennett et al. First-Year Wilkinson Microwave Anisotropy Probe (WMAP) Observations: Preliminary Maps and Basic Results. *The Astrophysical Journal Supplement Series*, 148(1):1–27, sep 2003. doi: 10.1086/377253. URL https://doi.org/10.1086%2F377253.

[33] C. L. Bennett et al. First-Year Wilkinson Microwave Anisotropy Probe (WMAP) Observations: Foreground Emission. *The Astrophysical Journal Supplement Series*, 148(1):97, sep 2003. doi: 10.1086/377252. URL https://dx.doi.org/10.1086/377252.

[34] C. L. Bennett et al. Nine-year wilkinson microwave anisotropy probe (wmap) observations: Final maps and results. *The Astrophysical Journal Supplement Series*, 208(2):20, sep 2013. doi: 10.1088/0067-0049/208/2/20. URL https://dx.doi.org/10.1088/0067-0049/208/2/20.

[35] A. Benoit-Lévy et al. Full-sky CMB lensing reconstruction in presence of sky-cuts. *A&A*, 555:A37, 2013. doi: 10.1051/0004-6361/201321048. URL https://doi.org/10.1051/0004-6361/201321048.

[36] A. Bernui. Is the cold spot responsible for the CMB North-South asymmetry? *Phys. Rev. D*, 80:123010, Dec 2009. doi: 10.1103/PhysRevD.80.123010. URL https://link.aps.org/doi/10.1103/PhysRevD.80.123010.

[37] A. Bernui et al. North-South non-Gaussian asymmetry in Planck CMB maps. *Journal of Cosmology and Astroparticle Physics*, 2014(10):041–041, oct 2014. doi: 10.1088/1475-7516/2014/10/041. URL https://doi.org/10.1088%2F1475-7516%2F2014%2F10%2F041.

[38] M. V. Berry and M. Tabor. Level clustering in the regular spectrum. *Proceedings of the Royal Society of London. A. Mathematical and Physical Sciences*, 356(1686): 375–394, 1977. doi: 10.1098/rspa.1977.0140.

[39] P. Bielewicz et al. Low-order multipole maps of cosmic microwave background anisotropy derived from WMAP. *Monthly Notices of the Royal Astronomical Society*, 355(4):1283–1302, 12 2004. ISSN 0035-8711. doi: 10.1111/j.1365-2966.2004.08405.x. URL https://doi.org/10.1111/j.1365-2966.2004.08405.x.

[40] H. Blaker. Confidence curves and improved exact confidence intervals for discrete distributions. *Canadian Journal of Statistics*, 28(4):783–798, 2000. doi: 10.2307/3315916. URL https://onlinelibrary.wiley.com/doi/abs/10.2307/3315916.

[41] G. R. Blumenthal et al. Formation of galaxies and large-scale structure with cold dark matter. *Nature*, 311(5986):517–525, Oct 1984. ISSN 1476-4687. doi: 10.1038/311517a0. URL https://doi.org/10.1038/311517a0.

[42] O. Bohigas et al. Characterization of Chaotic Quantum Spectra and Universality of Level Fluctuation Laws. *Phys. Rev. Lett.*, 52:1–4, Jan 1984. doi: 10.1103/PhysRevLett.52.1. URL https://link.aps.org/doi/10.1103/PhysRevLett.52.1.

[43] J. R. Bond and G. Efstathiou. The statistics of cosmic background radiation fluctuations. *Monthly Notices of the Royal Astronomical Society*, 226(3):655–687, 06 1987. ISSN 0035-8711. doi: 10.1093/mnras/226.3.655. URL https://doi.org/10.1093/mnras/226.3.655.

[44] S. A. Bonometto and M. Sakellariadou. Physical processes in the universe at the epoch of the quark-hadron transition. *The Astrophysical Journal*, 282:370–373, July 1984. doi: 10.1086/162212.

[45] F. R. Bouchet et al. Multifrequency Wiener filtering of cosmic microwave background data with polarization. *Monthly Notices of the Royal Astronomical Society*, 302(4):

663–676, 02 1999. ISSN 0035-8711. doi: 10.1046/j.1365-8711.1999.02118.x. URL https://doi.org/10.1046/j.1365-8711.1999.02118.x.

[46] V. Bromm and A. Loeb. Formation of the First Supermassive Black Holes. *The Astrophysical Journal*, 596(1):34, oct 2003. doi: 10.1086/377529. URL https://dx.doi.org/10.1086/377529.

[47] M. Bucher. Physics of the cosmic microwave background anisotropy. *Int. J. Mod. Phys.*, D24(02):1530004, 2015. doi: 10.1142/S0218271815300049.

[48] M. Bucher and T. Louis. Filling in cosmic microwave background map missing data using constrained Gaussian realizations. *Monthly Notices of the Royal Astronomical Society*, 424(3):1694–1713, 08 2012. ISSN 0035-8711. doi: 10.1111/j.1365-2966.2012.21138.x. URL https://doi.org/10.1111/j.1365-2966.2012.21138.x.

[49] E. F. Bunn et al. Wiener Filtering of the COBE Differential Microwave Radiometer Data. *Astrophysical Journal Letters*, 432:L75, Sept. 1994. doi: 10.1086/187515. URL https://ui.adsabs.harvard.edu/abs/1994ApJ...432L..75B.

[50] J.-F. Cardoso et al. Independent Component analysis of the Cosmic Microwave Background. In *4th International Symposium on Independent Component Analysis and Blind Signal Separation (ICA03)*, Nara, Japan, Apr. 2003. URL http://hal.in2p3.fr/in2p3-00022125.

[51] A. Challinor. CMB anisotropy science: a review. *Proceedings of the International Astronomical Union*, 8(S288):42–52, 2012. doi: 10.1017/S1743921312016663.

[52] P. Chanda and R. Saha. An unbiased estimator of the full-sky CMB angular power spectrum at large scales using neural networks. *Monthly Notices of the Royal Astronomical Society*, 508(3):4600–4609, 09 2021. ISSN 0035-8711. doi: 10.1093/mnras/stab2753. URL https://doi.org/10.1093/mnras/stab2753.

[53] Z. Chang et al. Finsler space–time can explain both parity asymmetry and power deficit seen in CMB temperature anisotropies. *Monthly Notices of the Royal Astronomical*

Society, 479(1):1327–1331, 06 2018. ISSN 0035-8711. doi: 10.1093/mnras/sty1689. URL https://doi.org/10.1093/mnras/sty1689.

[54] Z. Chang et al. Anisotropic power spectrum and the observed low-l power in PLANCK CMB data. *Research in Astronomy and Astrophysics*, 18(3):029, mar 2018. doi: 10.1088/1674-4527/18/3/29. URL https://doi.org/10.1088/1674-4527/18/3/29.

[55] Y. Chen et al. 14 - Applications of artificial intelligence in astronomical big data. In L. K. et al., editor, *Big Data in Astronomy*, pages 347–375. Elsevier, 2020. ISBN 978-0-12-819084-5. doi: 10.1016/B978-0-12-819084-5.00006-7. URL https://www.sciencedirect.com/science/article/pii/B9780128190845000067.

[56] C. Cheng and Q.-G. Huang. Probing the primordial Universe from the low-multipole CMB data. *Physics Letters B*, 738:140–143, 2014. ISSN 0370-2693. doi: 10.1016/j.physletb.2014.09.036. URL https://www.sciencedirect.com/science/article/pii/S0370269314006947.

[57] C. Cheng et al. Preferred axis of CMB parity asymmetry in the masked maps. *Physics Letters B*, 757:445 – 453, 2016. ISSN 0370-2693. doi: 10.1016/j.physletb.2016.04.030. URL http://www.sciencedirect.com/science/article/pii/S0370269316301034.

[58] P. Chingangbam et al. HOT AND COLD SPOT COUNTS AS PROBES OF NON-GAUSSIANITY IN THE COSMIC MICROWAVE BACKGROUND. *The Astrophysical Journal*, 755(2):122, aug 2012. doi: 10.1088/0004-637X/755/2/122. URL https://dx.doi.org/10.1088/0004-637X/755/2/122.

[59] P. Chingangbam et al. Tensor Minkowski Functionals for random fields on the sphere. *Journal of Cosmology and Astroparticle Physics*, 2017(12):023, dec 2017. doi: 10.1088/1475-7516/2017/12/023. URL https://dx.doi.org/10.1088/1475-7516/2017/12/023.

[60] C. Chiocchetta et al. Lack-of-correlation anomaly in CMB large scale polarisation maps. *Journal of Cosmology and Astroparticle Physics*, 2021(08):015, aug 2021. doi: 10.1088/1475-7516/2021/08/015. URL https://doi.org/10.1088/1475-7516/2021/08/015.

[61] M. Choudhury et al. Using artificial neural networks to extract the 21-cm global signal from the EDGES data. *Monthly Notices of the Royal Astronomical Society*, 502(2):2815–2825, 01 2021. ISSN 0035-8711. doi: 10.1093/mnras/stab180. URL https://doi.org/10.1093/mnras/stab180.

[62] S. Colombi et al. Extreme value statistics of smooth Gaussian random fields. *Monthly Notices of the Royal Astronomical Society*, 414(3):2436–2445, 06 2011. ISSN 0035-8711. doi: 10.1111/j.1365-2966.2011.18563.x. URL https://doi.org/10.1111/j.1365-2966.2011.18563.x.

[63] C. J. Copi et al. Multipole vectors: A new representation of the CMB sky and evidence for statistical anisotropy or non-Gaussianity at $2\leqslant l\leqslant 8$. *Phys. Rev. D*, 70: 043515, August 2004.

[64] C. J. Copi et al. On the large-angle anomalies of the microwave sky. *Monthly Notices of the Royal Astronomical Society*, 367(1):79–102, 03 2006. ISSN 0035-8711. doi: 10.1111/j.1365-2966.2005.09980.x. URL https://doi.org/10.1111/j.1365-2966.2005.09980.x.

[65] C. J. Copi et al. Uncorrelated universe: Statistical anisotropy and the vanishing angular correlation function in WMAP years 1–3. *Phys. Rev. D*, 75:023507, Jan 2007. doi: 10.1103/PhysRevD.75.023507. URL https://link.aps.org/doi/10.1103/PhysRevD.75.023507.

[66] C. J. Copi et al. No large-angle correlations on the non-Galactic microwave sky. *Monthly Notices of the Royal Astronomical Society*, 399(1):295–303, 10 2009. ISSN 0035-8711. doi: 10.1111/j.1365-2966.2009.15270.x. URL https://doi.org/10.1111/j.1365-2966.2009.15270.x.

[67] C. J. Copi et al. Large angle anomalies in the CMB. *Adv. Astron.*, 2010:847541, 2010. doi: 10.1155/2010/847541.

[68] C. J. Copi et al. Lack of large-angle TT correlations persists in WMAP and Planck. *Monthly Notices of the Royal Astronomical Society*, 451(3):2978–2985, 06 2015. ISSN 0035-8711. doi: 10.1093/mnras/stv1143. URL https://doi.org/10.1093/mnras/stv1143.

[69] R. Crittenden. A Dark Energy Primer. *AIP Conference Proceedings*, 1083(1):74–95, 12 2008. ISSN 0094-243X. doi: 10.1063/1.3058582. URL https://doi.org/10.1063/1.3058582.

[70] M. Cruz et al. Detection of a non-Gaussian spot in WMAP. *Monthly Notices of the Royal Astronomical Society*, 356(1):29–40, 01 2005. ISSN 0035-8711. doi: 10.1111/j.1365-2966.2004.08419.x. URL https://doi.org/10.1111/j.1365-2966.2004.08419.x.

[71] M. Cruz et al. The non-Gaussian cold spot in Wilkinson Microwave Anisotropy Probe: significance, morphology and foreground contribution. *Monthly Notices of the Royal Astronomical Society*, 369(1):57–67, 05 2006. ISSN 0035-8711. doi: 10.1111/j.1365-2966.2006.10312.x. URL https://doi.org/10.1111/j.1365-2966.2006.10312.x.

[72] M. Cruz et al. The Non-Gaussian Cold Spot in the 3 Year Wilkinson Microwave Anisotropy ProbeData. *The Astrophysical Journal*, 655(1):11–20, jan 2007. doi: 10.1086/509703. URL https://doi.org/10.1086%2F509703.

[73] M. Cruz et al. Anomalous variance in the WMAP data and Galactic foreground residuals. *Monthly Notices of the Royal Astronomical Society*, 412(4):2383–2390, 04 2011. ISSN 0035-8711. doi: 10.1111/j.1365-2966.2010.18067.x. URL https://doi.org/10.1111/j.1365-2966.2010.18067.x.

[74] J. C. N. de Araujo. The dark energy–dominated universe. *Astroparticle Physics*, 23(2):279–286, 2005. ISSN 0927-6505. doi: 10.1016/j.astropartphys.

2004.12.004. URL https://www.sciencedirect.com/science/article/pii/S0927650504002087.

[75] W. De Boer. Grand unified theories and supersymmetry in particle physics and cosmology. *Progress in Particle and Nuclear Physics*, 33:201–301, 1994. ISSN 0146-6410. doi: 10.1016/0146-6410(94)90045-0. URL https://www.sciencedirect.com/science/article/pii/0146641094900450.

[76] J. de Dios Rojas Olvera et al. Observational Cosmology with Artificial Neural Networks. *Universe*, 8(2), 2022. ISSN 2218-1997. doi: 10.3390/universe8020120. URL https://www.mdpi.com/2218-1997/8/2/120.

[77] A. de Oliveira-Costa et al. Significance of the largest scale CMB fluctuations in WMAP. *Phys. Rev. D*, 69:063516, Mar 2004. doi: 10.1103/PhysRevD.69.063516. URL https://link.aps.org/doi/10.1103/PhysRevD.69.063516.

[78] A. de Oliveira-Costa et al. The Significance of the largest scale CMB fluctuations in WMAP. *Phys. Rev. D*, 69:063516, 2004. doi: 10.1103/PhysRevD.69.063516.

[79] J. Delabrouille and J. F. Cardoso. Diffuse source separation in CMB observations. *arXiv e-prints*, art. astro-ph/0702198, Feb. 2007. URL https://ui.adsabs.harvard.edu/abs/2007astro.ph..2198D.

[80] J. Delabrouille et al. Multidetector multicomponent spectral matching and applications for cosmic microwave background data analysis. *Monthly Notices of the Royal Astronomical Society*, 346(4):1089–1102, 12 2003. ISSN 0035-8711. doi: 10.1111/j.1365-2966.2003.07069.x. URL https://doi.org/10.1111/j.1365-2966.2003.07069.x.

[81] J. Delabrouille et al. Exploring cosmic origins with CORE: Survey requirements and mission design. *Journal of Cosmology and Astroparticle Physics*, 2018(04):014, apr 2018. doi: 10.1088/1475-7516/2018/04/014. URL https://dx.doi.org/10.1088/1475-7516/2018/04/014.

[82] K. Dialektopoulos et al. Neural network reconstruction of late-time cosmology and null tests. *Journal of Cosmology and Astroparticle Physics*, 2022(02):023, feb 2022. doi: 10.1088/1475-7516/2022/02/023. URL https://dx.doi.org/10.1088/1475-7516/2022/02/023.

[83] E. Dimastrogiovanni et al. Non-Gaussianity and Statistical Anisotropy from Vector Field Populated Inflationary Models. *Advances in Astronomy*, 2010, July 2010.

[84] S. G. Djorgovski et al. Applications of AI in Astronomy, 2022. URL https://arxiv.org/abs/2212.01493.

[85] S. Dodelson. *Modern Cosmology*. Academic Press, Elsevier Science, 2003.

[86] A. Dolgov and A. Linde. Baryon asymmetry in the inflationary universe. *Physics Letters B*, 116(5):329–334, 1982. ISSN 0370-2693. doi: 10.1016/0370-2693(82)90292-1. URL https://www.sciencedirect.com/science/article/pii/0370269382902921.

[87] A. Dresden. The fourteenth western meeting of the American Mathematical Society. *Bulletin of the American Mathematical Society*, 26(9):385 – 396, 1920. doi: bams/1183425340. URL https://doi.org/bams/1183425340.

[88] S. R. Dubey et al. Activation Functions in Deep Learning: A Comprehensive Survey and Benchmark, 2021. URL https://arxiv.org/abs/2109.14545.

[89] A. Edelman et al. Beyond universality in random matrix theory. *The Annals of Applied Probability*, 26(3):1659 – 1697, 2016. doi: 10.1214/15-AAP1129. URL https://doi.org/10.1214/15-AAP1129.

[90] F. Emmert-Streib et al. An Introductory Review of Deep Learning for Prediction Models With Big Data. *Frontiers in Artificial Intelligence*, 3, 2020. ISSN 2624-8212. doi: 10.3389/frai.2020.00004. URL https://www.frontiersin.org/articles/10.3389/frai.2020.00004.

[91] H. K. Eriksen et al. On Foreground Removal from the Wilkinson Microwave Anisotropy Probe Data by an Internal Linear Combination Method: Limitations and Implications. *Astrophysical Journal*, 612(2):633–646, Sept. 2004. doi: 10.1086/422807. URL https://ui.adsabs.harvard.edu/abs/2004ApJ...612..633E.

[92] H. K. Eriksen et al. Asymmetries in the Cosmic Microwave Background Anisotropy Field. *The Astrophysical Journal*, 605(1):14, apr 2004. doi: 10.1086/382267. URL https://dx.doi.org/10.1086/382267.

[93] H. K. Eriksen et al. Testing for non-Gaussianity in the WMAP data: Minkowski functionals and the length of the skeleton. *Astrophys. J.*, 612:64–80, 2004. doi: 10.1086/422570.

[94] H. K. Eriksen et al. Hemispherical Power Asymmetry in the Third-Year Wilkinson Microwave Anisotropy Probe Sky Maps. *The Astrophysical Journal*, 660(2):L81, apr 2007. doi: 10.1086/518091. URL https://dx.doi.org/10.1086/518091.

[95] H. K. Eriksen et al. Joint Bayesian Component Separation and CMB Power Spectrum Estimation. *Astrophysical Journal Letters*, 676(1):10–32, Mar. 2008. doi: 10.1086/525277. URL https://ui.adsabs.harvard.edu/abs/2008ApJ...676...10E.

[96] C. Escamilla-Rivera et al. A deep learning approach to cosmological dark energy models. *Journal of Cosmology and Astroparticle Physics*, 2020(03):008, mar 2020. doi: 10.1088/1475-7516/2020/03/008. URL https://dx.doi.org/10.1088/1475-7516/2020/03/008.

[97] T. T. A. et al. The Accretion History of AGNs. I. Supermassive Black Hole Population Synthesis Model. *The Astrophysical Journal*, 871(2):240, feb 2019. doi: 10.3847/1538-4357/aafb77. URL https://dx.doi.org/10.3847/1538-4357/aafb77.

[98] European Space Agency. Planck Legacy Archive. https://pla.esac.esa.int/#maps, 2018.

[99] A. Faessler et al. Beta Decay and the Cosmic Neutrino Background. *EPJ Web of Conferences*, 71:00044, 2014. doi: 10.1051/epjconf/20147100044. URL https://doi.org/10.1051/epjconf/20147100044.

[100] R. Fernández-Cobos et al. Multiresolution internal template cleaning: an application to the Wilkinson Microwave Anisotropy Probe 7-yr polarization data. *Monthly Notices of the Royal Astronomical Society*, 420(3):2162–2169, 02 2012. ISSN 0035-8711. doi: 10.1111/j.1365-2966.2011.20182.x. URL https://doi.org/10.1111/j.1365-2966.2011.20182.x.

[101] R. Fisher. *Statistical methods for research workers*. Edinburgh Oliver & Boyd, 1925.

[102] N. I. Fisher et al. *Statistical Analysis of Spherical Data*. Cambridge University Press, 1987. doi: 10.1017/CBO9780511623059.

[103] D. J. Fixsen. THE TEMPERATURE OF THE COSMIC MICROWAVE BACKGROUND. *The Astrophysical Journal*, 707(2):916–920, nov 2009. doi: 10.1088/0004-637x/707/2/916. URL https://doi.org/10.1088%2F0004-637x%2F707%2F2%2F916.

[104] P. Fosalba and E. Gaztañaga. Explaining cosmological anisotropy: evidence for causal horizons from CMB data. *Monthly Notices of the Royal Astronomical Society*, 504(4):5840–5862, 04 2021. ISSN 0035-8711. doi: 10.1093/mnras/stab1193. URL https://doi.org/10.1093/mnras/stab1193.

[105] W. A. Fowler. *Nucleosynthesis in the Early Universe*, pages 129–134. Springer Netherlands, Dordrecht, 1993. ISBN 978-94-011-1707-4. doi: 10.1007/978-94-011-1707-4_11. URL https://doi.org/10.1007/978-94-011-1707-4_11.

[106] D. Gabor. Theory of communication. Part 1: The analysis of information. *Journal of the Institution of Electrical Engineers - Part III: Radio and Communication Engineering*, 93:429–441(12), November 1946. ISSN 0367-

7540. URL https://digital-library.theiet.org/content/journals/10.1049/ji-3-2.1946.0074.

[107] V. Ganesan and P. Chingangbam. Tensor Minkowski Functionals: first application to the CMB. *Journal of Cosmology and Astroparticle Physics*, 2017(06):023, jun 2017. doi: 10.1088/1475-7516/2017/06/023. URL https://dx.doi.org/10.1088/1475-7516/2017/06/023.

[108] R. Gannouji. Introduction to Electroweak Baryogenesis. *Galaxies*, 10(6), 2022. ISSN 2075-4434. doi: 10.3390/galaxies10060116. URL https://www.mdpi.com/2075-4434/10/6/116.

[109] L. Gao et al. The first generation of stars in the Λ cold dark matter cosmology. *Monthly Notices of the Royal Astronomical Society*, 378(2):449–468, 05 2007. ISSN 0035-8711. doi: 10.1111/j.1365-2966.2007.11814.x. URL https://doi.org/10.1111/j.1365-2966.2007.11814.x.

[110] K. Garrett and G. Duda. Dark Matter: A Primer. *Advances in Astronomy*, 2011:968283, Dec 2010. ISSN 1687-7969. doi: 10.1155/2011/968283. URL https://doi.org/10.1155/2011/968283.

[111] E. Gaztañaga et al. Two-point anisotropies in WMAP and the cosmic quadrupole. *Monthly Notices of the Royal Astronomical Society*, 346(1):47–57, 11 2003. ISSN 0035-8711. doi: 10.1046/j.1365-2966.2003.07067.x. URL https://doi.org/10.1046/j.1365-2966.2003.07067.x.

[112] E. Goceri and A. Gooya. On The Importance of Batch Size for Deep Learning. In *On The Importance of Batch Size for Deep Learning*, 07 2018.

[113] B. Gold et al. SEVEN-YEAR WILKINSON MICROWAVE ANISOTROPY PROBE (WMAP*) OBSERVATIONS: GALACTIC FOREGROUND EMISSION. *The Astrophysical Journal Supplement Series*, 192(2):15, jan 2011. doi: 10.1088/0067-0049/192/2/15. URL https://dx.doi.org/10.1088/0067-0049/192/2/15.

[114] J. A. V. Gonzalez et al. Inflationary cosmology: From theory to observations, 2020. URL https://rmf.smf.mx/ojs/index.php/rmf-e/article/view/513.

[115] I. Goodfellow et al. *Deep Learning*. MIT Press, 2016. http://www.deeplearningbook.org.

[116] C. Gordon et al. Spontaneous isotropy breaking: A mechanism for CMB multipole alignments. *Phys. Rev. D*, 72:103002, Nov 2005. doi: 10.1103/PhysRevD.72.103002. URL https://link.aps.org/doi/10.1103/PhysRevD.72.103002.

[117] K. M. Górski et al. HEALPix: A Framework for High-Resolution Discretization and Fast Analysis of Data Distributed on the Sphere. *Astrophysical Journal*, 622(2): 759–771, Apr. 2005. doi: 10.1086/427976. URL https://ui.adsabs.harvard.edu/abs/2005ApJ...622..759G.

[118] P. Graff et al. BAMBI: blind accelerated multimodal Bayesian inference. *Monthly Notices of the Royal Astronomical Society*, 421(1):169–180, 03 2012. ISSN 0035-8711. doi: 10.1111/j.1365-2966.2011.20288.x. URL https://doi.org/10.1111/j.1365-2966.2011.20288.x.

[119] D. J. Griffiths. Hyperfine splitting in the ground state of hydrogen. *American Journal of Physics*, 50(8):698–703, 08 1982. ISSN 0002-9505. doi: 10.1119/1.12733. URL https://doi.org/10.1119/1.12733.

[120] T. Guhr et al. Random-matrix theories in quantum physics: common concepts. *Physics Reports*, 299(4):189–425, 1998. ISSN 0370-1573. doi: 10.1016/S0370-1573(97)00088-4. URL https://www.sciencedirect.com/science/article/pii/S0370157397000884.

[121] A. H. Guth. Inflationary universe: A possible solution to the horizon and flatness problems. *Phys. Rev. D*, 23:347–356, Jan 1981. doi: 10.1103/PhysRevD.23.347. URL https://link.aps.org/doi/10.1103/PhysRevD.23.347.

[122] I. Gómez-Vargas et al. Neural network within a Bayesian inference framework. *Journal of Physics: Conference Series*, 1723(1):012022, jan 2021. doi: 10.1088/

1742-6596/1723/1/012022. URL https://dx.doi.org/10.1088/1742-6596/1723/1/012022.

[123] A. Hajian and T. Souradeep. The Cosmic Microwave Background Bipolar Power Spectrum: Basic Formalism and Applications, 2004.

[124] A. Hajian et al. Statistical Isotropy of the Wilkinson Microwave Anisotropy Probe Data: A Bipolar Power Spectrum Analysis. *The Astrophysical Journal*, 618(2):L63, dec 2004. doi: 10.1086/427652. URL https://dx.doi.org/10.1086/427652.

[125] A. Hajian et al. Statistical Isotropy of the CMB. *The Astrophysical Journal*, 618(2): L63–L66, January 2005.

[126] R. Hamazaki et al. Universality classes of non-Hermitian random matrices. *Phys. Rev. Research*, 2:023286, Jun 2020. doi: 10.1103/PhysRevResearch.2.023286. URL https://link.aps.org/doi/10.1103/PhysRevResearch.2.023286.

[127] F. K. Hansen et al. Gabor transforms on the sphere with applications to CMB power spectrum estimation. *Monthly Notices of the Royal Astronomical Society*, 336(4): 1304–1328, 11 2002. ISSN 0035-8711. doi: 10.1046/j.1365-8711.2002.05878.x. URL https://doi.org/10.1046/j.1365-8711.2002.05878.x.

[128] F. K. Hansen et al. Testing the cosmological principle of isotropy: local power-spectrum estimates of the WMAP data. *Monthly Notices of the Royal Astronomical Society*, 354(3):641–665, 11 2004. ISSN 0035-8711. doi: 10.1111/j.1365-2966.2004.08229.x. URL https://doi.org/10.1111/j.1365-2966.2004.08229.x.

[129] F. K. Hansen et al. POWER ASYMMETRY IN COSMIC MICROWAVE BACKGROUND FLUCTUATIONS FROM FULL SKY TO SUB-DEGREE SCALES: IS THE UNIVERSE ISOTROPIC? *The Astrophysical Journal*, 704(2):1448, oct 2009. doi: 10.1088/0004-637X/704/2/1448. URL https://dx.doi.org/10.1088/0004-637X/704/2/1448.

[130] T. Hartwig et al. Descendants of the first stars: the distinct chemical signature of second-generation stars. *Monthly Notices of the Royal Astronomical Society*, 478

(2):1795–1810, 05 2018. ISSN 0035-8711. doi: 10.1093/mnras/sty1176. URL https://doi.org/10.1093/mnras/sty1176.

[131] M. G. Hauser and E. Dwek. The Cosmic Infrared Background: Measurements and Implications. *Annual Review of Astronomy and Astrophysics*, 39(1):249–307, 2001. doi: 10.1146/annurev.astro.39.1.249. URL https://doi.org/10.1146/annurev.astro.39.1.249.

[132] G. Hinshaw et al. Two-Point Correlations in the *COBE-DMR* Four-Year Anisotropy Maps. *The Astrophysical Journal*, 464(1):L25–L28, jun 1996. doi: 10.1086/310076. URL https://doi.org/10.1086/310076.

[133] G. Hinshaw et al. First-Year Wilkinson Microwave Anisotropy Probe (WMAP) Observations: The Angular Power Spectrum. *The Astrophysical Journal Supplement Series*, 148(1):135–159, sep 2003. doi: 10.1086/377225. URL https://doi.org/10.1086%2F377225.

[134] G. Hinshaw et al. Three-Year Wilkinson Microwave Anisotropy Probe (WMAP) Observations: Temperature Analysis. *The Astrophysical Journal Supplement Series*, 170(2):288, jun 2007. doi: 10.1086/513698. URL https://dx.doi.org/10.1086/513698.

[135] G. Hinshaw et al. FIVE-YEAR WILKINSON MICROWAVE ANISOTROPY PROBE OBSERVATIONS: DATA PROCESSING, SKY MAPS, AND BASIC RESULTS. *The Astrophysical Journal Supplement Series*, 180(2):225, feb 2009. doi: 10.1088/0067-0049/180/2/225. URL https://dx.doi.org/10.1088/0067-0049/180/2/225.

[136] G. Hinshaw et al. NINE-YEAR WILKINSON MICROWAVE ANISOTROPY PROBE (WMAP) OBSERVATIONS: COSMOLOGICAL PARAMETER RESULTS. *The Astrophysical Journal Supplement Series*, 208(2):19, sep 2013. doi: 10.1088/0067-0049/208/2/19. URL https://doi.org/10.1088/0067-0049/208/2/19.

[137] G. E. Hinton et al. Improving neural networks by preventing co-adaptation of feature detectors, 2012. URL https://arxiv.org/abs/1207.0580.

[138] E. Hivon et al. MASTER of the Cosmic Microwave Background Anisotropy Power Spectrum: A Fast Method for Statistical Analysis of Large and Complex Cosmic Microwave Background Data Sets. *The Astrophysical Journal*, 567(1):2, mar 2002. doi: 10.1086/338126. URL https://dx.doi.org/10.1086/338126.

[139] Y. Hoffman and E. Ribak. Constrained Realizations of Gaussian Fields: A Simple Algorithm. *The Astrophysical Journal Letters*, 380:L5, Oct. 1991. doi: 10.1086/186160.

[140] J. Hoftuft et al. INCREASING EVIDENCE FOR HEMISPHERICAL POWER ASYMMETRY IN THE FIVE-YEAR WMAP DATA. *The Astrophysical Journal*, 699(2):985, jun 2009. doi: 10.1088/0004-637X/699/2/985. URL https://dx.doi.org/10.1088/0004-637X/699/2/985.

[141] H. J. Hortua et al. Accelerating MCMC algorithms through Bayesian Deep Networks, 2020. URL https://arxiv.org/abs/2011.14276.

[142] Z. Hou et al. The hot and cold spots in five–year WMAP data. *Monthly Notices of the Royal Astronomical Society*, 396(3):1273–1286, 06 2009. ISSN 0035-8711. doi: 10.1111/j.1365-2966.2009.14810.x. URL https://doi.org/10.1111/j.1365-2966.2009.14810.x.

[143] T. Hovatta and E. Lindfors. Relativistic Jets of Blazars. *New Astronomy Reviews*, 87: 101541, 2019. ISSN 1387-6473. doi: 10.1016/j.newar.2020.101541. URL https://www.sciencedirect.com/science/article/pii/S138764732030018X.

[144] W. Hu. CMB temperature and polarization anisotropy fundamentals. *Annals of Physics*, 303(1):203–225, 2003. ISSN 0003-4916. doi: 10.1016/S0003-4916(02)00022-2. URL https://www.sciencedirect.com/science/article/pii/S0003491602000222.

[145] E. Hüllermeier and W. Waegeman. Aleatoric and epistemic uncertainty in machine learning: an introduction to concepts and methods. *Machine Learning*, 110(3): 457–506, Mar 2021. ISSN 1573-0565. doi: 10.1007/s10994-021-05946-3. URL https://doi.org/10.1007/s10994-021-05946-3.

[146] L. Husdal. On Effective Degrees of Freedom in the Early Universe. *Galaxies*, 4(4), 2016. ISSN 2075-4434. doi: 10.3390/galaxies4040078. URL https://www.mdpi.com/2075-4434/4/4/78.

[147] K. Ichiki. CMB foreground: A concise review. *Progress of Theoretical and Experimental Physics*, 2014(6), 06 2014. ISSN 2050-3911. doi: 10.1093/ptep/ptu065. URL https://doi.org/10.1093/ptep/ptu065. 06B109.

[148] N. Jarosik et al. First-Year Wilkinson Microwave Anisotropy Probe (WMAP)* Observations: On-Orbit Radiometer Characterization. *The Astrophysical Journal Supplement Series*, 148(1):29, sep 2003. doi: 10.1086/377221. URL https://dx.doi.org/10.1086/377221.

[149] I. T. Jolliffe and J. Cadima. Principal component analysis: a review and recent developments. *Philos. Trans. A Math. Phys. Eng. Sci.*, 374(2065):20150202, Apr. 2016.

[150] M. Kamionkowski et al. Statistics of cosmic microwave background polarization. *Phys. Rev. D*, 55:7368–7388, Jun 1997. doi: 10.1103/PhysRevD.55.7368. URL https://link.aps.org/doi/10.1103/PhysRevD.55.7368.

[151] A. Kashlinsky. Cosmic infrared background and Population III: an overview, 2006.

[152] K. I. Kellermann. The discovery of quasars. *Bulletin of the Astronomical Society of India*, 41(1):1, Mar. 2013. doi: 10.48550/arXiv.1304.3627.

[153] M. I. Khan and R. Saha. Level correlations of CMB temperature angular power spectrum. *Journal of Astrophysics and Astronomy*, 43(2), dec 2022. doi: 10.1007/s12036-022-09893-w. URL https://doi.org/10.1007%2Fs12036-022-09893-w.

[154] M. I. Khan and R. Saha. Isotropy statistics of CMB hot and cold spots. *Journal of Cosmology and Astroparticle Physics*, 2022(06):006, jun 2022. doi: 10.1088/1475-7516/2022/06/006. URL https://doi.org/10.1088%2F1475-7516%2F2022%2F06%2F006.

[155] C. KIEFER et al. QUANTUM-TO-CLASSICAL TRANSITION FOR FLUCTUATIONS IN THE EARLY UNIVERSE. *International Journal of Modern Physics D*, 07(03):455–462, 1998. doi: 10.1142/S0218271898000292. URL https://doi.org/10.1142/S0218271898000292.

[156] J. Kim and P. Naselsky. ANOMALOUS PARITY ASYMMETRY OF THEWILKINSON MICROWAVE ANISOTROPY PROBEPOWER SPECTRUM DATA AT LOW MULTIPOLES. *The Astrophysical Journal*, 714(2):L265–L267, April 2010. doi: 10.1088/2041-8205/714/2/l265. URL https://doi.org/10.1088%2F2041-8205%2F714%2F2%2Fl265.

[157] J. Kim and P. Naselsky. Anomalous parity asymmetry of WMAP 7-year power spectrum data at low multipoles: Is it cosmological or systematics? *Phys. Rev. D*, 82: 063002, Sep 2010. doi: 10.1103/PhysRevD.82.063002. URL https://link.aps.org/doi/10.1103/PhysRevD.82.063002.

[158] J. Kim and P. Naselsky. LACK OF ANGULAR CORRELATION AND ODD-PARITY PREFERENCE IN COSMIC MICROWAVE BACKGROUND DATA. *The Astrophysical Journal*, 739(2):79, Oct. 2011. ISSN 0004-637X, 1538-4357. doi: 10.1088/0004-637X/739/2/79. URL https://iopscience.iop.org/article/10.1088/0004-637X/739/2/79.

[159] J. Kim et al. Symmetry and Antisymmetry of the CMB Anisotropy Pattern, Aug 2012. URL https://www.hindawi.com/journals/aa/2012/960509/.

[160] D. P. Kingma and J. Ba. Adam: A Method for Stochastic Optimization, 2014. URL https://arxiv.org/abs/1412.6980.

[161] E. Komatsu. The Pursuit of Non-Gaussian Fluctuations in the Cosmic Microwave Background, 2002.

[162] E. Komatsu et al. SEVEN-YEAR WILKINSON MICROWAVE ANISOTROPY PROBE (WMAP) OBSERVATIONS: COSMOLOGICAL INTERPRETATION. *ApJS*, 192(2):18, jan 2011. doi: 10.1088/0067-0049/192/2/18. URL https://doi.org/10.1088/0067-0049/192/2/18.

[163] L. M. Krauss et al. Primordial Gravitational Waves and Cosmology. *Science*, 328(5981):989–992, 2010. doi: 10.1126/science.1179541. URL https://www.science.org/doi/abs/10.1126/science.1179541.

[164] S. Kundu. Inflation with general initial conditions for scalar perturbations. *Journal of Cosmology and Astroparticle Physics*, 2012(2):005, Feb. 2012. doi: 10.1088/1475-7516/2012/02/005. URL https://ui.adsabs.harvard.edu/abs/2012JCAP...02..005K.

[165] H. Kurki-Suonio. Cosmological Perturbation Theory, part 1. http://www.helsinki.fi/~hkurkisu/CosPer.pdf, 2022.

[166] K. Land and J. Magueijo. Is the universe odd? *Phys. Rev. D*, 72:101302, Nov 2005. doi: 10.1103/PhysRevD.72.101302. URL https://link.aps.org/doi/10.1103/PhysRevD.72.101302.

[167] K. Land and J. Magueijo. Examination of evidence for a preferred axis in the cosmic radiation anisotropy. *Phys. Rev. Lett*, 95:071301, August 2005.

[168] D. Langlois. Inflation, quantum fluctuations and cosmological perturbations, 2004.

[169] D. L. Larson and B. D. Wandelt. The Hot and Cold Spots in the Wilkinson Microwave Anisotropy Probe Data Are Not Hot and Cold Enough. *The Astrophysical Journal*, 613 (2):L85, sep 2004. doi: 10.1086/425250. URL https://dx.doi.org/10.1086/425250.

[170] D. Larson et al. COMPARING PLANCK AND WMAP: MAPS, SPECTRA, AND PARAMETERS. *The Astrophysical Journal*, 801(1):9, feb 2015. doi: 10.1088/0004-637x/801/1/9. URL https://doi.org/10.1088%2F0004-637x%2F801%2F1%2F9.

[171] C. J. Law et al. Mapping Protoplanetary Disk Vertical Structure with CO Isotopologue Line Emission. *The Astrophysical Journal*, 948(1):60, may 2023. doi: 10.3847/1538-4357/acb3c4. URL https://dx.doi.org/10.3847/1538-4357/acb3c4.

[172] S. M. Leach et al. Component separation methods for the PLANCK mission. *Astronomy and Astrophysics*, 491(2):597–615, Nov. 2008. doi: 10.1051/0004-6361:200810116. URL https://ui.adsabs.harvard.edu/abs/2008A&A...491..597L.

[173] J. Lederer. Activation Functions in Artificial Neural Networks: A Systematic Overview, 2021. URL https://arxiv.org/abs/2101.09957.

[174] G. LEMAÎTRE. The beginning of the world from the point of view of quantum theory. *Nature*, 127(3210):706–706, May 1931. ISSN 1476-4687. doi: 10.1038/127706b0. URL https://doi.org/10.1038/127706b0.

[175] A. G. Lemaître and A. S. Eddington. The Expanding Universe. *Monthly Notices of the Royal Astronomical Society*, 91(5):490–501, 03 1931. ISSN 0035-8711. doi: 10.1093/mnras/91.5.490. URL https://doi.org/10.1093/mnras/91.5.490.

[176] A. Lewis et al. Efficient Computation of Cosmic Microwave Background Anisotropies in Closed Friedmann-Robertson-Walker Models. *The Astrophysical Journal*, 538(2): 473–476, Aug. 2000. doi: 10.1086/309179.

[177] X. Li and H.-N. Lin. Finslerian dipolar modulation of the CMB power spectra at scales $2 < l < 600$. *The European Physical Journal C*, 77:5, May 2017.

[178] A. R. Liddle. The inflationary energy scale. *Phys. Rev. D*, 49:739–747, Jan 1994. doi: 10.1103/PhysRevD.49.739. URL https://link.aps.org/doi/10.1103/PhysRevD.49.739.

[179] A. Lidz et al. INTENSITY MAPPING WITH CARBON MONOXIDE EMISSION LINES AND THE REDSHIFTED 21 cm LINE. *The Astrophysical Journal*, 741(2): 70, oct 2011. doi: 10.1088/0004-637X/741/2/70. URL https://dx.doi.org/10.1088/0004-637X/741/2/70.

[180] A. Linde. A new inflationary universe scenario: A possible solution of the horizon, flatness, homogeneity, isotropy and primordial monopole problems. *Physics Letters B*, 108(6):389–393, 1982. ISSN 0370-2693. doi: 10.1016/0370-2693(82)91219-9. URL https://www.sciencedirect.com/science/article/pii/0370269382912199.

[181] A. Linde. Chaotic inflation. *Physics Letters B*, 129(3):177–181, 1983. ISSN 0370-2693. doi: 10.1016/0370-2693(83)90837-7. URL https://www.sciencedirect.com/science/article/pii/0370269383908377.

[182] P. Lipari. Introduction to neutrino physics. In *1st CERN-CLAF School of High-Energy Physics*, pages 115–199, 5 2001.

[183] J. Liu. Artificial neural network in cosmic landscape. *Journal of High Energy Physics*, 2017(12), dec 2017. doi: 10.1007/jhep12(2017)149. URL https://doi.org/10.1007%2Fjhep12%282017%29149.

[184] R. E. Lopez et al. Precision Detection of the Cosmic Neutrino Background. *Phys. Rev. Lett.*, 82:3952–3955, May 1999. doi: 10.1103/PhysRevLett.82.3952. URL https://link.aps.org/doi/10.1103/PhysRevLett.82.3952.

[185] T.-T. Lu and S.-H. Shiou. Inverses of 2 × 2 block matrices. *Computers & Mathematics with Applications*, 43(1):119–129, 2002. ISSN 0898-1221. doi: 10.1016/S0898-1221(01)00278-4. URL https://www.sciencedirect.com/science/article/pii/S0898122101002784.

[186] C. M. Bishop. *Pattern Recognition and Machine Learning*. Information Science and Statistics. Springer, New York, NY, Aug. 2016.

[187] A. Macías and A. Camacho. On the incompatibility between quantum theory and general relativity. *Physics Letters B*, 663(1):99–102, 2008. ISSN 0370-2693. doi: 10.1016/j.physletb.2008.03.052. URL https://www.sciencedirect.com/science/article/pii/S0370269308003936.

[188] A. Maleknejad et al. Gauge fields and inflation. *Physics Reports*, 528(4):161–261, 2013.

[189] A. Marcos-Caballero and E. Martínez-González. Scale-dependent dipolar modulation and the quadrupole-octopole alignment in the cmb temperature. *Journal of Cosmology and Astroparticle Physics*, 2019(10):053, oct 2019. doi: 10.1088/1475-7516/2019/10/053. URL https://dx.doi.org/10.1088/1475-7516/2019/10/053.

[190] A. Marcos-Caballero et al. The shape of cmb temperature and polarization peaks on the sphere. *Journal of Cosmology and Astroparticle Physics*, 2016(04):058, apr 2016. doi: 10.1088/1475-7516/2016/04/058. URL https://dx.doi.org/10.1088/1475-7516/2016/04/058.

[191] A. Marcos-Caballero et al. Local properties of the large-scale peaks of the cmb temperature. *Journal of Cosmology and Astroparticle Physics*, 2017(05):023, may 2017. doi: 10.1088/1475-7516/2017/05/023. URL https://dx.doi.org/10.1088/1475-7516/2017/05/023.

[192] A. Marcos-Caballero et al. Multiscale analysis of the CMB temperature derivatives. *Journal of Cosmology and Astroparticle Physics*, 2017(02):026, feb 2017. doi: 10.1088/1475-7516/2017/02/026. URL https://dx.doi.org/10.1088/1475-7516/2017/02/026.

[193] J. Martin et al. Encyclopædia inflationaris. *Physics of the Dark Universe*, 5-6:75–235, 2014. ISSN 2212-6864. doi: 10.1016/j.dark.2014.01.003. URL https://www.sciencedirect.com/science/article/pii/S2212686414000053. Hunt for Dark Matter.

[194] E. Martínez-González et al. The non-Gaussian cold spot in WMAP. *New Astronomy Reviews*, 50(11):875–879, 2006. ISSN 1387-6473. doi: 10.1016/j.newar.2006.09.018. URL https://www.sciencedirect.com/science/article/pii/S1387647306001989. Fundamental Physics with Cosmic Microwave Background Radiation.

[195] W. S. McCulloch and W. Pitts. A logical calculus of the ideas immanent in nervous activity. *The Bulletin of Mathematical Biophysics*, 5(4):115–133, 1943. doi: 10.1007/bf02478259.

[196] M. L. Mehta. *Random Matrices*. Academic Press, New York, 3rd edition, 2004.

[197] A. Mennella et al. Imaging the first light: experimental challenges and future perspectives in the observation of the Cosmic Microwave Background Anisotropy, 2004.

[198] A. Mesinger, editor. *Understanding the Epoch of Cosmic Reionization*. Springer International Publishing, 2016. doi: 10.1007/978-3-319-21957-8. URL https://doi.org/10.1007%2F978-3-319-21957-8.

[199] G. Mikelsons et al. Cosmic microwave background anomalies viewed via Gumbel statistics. *Monthly Notices of the Royal Astronomical Society*, 400(2):898–902, 11 2009. ISSN 0035-8711. doi: 10.1111/j.1365-2966.2009.15503.x. URL https://doi.org/10.1111/j.1365-2966.2009.15503.x.

[200] A. Miller. A review of neural network applications in Astronomy. *Vistas in Astronomy*, 36:141–161, 1993. ISSN 0083-6656. doi: 10.1016/0083-6656(93)90118-4. URL https://www.sciencedirect.com/science/article/pii/0083665693901184.

[201] J. Miralda-Escudé. The dark age of the universe. *Science*, 300(5627):1904–1909, 2003. doi: 10.1126/science.1085325. URL https://www.science.org/doi/abs/10.1126/science.1085325.

[202] C. Monteserín et al. A low cosmic microwave background variance in the Wilkinson Microwave Anisotropy Probe data. *Monthly Notices of the Royal Astronomical Society*,

387(1):209–219, 05 2008. ISSN 0035-8711. doi: 10.1111/j.1365-2966.2008.13149.x. URL https://doi.org/10.1111/j.1365-2966.2008.13149.x.

[203] A. Moradinezhad Dizgah et al. Probing Cosmic Origins with CO and [C ii] Emission Lines. *The Astrophysical Journal Letters*, 870(1):L4, jan 2019. doi: 10.3847/2041-8213/aaf813. URL https://dx.doi.org/10.3847/2041-8213/aaf813.

[204] M. Moresco et al. Unveiling the Universe with emerging cosmological probes. *Living Reviews in Relativity*, 25(1):6, Dec 2022. ISSN 1433-8351. doi: 10.1007/s41114-022-00040-z. URL https://doi.org/10.1007/s41114-022-00040-z.

[205] A. Moss. Accelerated Bayesian inference using deep learning. *Monthly Notices of the Royal Astronomical Society*, 496(1):328–338, 05 2020. ISSN 0035-8711. doi: 10.1093/mnras/staa1469. URL https://doi.org/10.1093/mnras/staa1469.

[206] V. Mukhanov. *Physical Foundations of Cosmology*. Cambridge University Press, nov 2005. doi: 10.1017/cbo9780511790553. URL https://doi.org/10.1017%2Fcbo9780511790553.

[207] M. E. Muller. A note on a method for generating points uniformly on n-dimensional spheres. *Commun. ACM*, 2(4):19–20, apr 1959. ISSN 0001-0782. doi: 10.1145/377939.377946. URL https://doi.org/10.1145/377939.377946.

[208] P. Naselsky et al. Is the cosmic microwave background asymmetry due to the kinematic dipole? *The Astrophysical Journal*, 749(1):31, mar 2012. doi: 10.1088/0004-637X/749/1/31. URL https://dx.doi.org/10.1088/0004-637X/749/1/31.

[209] National Aeronautics and Space Administration. WMAP 9 year ILC map. https://lambda.gsfc.nasa.gov/product/map/dr5/ilc_map_get.cfm, 2012.

[210] J. Neyman. Outline of a Theory of Statistical Estimation Based on the Classical Theory of Probability. *Phil. Trans. Roy. Soc. Lond.*, A236(767):333–380, 1937. doi: 10.1098/rsta.1937.0005.

[211] A. Notari and M. Quartin. On the proper kinetic quadrupole CMB removal and the quadrupole anomalies. *Journal of Cosmology and Astroparticle Physics*, 2015(06): 047–047, jun 2015. doi: 10.1088/1475-7516/2015/06/047. URL https://doi.org/10.1088/1475-7516/2015/06/047.

[212] V. Oganesyan and D. A. Huse. Localization of interacting fermions at high temperature. *Phys. Rev. B*, 75:155111, Apr 2007. doi: 10.1103/PhysRevB.75.155111. URL https://link.aps.org/doi/10.1103/PhysRevB.75.155111.

[213] P. S. Osmer. Quasars as probes of the distant and early universe. *Scientific American*, 246(2):126–139, 2023/06/11/ 1982. URL http://www.jstor.org/stable/24966527. Full publication date: February 1982.

[214] M. Ouchi et al. Observations of the Lyman-α Universe. *Annual Review of Astronomy and Astrophysics*, 58(1):617–659, 2020. doi: 10.1146/annurev-astro-032620-021859. URL https://doi.org/10.1146/annurev-astro-032620-021859.

[215] F. Paci et al. Power asymmetries in the cosmic microwave background temperature and polarization patterns. *Monthly Notices of the Royal Astronomical Society*, 407(1): 399–404, 08 2010. ISSN 0035-8711. doi: 10.1111/j.1365-2966.2010.16905.x. URL https://doi.org/10.1111/j.1365-2966.2010.16905.x.

[216] S. Pal and R. Saha. Reconstruction of full sky cmb e and b modes spectra removing e-to-b leakage from partial sky using deep learning, 2022. URL https://arxiv.org/abs/2211.09112.

[217] S. Pal et al. Estimation of Full Sky CMB Angular Power Spectrum from High Resolution Partial Sky CMB Map Using Artificial Neural Network, 2022. URL https://arxiv.org/abs/2203.14060.

[218] R. Penrose. A generalized inverse for matrices. *Mathematical Proceedings of the Cambridge Philosophical Society*, 51(3):406–413, 1955. doi: 10.1017/S0305004100030401.

[219] P. Petitjean et al. The Lyα forest at low redshift: tracing the dark matter filaments. *Astronomy and Astrophysics*, 295:L9–L12, Mar. 1995. doi: 10.48550/arXiv.astro-ph/9502100.

[220] C. H. Peñaloza et al. Using CO line ratios to trace the physical properties of molecular clouds. *Monthly Notices of the Royal Astronomical Society*, 465(2):2277–2285, 11 2016. ISSN 0035-8711. doi: 10.1093/mnras/stw2892. URL https://doi.org/10.1093/mnras/stw2892.

[221] S. Pfalzner et al. The formation of the solar system. *Physica Scripta*, 90(6):068001, apr 2015. doi: 10.1088/0031-8949/90/6/068001. URL https://dx.doi.org/10.1088/0031-8949/90/6/068001.

[222] C. Pitrou. The tight-coupling approximation for baryon acoustic oscillations. *Physics Letters B*, 698(1):1–5, 2011. ISSN 0370-2693. doi: 10.1016/j.physletb.2011.02.058. URL https://www.sciencedirect.com/science/article/pii/S0370269311002279.

[223] D. Pogosyan et al. Non-Gaussian extrema counts for CMB maps. *Phys. Rev. D*, 84:083510, Oct 2011. doi: 10.1103/PhysRevD.84.083510. URL https://link.aps.org/doi/10.1103/PhysRevD.84.083510.

[224] F. Porcelli and G. Scibona. Large-scale structure formation via quantum fluctuations and gravitational instability, May 2014. URL https://www.scirp.org/journal/paperinformation.aspx?paperid=46224.

[225] N. Prantzos and S. Ekström. *Stellar Nucleosynthesis*, pages 1584–1592. Springer Berlin Heidelberg, Berlin, Heidelberg, 2011. ISBN 978-3-642-11274-4. doi: 10.1007/978-3-642-11274-4_1084. URL https://doi.org/10.1007/978-3-642-11274-4_1084.

[226] J. R. Pritchard and A. Loeb. 21 cm cosmology in the 21st century. *Reports on Progress in Physics*, 75(8):086901, jul 2012. doi: 10.1088/0034-4885/75/8/086901. URL https://dx.doi.org/10.1088/0034-4885/75/8/086901.

[227] U. Purkayastha et al. An accurate reconstruction of CMB E-mode signal over large angular scales using prior information of CMB covariance matrix in ILC algorithm. *Monthly Notices of the Royal Astronomical Society*, 501(4):4877–4887, 12 2020. ISSN 0035-8711. doi: 10.1093/mnras/staa3935. URL https://doi.org/10.1093/mnras/staa3935.

[228] Y.-Z. Qian and G. J. Wasserburg. Hierarchical structure formation and chemical evolution of galaxies. *The Astrophysical Journal*, 612(2):615, sep 2004. doi: 10.1086/422805. URL https://dx.doi.org/10.1086/422805.

[229] M. Quartin and A. Notari. On the significance of power asymmetries in planck CMB data at all scales. *Journal of Cosmology and Astroparticle Physics*, 2015(01):008–008, jan 2015. doi: 10.1088/1475-7516/2015/01/008. URL https://doi.org/10.1088/1475-7516/2015/01/008.

[230] J. F. Radcliffe et al. The radio emission from active galactic nuclei. *A&A*, 649: L9, 2021. doi: 10.1051/0004-6361/202140791. URL https://doi.org/10.1051/0004-6361/202140791.

[231] J. Rafelski and J. Birrell. Traveling through the universe: Back in time to the quark-gluon plasma era. *Journal of Physics: Conference Series*, 509(1):012014, may 2014. doi: 10.1088/1742-6596/509/1/012014. URL https://dx.doi.org/10.1088/1742-6596/509/1/012014.

[232] J. P. Ralston and P. Jain. The virgo alignment puzzle in propagation of radiation on cosmological scales. *International Journal of Modern Physics D*, 13:09, 2004.

[233] A. Rassat and J.-L. Starck. On preferred axes in WMAP cosmic microwave background data after subtraction of the integrated Sachs-Wolfe effect. *Astronomy & Astrophysics*, 557, September 2013.

[234] A. Rassat et al. Removal of two large-scale cosmic microwave background anomalies after subtraction of the integrated Sachs-Wolfe effect. *Astronomy and As-*

trophysics - A&A, 557:A32, 2013. doi: 10.1051/0004-6361/201219793. URL https://hal-cea.archives-ouvertes.fr/cea-01135418.

[235] A. Rassat et al. Planck CMB anomalies: astrophysical and cosmological secondary effects and the curse of masking. *Journal of Cosmology and Astroparticle Physics*, 2014(8):006, Aug. 2014. doi: 10.1088/1475-7516/2014/08/006.

[236] P. K. Rath and P. Jain. Testing the dipole modulation model in CMBR. *Journal of Cosmology and Astroparticle Physics*, 2013(12):014, dec 2013. doi: 10.1088/1475-7516/2013/12/014. URL https://dx.doi.org/10.1088/1475-7516/2013/12/014.

[237] P. K. Rath et al. Relating the inhomogeneous power spectrum to the CMB hemispherical anisotropy. *Phys. Rev. D*, 91:023515, Jan 2015. doi: 10.1103/PhysRevD.91.023515. URL https://link.aps.org/doi/10.1103/PhysRevD.91.023515.

[238] S. Reynaud et al. Quantum vacuum fluctuations. *Comptes Rendus de l'Académie des Sciences - Series IV - Physics*, 2(9):1287–1298, 2001. ISSN 1296-2147. doi: 10.1016/S1296-2147(01)01270-7. URL https://www.sciencedirect.com/science/article/pii/S1296214701012707.

[239] A. Ringwald. Prospects for the direct detection of the cosmic neutrino background. *Nuclear Physics A*, 827(1):501c–506c, 2009. ISSN 0375-9474. doi: 10.1016/j.nuclphysa.2009.05.109. URL https://www.sciencedirect.com/science/article/pii/S0375947409003753. PANIC08.

[240] F. Rosenblatt. The perceptron: a probabilistic model for information storage and organization in the brain. *Psychological review*, 65 6:386–408, 1958.

[241] D. E. Rumelhart et al. Learning representations by back-propagating errors, 1986. URL https://www.nature.com/articles/323533a0.

[242] R. Saha. A FOREGROUND-CLEANED COSMIC MICROWAVE BACKGROUND MAP FROM NON-GAUSSIANITY MEASUREMENT. *The Astrophysical Journal*, 739(2):L56, sep 2011. doi: 10.1088/2041-8205/739/2/l56. URL https://doi.org/10.1088/2041-8205/739/2/l56.

[243] M. N. Saha D.Sc. LIII. Ionization in the solar chromosphere. *The London, Edinburgh, and Dublin Philosophical Magazine and Journal of Science*, 40(238):472–488, 1920. doi: 10.1080/14786441008636148. URL https://doi.org/10.1080/14786441008636148.

[244] R. Saha et al. A Blind Estimation of the Angular Power Spectrum of CMB Anisotropy from WMAP. *Astrophysical Journal Letters*, 645(2):L89–L92, July 2006. doi: 10.1086/506321. URL https://ui.adsabs.harvard.edu/abs/2006ApJ...645L..89S.

[245] D. J. Saikia. Jets in radio galaxies and quasars: an observational perspective. *Journal of Astrophysics and Astronomy*, 43(2):97, Dec 2022. ISSN 0973-7758. doi: 10.1007/s12036-022-09863-2. URL https://doi.org/10.1007/s12036-022-09863-2.

[246] P. K. Samal et al. Testing isotropy of cosmic microwave background radiation. *Monthly Notices of the Royal Astronomical Society*, 385(4):1718–1728, 2008.

[247] P. K. Samal et al. Signals of statistical anisotropy in WMAP foreground-cleaned maps. *Monthly Notices of the Royal Astronomical Society*, 396(1):511–522, 2009.

[248] M. V. Sazhin. Hot and cold spots in the microwave background radiation. *Monthly Notices of the Royal Astronomical Society*, 216(1):25P–28P, 09 1985. ISSN 0035-8711. doi: 10.1093/mnras/216.1.25P. URL https://doi.org/10.1093/mnras/216.1.25P.

[249] A. E. SCHEIDEGGER. On the statistics of the orientation of bedding planes, grain axes, and similar sedimentological data. In *GEOLOGICAL SURVEY RESEARCH 1965 Chapter C*, pages 164–167. U.S. Geol. Survey Prof. , 1965.

[250] D. Schwarz. The first second of the Universe. *Annalen der Physik*, 515(4):220–270, 2003. doi: 10.1002/andp.20035150402. URL https://onlinelibrary.wiley.com/doi/abs/10.1002/andp.20035150402.

[251] D. J. Schwarz et al. Is the low-ℓ microwave background cosmic? *Phys. Rev. Lett*, 93 (22130):1, November 2004.

[252] D. J. Schwarz et al. Is the low-l microwave background cosmic? *Phys. Rev. Lett.*, 93: 221301, 2004. doi: 10.1103/PhysRevLett.93.221301.

[253] D. J. Schwarz et al. CMB anomalies after Planck. *Classical and Quantum Gravity*, 33(18):184001, aug 2016. doi: 10.1088/0264-9381/33/18/184001. URL https://doi.org/10.1088%2F0264-9381%2F33%2F18%2F184001.

[254] S. Seager et al. How exactly did the universe become neutral? *The Astrophysical Journal Supplement Series*, 128(2):407, jun 2000. doi: 10.1086/313388. URL https://dx.doi.org/10.1086/313388.

[255] U. Seljak and M. Zaldarriaga. CMBFAST: A microwave anisotropy code. Astrophysics Source Code Library, record ascl:9909.004, Sept. 1999.

[256] H. Shimabukuro and B. Semelin. Analysing the 21cm signal from the epoch of reionization with artificial neural networks. *Monthly Notices of the Royal Astronomical Society*, 468(4):3869–3877, 03 2017. ISSN 0035-8711. doi: 10.1093/mnras/stx734. URL https://doi.org/10.1093/mnras/stx734.

[257] C. Sivaram. Evolution of the universe through the planck epoch. *Astrophysics and Space Science*, 125(1):189–199, Aug 1986. ISSN 1572-946X. doi: 10.1007/BF00643984. URL https://doi.org/10.1007/BF00643984.

[258] J. Soda. Statistical anisotropy from anisotropic inflation. *Classical and Quantum Gravity*, 29:8, April 2012.

[259] T. Souradeep and A. Hajian. Statistical isotropy of the cosmic microwave background. *Pramana*, 62(3):793–796, 2004.

[260] D. N. Spergel et al. First-Year Wilkinson Microwave Anisotropy Probe (WMAP) Observations: Determination of Cosmological Parameters. *The Astrophysical Journal Supplement Series*, 148(1):175–194, sep 2003. doi: 10.1086/377226. URL https://doi.org/10.1086/377226.

[261] A. Spurio Mancini et al. CosmoPower: emulating cosmological power spectra for accelerated Bayesian inference from next-generation surveys. *Monthly Notices of the Royal Astronomical Society*, 511(2):1771–1788, 01 2022. ISSN 0035-8711. doi: 10.1093/mnras/stac064. URL https://doi.org/10.1093/mnras/stac064.

[262] J.-L. Starck et al. Low-b analysis and inpainting. *A&A*, 550:A15, 2013. doi: 10.1051/0004-6361/201220332. URL https://doi.org/10.1051/0004-6361/201220332.

[263] A. Starobinsky. A new type of isotropic cosmological models without singularity. *Physics Letters B*, 91(1):99–102, 1980. ISSN 0370-2693. doi: 10.1016/0370-2693(80)90670-X. URL https://www.sciencedirect.com/science/article/pii/037026938090670X.

[264] V. Sudevan and R. Saha. A Global ILC Approach in Pixel Space over Large Angular Scales of the Sky Using CMB Covariance Matrix. *The Astrophysical Journal*, 867 (1):74, Nov. 2018. ISSN 1538-4357. doi: 10.3847/1538-4357/aae439. URL https://iopscience.iop.org/article/10.3847/1538-4357/aae439.

[265] V. Sudevan and R. Saha. An application of the global ILC algorithm over large angular scales to estimate the CMB posterior using gibbs sampling. *The Astrophysical Journal*, 897(1):30, jun 2020. doi: 10.3847/1538-4357/ab964e. URL https://doi.org/10.3847/1538-4357/ab964e.

[266] R. A. Sunyaev and J. Chluba. Signals from the epoch of cosmological recombination – Karl Schwarzschild Award Lecture 2008. *Astronomische Nachrichten*, 330(7):657–674, 2009. doi: 10.1002/asna.200911237. URL https://onlinelibrary.wiley.com/doi/abs/10.1002/asna.200911237.

[267] I. Szapudi et al. Detection of a supervoid aligned with the cold spot of the cosmic microwave background. *Monthly Notices of the Royal Astronomical Society*, 450(1):288–294, 04 2015. ISSN 0035-8711. doi: 10.1093/mnras/stv488. URL https://doi.org/10.1093/mnras/stv488.

[268] R. Tagliaferri et al. Neural networks in astronomy. *Neural Netw.*, 16(3-4):297–319, Apr. 2003.

[269] M. Tegmark and G. Efstathiou. A method for subtracting foregrounds from multi-frequency CMB sky maps. *Mon. Not. Roy. Astron. Soc.*, 281:1297, 1996. doi: 10.1093/mnras/281.4.1297. URL https://ui.adsabs.harvard.edu/abs/1996MNRAS.281.1297T.

[270] M. Tegmark et al. Foregrounds and Forecasts for the Cosmic Microwave Background. *The Astrophysical Journal*, 530(1):133–165, feb 2000. doi: 10.1086/308348. URL https://doi.org/10.1086/308348.

[271] M. Tegmark et al. A high resolution foreground cleaned CMB map from WMAP. *Phys. Rev. D*, 68:123523, 2003. doi: 10.1103/PhysRevD.68.123523.

[272] A. Vafaei Sadr and S. M. S. Movahed. Clustering of local extrema in Planck CMB maps. *Monthly Notices of the Royal Astronomical Society*, 503(1):815–829, 03 2021. ISSN 0035-8711. doi: 10.1093/mnras/stab368. URL https://doi.org/10.1093/mnras/stab368.

[273] H. Van de Hulst. Radiogolven uit het wereldruim: II. Herkomst der radiogolven; Radiogolven uit het wereldruim: II. Herkomst der radiogolven; Radio waves from space. *Nederlandsch Tijdschrift voor Natuurkunde*, 11:210–221, 1945.

[274] D. A. Varshalovich et al. *Quantum Theory of Angular Momentum*. World Scientific, 1988. doi: 10.1142/0270.

[275] A. Verhamme et al. Recovering the systemic redshift of galaxies from their Lyman alpha line profile. *Monthly Notices of the Royal Astronomical Society: Letters*, 478 (1):L60–L65, 04 2018. ISSN 1745-3925. doi: 10.1093/mnrasl/sly058. URL https://doi.org/10.1093/mnrasl/sly058.

[276] P. Vielva. A comprehensive overview of the cold spot, Nov 2010. URL https://www.hindawi.com/journals/aa/2010/592094/.

[277] P. Vielva et al. Detection of Non-Gaussianity in the Wilkinson Microwave Anisotropy Probe First-Year Data Using Spherical Wavelets. *The Astrophysical Journal*, 609 (1):22–34, jul 2004. doi: 10.1086/421007. URL https://doi.org/10.1086%2F421007.

[278] O. J. Vija Suarez. Characterization of the radiation and matter transfer functions. *Scientia et Technica*, 23(3):381–385, sep. 2018. doi: 10.22517/23447214.17301. URL https://revistas.utp.edu.co/index.php/revistaciencia/article/view/17301.

[279] J. von Neumann and R. T. Beyer. *Mathematical foundations of quantum mechanics*. Princeton Landmarks in mathematics and physics. Princenton University Press, Princenton (New Jersey), 1996. ISBN 0691028931; 9780691028934; 0691080038; 9780691080031.

[280] B. D. Wandelt, Sep 2003. URL https://www.slac.stanford.edu/econf/C030908/papers/THAT004.pdf.

[281] B. D. Wandelt et al. Cosmic microwave background anisotropy power spectrum statistics for high precision cosmology. *Phys. Rev. D*, 64:083003, Sep 2001. doi: 10.1103/PhysRevD.64.083003. URL https://link.aps.org/doi/10.1103/PhysRevD.64.083003.

[282] G.-J. Wang et al. Reconstructing functions and estimating parameters with artificial neural networks: A test with a hubble parameter and sne ia. *The Astrophysical Journal Supplement Series*, 246(1):13, jan 2020. doi: 10.3847/1538-4365/ab620b. URL https://dx.doi.org/10.3847/1538-4365/ab620b.

[283] G.-J. Wang et al. Recovering the CMB Signal with Machine Learning. *The Astrophysical Journal Supplement Series*, 260(1):13, may 2022. doi: 10.3847/1538-4365/ac5f4a. URL https://dx.doi.org/10.3847/1538-4365/ac5f4a.

[284] K. Wang et al. Computational intelligence in astronomy: A survey. *International*

Journal of Computational Intelligence Systems, 11:575–590, 2018. ISSN 1875-6883. doi: 10.2991/ijcis.11.1.43. URL https://doi.org/10.2991/ijcis.11.1.43.

[285] G. S. Watson. Equatorial distributions on a sphere. *Biometrika*, 52(1/2):193–201, 1965. ISSN 00063444. URL http://www.jstor.org/stable/2333824.

[286] G. S. Watson. The statistics of orientation data. *The Journal of Geology*, 74(5):786–797, 1966. ISSN 00221376, 15375269. URL http://www.jstor.org/stable/30060119.

[287] D. H. Weinberg et al. The Lyman-α Forest as a Cosmological Tool. *AIP Conference Proceedings*, 666(1):157–169, 05 2003. ISSN 0094-243X. doi: 10.1063/1.1581786. URL https://doi.org/10.1063/1.1581786.

[288] A. Weiß et al. ALMA REDSHIFTS OF MILLIMETER-SELECTED GALAXIES FROM THE SPT SURVEY: THE REDSHIFT DISTRIBUTION OF DUSTY STAR-FORMING GALAXIES. *The Astrophysical Journal*, 767(1):88, mar 2013. doi: 10.1088/0004-637X/767/1/88. URL https://dx.doi.org/10.1088/0004-637X/767/1/88.

[289] H. Weytjens and J. De Weerdt. Learning uncertainty with artificial neural networks for improved remaining time prediction of business processes. In A. Polyvyanyy, M. T. Wynn, A. Van Looy, and M. Reichert, editors, *Business Process Management*, pages 141–157, Cham, 2021. Springer International Publishing. ISBN 978-3-030-85469-0.

[290] M. White et al. Cosmic Variance in Cosmic Microwave Background Anisotropies: From 1 degrees to COBE. *The Astrophysical Journal*, 418:535, Dec. 1993. doi: 10.1086/173415.

[291] R. W. Wilson et al. A determination of the carbon and oxygen isotopic ratios in the local interstellar medium. *The Astrophysical Journal Letters*, 243:L47–L52, Jan. 1981. doi: 10.1086/183440.

[292] N. Woodcock and M. Naylor. Randomness testing in three-dimensional orientation data. *Journal of Structural Geology*, 5(5):539–548, 1983. ISSN 0191-8141. doi: 10.

1016/0191-8141(83)90058-5. URL https://www.sciencedirect.com/science/article/pii/0191814183900585.

[293] N. H. WOODCOCK. Specification of fabric shapes using an eigenvalue method. *GSA Bulletin*, 88(9):1231–1236, 09 1977. ISSN 0016-7606. doi: 10.1130/0016-7606(1977)88<1231:SOFSUA>2.0.CO;2. URL https://doi.org/10.1130/0016-7606(1977)88<1231:SOFSUA>2.0.CO;2.

[294] S. K. Yadav and R. Saha. A Bayesian ILC Method for CMB B-mode Posterior Estimation and Reconstruction of Primordial Gravity Wave Signal. *The Astrophysical Journal*, 914(2):119, jun 2021. doi: 10.3847/1538-4357/abfd9b. URL https://doi.org/10.3847/1538-4357/abfd9b.

[295] C. Yanagisawa. Looking for cosmic neutrino background. *Frontiers in Physics*, 2, 2014. ISSN 2296-424X. doi: 10.3389/fphy.2014.00030. URL https://www.frontiersin.org/articles/10.3389/fphy.2014.00030.

[296] S. Yeung and M.-C. Chu. Directional variations of cosmological parameters from the Planck CMB data. *Phys. Rev. D*, 105:083508, Apr 2022. doi: 10.1103/PhysRevD.105.083508. URL https://link.aps.org/doi/10.1103/PhysRevD.105.083508.

[297] X. Ying. An overview of overfitting and its solutions. *Journal of Physics: Conference Series*, 1168(2):022022, feb 2019. doi: 10.1088/1742-6596/1168/2/022022. URL https://dx.doi.org/10.1088/1742-6596/1168/2/022022.

[298] B. Yu and T. Lu. CMB angular power spectrum from correlated primordial fluctuation. *Phys. Rev. D*, 79:043015, Feb 2009. doi: 10.1103/PhysRevD.79.043015. URL https://link.aps.org/doi/10.1103/PhysRevD.79.043015.

[299] M. Zaldarriaga and U. Seljak. All-sky analysis of polarization in the microwave background. *Phys. Rev. D*, 55:1830–1840, Feb 1997. doi: 10.1103/PhysRevD.55.1830. URL https://link.aps.org/doi/10.1103/PhysRevD.55.1830.

[300] S. Zaroubi. *The Epoch of Reionization*, pages 45–101. Springer Berlin Heidelberg, Berlin, Heidelberg, 2013. ISBN 978-3-642-32362-1. doi: 10.1007/

978-3-642-32362-1_2. URL https://doi.org/10.1007/978-3-642-32362-1_2.

[301] W. Zhao. Directional dependence of CMB parity asymmetry. *Phys. Rev. D*, 89: 023010, Jan 2014. doi: 10.1103/PhysRevD.89.023010. URL https://link.aps.org/doi/10.1103/PhysRevD.89.023010.

[302] Y. Zhou. Methods of Discovering New Physics from the Cosmic Neutrino Background. *Journal of Physics: Conference Series*, 2381(1):012079, dec 2022. doi: 10.1088/1742-6596/2381/1/012079. URL https://dx.doi.org/10.1088/1742-6596/2381/1/012079.

[303] K. Šekrst. Much ado about nothing: cosmological and anthropic limits of quantum fluctuations, 2020.

Appendices

Appendix I: List of Publications

- **Level correlations of CMB temperature angular power spectrum**

  Authors: **Md Ishaque Khan** and Rajib Saha

  Published in the Journal of Astrophysics and Astronomy (**JOAA**),

  Volume 43, Article number 100, December 19, 2022.

  Publisher doi: https://link.springer.com/article/10.1007/s12036-022-09893-w.

  Preprint doi: https://arxiv.org/abs/2101.06731.

- **Isotropy statistics of CMB hot and cold spots**

  Authors: **Md Ishaque Khan** and Rajib Saha

  Published in the Journal of Cosmology and Astroparticle Physics (**JCAP**),

  Volume 2022, Issue June 2022, Article number 006, June 8, 2022.

  Publisher doi: https://iopscience.iop.org/article/10.1088/1475-7516/2022/06/006.

  Preprint doi: https://arxiv.org/abs/2111.05886.

- **Detection of Dipole Modulation in CMB Temperature Anisotropy Maps from WMAP and Planck using Artificial Intelligence**

  Authors: **Md Ishaque Khan** and Rajib Saha

  Published in the Astrophysical Journal (**ApJ**),

  Volume 947, Issue Number 2, Article number 47, April 19, 2023.

  Publisher doi: https://iopscience.iop.org/article/10.3847/1538-4357/acbfa9.

  Preprint doi: https://arxiv.org/abs/2212.04438.

Appendix II: Curriculum Vitae

Name: Md Ishaque Khan

Address: Room 314, Hostel 1,
IISER Bhopal,
Bhopal Bypass Road,
Bhauri, Bhopal-462066,
Madhya Pradesh, India

Affiliation status: Integrated PhD student under Dr. Rajib Saha,
Department of Physics, IISER Bhopal, India

Email IDs: md.ishaque.khan113@gmail.com, ishaque16@iiserb.ac.in

Phone: (+91) 9007548149

Education

Indian Institute of Science Education and Research (IISER) Bhopal, India

Master of Science (MS) under the Integrated PhD programme, Physics

May 2019 CPI: 9.87/10.00

[*The Integrated PhD programme consists of a Master of Science degree which is awarded after* 3 *years and a PhD degree which may be awarded at the end of the complete programme of* 6-7 *years*]

Scottish Church College, University of Calcutta, Kolkata (West Bengal, India)

Bachelor of Science (Honours), Physics

June 2016 Aggregate: 82.75%

St. Thomas' Boys' School, Kolkata (West Bengal, India)

Class XII , ISC

May 2013 94.75%

St. Thomas' Boys' School, Kolkata (West Bengal, India)

Class X , ICSE

May 2011 95.80%

Technical skills

Programming Languages : Fortran, IDL/GDL, Python

Software Packages : Mathematica, Machine Learning related libraries in Python (TensorFlow, Keras, etc.), DeepSphere, HEALPix, CAMB

General : Numerical and computational methods, data analysis techniques, Monte Carlo and Molecular Dynamics simulations, Machine learning with dense and convolutional artificial neural networks (ANNs).

Academic experience

Completed projects as a Ph.D. student (2019-2022):

(a) We *devised a novel correlation estimator* based on the concept of level spacings and found a robust signal of an anomalously low mean spacing of even multipoles of Cosmic Microwave Background (CMB) temperature angular power spectrum (APS) from observed data. This work indicates *a correlation deficit which causes the even parity APS to unusually cluster together on an average.*

(b) We appropriately modified the orientation matrix to *study the extent of isotropy of CMB hot spots and cold spots* by finding the shape and strength of any non-uniformity in their placement. The results indicate an *unusually weak non-uniformity in the placement of hot and cold spots* of the CMB temperature anisotropy field, which may *share a common origin with the low temperature variance and anomalous contributions of the quadrupole and octupole*.

(c) We constructed ANNs as a demonstrative example of the *application of Artificial Intelligence to detect the dipolar modulation signal* (hypothesised to explain the hemispherical power asymmetry in the CMB). We applied our method to observed foreground-cleaned CMB maps, and were able to robustly and independently corroborate the findings in existing literature by performing a positive *detection of dipole modulation signal across all data releases from Planck and WMAP satellites, with high confidence*.

MS thesis 2018-2019: Calculated power spectrum for a power law model of conformal time and constrained the value of the power exponent using observational data (Making use of Cosmological Perturbation theory and the Arnowitt-Deser-Misner formalism).

Summer Internship 2018: As an S.N. Bose Scholar to the University of Wisconsin, Madison, U.S., in the summer of 2018, worked under Prof. Daniel J.H. Chung on a project that dealt with strongly blue tilted isocurvature perturbations possibly resulting from axions (a dark matter candidate) at the time of inflation.

Summer Internship 2017:(a) Under Dr. Rajib Saha, IISER Bhopal, studied inflation, and dark matter and dark energy candidates/models in cosmology.
(b) Under Dr. Suhas Gangadhariah, IISER Bhopal read about Random Matrix theory.

Publications

- **Detection of Dipole Modulation in CMB temperature anisotropy maps from WMAP and Planck using Artificial Intelligence**
  Authors: **Md Ishaque Khan** and Rajib Saha
  Published in the Astrophysical Journal (**ApJ**).
  Publisher doi: https://iopscience.iop.org/article/10.3847/1538-4357/acbfa9.
  Preprint doi: https://arxiv.org/abs/2212.04438.

- **Level correlations of CMB temperature angular power spectrum**
  Authors: **Md Ishaque Khan** and Rajib Saha
  Published in the Journal of Astrophysics and Astronomy (**JOAA**).
  Publisher doi: https://link.springer.com/article/10.1007/s12036-022-09893-w.

Preprint doi: https://arxiv.org/abs/2101.06731.

- **Isotropy statistics of CMB hot and cold spots**

  Authors: **Md Ishaque Khan** and Rajib Saha

  Published in the Journal of Cosmology and Astroparticle Physics (**JCAP**).

  Publisher doi: https://iopscience.iop.org/article/10.1088/1475-7516/2022/06/006.

  Preprint doi: https://arxiv.org/abs/2111.05886.

List of Referees

1. **Dr. Rajib Saha**

   Associate Professor

   Department of Physics, IISER Bhopal

   Email id: rajib@iiserb.ac.in

   Dr. Saha is a theoretical cosmologist and my Ph.D. advisor. He has been a course instructor for courses on Quantum Mechanics and Cosmology taught during my initial years of Graduate School.

2. **Dr. Subhash Chaturvedi**

   Visiting Professor

   Department of Physics, IISER Bhopal

   Email id: subhash@iiserb.ac.in

   Dr. Chaturvedi works in Quantum Information and Quantum Optics and has been a course instructor for courses on Mathematical Physics, Statistical Mechanics and Quantum Information Theory, taught during my initial years of Graduate School.

3. **Dr. Sukanta Panda**

Professor

Department of Physics, IISER Bhopal

Email id: sukanta@iiserb.ac.in

Dr. Panda is a theoretical cosmologist and has been a course instructor for courses on Quantum Field Theory, Cosmology and General Theory of Relativity taught during my initial years of Graduate School.

4. **Dr. Snigdha Thakur**

   Associate Professor

   Department of Physics, IISER Bhopal

   Email id: sthakur@iiserb.ac.in

   Dr. Thakur works in theoretical soft condensed matter physics and has been a course instructor for courses on Thermal Physics, Numerical Methods and Programming and Computational Physics, taught during my initial years of Graduate School.

Academic Achievements

- Stood 1$^{\text{st}}$ among all colleges in the **University of Calcutta, India** in the **B.Sc.(Honours) Physics** course of the period **2013-2016**.

- Selected as an **S.N. Bose Scholar, 2018**, to the University of Wisconsin-Madison, U.S. [The programme is conducted under the aegis of IUSSTF (Indo-US Science and Technology Forum), with collaborative funding by SERB (Science Engineering and Research Board), Government of India and WINStep Forward].

- Qualified the Joint Entrance Screening Test (**JEST**) in Physics 2016 [This exam is taken by undergraduates for admission to Integrated PhD programmes and by post graduates seeking admission to PhD programmes at premier institutes in India].

- Qualified the Joint Admission Test for M.Sc. (**JAM**) in Physics 2016 [This exam is taken by undergraduates for admission to M.Sc. programmes at various Indian Institutes].

- Qualified the Graduate Aptitude Test in Engineering (**GATE**) in Physics, 2018 [This exam is taken by Postgraduates in Science and Engineering for admission to PhD programmes in premier institutes or for recruitment in India].

Workshops / Schools / Conferences

- Presented a talk on the detection of the dipolar modulation signal in the CMB, and a poster on estimators of the isotropy of placements of hot and cold spots of the CMB, at the In-House Symposium of the Department of Physics, IISER Bhopal, March, 2023.

- Attended 'Frontiers in Cosmology' conference held at the Raman Research Institute, Bangalore, India from 20-24 February, 2023, and presented a poster (titled 'Isotropy statistics of CMB hot and cold spots') and a lightning talk.

- Attended 'Galaxy Formation And Evolution Across The Cosmic Time (GFEACT-2022)', organised by the Department of Physics, Visva-Bharati, Santiniketan, India, in online mode, from 13-14 December, 2022.

- Attended 'BeyondPlanck Release Conference' organised by the University of Oslo, Norway, held in online mode, 18-20 November, 2020.

- Presented a poster on the anomalously low even multipole spacings of the CMB at the In-house Symposium, Department of Physics, IISER Bhopal, January 2020.

- Attended the Winter School on ‘Cosmic Neutrino Observations at Ultra High Energy’, Indian Institute of Technology (IIT) Kanpur, India, 16-24 December, 2019.

- Attended a Workshop on ‘Geometrical and Topological Methods for Cosmological Data Analysis’, School of Physical Sciences, National Institute of Science Education and Research (NISER), Bhubaneswar, India, 20-23 July, 2019.

Awards / Honours

- In general categories (2015-16) from Scottish Church College, India:
  - Krishnalal De Medal - The most distinguished Honours student (Science), 2015-16
  - Dr. Alexander Duff Memorial Prize (Science), 2015-16.
- Categories specific to The Department of Physics, Scottish Church College, India, 2016:
  - Bhim Charan Samanta Memorial Prize
  - Charu Chandra Chaudhury Medal
  - Dhirendra Mohan Saha Roy Gold Medal
  - Lala Gopal Prosad Memorial Prize
  - Mrs. P.R. Das Memorial Medal
  - Pravat Kumar Ghosh Medal & Cash Prize
  - Rajani Kanta De Prize
  - Sachindranath Sengupta Memorial Prize
  - Anil Kumar Sen Centenary Memorial Prize
  - Certificates of merit for 1^{st}, 2^{nd} and 3^{rd} year, and a combined certificate of merit for scoring the highest in the B.Sc. (Honours) Physics course in all three years.

- 1^{st} prize in the debate on 'Nuclear energy is the energy of the future' for speaking in favour of the motion, under 'National Science Day Celebration - 2015', held at Variable Energy Cyclotron Centre (VECC), Kolkata, India, 28^{th} February, 2015.

Other Academic Roles

Worked as a *Teaching Assistant* at IISER Bhopal for four courses:

- Physics through Computational Thinking (Spring semester, 2021)
- Introduction to Astrophysics (Fall semester, 2020)
- Physics through Computational Thinking (Spring semester, 2020)
- Waves and Optics (Fall semester, 2019)

Co-curricular activities

- Editor-in-Chief, Uday (The Institute Magazine of IISER Bhopal), 2019-20.
- Academic Student Representative (Post-Graduate), IISER Bhopal, 2019-20.
- Integrated PhD Department Representative for Physics, IISER Bhopal, 2017-18.
- Board Member, Editorial (English), Uday (The Institute Magazine of IISER Bhopal), 2016-2019.
- Member of "Hoonkar", the Nukkad Natak (Street-Play) group of IISER Bhopal, 2016-2022.
- Student Writer (Coordinator) for Voices, The Statesman, Kolkata, 2008-2013, and recipient of the Sukanya Sengupta Memorial Rolling Trophy for the Best Coordinator (Voices), 2010-2011.

Community Service

Taught underprivileged children of non-staff employees of IISER Bhopal, as a member of 'Shiksha Kendra', 2017-19.